Universidade de São Paulo
Instituto de Física

Emaranhamento de quatro modos de banda lateral em um processo de mistura de quatro ondas

Raúl Leonardo Rincón Celis

Orientador: Prof. Dr. Marcelo Martinelli

Tese apresentada ao Instituto de Física da Universidade de São Paulo, para obtenção do título de Doutor em Ciências:

Banca Examinadora:
Dr. Marcelo Martinelli - Orientador (IFUSP)
Dra. Nadja Kolb Bernardes (UFPE)
Dra. Gabriela Barreto Lemos (UFRJ)
Dr. Sergio Ricardo Muniz (USP-IFSC)
Dra. Valentina Martelli (IFUSP)

São Paulo
2022

FICHA CATALOGRÁFICA
Preparada pelo Serviço de Biblioteca e Informação
do Instituto de Física da Universidade de São Paulo

Rincon Celis, Raul Leonardo

Emaranhamento de quatro modos de banda lateral em um processo de mistura de quatro ondas. São Paulo, 2022.

Tese (Doutorado) – Universidade de São Paulo. Instituto de Física. Depto. de Física Experimental.

Orientador(a): Prof. Dr. Marcelo Martinelli.

Área de Concentração: Ótica.

Unitermos: 1. Emaranhamento; 2. Mistura de quatro ondas; 3. óptica quâtica; 4. Compressão de ruído; 5. Matriz de covariância

USP/IF/SBI-68/2022

University of São Paulo
Physics Institute

Sideband four-mode entanglement in a Four-wave mixing process

Raúl Leonardo Rincón Celis

Supervisor: Prof. Marcelo Martinelli

Ph.D thesis presented to the graduate program in Physics at the Instituto de Física, Universidade de São Paulo, Brazil, to obtain the degree of Doctor of Science:

Examining Committee:
Dr. Marcelo Martinelli - Supervisor (IFUSP)
Dra. Nadja Kolb Bernardes (UFPE)
Dra. Gabriela Barreto Lemos (UFRJ)
Dr. Sergio Ricardo Muniz (USP-IFSC)
Dra. Valentina Martelli (IFUSP)

São Paulo
2022

A minha familia

Acknowledgements

Quiero comenzar agradeciendo a mi núcleo familiar. A mi madre Claudia Patricia Celis, mi padre Victor Raúl Rincón Pascagaza, el gran amor de mi vida, mi abuelita María Celina Celis; claramente a mis hermanes Santiago y Melissa. Todo el amor que me han entregado ha sido el combustible para seguir creciendo y alcanzando mis metas.

Quero expressar o profundo agradecimento pelo time de trabalho que foi construído no nosso laboratório, agradecimento a todas as pessoas que foram essenciais pro meu desenvolvimento como cientista e como ser humano. Nesse processo, é imensurável o apoio do professor Marcelo Martinelli e do Dr. Hans Marin, que sempre estiveram dispostos para beber um café acompanhado de uma discussão física, sobre a montagem experimental, considerações da teoria, conceitos fundamentais, etc. A sua mentoria me ensinou o significado de orientar uma pesquisa, aprendi sobre a ética do físico, e sobre como ser um excelente orientador. É nesse ponto onde também quero agradecer ao professor Paulo Nussenzveig sendo que, junto com o Marcelo e o Hans, levaram essa mentoria além do profissional, virando um apoio moral e sendo conselheiros diante qualquer dúvida sobre o futuro e o trabalho como cientista num nível mais pessoal.

I would also like to acknowledge Professor Alberto Marino and my colleague Gaurav Nirala from the University of Oklahoma, who were part of this project. Our discussions about the experimental setup were crucial for generating the FWM and for understanding the observed effects.

Mi estadía en São Paulo no podría ser completa sin las personas que conocí y que se volvieron mi familia. Alvaro Montaña Guerrero, Roger Alfredo Kogler, Mayara Santana Pinto, Théo Louzada Meireles, Gabriel Couto Rickli, Felipe Lucas Gewers, Lucas Nunes Faria, Beatriz Vilela de Moura, Yuri Sacha Correa Lopes da Silva, Luiz Couto Corrêa Pinto. Ana María Paiba Amaya, Andrés Cárdenas Bocanegra, Sebastián Romero, Estefanía Vargas, Luisa Fernanda Ramíres Ochoa, Rafael Ricardo Rojas Lopez. A todos ustedes les agradezco por dejarme ser parte de su vida y por volverse mi familia.

Quienes estuvieron para guiarme cuando llegué al laboratorio y con quienes compartí largos periodos de discusions de física también hacen parte de este proceso. Igor Konieczniak, Tulio Brito Brasil, Rayssa Bruzaca de Andrade, Renné Medeiros de Araujo, Breno Marques Gonçalves Texeira, Renato Ribeiro Domeneguetti, Carlos Andrés González

Arciniegas, Pablo Jaime Palacios Ávila.

Finalmente, gostaria de agradecer ao Instituto de Física da Universidade de São Paulo pelo apoio administrativo e técnico que permitiu o desenvolvimento desse projeto. Uma total admiração e agradecimento ao Marcos Santos de Souza, Eduardo Monteiro and Sergio Kunihiro Korogui, pela assistência técnica e a total disposição para contribuir com ideias e soluções para cada problema no projeto. À Edneia Alves de Rezende, Luiz Antônio de Queiroz e Silva, Andrea Wirkus e o Éber De Patto Lima, pela ajuda sempre oportuna nas questões administrativas.

Essa tese foi financiada pela *Fundação de Amparo à Pesquisa do Estado de São Paulo*-Fapesp processo 2019/12840-0.

Abstract

We present a detailed characterization of the entanglement in a stimulated Four-wave mixing process. This process is widely studied by the *homodyne detection*, a technique insensitive to the details of the sideband modes of the involved beams. The emission profile of the FWM process in atomic media shows an imbalance in the amplification of the sidebands, which suggest an asymmetry in the entanglement of the generated states, that can not be observed by the homodyne detection.

The stimulated FWM consists on a single frequency pump and a seed beam interacting with the hot rubidium atoms, generating a pair of entangled states, the probe and the conjugated. By the implementation of the *resonantor detection*, we revealed the hidden entanglement structure of the generated beams.

We found that the usual characterization of the state through the homodyne detection is incomplete. On the contrary, the reconstruction of the covariance matrix from the *resonant detection* allows the full characterization of the quantum correlations and a more complete entanglement structure between the sideband frequency modes. Therefore, with the measurement using *resonant detection* over a Four-wave mixing process, we can demonstrate the advantage of the detection to reveal entanglement that would be hidden if the usual two-mode description is used.

Key words: Entanglement, four-wave mixing, quantum optics, squeezing, covariance matrix.

Resumo

Nesse projeto apresentamos a caracterização do emaranhamento presente em um sistema de mistura de quatro ondas estimulado (FWM). Este sistema é amplamente estudado usando a detecção homodina, técnica insensível aos detalhes dos modos de bandas laterais dos feixes gerados. O espectro de emissão do processo de mistura de quatro ondas em meios atômicos, apresenta um desbalanceio no processo de amplificação das bandas laterais, sugerindo uma assimetria no emaranhamento dos estados gerados, efeito não mensurável na detecção homodina.

O processo de mistura de quantro ondas estimulado consiste em um bombeio de frequência única e uma semente interagindo com átomos de rubídio quentes, gerando um par de estado emaranhados, o prova e conjugado. Mediante a implementação da *detecção assistida por ressonadores*, evidenciamos a estrutura oculta de emaranhamento dos feixes gerados.

Encontramos que a caracterização usando detecção homodina é incompleta. Por outro lado, a reconstrução da matriz de covariância usando ressonadores, permite a caracterização completa das correlações quânticas e a descrição integral do emaranhamento entre as bandas laterais. Portanto, mediante a medida do processo de mistura de quatro ondas implementando a *detecção assistida por ressonadores*, podemos demonstrar o benefício da detecção para evidenciar uma estrutura de emaranhamento mais completa, encoberta pela descrição de dois modos gerados.

Palavras-chave: Emaranhamento, mistura de quatro ondas, óptica quântica, compressão de ruído, matriz de covariância.

List of Figures

List of Tables

List of symbols

FWM	Four-wave mixing
$\hat{p}$	Amplitude quadrature
$\hat{q}$	Phase quadrature
$\mathbb{V}$	Covariance matrix
$\delta\hat{p}$	Fluctuations of the amplitude quadrature
$\delta\hat{q}$	Fluctuations of the phase quadrature
α_{ca}	Amplitude of the carrier
ω_{ca}	Carrier frequency
Ω	Analysis frequency
$\hat{\mathbf{X}}_{\pm\Omega}$	Quadratures in the sideband basis
$\hat{\mathbf{X}}_{s,a}$	Quadratures in the symmetric/anti-symmetric basis
$S(\Omega)$	Noise spectrum. Power spectrum. Spectral noise density.
ω_P	Pump frequency
ω_{pr}	Probe frequency
ω_{cj}	Conjugated frequency
Δ_1	One-photon detuning or pump frequency
Δ_2	Probe detuning
Δ_{ca}	Relative frequency between the carrier and the analysis cavity resonance frequency normalized by the analysis cavity bandwidth
Γ	Analysis cavity bandwidth (Half-width at half maximum)
Γ_{FWM}	FWM emission bandwidth
f	Mismatch factor

Contents

1

Introduction

Entanglement is a physical resource for quantum applications and fundamental research. It is a phenomenon where a composite system can not be described by the individual information of the constituent subsystems. Entanglement is a key property for quantum information protocols such as quantum teleportation [1], quantum memories [2], or quantum computing [3] for achieving the proclaimed advantage over classical protocols. However, the applicability of the entangled states is bound to the strength and robustness of the generated quantum correlations. Therefore, many platforms have been implemented to pursue the best source of entangled states, for instance, optical parametric oscillators (OPO) based on non-linear crystal [4], on chip OPO [5, 6], optical parametric amplifier (OPA) on rubidium atoms or on chip [7, 8]. Nowadays, the efforts are focused on the generation of multipartite quantum states which are scalable and reconfigurable [9, 10, 11].

Among these platforms, alkali atoms present some desired quantum features. Their atomic structure is simple and the coupling between ground and excited states can be tuned by the pump frequency, controlling the coupling between the energy levels which is translated into the control of the spontaneous emission. Alkali atoms have proven to be useful for the generation of quantum effects, for instance, quantum interference effects that permit the temporal delay of a quantum state using *Electromagnetic induced transparency* (EIT) [2], states with noise fluctuations below the classical limit denominated *squeezed states* for single-mode or two-mode state [12], or quantum *entanglement* [13, 14]. A reliable source of entangled states using alkali atoms is the Four-wave mixing process (FWM) where a 4-level system interacts with an off-resonant pump beam, coupling the two ground states and two virtual excited states. The FWM process generate a pair of conjugated variables that presents noise fluctuations below the classical bound, denominated a two-mode squeezed state.

FWM has been generated using sodium atoms (Na) where states with -0.3 dB of

squeezing were generated [15], cesium (Cs) where they generated -6 dB squeezed states [16], and even potassium (K) generating -1.1 dB of squeezing [17]. Among those elements, the rubidium atoms (Rb) have proven to own remarkable properties. They can be found naturally in two stable isotopes, rubidium 85 (^{85}Rb) and rubidium 87 (^{87}Rb). They have been widely studied for the generation of squeezed states and compared to K and Na, hold the record for the maximum two-mode squeezing level attaining -9.2 dB working with ^{85}Rb [18]. Compared to Cs, there are more available lasers for the Rb energy transitions. The two isotopes of rubidium are feasible for the FWM process. However, ^{87}Rb requires more resources, namely pump power and temperature, for the generation of squeezing levels near the typical values reached with ^{85}Rb. On the other hand, the internal structure of ^{85}Rb allows the generation of FWM working with the D1 (795 nm) and the D2 (780 nm) lines. Nevertheless, the D2 line presents a much smaller squeezing level [19]. Therefore, during this project, we will be working with ^{85}Rb isotope in the D1 line.

The study of the generated correlations by the FWM process, and in general continuous variable systems, is done by the reconstruction of the covariance matrix which contains the correlations between the fluctuations of a pair of conjugated observables, the amplitude and phase quadratures, of each of the generated states. In the frequency domain, the fluctuations can be decomposed into a set of relative frequencies defined as positive/upper or negative/lower, denominated the sideband of the carrier. Hence, we must measure the fluctuations of the quadratures to reconstruct the covariance matrix.

The most common method for achieving this goal is the *homodyne detection* [20]. This method uses an auxiliary beam that interferes with the state under study to amplify its fluctuations. Further processing determines if the fluctuations are below the classical limit or not. In this scheme, the generated beams are considered as a single-mode. The homodyne detection has proven to be useful for the characterization of entanglement in different systems, for instance, quantum imaging [21], multipartite states with rubidium atoms [22, 14], or multipartite entangled states generated by an OPO based on second order non-linear interactions [9, 10]. However, it lacks the capacity for distinguishing between the sideband regions and may fall into a incomplete reconstruction of the covariance matrix. This situation becomes relevant whenever the emission bandwidth of the entangled source responds differently at different sideband regions. Therefore, it is necessary to implement a detection scheme that is sensible to the incoming frequency. The *resonator detection* solves this difficulty. In this method, a resonator induces a dephasing that is sensible to the frequency such that there is an interference between different frequency components that controls the sideband and their quadratures. Simultaneously, the resonator induces a frequency-dependent attenuation, depleting the spectral mode in resonance.

The *resonator detection* has been implemented extensively at LMCAL (Laboratory for Coherent Manipulation of Atoms and Light) for the characterization of entanglement.

For instance, employing solid states crystals on an OPO, former students were able to produce multipartite states [4, 23]. A second system generates correlated states via *Four-Wave Mixing* based on chip. Chips work at room temperature and can be coupled to the current telecommunication technologies given that their spectrum is in the infrared ($1500\,nm$), representing an advantage for its implementation [24]. Finally, we implemented an OPO based on rubidium vapor cell and reconstruct the covariance matrix, finding that the output modes of the system were entangled [25].

The entanglement present in the FWM process in rubidium cell has been reported before. Previous works on FWM, characterized the quantum correlations implementing the homodyne detection [16, 21, 14, 26, 27, 7, 12]. Nonetheless, the asymmetry in the emission profile of the FWM process shows an imbalance in the amplification process of the sidebands, which suggests an asymmetry in the entanglement of the generated states, not seen by the homodyne detection. Based on the mentioned experimental results and motivated by the current research, our project aims to measure the entanglement using the *resonator detection* to determine the hidden entanglement structure of the generated beams from the FWM process using vapor rubidium cells.

This document is divided into three main parts, the theoretical concepts, experimental setup and results, and conclusions. The second chapter 2, introduces the basic properties of Gaussian states. We start with a rapid mention of the quantization of light, then we discuss the different Gaussian states with which we can represent the electromagnetic field, and we introduce the single and two-modes squeezed states as a fundamental concept for understanding quantum correlations in the continuous variable regime. Afterward, we discuss entanglement and how it is characterized through the covariance matrix and the photodetection scheme. At the end of the second chapter, we study the separability criteria that determine if a state is entangled.

The third chapter (3) presents the concept of FWM and the theoretical approach to the process. Two frameworks are presented, the first denominated phenomenological approach, where the FWM is studied as an effective interaction between light and atoms. Later we present the microscopic approach based on the Heisenberg-Langevin equations which brings a complete and accurate description of the light-matter interaction. The third chapter ends with the definition of the covariance matrix as a function of the defined variables.

The second part of the thesis involves the experimental setup and results. In the experimental setup (4) we present a detailed description of each part composing our system. The description includes the saturation spectrum for explaining how to lock the pump laser, the generation of the seed beam, and the detection scheme. We also include a detailed description of the resonator detection when the mismatch factor is included. A careful description of the electronic response of the system is also presented.

The fifth chapter corresponds to the results 5. We show the characterization of the amplification process as a function of the probe detuning Δ_2. Then we show the experimental characterization of the intensity squeezing. Finally, we present the results for the reconstruction of the covariance matrix and the entanglement characterization.

The third part of the thesis corresponds to the conclusions and the next steps. Further characterization of the experiment is found in the Appendix.

I

THEORETICAL CONCEPTS

2

Gaussian states

In the continuous variable (CV) regime, enconding and processing of the quantum information is done considering operators that belong to an infinite dimensional Hilbert space $\mathcal{H}$ and its eigenstates form a basis. A subspace of CV states which play an important role in quantum implementations are *Gaussian states*, for instance quantum teleportation [1], and quantum cryptography [28]. They are versatile resources for research in fundamental quantum correlations, and nowadays there are multiple systems capable of generating Gaussian states [15, 23, 9, 29]. They have been studied in such a detail that there are well established experimental methods for their characterization, namely, the homodyne detection [20] and resonator detection [30]. Examples of Gaussian states are thermal states, coherent states, squeezed states and the vacuum state, all of them daily present in a quantum optics laboratory. Involving the Gaussian states, there are so called *Gaussian operations* corresponding to transformations on the states that maps Gaussian states into Gaussian states. For systems with arbitrary number of modes, the operators that preserve gaussianity depends at most quadratically in the bosonic operators $\hat{a}$ and $\hat{a}^\dagger$. This set involves squeezers, beam splitters, phase shifters and their combinations.

Gaussian states and Gaussian maps are interesting since they simplify the theoretical and the experimental description of a CV system. They are characterized by their first and second moments. Higher than second order cumulants equal to zero [I]. Hence, the equations for the higher order moments depend on the first and second moments, such that we can fully describe the Gaussian states with them. A non-Gaussian state would depend on higher order cumulants describing states with a more complex representation [31, 32, 33]. Therefore, for Gaussian states the problem of working with an infinite Hilbert space is reduced to the expectation value of a product.

[I] The first order cumulant is the *mean*. The second order cumulant is the *variance*. In the case of Gaussian distributions, the first and second cumulants are equal to the central first and second moments.

Along this chapter we offer the basic toolkit for understanding quantum states in the CV regime. We start by the definition of the observables we are interested in measuring, the quadratures of the electric field and then introduce the definition and properties of some of the most relevant Gaussian states. At the end of this chapter we describe how the covariance matrix is sufficient for the reconstruction of the Gaussian states and the criteria for quantum entanglement. This chapter is based on references [34] and [3].

2.1 Field quadratures

The quantized-electromagnetic field is represented by the Hamiltonian

$$\hat{H} = \sum_{\mathbf{k},s} \hbar\omega_{\mathbf{k}s} \left(\hat{a}^\dagger_{\mathbf{k}s} \hat{a}_{\mathbf{k}s} + \frac{1}{2} \right). \tag{2.1}$$

where $\mathbf{k}$ is the wave vector, and s refers to the polarization. The Hamiltonian corresponds to the radiated energy of harmonic oscillators plus the vacuum energy for each mode $\mathbf{k}s$, representing the ground state of the quantized-electromagnetic field and its minimal energy [II] [35].

The bosonic operators $\hat{a}_{\mathbf{k}s}$ and $\hat{a}^\dagger_{\mathbf{k}s}$ satisfy:

$$[\hat{a}_{\mathbf{k}s}(t), \hat{a}_{\mathbf{k}'s'}(t)] = \left[\hat{a}^\dagger_{\mathbf{k}s}(t), \hat{a}^\dagger_{\mathbf{k}'s'}(t)\right] = 0, \tag{2.2}$$

$$\left[\hat{a}_{\mathbf{k}s}(t), \hat{a}^\dagger_{\mathbf{k}'s'}(t)\right] = \delta_{\mathbf{k},\mathbf{k}'}\delta_{s,s'}. \tag{2.3}$$

Hereafter, we will simplify the notation by considering only a single mode $\mathbf{k}s$ and $\hbar\omega_{\mathbf{k}s} = 1$ [III]. The bosonic operators $\hat{a}$ and $\hat{a}^\dagger$ can be arranged to define *mode quadratures of the field*, named $\hat{p}$ and $\hat{q}$, as follows:

$$\hat{p}_\varphi = \left(\hat{a}(t)\mathrm{e}^{-i\varphi} + \hat{a}^\dagger(t)\mathrm{e}^{i\varphi}\right), \tag{2.4}$$

$$\hat{q}_\varphi = -i\left(\hat{a}(t)\mathrm{e}^{-i\varphi} - \hat{a}^\dagger(t)\mathrm{e}^{i\varphi}\right). \tag{2.5}$$

During this thesis we will be working with bright states represented in Figure 1. A bright state can be represented in the phasor diagram by a mean value $|\alpha|$ and the phase of the state φ. Hence, we define the quadrature $\hat{p}$ aligned with the mean field of the state and will be called the *amplitude quadrature*. On the other hand, the conjugated quadrature

[II] The solutions to the Maxwell equations are denominated *modes*.

[III] We chose $\hbar\omega_{\mathbf{k}s} = 1$ for convenience but we are not redefining units. In the description of the system we will have to normalize the mathematical representation of the states and hence, the $\hbar\omega_{\mathbf{k}s}$ would be canceled.

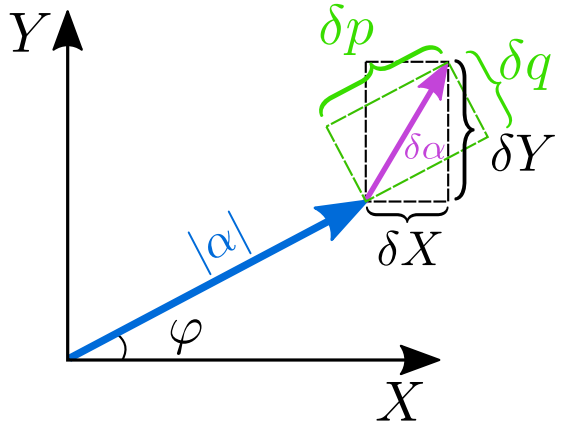

Figure 1. Quadratures of the modes of the electric field. A phasor diagram is used for representing the fields. $|\alpha|$ corresponds to the amplitude of the electric field, φ is its phase. The light green axis δp and δq, corresponds to the fluctuations of the quadratures.

$\hat{q}$ will be called the *phase quadrature*. In the figure we represent the fluctuations of the quadratures as $\delta\hat{p}$ and $\delta\hat{q}$.

2.2 Quantum states of light

Each mode of the EM field can be quantized within the framework of second quantization. Hence, each classical mode will have an associated Hilbert Space and a set of quantum states which in the context of this thesis corresponds to Gaussian states. Hence, in this section we present some of the more relevant Gaussian states.

Fock states

The operator $\hat{a}^\dagger\hat{a}$ defined in Equation 2.1 is the *number operator* ($\hat{N}$) which counts how many excitations are present in a given mode $\mathbf{k}s$. Therefore, it is an eigen-state of the Hamiltonian such that:

$$\hat{H}\,|n\rangle = E_n\,|n\rangle \tag{2.6}$$

where $E_n = (n + 1/2)$. The $|n\rangle$ states are known as *Fock states*. As $\hat{H}$ is hermitian, the Fock states are a complete orthonormal base and have real eigenvalues.

The annihilator operator $\hat{a}$ acts on the Fock state lowering the number of excitations $\hat{a}^n\,|n\rangle = \hat{a}^{n-1}\sqrt{n}\,|n-1\rangle \rightarrow \hat{a}^n\,|n\rangle = \sqrt{n!}\hat{a}\,|1\rangle$. After n successive applications, we reach the vacuum state with the corresponding energy $1/2$ such that:

$$\hat{a}^n\,|n\rangle = \frac{1}{2}\,|0\rangle\,. \tag{2.7}$$

The Fock states are non-Gaussian states. However, they form a useful basis for the representation of Gaussian states. The variances of the quadratures Equation 2.4 in the

base of the Fock states is:

$$\Delta^2\hat{p}_\varphi = \Delta^2\hat{q}_\varphi = n + \frac{1}{2}. \tag{2.8}$$

We can also associate an uncertainty relation for the generalized quadratures in the Fock basis:

$$\Delta^2\hat{p}_\varphi \Delta^2\hat{q}_\varphi = \left(n + \frac{1}{2}\right)^2. \tag{2.9}$$

The uncertainty relation increases with the number of excitations. When the Fock state is $|0\rangle$ the system is in the vacuum state, $n = 0$, and the uncertainty relation reaches its minimum value corresponding to the fluctuations of the vacuum state. The vacuum state is represented in a phasor diagram in Figure 2a by the black dashed line as a contour line at a 2D Gaussian. As the vacuum state has amplitude equal to zero, it lies at the origin of the space making its phase completely unknown. The fluctuations from a vacuum state are denominated *Standard quantum limit* (SQL), and are used as a benchmark for classicality or quantumness. An example of Gaussian states presenting fluctuations above this level are thermal states (orange area in Figure 2b). On the other hand, states presenting fluctuations below the SQL have quantum properties and are denominated squeezed states.

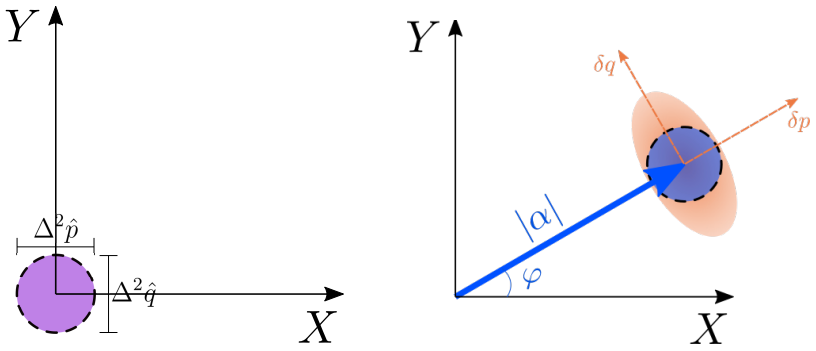

(a) Vacuum state.

(b) Coherent state and thermal state.

Figure 2. **(a)** The black dashed line represents an state that satisfy the minimum of uncertainty, the standard quantum limit. In purple there is the vacuum state with the same amount of noise and mean field equal to zero. **(b)** The coherent state, represented in blue, is a minimum uncertainty state with amplitude α and phase φ. The orange area represents a state with excess of noise, a displaced squeezed thermal state. δq and δp are the phase and amplitude quadratures correspondingly.

Coherent states

Coherent states are uncertainty limited states and have equal amount of uncertainty in amplitude and phase ($\Delta^2\hat{p} = \Delta^2\hat{q} = 1/2$). Figure 2b shows the representation of a

coherent state in the phase-space. The state is represented by a region in space and a pair of conjugated operators $\hat{p}$ and $\hat{q}$. The area of the colored region represents the product of the variances, and hence the uncertainty principle. In the case of the coherent state it is represented in blue with an amplitude α and phase φ. The coherent states can be generated by applying a *displacement operator* on the vacuum state as follows [36]:

$$|\alpha\rangle = \mathcal{D}(\alpha)\,|0\rangle\,, \tag{2.10}$$
$$= e^{-|\alpha|^2/2} e^{\alpha\hat{a}^\dagger} e^{-\alpha^*\hat{a}}\,|0\rangle\,, \tag{2.11}$$
$$= e^{\alpha\hat{a}^\dagger - \alpha^*\hat{a}}\,|0\rangle\,. \tag{2.12}$$

Therefore, the coherent states are displaced vacuum states that preserve their noise properties and satisfy the Heisenberg principle, $\Delta^2\hat{p}\Delta^2\hat{q} = 1/4$.

Squeezed states

The Heisenberg principle shows a relation between the variances of two conjugated operators and restricts the product of the fluctuations of the operators to a inequality. But it does not restrict the values of each of the variances. Therefore, it is possible to generate states where on quadrature presents a signal below the SQL, at the expense of an increase in the variance of the orthogonal quadrature, respecting the Heisenberg principle. These are the squeezed states.

Since the first experimental demonstration of squeezing using sodium atoms (around $-0.3\,dB$) [15] many systems were explored for the generation of squeezed states Among them, parametric down conversion (PDC) [37], optical parametric oscillators (OPO's) [38], and atomic systems [7]. Figure 3 shows the representation of a squeezed vacuum state (red ellipse), which can be generated by an OPO below threshold [9], and a squeezed coherent state (green ellipse), which can be generated by an OPO above threshold [4]. For a historical review of the squeezed states see [39].

Single-mode squeezed state

The squeezed states can be generated (mathematically) by an unitary transformation $S(\zeta)$, the *squeezing operator*, on a vacuum or a coherent state. For a degenerate process, the squeezing operator is [IV]:

$$S(\zeta) = e^{\left(\frac{1}{2}\zeta^*\hat{a}^2 - \frac{1}{2}\zeta\hat{a}^{\dagger 2}\right)}, \tag{2.13}$$

[IV] A degenerate process generates squeezing only in a single-mode of the field. For instance a parametric down conversion process in a medium with a second-order non-linearity χ^2 where two photons of frequency ω are generated from one with frequency 2ω.

where $\zeta = re^{i\vartheta}$ is a complex number, r is the degree of squeezing of the state and ϑ is a real number indicating the angle respect to the X axis. The squeezed state is represented in the phase-space as shown in Figure 3. For a initial vacuum state $|0\rangle$, the squeezing operator will reduce the variance of one quadrature, let say $\Delta^2\hat{p}$ at the cost of the increase of the conjugated one $\Delta^2\hat{q}$ such that the minimum uncertainty is respected.

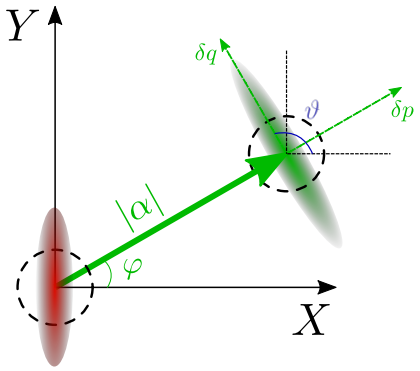

Figure 3. In red we show the squeezed vacuum state $|0,\zeta\rangle$. The green ellipse is a squeezed coherent state $|\alpha,\zeta\rangle$. ϑ is an angle respect to the X axis.

In the specific case of a squeezed coherent state, it can be generated from the vacuum state by applying the displacement operator followed by the squeezing operator [V]:

$$|\alpha,\zeta\rangle = S(\zeta)\mathcal{D}(\alpha)\,|0\rangle\,. \tag{2.14}$$

Calculating the variances of the generalized quadratures in the base of coherent states:

$$\Delta^2\hat{p}_\varphi = \frac{1}{2}\left[e^{2r}\sin^2(\varphi-\vartheta/2) + e^{-2r}\cos^2(\theta-\vartheta/2)\right]. \tag{2.15}$$

By varying ϑ it is possible to scan the variance of the state from the minimum (fluctuations below the Heisenberg limit) to the maximum (excess of noise) as illustrated in Figure 3. A similar procedure give the result for the orthogonal quadrature $\hat{q}_\varphi$ and the uncertainty relation becomes:

$$\begin{aligned}\Delta^2\hat{p}_\varphi\Delta^2\hat{q}_\varphi \;\geq\; & \frac{1}{4}\Big[\sin^4(\varphi-\vartheta/2)+\cos^4(\varphi-\vartheta/2)\\ & + 2\sin^2(\varphi-\vartheta/2)\cos^2(\varphi-\vartheta/2)\cosh(4r)\Big]\,.\end{aligned} \tag{2.16}$$

The equality is fulfilled in two cases. Firstly, when $r=0$ indicating the state is in a vacuum state, or secondly, when $2\varphi = \vartheta + n\pi$, case where the variance of one quadrature is e^{2r} and the other one is e^{-2r}. When $\varphi = \vartheta$ the ($\hat{p}$ and $\hat{q}$ defined in Equation 2.4).

[V] It is possible to produce the squeezed state by applying $\mathcal{D}(\alpha)S(\zeta)\,|0\rangle$ but the final state will be different. In [40] Chapter 21 there is a great explanation about this.

$$\Delta^2 p = \frac{1}{2}\mathrm{e}^{-2r}, \tag{2.17}$$

$$\Delta^2 q = \frac{1}{2}\mathrm{e}^{2r}, \tag{2.18}$$

such that $\Delta^2 p \Delta^2 q = 1/4$. As mentioned before, r is the compression factor indicating that the p quadrature is squeezed (below the Heisenberg limit) and the q quadrature anti-squeezed (above Heisenberg limit).

A useful insight can be obtained when operating the squeezing operator on the vacuum state in the Fock basis:

$$S(\zeta)\left|0\right\rangle = \sqrt{\mathrm{arcCosh}(r)}\sum_{n=0}^{\infty}\frac{\sqrt{(2n)!}}{n!}\left[-\frac{1}{2}\mathrm{e}^{i\theta}\tanh(r)\right]^n\left|2n\right\rangle. \tag{2.19}$$

Equation 2.19 indicates that the squeezed vacuum state is a superposition of even pair of photons. Therefore the number of photons fluctuates around zero and moreover, if the compression operator increases the mean number of photons increases as $\sinh^2(r)$; most of the excitations are generated on the first modes ($\left|0\right\rangle, \left|2\right\rangle, \left|4\right\rangle, \cdots$) [41].

Two-mode squeezed state

The squeezing can also be present in a non-degenerate process. As an example, consider the non-degenerate parametric down conversion process in a material with second order non-linearity $\chi^{(2)}$, characterized by the generation of a pair of correlated states at different frequencies ω_2 and ω_3, from an initial state with frequency ω_1 such that the energy is conserved $\omega_1 = \omega_2 + \omega_3$. The process prepare correlated states, similar to the ones in the Einstein-Podolsky-Rosen paradox [42], and for this reason the two-mode squeezed states are known as EPR-like states.

In a similar way as the single-mode, the two-mode squeezed coherent state can be generated from the vacuum by the action of the displacement operator on each mode, followed by the squeezing operator:

$$\begin{aligned}\left|\alpha_1, \alpha_2, \zeta\right\rangle &= S_{12}(\zeta)D(\alpha_1)D(\alpha_2)\left|0\right\rangle \\ &= \mathrm{e}^{\left(\zeta^*\hat{a}_1\hat{a}_2 - \zeta\hat{a}_1^\dagger\hat{a}_2^\dagger\right)}\mathrm{e}^{\left(\alpha_1\hat{a}_1^\dagger - \alpha_1^*\hat{a}_1\right)}\mathrm{e}^{\left(\alpha_2\hat{a}_2^\dagger - \alpha_2^*\hat{a}_2\right)}\left|0\right\rangle.\end{aligned} \tag{2.20}$$

On the other hand, when operated on a two mode vacuum state, the two-mode squeezed vacuum state is:

$$|\zeta_{1,2}\rangle = S_{1,2}(\zeta)\,|0_1;0_2\rangle \tag{2.21}$$

$$= \text{arcCosh}(r)\sum_{n=0}^{\infty}\left[-\mathrm{e}^{i\theta}\tanh(r)\right]^n|n_1;n_2\rangle\,. \tag{2.22}$$

The two-mode squeezed vacuum state is a superposition of the same number of photons on each mode. It is also an entangled state given that it can not be expressed as the tensor product of the composite system. We will extend the discussion about entanglement later.

An interesting fact of the two-mode squeezing states comes from the study of the statistics of each mode. Consider the mean value of an arbitrary operator $\hat{O}_i$, where $i = 1, 2$, in the base of the two-mode squeezed vacuum states:

$$\langle\zeta_{1,2}|\,\hat{O}_i\,|\zeta_{1,2}\rangle = \text{arcCosh}^2(r)\sum_{n=0}^{\infty}\left(\tanh^2(r)\right)^{2n}\langle n_i|\,\hat{O}_i\,|n_i\rangle\,, \tag{2.23}$$

and compare it to the density matrix of a thermal state:

$$\rho = \sum_{n=0}^{\infty}\left(1-\mathrm{e}^{-\beta\hbar\omega}\right)\mathrm{e}^{-\beta n\hbar\omega}\,|n\rangle\,\langle n|\,. \tag{2.24}$$

If $\tanh^2(r) = \mathrm{e}^{-\beta\hbar\omega}$ and $\overline{n} = \sinh^2(r)$, Equation 2.23 has the form of the mean value of a thermal state, independently of the operator $\hat{O}$. Therefore, the individual modes are in a thermal state, there is no possibility of full knowledge of the system by individual measurements. However, we can find the quantum correlations when studying combinations of the quadratures, saying addition or subtraction of quadratures of individual modes as depicted in Equation 2.25:

$$\hat{p}_{\pm} = \hat{p}_1 \pm \hat{p}_2, \tag{2.25}$$

$$\hat{q}_{\pm} = \hat{q}_1 \pm \hat{q}_2, \tag{2.26}$$

where the sub-index refer to two different modes. This is shown in Figure 4 where the $\delta\hat{p}_-$ and the $\delta\hat{q}_+$ quadratures presents signals below the SQL.

The advantage of the squeezing states is the possibility of enhancing the precision of measurements since $[p_{\pm}, q_{\mp}] = 0$, so there is no theoretical limitation for a precise and simultaneous measurement of both operators. The variances for the quadratures are:

$$\Delta^2 p_{\mp} = \frac{1}{2}\mathrm{e}^{\mp 2r}, \tag{2.27}$$

$$\Delta^2 q_{\pm} = \frac{1}{2}\mathrm{e}^{\mp 2r}. \tag{2.28}$$

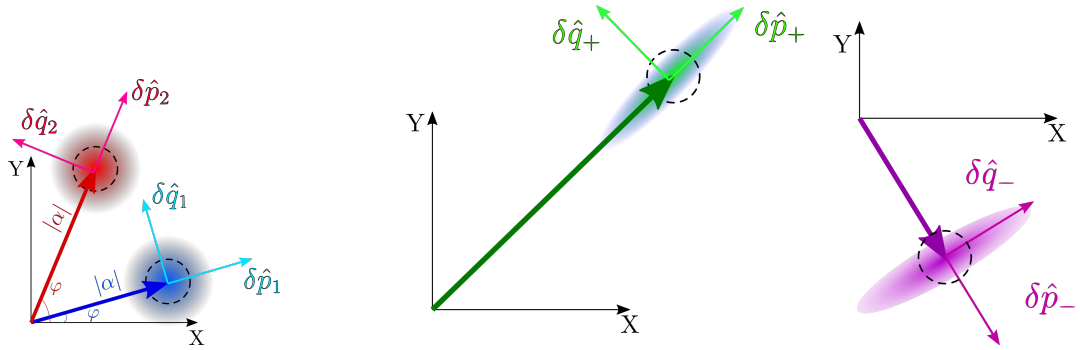

(a) Thermal state on mode 1.

(b) Thermal state on mode 2.

Figure 4. In the two-mode squeezing, individual modes are in thermal states **(a)**. When looking at the addition and subtraction of quadratures the squeezing is present in the orthogonal quadratures $\delta\hat{p}_-$ and $\delta\hat{q}_+$.

In the case of an ideal EPR state, $r \to \infty$ and we should have infinite squeezing in the $\hat{p}_-$ and in the $\hat{q}_+$ quadratures. Furthermore, the two-mode squeeze states constitute a pure state [36]. However, for quantum computing it is not necessary such a level of squeezing and the real two-mode states are not pure states. Some recent works shown that squeezing levels around $20\,dB$ are sufficient for fault-tolerant quantum computing [43].

2.3 Covariance Matrix

Given a set of N modes, we can define a $2N$ vector containing every quadrature of the modes

$$\hat{X} = (\hat{p}_1, \hat{q}_1, \ldots, \hat{p}_N, \hat{q}_N)^T, \tag{2.29}$$

such that the commutation relation is written as

$$\left[\hat{X}_n, \hat{X}_l\right] = i\mathbf{\Omega}_{nl}, \tag{2.30}$$

where $\mathbf{\Omega}$ is the N-mode symplectic form [29]

$$\mathbf{\Omega} = \bigoplus_{j=1}^{N} (i\sigma_y). \tag{2.31}$$

The symbol $\oplus$ indicates the blockwise composition of matrices, N the number of described modes, and σ_y the Y-Pauli matrix. For instance, for a two level system $N = 2$, $\hat{X} = (\hat{p}_1, \hat{q}_1, \hat{p}_2, \hat{q}_2)$ such that,

$$\mathbf{\Omega} = \begin{pmatrix} 0 & 1 & 0 & 0 \\ -1 & 0 & 0 & 0 \\ 0 & 0 & 0 & 1 \\ 0 & 0 & -1 & 0 \end{pmatrix}.$$

The latter relationships are not exclusive for Gaussian states but for any state in the CV regime. For the case of the Gaussian states, their physical properties are completely defined by the first and second moments organized in a $2N \times 2N$ covariance matrix $\mathbb{V}$ with entries given by

$$\begin{aligned} \mathbb{V}_{ij} &= \frac{1}{2}\langle\{X_i, X_j\}\rangle - \langle X_i\rangle\langle X_j\rangle, \\ &= \frac{1}{2}\langle\{\delta X_i, \delta X_j\}\rangle, \end{aligned} \tag{2.32}$$

where ij corresponds to the matrix element of the covariance matrix, and $\delta\hat{O} = \hat{O} - \langle\hat{O}\rangle$ is the fluctuation operator. The diagonal elements of the covariance matrix $\mathbb{V}$ correspond to the variances of the quadratures whereas the off-diagonal terms, to the correlations between quadratures.

The covariance matrix $\mathbb{V}$ is real, symmetric, and positive semi-definite matrix and must fulfill the relation

$$\mathbb{V} + i\mathbf{\Omega} \geq 0, \tag{2.33}$$

which is a necessary and sufficient condition for having a positive semi-definite density matrix ρ, hence, is a condition that any CV state must satisfy. The latter relation is known as the Robertson-Schrödinger uncertainty principle [34]. It must be respected by any covariance matrix in order to describe *physical states*. Hence, it is possible to establish a criteria for the *physicality* of a state by considering Equation 2.33 such that [34]:

$$Eigs\left[-(\mathbb{V}\mathbf{\Omega})^2\right] \geq 1, \tag{2.34}$$

where $Eigs$ stands for eigenvalues. Therefore, we now have a method for identifying the validity of a covariance matrix, in other words, if $\mathbb{V}$ describes physical states. Equation 2.34 will be useful as a sanity test since each reconstructed covariance matrix must be physical, as well as in the analysis of quantum correlations as will be discussed in later chapters.

2.4 Photodetection

Measurement of the properties of a state in the CV regime, implies the detection of the quadratures' statistics. As far as we are generating bright light beams, we can use

photodiodes that convert light into photocurrent. Usually, a conversion factor between light and photocurrent, called *quantum efficiency*, above 80% is desired for a reasonable reconstruction of the state. The photocurrent involves the measurement of a field composed of a bright carrier centered at frequency ω_{ca} and a full spectrum of *sidebands* at $\omega_{ca} \pm \Omega$. In the time domain (Figure 5a), the photocurrent is composed by a mean value (blue continuous line) and the fluctuations around it (purple line). In the frequency domain (Figure 5b), the photocurrent is visualized as a central peak at ω_{ca} in which most of the energy is stored (blue curve), and the sidebands situated at frequencies far from the carrier (purple lines). It is in the fluctuations of the quadratures of different modes on the sidebands that we will be looking for the quantum signatures.

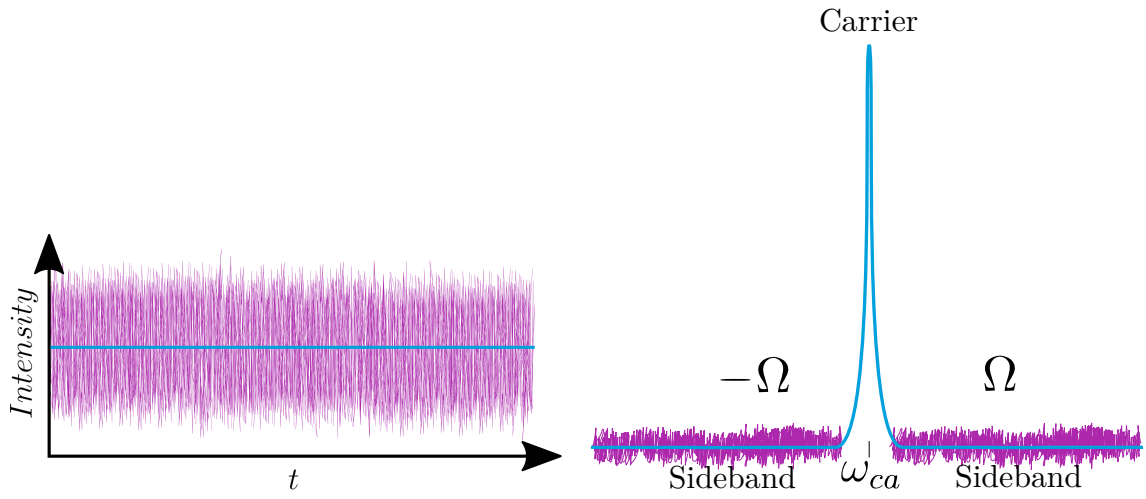

(a) Electromagnetic field in the time domain. The field can be decomposed in a mean value $\langle I \rangle$ and fluctuations ΔI around it.

(b) Electromagnetic field in the frequency domain. At the carrier frequency ω_{ca} most of the energy is stored. Around it are the sidebands.

Figure 5. Carrier and sideband representation.

The photocurrent of a single light beam is described by [44]:

$$i(t) = \kappa \hat{\mathbf{E}}^{-}(t)\hat{\mathbf{E}}^{+}(t), \tag{2.35}$$

where $i(t)$ is the photocurrent, κ is a factor that includes photodiode characteristics such as the gain and the quantum efficiency, and electronic gain, and $\hat{\mathbf{E}}^{\pm}$ is the quantized electric field.

Given an incoming beam to the photodiode, its total Hilbert space is the tensor product between the space of the carrier (considered a coherent state) and the space of the sidebands, such that the incoming state is $|\Phi\rangle = |\alpha_{ca}\rangle\,|\psi_{sd}\rangle$. The electric field is written as a combination of the carrier and the sidebands such that in the reference frame of the photodiode at $\mathbf{r} = 0$,

$$\hat{\mathbf{E}}^{+}(t) = \hat{\mathbf{E}}^{+}_{ca}(t) + \hat{\mathbf{E}}^{+}_{sd}(t) \tag{2.36}$$
$$= \alpha_{ca} + \delta\hat{a}_{sd}. \tag{2.37}$$

Here, we distinguish the carrier with the subscript *ca* and the sidebands with the subscript *sd*. Therefore, Equation 2.35 can be organized in terms of the mean field of the carrier α_{ca} and the *quadrature operator* $\delta\hat{p}_{\theta_{ca}}$ defined in Equation 2.4

$$\begin{aligned} i(t) &\approx |\alpha_{ca}|^2 + |\alpha_{ca}| \left[\delta\hat{a}_{sd}(t)\mathrm{e}^{-i\theta_{ca}} + \delta\hat{a}^{\dagger}_{sd}(t)\mathrm{e}^{i\theta_{ca}}\right] \\ i(t) &\approx |\alpha_{ca}|^2 + |\alpha_{ca}| \left[\delta\hat{p}_{\theta_{ca}}(t)\right], \end{aligned} \tag{2.38}$$

where the term $\delta\hat{a}^{\dagger}_{sd}\delta\hat{a}_{sd}$ was ignored since is much smaller than $|\alpha_{ca}|$. Equation 2.38 corresponds to the photocurrent measured by the photodiodes. The first part $|\alpha_{ca}|$ corresponds to the carrier intensity, term that will be defined as the low frequency component (DC component). The second term corresponds to the fluctuations of the quadratures on the sideband modes $\delta\hat{p}_{sd}$ that is called the high frequency component (HF component). Notice that the mean field of the carrier $|\alpha_{ca}|$ amplifies the signal coming from the fluctuations, hence, it is considered as part of the detection scheme.

A convenient transformation into the reference frame of the carrier ($\hat{a}(t) = \hat{a}\mathrm{e}^{-i\omega_{ca}t}$) eliminates the explicit time dependence. We keep the same notation for the ladder operators for simplicity.

So far we have been working in the time domain. Nonetheless, our characterization is done in the frequency domain. Therefore, we must Fourier-transform the quadrature operators $\hat{p}(t)$ and $\hat{q}(t)$. The lowering and raising operators, $\hat{a}$ and $\hat{a}^{\dagger}$, transforms as:

$$\hat{a}_{sd}(t) = \int_{\delta\omega_{ca}}^{\infty} \hat{a}_{sd}(\omega)\mathrm{e}^{-i(\omega-\omega_{ca})t}d\omega \quad ; \quad \hat{a}^{\dagger}_{sd}(t) = \int_{\delta\omega_{ca}}^{\infty} \hat{a}^{\dagger}_{sd}(\omega)\mathrm{e}^{-i(\omega-\omega_{ca})t}d\omega,$$

where ω_{ca} corresponds to the central frequency of the carrier, and $\delta\omega_{ca}$ to the linewidth of the carrier beam. The integral is done over the high frequency region, thus, the sidebands must be considered above the cutting frequency $\delta\omega_{ca}$.

In our photodiode this cutting frequency $\delta\omega_{ca}$ is 600 kHz. Hence, we define two frequency regions, the low frequency component (DC) with frequencies $|\omega_{ca} \pm \Omega| < 600$kHz, and the high frequency component (HF) composed by frequencies above 600 kHz. However, considering all the other experimental implementations, its parameters and technical limitations, the cutting frequency increases up to units of MHz from the the carrier linewidth $\delta\omega_{ca}$ [VI]. Hence, we can approximate $\delta\omega_{ca} \to 0$.

[VI] For instance, the analysis cavity has a lower frequency for measurements in the order of units of MHz

A suitable change of variable $\omega \to \omega_{ca} + \Omega$ modifies the limits of the integral such that

$$\int_0^\infty \hat{a}_{sd}(\omega) \mathrm{e}^{-i(\omega-\omega_{ca})t} d\omega \to \int_{-\omega_{ca}}^\infty \mathrm{e}^{-i\Omega t} \hat{a}_{sd}(\Omega + \omega_{ca}) d\Omega.$$

As long as $\omega_{ca} \gg \Omega$ –ω_{ca} is of the order of hundreds of THz while Ω of the order of MHz– we can approximate the lower limit of the integral $\omega_{ca} \to \infty$ to obtain:

$$\int_{-\omega_{ca}}^\infty \mathrm{e}^{-i\Omega t} \hat{a}_{sd}(\Omega + \omega_{ca}) d\Omega \approx \int_{-\infty}^\infty \mathrm{e}^{-i\Omega t} \hat{a}_{sd}(\Omega + \omega_{ca}) d\Omega.$$

We can simplify the notation by making $\omega_{ca} + \Omega \to \Omega$. Therefore, the Fourier-transform relations now reads:

$$\hat{a}_{sd}(t) = \int_{-\infty}^\infty \mathrm{e}^{-i\Omega t} \hat{a}_{sd}(\Omega) d\Omega, \tag{2.39}$$

$$\hat{a}_{sd}(\Omega) = \int_{-\infty}^\infty \mathrm{e}^{i\Omega t} \hat{a}_{sd}(t) dt, \tag{2.40}$$

and its adjoint operator

$$\hat{a}^\dagger_{sd}(t) = \int_{-\infty}^\infty \mathrm{e}^{-i\Omega t} \hat{a}^\dagger_{sd}(\Omega) d\Omega, \tag{2.41}$$

$$[\hat{a}_{sd}(\Omega)]^\dagger = \int_{-\infty}^\infty \mathrm{e}^{-i\Omega t} \hat{a}^\dagger_{sd}(t) dt = \hat{a}^\dagger(-\Omega). \tag{2.42}$$

The quadratures of the electric field in the frequency domain now read:

$$\hat{p}_\theta(\Omega) = \frac{1}{\sqrt{2}} \left(\hat{a}(\Omega) \mathrm{e}^{-i\theta} + \hat{a}^\dagger(\Omega) \mathrm{e}^{i\theta} \right), \tag{2.43}$$

$$\hat{q}_\theta(\Omega) = -\frac{i}{\sqrt{2}} \left(\hat{a}(\Omega) \mathrm{e}^{-i\theta} - \hat{a}^\dagger(\Omega) \mathrm{e}^{i\theta} \right), \tag{2.44}$$

and fulfill the commutation relation:

$$\left[\hat{a}(\Omega), \hat{a}^\dagger(\Omega') \right] = \delta(\Omega + \Omega'), \tag{2.45}$$

$$[\hat{p}_\theta(\Omega), \hat{q}_\theta(\Omega')] = i\delta(\Omega + \Omega'). \tag{2.46}$$

However, notice that $[\hat{a}_{sd}(\Omega)]^\dagger \neq \hat{a}^\dagger_{sd}(\Omega)$ since its inverse Fourier transform follows

$$\hat{a}^\dagger(\Omega) = \int_{-\infty}^\infty \mathrm{e}^{i\Omega t} \hat{a}^\dagger(t) dt. \tag{2.47}$$

From the commutation relations in Equation 2.45, we observe that the quadratures as defined so far, are composed by ladder operators of different frequency modes [45]. Hence, the quadratures in Equation 2.43 are not Hermitian operators. However, it is possible to define quadratures for a single frequency mode, denoted by the subscript $\hat{a}_{\Omega'}$ and $\hat{a}^\dagger_{\Omega'}$ and relate them to the previous ladder operators as follow:

$$\begin{aligned} \hat{a}(\Omega') \to \hat{a}_{\Omega'} \quad ; \qquad & \hat{a}(-\Omega') \to \hat{a}_{-\Omega'} \\ \hat{a}^\dagger(\Omega') \to \hat{a}^\dagger_{-\Omega'} \quad ; \qquad & [\hat{a}(\Omega')]^\dagger \to \hat{a}^\dagger_{\Omega'} \end{aligned}$$

such that, the quadratures of a single frequency mode named *sideband basis* are:

$$\hat{p}_{\pm\Omega'} = \hat{a}_{\pm\Omega'} + \hat{a}^\dagger_{\pm\Omega'}, \tag{2.48}$$

$$\hat{q}_{\pm\Omega'} = -i\left(\hat{a}_{\pm\Omega'} - \hat{a}^\dagger_{\pm\Omega'}\right), \tag{2.49}$$

fulfilling the commutation relations

$$[\hat{p}_\Omega, \hat{q}_{\Omega'}] = i\delta(\Omega - \Omega'). \tag{2.50}$$

In the *sideband basis*, the frequency Ω' refers to the frequency of the sideband around the carrier. When $\Omega' = +\Omega$ we will be referring to the *upper* sideband mode, while where $\Omega' = -\Omega$ we will be referring to the *lower* sideband. Notice that in the *sideband basis* the quadratures are hermitian operators on a single mode Ω'. The definition of the quadratures for a single sideband enable the study of quantum correlations between the upper and the lower sideband modes separately. In the following chapters we will show that the study of quantum correlations in the sideband basis reveals a richer structure of the quantum correlations.

The quadratures defined in Equation 2.43 are related to the *sideband basis* by the transformation

$$\begin{aligned} \hat{\mathbf{X}}_\Omega &= \frac{1}{2}\begin{pmatrix} 1 & i & 1 & -i \\ -i & 1 & i & 1 \\ 1 & -i & 1 & i \\ i & 1 & -i & 1 \end{pmatrix} \hat{\mathbf{X}}(\Omega), \\ \hat{\mathbf{X}}_\Omega &= \mathbf{L}\hat{\mathbf{X}}(\Omega), \end{aligned} \tag{2.51}$$

where $\hat{\mathbf{X}}_\Omega = \left(\hat{p}_{-\Omega}, \hat{q}_{-\Omega}, \hat{p}_\Omega, \hat{q}_\Omega\right)^T$, $\hat{\mathbf{X}}(\Omega) = (\hat{p}(-\Omega), \hat{q}(-\Omega), \hat{p}(\Omega), \hat{q}(\Omega))^T$. This transformation is only applicable for one mode. When dealing with two modes the space must be doubled.

A useful set of quadratures, corresponding to the *symmetric/anti-symmetric basis* (SA) must be defined. They are relevant since they appear naturally in the reconstruction of the state. The quadratures in the (SA) are defined in terms of Equation 2.49 as

$$\hat{p}_{s/a} = \hat{p}_{\Omega} \pm \hat{p}_{-\Omega}, \tag{2.52}$$

$$\hat{q}_{s/a} = \hat{q}_{\Omega} \pm \hat{q}_{-\Omega}. \tag{2.53}$$

It is possible to check that the quadratures in the SA basis fulfill the commutation relations Equation 2.45.

Finally, the quadratures in the *sideband basis* are related to the quadratures in the SA basis through a transformation (we exemplify for the case of four modes given is the case related to our experiment)

$$\hat{\mathbf{X}}_{\Omega} = \frac{1}{\sqrt{2}} \begin{pmatrix} 1 & 0 & 0 & 0 & -1 & 0 & 0 & 0 \\ 0 & 1 & 0 & 0 & 0 & -1 & 0 & 0 \\ 0 & 0 & 1 & 0 & 0 & 0 & -1 & 0 \\ 0 & 0 & 0 & 1 & 0 & 0 & 0 & -1 \\ 1 & 0 & 0 & 0 & 1 & 0 & 0 & 0 \\ 0 & 1 & 0 & 0 & 0 & 1 & 0 & 0 \\ 0 & 0 & 1 & 0 & 0 & 0 & 1 & 0 \\ 0 & 0 & 0 & 1 & 0 & 0 & 0 & 1 \end{pmatrix} \hat{\mathbf{X}}_{s/a},$$

$$\hat{\mathbf{X}}_{\Omega} = \Lambda \hat{\mathbf{X}}_{s/a}, \tag{2.54}$$

where the vectors on each basis are defined by

$$\hat{\mathbf{X}}_{\Omega} = \left\{ p_{-\Omega}^{(1)}, q_{-\Omega}^{(1)}, p_{-\Omega}^{(2)}, q_{-\Omega}^{(2)}, p_{\Omega}^{(1)}, q_{\Omega}^{(1)}, p_{\Omega}^{(2)}, q_{\Omega}^{(2)} \right\}^{T} \tag{2.55}$$

$$\hat{\mathbf{X}}_{s/a} = \left\{ p_{s}^{(1)}, q_{s}^{(1)}, p_{s}^{(2)}, q_{s}^{(2)}, p_{a}^{(1)}, q_{a}^{(1)}, p_{a}^{(2)}, q_{a}^{(2)} \right\}^{T}. \tag{2.56}$$

In general, the vectors $\hat{\mathbf{X}}$ have size of $1 \times 2k$, where 2 corresponds to the pair of quadratures $\hat{p}$, $\hat{q}$ and k to the number of modes.

During the experimental characterization, both the SA and the sideband basis will be used for the characterization of the states.

2.4.1 Noise Spectrum

The reconstruction of the state is done through the observation of the *Noise spectrum*. It corresponds to the Fourier transform of the temporal autocorrelation function

$(C(t,t'))$ of a stationary process [VII] [40] yielding the photocurrent fluctuations in a time interval τ,

$$\begin{aligned} C(\tau) &= \langle \delta i(t)\, \delta i(t+\tau) \rangle\,, \\ S(\Omega) &= \int_{-\infty}^{\infty} C(\tau) \mathrm{e}^{i\Omega\tau} d\tau. \end{aligned} \tag{2.57}$$

In terms of the photocurrent, the noise spectrum is given by

$$\begin{aligned} \langle \delta i(\Omega)\delta i(\Omega') \rangle &= \left\langle \int_{-\infty}^{\infty} \delta i(t) \mathrm{e}^{i\Omega t} dt \int_{-\infty}^{\infty} \delta i(t') \mathrm{e}^{i\Omega t'} dt' \right\rangle \\ &\quad \text{taking } \tau = t' - t \\ &= \left\langle \int_{-\infty}^{\infty} \delta i(t)\delta i(t+\tau') \mathrm{e}^{i\Omega'\tau} d\tau \int_{-\infty}^{\infty} \mathrm{e}^{it(\Omega'+\Omega)} dt \right\rangle \\ &= \int_{-\infty}^{\infty} C(\tau) \mathrm{e}^{i\Omega' t} d\tau\, 2\pi\delta\left(\Omega + \Omega'\right) \\ \langle \delta i(\Omega)\delta i(\Omega') \rangle &= S(\Omega)\delta\left(\Omega + \Omega'\right), \end{aligned} \tag{2.58}$$

where $S(\Omega)$ is the strength of the fluctuations at frequency Ω. Equation 2.58 is know as the *Wiener-Khintchine theorem* [40], that relates the variance of a measurement, the photocurrent or the fluctuation of the quadratures in our case, with the noise spectral density S of a stationery process.

From Equation 2.58 we can reconstruct the covariance matrix Equation 2.32. This will be shown in section 4.6.

2.4.2 Shot noise

The noise spectrum by itself does not yield much information, we must have a benchmark that provides a clear difference between the classical and the quantum correlations. The *standard quantum limit* (SQL) is the concept that takes this role. It was introduced in section 2.2 as a Heisenberg limited state that provides a limiting case for the precision in classical measurements. Moreover, it will be used for the calibration of the imbalance between the electronic channels and the lower bound noise level of the system. This characterization must be done for each analysis frequency Ω given that electronic components respond differently at different frequencies.

The photodetectors are only sensitive to intense fields, hence, we determine our benchmark through the *shot noise*, employing a balanced detection scheme as shown in

[VII] In a stationary process, the autocorrelation function only depends on the difference $\tau = t - t'$.

Figure 6 [20]. Consider two input beams $\hat{a}_0$ and $\hat{a}_1$ interfering in a balanced beam splitter (BS) generating two output fields $\hat{a}_3$ and $\hat{a}_4$ according to the relation

$$\begin{pmatrix} \hat{a}_3 \\ \hat{a}_4 \end{pmatrix} = \begin{pmatrix} |r| & |t| \\ |t| & -|r| \end{pmatrix} \begin{pmatrix} \hat{a}_1 \\ \hat{a}_0 \end{pmatrix}. \tag{2.59}$$

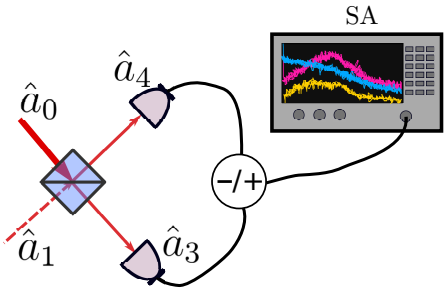

Figure 6. Balanced detection. Two input beams interfere on a beam splitter. The output is measured and the photocurrents are subtracted giving the information of the *shot noise*.

The classical fluctuations are divided equally by the balanced beam splitter and canceled in the subtraction of signals. However, the random quantum fluctuations remain and are detected. The photocurrent at ports 3 and 4 are recorded and subtracted; the photocurrent will be proportional to $\hat{I}_3 = \kappa \hat{a}_3^\dagger \hat{a}_3$ and $\hat{I}_4 = \kappa \hat{a}_4^\dagger \hat{a}_4$. Considering $\hat{a}_0$ a coherent state $|\beta\rangle$ with amplitude $\beta = |\beta| e^{i\theta}$ we would find

$$\Delta^2 I_+ = \kappa \left(\Delta^2 \hat{n}_{a_1} + \langle I_{a_0} \rangle \right), \tag{2.60}$$

$$\Delta^2 I_- = \kappa \left(\langle \hat{a}_1^\dagger \hat{a}_1 \rangle + |\beta|^2 \Delta^2 \hat{p}_\theta \right). \tag{2.61}$$

If we consider $\hat{a}_1$ as the operator from a vacuum state, the previous relation reads

$$\Delta^2 I_+ = \kappa \Delta^2 \hat{n}_a, \tag{2.62}$$

$$\Delta^2 I_- = \kappa |\alpha_1|^2 \Delta^2 \hat{X}_v. \tag{2.63}$$

Equation 2.60 describes the noise from an arbitrary state entering through port $\hat{a}_1$, whereas Equation 2.62 is the noise from the vacuum state. Equation 2.63 defines the *Shot Noise* level. It corresponds to the intensity noise from a coherent state and depends on the ampitude of the beam. The shot noise is used as the reference for measuring quantum correlations by taking the rate $\Delta^2 I_+ / \Delta^2 I_-$. If $\Delta^2 I_+ / \Delta^2 I_- > 1$ the state has excess of noise whereas the contrary case, $\Delta^2 I_+ / \Delta^2 I_- < 1$ indicates a squeezed state. In the proposed case where a vacuum state enter through the port $\hat{a}_1$, $\Delta^2 I_+ = \Delta^2 I_- = 1$. This detection scheme will be implemented in the section 4.5 when studying the intensity correlations.

2.5 Separability criteria and entanglement

The concept of *entanglement* is essential in quantum information. It is refereed as a phenomenon where a quantum state can not be fully described by a statistical mixture of their subsystems, but has to be described relating every subsystem by their joint density matrix sharing information at the quantum level. Mathematically, a quantum state that can not be written as a convex sum of tensor products of each of the subsystems is refereed as an *entangled state*, on the contrary it is a *separable state*.

In the formalism of the covariance matrix, a necessary and sufficient condition for separability of states implies that a multipartite state composed by k modes is *separable* if and only the following inequality holds:

$$\mathbb{V} \geq \mathbb{V}_A \oplus \mathbb{V}_B \oplus \cdots \oplus \mathbb{V}_k \tag{2.64}$$

where $\oplus$ indicates the block wise composition of the k matrices [46]. If this condition is not satisfied, the state is *entangled*.

Testing the entanglement is not easy by the definition itself. Several operational criteria based on the covariance matrix were proposed which are useful in experimental characterizations, among them, the *DGCZ criterion*, henceforth refereed as the *Duan criterion*, and the *Positivity under partial transpose* (PPT), which are explored in this thesis. In our experiment we will be exploring the entanglement between four modes in the SA basis or the sideband basis, two for each generated beam. Hence, we present the separability criteria in terms of the covariance matrix on each basis.

2.5.1 Duan criterion

The Duan criterion is a inseparability criterion based on the calculation of the variance of a Einstein-Podolsky-Rosen (EPR) type states as the ones presented in section 2.2. In their work, Duan and colleagues found that for separable states, the variance of the EPR-like states respect the following inequation [47]

$$\Delta^2 \hat{p}_- + \Delta^2 \hat{q}_+ \geq 1, \tag{2.65}$$

where we defined the combination of quadratures in Equation 2.25. Equation 2.65 defines a sufficient inseparability condition for Gaussian states. Nonetheless, it is not a necessary criterion since fulfillment of the inequality does not imply separability. In Figure 7 we exemplify an entangled state corresponding to the typical configuration of an EPR-state where the $\hat{q}_+$ and the $\hat{p}_-$ quadrature presents noise level below the SQL.

While the Duan criterion is enough for characterizing the entanglement for quantum teleportation [1], it ignores a certain amount of correlations since it only depends on few

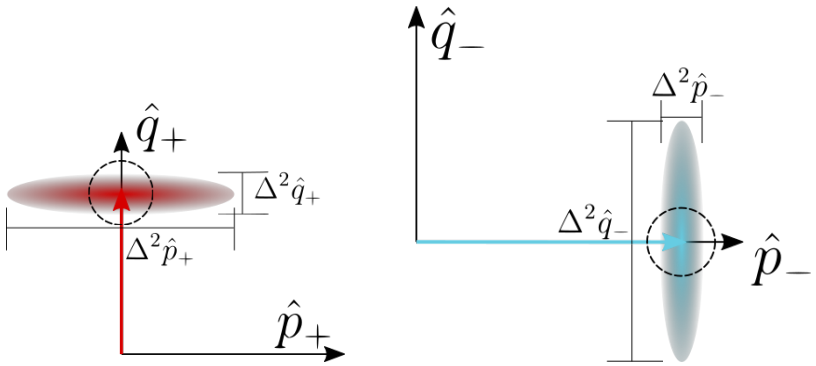

(a) Noise compression in the $\hat{q}_+$ quadrature.

(b) Noise compression in the $\hat{p}_-$ quadrature.

Figure 7. Example of an entangled state. A two-mode squeezed state presents noise signal below the SQL either in the $\hat{q}_+$ quadrature and the $\hat{p}_-$ quadrature.

elements of the covariance matrix. We discuss more about this in the appendix section A.1.

2.5.2 PPT criterion

A second approach for the study of entanglement is the *Positivity under partial transpose* criterion (PPT). This name comes from its analog in discrete variables were given a joint density matrix describing k modes, the criteria is evaluated by taking the partial transpose over selected modes [48, 49]. In the CV regime, the partial transposition amounts to a mirror reflection of one quadrature of a mode k, for instance, for a single mode

$$\hat{X} = (\hat{p}_1, \hat{q}_1)^T \xrightarrow{PT} (\hat{p}_1, -\hat{q}_1)^T . \tag{2.66}$$

This operation can be expanded to bipartite states or even multipartite states. Given a covariance matrix $\mathbb{V}$ of a quantum state of $l + k$ modes, the partial transposition of the k states is given by

$$\begin{aligned} \mathbb{V}_{PPT} &= T\mathbb{V}T, \qquad \text{with} \\ T &= \mathbb{I}_{2l} \oplus \Sigma_k, \\ \Sigma_k &= \bigoplus_{j=1}^{k} \sigma_z, \end{aligned} \tag{2.67}$$

with σ_z is the z Pauli matrix. In this way, T flips the momentum operator sign ($\hat{q}_k \to -\hat{q}_k$) of the last k modes.

Under this construction, we can evaluate the separability criterion. Given a state described by covariance matrix $\mathbb{V}$, the separable state implies in a physical matrix $\mathbb{V}_{PPT}$. If not, the state is entangled.

The PPT criteria allows the study of entanglement between bipartitions arranged in different sets. For instance, Figure 8 shows a set of modes described by its own covariance matrix V_i, $i = A, B, C, D \cdots$.The gray region represent one bipartition, whereas the light yellow represents the second bipartition under study.

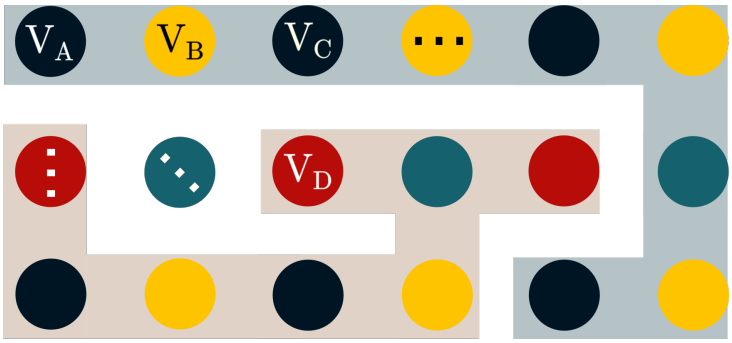

Figure 8. Bipartitions in the PPT criterion. The gray region represents one bipartition. The light yellow represents the second bipartition.

The PPT has the advantage of being a necessary and sufficient condition of entanglement for bipartitions of the form $1 \times k$ for Gaussian states.

□ □ □

This chapter was a brief introduction of Gaussian states. We presented examples of this set of states and how to fully characterize them through the first and second moments. I highly recommend the young researchers to take a look at [34, 29] for a broader introduction to the Gaussian states an its applications. Afterwards, we introduced the notion of photodetection and noise spectrum, quantum fluctuations and quadratures in the measurement setup. We established the relation between the noise spectrum and the covariance matrix for the reconstruction of the state and discuss the different interpretation between the chosen basis. At the end of the chapter we described the separability criteria that we will be using for the analysis of our experiment, namely the Duan criterion and the PPT criterion. We presented the intuition behind their formulation, and the method for their calculation. In the following chapter we discuss the use quadratures in the SA basis and the *sideband basis* for the theoretical description of the FWM process.

3

Generation of correlations by light-matter interaction

In this chapter we describe the structure of the atomic system and the light-atom interaction that generates the four-wave mixing (FWM) process. We start by the hyperfine structure of rubidium 85. Afterwards, we study the interaction between light and atoms by two different approaches: firstly, the phenomenological description of the amplification process starting from a classical description of the amplification process, and the introduction of the field operators for the study of quantum correlations. A second description, named the microscopic approach, takes into account every light-atom parameter such as the seed frequency, pump detuning, light power, atom density and among others, in the description of the Four-wave mixing process. We use the microscopic description to have a complete description of the quantum correlations produced in the generated beams of the FWM process. A broader introduction to the FWM process can be found in [50].

3.1 Four-Wave Mixing

The *Four-wave mixing* (FWM) is a parametric process in which two modes interact with a third order non-linear medium to generate a pair of new modes. It can be generated using different media, for instance, atoms [12], optical fibers [51], and silicon chips [5]. In our case, we pump an ensemble of hot rubidium atoms and use a seed beam to generate non-degenerate FWM, all in free space.

Figure 9 shows the FWM process in rubidium 85 isotope in the $D1$ line (Coupling between $5^2S_{1/2} \rightarrow 5^2P_{1/2}$ at 795 nm). The ground states $|0\rangle$ an $|1\rangle$ corresponds to the real energy levels $|5^2S_{1/2}, F = 2\rangle$ and $|5^2S_{1/2}, F = 3\rangle$ respectively. The frequency splitting between these levels is 3.035 GHz [52]. The states $|2\rangle$ and $|3\rangle$ are off-resonance levels

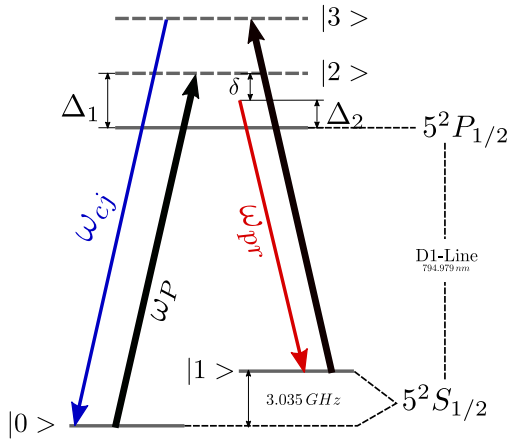

Figure 9. FWM energy levels on Rubidium 85. The two black arrows represents the pump beam. It excites the electrons from lower energy level ($|0\rangle$ and $|1\rangle$) to the excited virtual levels $|2\rangle$ and $|3\rangle$. The probe (red downwards arrow) and conjugated (blue downwards) beams are generated such that there is conservation of energy and momentum. Δ_1 and Δ_2 are the detuning of the pump and probe from the $5^2P_{1/2}$ transition.

denominated *virtual states*, used to explain the FWM process. The real excited states corresponds to $|5^2P_{1/2}, F = 2\rangle$ and $|5^2P_{1/2}, F = 3\rangle$ with a frequency splitting of 361.58 MHz. The excited levels can be ignored as far as the pump frequency is 1 GHz above these transitions.

The pump beam (black upward arrows) couples levels $|0\rangle \rightarrow |2\rangle$, and levels $|1\rangle \rightarrow |3\rangle$. The input seed beam at frequency ω_{pr} couples the levels $|1\rangle$ to $|2\rangle$; by the interaction with the atomic cloud the seed beam is amplified and generates the probe beam (red downward arrow) at the same frequency. Given the conservation of energy, the conjugated beam with frequency ω_{cj} is generated between levels $|3\rangle$ and $|0\rangle$, closing a double-Λ structure (blue downward arrow). Under this configuration, the lower frequency generated is said to be in the *Stokes channel* (ω_{pr}), whereas the higher frequency (ω_{cj}) is said to be in the *Anti-Stokes* channel [I].

Some important parameters are defined in Figure 9: Δ_1 is known as the *one-photon detuning*, which is the relative frequency between the pump frequency and the $5^2P_{1/2}$ level. Δ_1 will be called *pump detuning*. Δ_2 is the seed frequency relative to the excited state $5^2P_{1/2}$; through this document Δ_2 is denominated *probe detuning*. In the literature it is common to find the *two-photon detuning* $\delta = \Delta_1 - \Delta_2$ as the relevant quantity since it indicates the distance to the resonance . However, we had direct control over Δ_2 and

[I] The double-Λ structure could also be satisfied if the seed frequency where at the Anti-Stokes channel. In this case the conjugated frequency would be generated in the Stokes channel and would be coupling levels $|2\rangle$ and $|1\rangle$. The seed frequency was selected in accordance with most of the articles cited during the chapter.

hence we adopted this parameter. The FWM process satisfy energy conservation

$$2\omega_P - \omega_{cj} - \omega_{pr} = 0, \tag{3.1}$$

where ω_P is the pump frequency, ω_{pr} the probe (or seed) frequency and ω_{cj} the conjugated frequency. In addition, the seed beam entering in the Stokes channel imposes a condition for conservation of momentum. In other words, it defines the output direction of the probe and conjugated beams. Hence, the conservation of momentum is given by

$$2\mathbf{k}_P - \mathbf{k}_{cj} - \mathbf{k}_{pr} = 0. \tag{3.2}$$

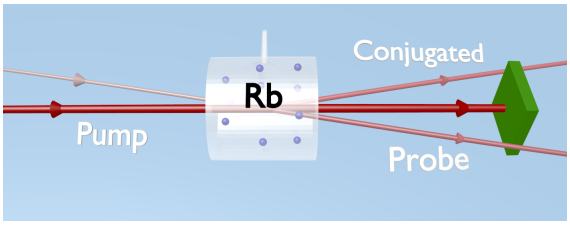

Figure 10. Seeded FWM. An input weak beam will define the direction for the generation of the beams. The frequencies of the generated beams conserve energy and the direction conserve momentum.

3.2 Amplification process

In the FWM process the seed beam is amplified and, simultaneously, the conjugated beam is generated. This process can be studied from two different approaches: firstly a phenomenological description where the system is considered as a non-linear "black box" that generates the amplification and the quantum correlations. In such model, the interaction between atoms and light is treated as an effective interaction. The second approach, the microscopic description, study the FWM considering the field-matter interaction by the dipole moment term. The section is highly based on the work done in [53].

3.2.1 Phenomenological description

The amplification process can be described from the Maxwell equations by considering the propagation of the beams through a "black-box" of length L with a third order non-linear medium inside. Consider the probe and the conjugated beams as plane-waves with linear polarization, traveling in the z direction through the material. Each field has the form:

$$E_i(z,t) = \mathcal{E}_i(z)\mathrm{e}^{i(k_i z - \omega_i t)} + c.c., \tag{3.3}$$

where i stands for the probe (pr), conjugated (cj) or pump (P) beam; $\mathcal{E}_i$ is a complex amplitude dependent on z and k_i is the projection of the wave-vector on the z direction.

By the effect of the electromagnetic field, the material becomes polarized and could generate new frequencies on the electromagnetic field [54]. In this case, the wave-equation for the electric field is

$$\frac{\partial^2}{\partial z^2}E(z,t) = \frac{1}{c^2}\frac{\partial^2}{\partial t^2}E(z,t) + \frac{1}{\epsilon_o c^2}\frac{\partial^2}{\partial t^2}P(z,t), \tag{3.4}$$

where P is the polarization of the material due to the field. We are considering absence of free charge and free current.

The total field inside the material is the superposition of the three of them $E_T(z,t) = E_P(z,t) + E_{pr}(z,t) + E_{cj}(z,t)$. The pump beam is much stronger than the probe and conjugated fields such that there is no depletion of its amplitude, and hence, $E_P(z) \to E_P$ [II]; the material presents a third order non-linearity $P(z,t)$ given by [III]:

$$P(z,t) = \chi^{(3)}E^3(z,t). \tag{3.5}$$

Under the slow varying envelope approximation $\left(\frac{\partial^2\mathcal{E}(z)}{\partial z^2} \ll k\frac{\partial\mathcal{E}(z)}{\partial t},\ \mathcal{E}_j(z) \to \mathcal{E}_j\right)$ [IV], and considering the phase-matching condition Equation 3.2, the expansion of the cubic dependence of the electric field becomes

$$\frac{\partial\mathcal{E}_{pr}(z)}{\partial z} = i\left[\kappa_{pr}\mathcal{E}_{pr}(z) + \eta_{pr}\mathcal{E}^*_{cj}(z)\right], \tag{3.6}$$

$$\frac{\partial\mathcal{E}_{cj}(z)}{\partial z} = i\left[\kappa_{cj}\mathcal{E}_{cj}(z) + \eta_{cj}\mathcal{E}^*_{pr}(z)\right], \tag{3.7}$$

where $\kappa_j(z) = \frac{3\omega_j}{4\epsilon_o c}\chi^{(3)}|\mathcal{E}_P|^2$, $\eta_j(z) = \frac{3\omega_j}{4\epsilon_o c}\chi^{(3)}\mathcal{E}_P^2$, with j standing for probe pr or conjugated cj refractive index. The imaginary part of κ_j ($Im\{\kappa_j\}$) is responsible for the absorption of the medium. As shown in [26], when the two-photon detuning δ is zero the absorption

II The efficiency of the process depends on the geometric phase matching condition. If it is completely satisfied, the efficiency is 1 meaning that this configuration provides the maximum generation rate. However, a perfect geometric phase matching condition results in a gain factor so small that the signal of the generated beams is mixed with the electronic background noise. Hence, there must be a small angle between the pump and the seed causing the efficiency to drop. This will cause that many photons from the pump beam would not be affected in the FWM process. Moreover, if we consider the fact that in our experiment the pump is 10^3 times stronger than the seed beam, and 10^2 stronger than the generated beams, we can assume that the pump beam is not affected by the FWM process [26,55]

III χ is considered a scalar, meaning it is a nonlinear material with isotropic behavior.

IV The amplitude of the field varies too slow in a period.

rate is maximum due to Raman absorption [V]. The real part $Re\{\kappa_j\}$ is taken into account as the change of the refractive index. In the same work, the authors show that only the probe beam suffers a considerable change in its refractive index due to the pump beam, different from the conjugated beam which remains unaltered. The parameter η_j is the responsible for the generation of the FWM and the quantum correlations.

If we consider that the pump beam is undepleted (which is the experimental case), $\kappa_j(z) \to \kappa_j$ and $\eta_j(z) \to \eta_j$. Therefore, the effect of κ_j is a phase shift in the probe and conjugated beam of the form:

$$\tilde{\mathcal{E}}_j = \mathcal{E}_j \mathrm{e}^{-i\kappa_j z},$$

and equations 3.6 and 3.7 can be written as first order coupled linear differential equations:

$$\frac{\partial \mathcal{E}_{pr}(z)}{\partial z} = i\eta_{pr}\mathcal{E}^*_{cj}(z), \tag{3.8}$$

$$\frac{\partial \mathcal{E}_{cj}(z)}{\partial z} = i\eta_{cj}\mathcal{E}^*_{pr}(z). \tag{3.9}$$

Equations 3.8 and 3.9 are coupled linear equations whose solution will be determined by the boundary conditions. In the case of the probe field, $E_{pr}(z=0) = E_{in}$; while for the conjugated field $E_{cj}(z=0) = 0$. Hence, the amplitude of the fields at each point inside the cell is:

$$E_{pr}(z) = E_{in}\cosh\left(\sqrt{\eta_{pr}\eta^*_{cj}}z\right), \tag{3.10}$$

$$E_{cj}(z) = -i\sqrt{\frac{\eta^*_{cj}}{\eta_{pr}}}E_{in}\cosh\left(\sqrt{\eta_{pr}\eta^*_{cj}}z\right). \tag{3.11}$$

So far, we have mentioned the change in the refractive index suffered only by the probe beam due to the action of the pump on the atomic vapour. This will modify the phase matching condition (Equation 3.2) in such a way that:

$$\begin{aligned} \mathbf{k}_{pr} &= n_P \mathbf{k}^{fr}_{pr}, \\ 2\mathbf{k}_P - \mathbf{k}_{cj} - \mathbf{k}_{pr} &= 0, \end{aligned} \tag{3.12}$$

where $n_P = \sqrt{1 + Re\{\kappa_{pr}\}}$ is the refractive index for the probe beam generated by the pump beam, and $\mathbf{k}^{fr}_{pr}$ is the wave-vector of the probe beam in free space. In Figure 11

[V] The Raman process is different from the FWM in the sense that in a Raman effect, a inelastic scattering happens, exciting the atom into a virtual state and generating a frequency detuned photon. The frequency difference between the absorbed and the emitted photon reveals information about the vibrational modes in the system.

we illustrate the possible cases of phase matching. When the propagation is colinear (Figure 11a), the phase-matching is fulfilled. If we consider the change in the susceptibility, the energy conservation preserve the phase-matching condition [26]. When the seed $\mathbf{k}_{pr}^{fr}$ and the pump $\mathbf{k}_P$ are not colinear, the cross-phase modulation induced by the pump will modify the refractive index of the atoms and will affect the wave-vector of the probe such that $\mathbf{k}_{pr} = n_P \mathbf{k}_{pr}^{fr}$, satisfying the phase-matching. Any deviations in the angle do not modify equations 3.8 and 3.9, it just alters the efficiency of the process.

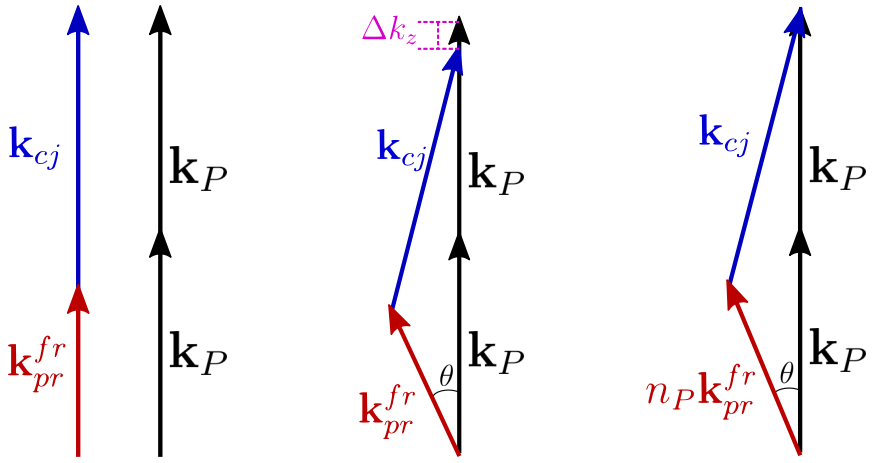

(a) Phase matching in colinear propagation. **(b)** Phase mismatch. **(c)** Phase matching.

Figure 11. **(a)** Colinear configuration: the phase matching is satisfied. **(b)**: When the seed enters the system with an angle θ, a Δk_z appears. However, if the pump is strong enough it will modify the refractive index of the medium and the wave-vector of the seed is modified **(c)** such that the phase-matching is fulfilled.

Gain factor phenomenological approach

In order to illustrate the physics involved in the process, we can consider a degenerate case where $\omega_{pr} \approx \omega_{cj} \rightarrow \eta_{pr} \approx \eta_{cj} \approx \eta_{(3)}$, where the subscript (3) indicates the third order non-linearity, and take the squared norm of Equation 3.10. This is justified by the fact that the frequency difference between probe and conjugated is 6 GHz, which in terms of wavelength corresponds to a difference $\Delta\lambda \approx 1 \times 10^{-3} nm$. After taking into account the boundary condition at $z = L$ we will find the following relations:

$$|E_{pr}(L)|^2 = G\,|E_{in}|^2\,, \tag{3.13}$$

$$|E_C(L)|^2 = (G-1)\,|E_{in}|^2\,, \tag{3.14}$$

where $G = \cosh^2\left(|\eta_{(3)}|L\right)$. In the case that $|\eta_{(3)}|L \gg 1$

$$|E_{pr}(L)|^2 = |E_C(L)|^2 \approx |E_{in}|^2\, \mathrm{e}^{|\eta_{(3)}|L}, \tag{3.15}$$

resulting in an amplified probe and a generated conjugated beam. Under the phenomenological approach, three factors contribute to the amplification process: the length of the material L, the pump power $|E_P|^2$ and the non-linear coefficient $\chi^{(3)}$. Some undesired effects can appear in extreme cases. If the cell is too long, the absorption can be higher than the amplification and no beams will be generated. In contrast, if the pump is too intense, some other non-linear effects could be induced as thermal lensing or self-modulations [VI] [56].

This simplified model is useful for describing the generation of the beams and the quantum correlations. However, it does not take into account many parameters in the interaction. A better understanding is given by the quantum treatment we we show in the next section.

Quantum phenomenological approach

Starting from the simplified description we can go a step further to a quantized description of the process. This model also allows the study of the correlations between the quadratures of the generated fields.

The amplification process is described by the transformation

$$\hat{a}_{out} = \sqrt{G}\,\hat{a}_{in} + \sqrt{G-1}\,\hat{b}^{\dagger}_{in} \tag{3.16}$$

$$\hat{b}^{\dagger}_{out} = \sqrt{G}\,\hat{b}^{\dagger}_{in} + \sqrt{G-1}\,\hat{a}_{in}, \tag{3.17}$$

where $G > 1$ is the gain coefficient, $\hat{a}_{in}$ is associated with a weak coherent state at the input, unlike the conjugated $\hat{b}_{in}$ being a vacuum state at the input. $\hat{a}_{out}$ is the probe beam, $\hat{b}_{in}$ is the conjugated beam. Each of the operators $\hat{a}$ and $\hat{b}$ can be decomposed by a mean value and a fluctuation term as $\hat{a} = a + \delta\hat{a}$ and $\hat{b} = b + \delta\hat{b}$, with a and b being complex amplitude of the fields.

Up to this point we have described the amplification process. Hereafter, we will be interested in the study of the quantum properties available in the FWM. The intensity correlations or intensity-difference squeezing is the first quantum property we will discuss. It refers to a two mode squeezed state where the subtraction of the photocurrent provides a signal below the shot noise limit. It is measured by the difference between the intensities $\hat{N}_{-,out} = \hat{a}^{\dagger}_{out}\hat{a}_{out} - \hat{b}^{\dagger}_{out}\hat{b}_{out}$ such that:

[VI] Kerr effects is a non-optical linear effect that occur when an intense beam propagates in a medium with third-order non linearities. It is characterized by a change in the refractive index of the medium proportional to the intensity of light. In the self-phase modulation, the phase from a single beam is affected by the changes in the refractive index generated by the same beam. On the other hand, the cross-phase modulation, generates a dephasing in a second beam due to the action of a first intense beam. Both effects can generate lensing´ effects, meaning deformations on their spatial profile due to the change in the refractive index.

$$\begin{aligned}\delta N_{-,out} &= G\left[a_{in}^{*}\delta\hat{a}_{in} + a_{in}\delta\hat{a}_{in}^{\dagger} + \delta\hat{a}_{in}^{\dagger}\delta\hat{a}_{in} - \delta\hat{b}_{in}^{\dagger}\delta\hat{b}_{in}\right] \\ &+ (G-1)\left[\delta\hat{b}_{in}\delta\hat{b}_{in}^{\dagger} - a_{in}\delta\hat{a}_{in}^{\dagger} - a_{in}^{*}\delta\hat{a}_{in} - \delta\hat{a}_{in}\delta\hat{a}_{in}^{\dagger}\right].\end{aligned} \tag{3.18}$$

The noise spectrum for $\delta N_{-,out}$ can be calculated by Equation 2.58, and becomes:

$$S(\hat{N}_{-,out}) = \frac{\langle\delta\hat{N}_{-,out}\delta\hat{N}_{-,out}\rangle}{\langle\hat{N}_{+,out}\rangle} = \frac{1}{2G-1}. \tag{3.19}$$

The noise spectrum under the phenomenological description has an inverse relation with the gain of the process, the higher the gain, the more squeezing. This description is incomplete since experimentally there has been found an upper limit for the amplification in which the squeezing will decrease. For instance, at higher temperature the gain factor increases as a consequence of having a higher density of atoms. However, other undesired non-linear effects occur, limiting the generation of correlations [7]. The simplified model lacks of degrees of freedom that describes the experimental situation and connects the quantum correlations with the gain factor. A more exhaustive description must be done in order to have a better understanding of the process.

3.3 Microcopic description of the FWM

In this section we present the *microscopic description* of the FWM. This model takes into account different parameters like atomic structure, atomic density, fields relative frequencies and so on, such that we will have a better control on the simulations in order to reproduce with higher fidelity the experimental results. We consider that the propagation between the beams is colinear and the momentum conservation is satisfied. This section is highly base on [53, 13].

The interactions present at the light-atom system are described by the total Hamiltonian $\hat{H}_T$ as follow:

$$\hat{H}_T(\mathbf{r},t) = \hat{H}_A + \hat{H}_{pr}^{F}(\mathbf{r},t) + \hat{H}_{cj}^{F}(\mathbf{r},t) + \hat{H}_I(\mathbf{r},t), \tag{3.20}$$

$$\begin{aligned}\hat{H}_A(\mathbf{r},t) &= \hbar\int_0^L \left[\omega_0\hat{\sigma}_{00}(\mathbf{r},t) + \omega_1\hat{\sigma}_{11}(\mathbf{r},t) + \omega_2\hat{\sigma}_{22}(\mathbf{r},t) + \omega_3\hat{\sigma}_{33}(\mathbf{r},t)\right] dz, \\ H_j^F &= \sum\hbar\omega_j\left(\hat{a}_j^{\dagger}\hat{a}_j + \frac{1}{2}\right),\end{aligned} \tag{3.21}$$

where $\hat{H}_A$ is the free atomic Hamiltonian, $\hat{H}_j^F$ are the free fields hamiltonian ($j = pr, cj$), $\sigma_{ij} = |i\rangle\langle j|$ are the atomic operators describing the populations ($i = j$) or the coherence ($i \neq j$), and ω_i are the frequencies of the atomic levels.

Additionally, the interaction Hamiltonian H_I has the form:

$$\begin{aligned}\hat{H}_I &= -\sum_k \hat{d}_k \cdot \hat{E}(\mathbf{r}_k, t) \\ &= \hbar \int_0^L \Big[\Omega_P e^{i\Omega_P t}\hat{\sigma}_{02}(z) + \Omega_P e^{i\Omega_P t}\hat{\sigma}_{13}(z) \\ &\quad + g_2\hat{\sigma}_{21}(z)\hat{a}(z,t)e^{i\omega_{pr}t} + g_3\hat{\sigma}_{30}\hat{b}(z,t)e^{i\omega_{cj}t} + h.c.\Big]\rho A dz.\end{aligned} \tag{3.22}$$

The interaction Hamiltonian ,H_I corresponds to a field-matter interaction between the pump, probe, and conjugated beams with the atoms [57]. Ω_P is the Rabi frequency defined by the dipolar interaction (d_{ij}) between pump and atoms. Ω_P is related to the pump power through the relation $\Omega_P = (d_{ij}/\hbar)(\sqrt{(2P)\,/\,(\epsilon_0 c\pi W_o^2)})$, where P is the pump power and W_o is the pump waist. ω_{pr} is the optical frequency of the probe field and ω_{cj} is the frequency of the conjugated field. g_2 is the atomic coupling constant of the probe beam with the transition $|2\rangle \rightarrow |1\rangle$. g_3 is the atomic coupling constant of the conjugated beam with the transition $|3\rangle \rightarrow |0\rangle$ [VII]. The spatial dependence in the atomic operators and the integral in z, takes into account the difference in the atomic density throughout the cell. The pump field have such a high power that it is considered as a classical field, therefore its properties do not change during the FWM process. The probe and the conjugated beams are considered quantum fields and have bosonic operators $\hat{a}$ and $\hat{b}$ correspondingly.

In the Heisenberg picture, the evolution is governed by the Heisenberg-Langevin equation [13]:

$$\frac{d\hat{\sigma}_{ij}}{dt} = -\frac{i}{\hbar}\left[\hat{\sigma}_{ij}, \hat{H}_T\right] + \mathcal{L}(\hat{\sigma}_{ij}) + \hat{\mathcal{F}}_{ij}(t), \tag{3.23}$$

with $\mathcal{L} = \{\hat{\sigma}_{02}, \hat{\sigma}_{12}, \hat{\sigma}_{03}, \hat{\sigma}_{13}\}$ being the Lindblad super operator that takes into account the allowed spontaneous decay transitions, and $\hat{\mathcal{F}}_{ij}$ stochastic operators carrying the noise entering the system and simulates the coupling with the environment. Equation 3.23 is called the *Heisenberg-Langevin equation* for the atomic operators.

On the other hand, the dynamics of the optical field of the probe and conjugated beams is defined by the following equations [VIII],

$$\frac{\partial\hat{a}(z,t)}{\partial t} + c\frac{\partial\hat{a}(z,t)}{\partial z} = -\frac{i}{\hbar}\left[\hat{a}(z,t), \hat{H}_I(z,t)\right] \tag{3.24}$$

$$\frac{\partial\hat{b}(z,t)}{\partial t} + c\frac{\partial\hat{b}(z,t)}{\partial z} = -\frac{i}{\hbar}\left[\hat{b}(z,t), \hat{H}_I(z,t)\right], \tag{3.25}$$

[VII] The atomic coupling constant $g_i = e\sqrt{\frac{\omega_i}{2\epsilon_0\hbar V}}\mu_i$ depends on the frequency between levels and the dipole μ formed between them.

[VIII] In principle, the evolution of the field operators is given by the Heisenberg equation using the total Hamiltonian $\hat{H}_T$. But in [58], they show how the evolution equation transforms into Equation 3.24 where it is used the interaction Hamiltonian $\hat{H}_I$.

where c is the speed of light in vacuum.

These dynamic equations allow us to simulate the amplification process, the noise contribution and the correlations between the two generated fields.

In the case of the atomic operators in Equation 3.23, we can arrange a matrix equation by transforming into the Liouville space such that the evolution of the atomic states is given by:

$$\frac{d\vec{\sigma}(z,t)}{dt} = \mathcal{M}(t)\vec{\sigma}(z,t) + \hat{\mathcal{G}}(t)\hat{\mathcal{A}}(z,t) + \hat{\mathcal{F}}(z,t), \tag{3.26}$$

where $\vec{\sigma} = (\sigma_{00},\, \sigma_{01},\, \sigma_{02} \cdots \sigma_{33})^T_{1\times 16}$ is a vector of the atomic population and coherence. $\hat{\mathcal{A}} = \left(\hat{a}_{pr}(z,t),\, \hat{a}^\dagger_{pr}(z,t),\, \hat{a}_{cj}(z,t),\, \hat{a}^\dagger_{cj}(z,t)\right)^T$ is a vector containing the field operators; $\mathcal{M}(t)$ is a matrix containing the Rabi frequency Ω_P, frequencies of the fields $(\omega_{pr}\,, \omega_{cj})$, and the spontaneous emission rates. $\hat{\mathcal{G}}(t)$ is an operator that depends on the coupling constants between levels (g_i) and the atomic operators $\hat{\sigma}_{ij}$, and $\hat{\mathcal{F}}$ are the fluctuation terms. Matrix $\mathcal{M}$ has the form:

$$\begin{aligned}
\mathcal{M}_{ij} \;=\; & \frac{-iL}{N}\left[\omega_0\left(\sigma_{i0}\delta_{j0} - \sigma_{0j}\delta_{i0}\right) + \omega_1\left(\sigma_{i1}\delta_{j1} - \sigma_{1j}\delta_{i1}\right)\right. \\
& +\omega_2\left(\sigma_{i2}\delta_{j2} - \sigma_{2j}\delta_{i2}\right) + \omega_3\left(\sigma_{i3}\delta_{j3} - \sigma_{3j}\delta_{i3}\right) \\
& +\Omega_1 \mathrm{e}^{i\omega_P t}\left(\sigma_{i2}\delta_{j0} - \sigma_{0j}\delta_{i2}\mathrm{e}^{i\phi_1}\right) + \Omega_1 \mathrm{e}^{i\omega_P t}\left(\sigma_{i3}\delta_{j1} - \sigma_{1j}\delta_{i3}\right) \\
& \left.+\Omega_1^* \mathrm{e}^{-i\omega_P t}\left(\sigma_{i0}\delta_{j2} - \sigma_{2j}\delta_{i0}\right) + \Omega_1^* \mathrm{e}^{-i\omega_P t}\left(\sigma_{i1}\delta_{j3} - \sigma_{3j}\delta_{i1}\right) + \gamma_{ij}\sigma_{ij}\right],
\end{aligned} \tag{3.27}$$

where γ_{ij} corresponds to the spontaneous emission rate of allowed transitions.

The $\hat{\mathcal{G}}$ operator depends on the atomic operator $\hat{\sigma}_{ij}$. It has the form:

$$\mathcal{G}_{ij} = \frac{-iL}{N}\left[g_2 \mathrm{e}^{i\omega_{pr} t}\left(\sigma_{i1}\delta_{j2} - \sigma_{2j}\delta_{i1}\right) + g_3 \mathrm{e}^{i\omega_C}\left(\sigma_{i0}\delta_{j3} - \sigma_{3j}\delta_{i0}\right) + h.c.\right]. \tag{3.28}$$

Applying the transformation to the rotating frame, we eliminate the explicit time dependences on terms of the form $\mathrm{e}^{i\omega_i t}$ resulting in the form

$$\frac{d\tilde{\sigma}(z,t)}{dt} = \tilde{\mathbf{M}}\,\tilde{\sigma}(z,t) + \tilde{\mathbf{G}}\tilde{\mathbf{A}}(z,t) + \tilde{\mathbf{F}}(z,t), \tag{3.29}$$

where $\tilde{\mathbf{M}}$ only depends on the relative frequencies between fields and atomic levels Δ_i, Rabi frequencies Ω_i and decaying term. $\tilde{\mathbf{G}}$ now depends on the coupling coefficients and on atomic operators which is problematic since Equation 3.26 results in a coupled differential equation. To overcome this problem, we adopt a perturbative approach explained in the appendix section B.1, such that $\tilde{\mathbf{G}}$ is written in terms of the mean values of the atomic

operators $\langle\tilde{\sigma}(z,t)\rangle^{st}$ corresponding to the stationary state of the atoms prepared by the pump beam. Therefore, Equation 3.29 now reads:

$$\frac{d\tilde{\sigma}(z,t)}{dt} = \tilde{\mathbf{M}}\,\tilde{\sigma}(z,t) + \tilde{\mathbf{G}}^{st}\tilde{\mathbf{A}}(z,t) + \tilde{\mathbf{F}}(z,t). \tag{3.30}$$

Equation 3.30 is a differential equation of the first order on $\tilde{\sigma}$ with an inhomogeneous term corresponding to the field operators and the stochastic terms.

3.3.1 Gain Coefficient: microscopic description

Now that we have a simplified version of the differential equation for the atomic states, we can study the propagation of the probe and conjugate beams through the medium. Recalling Equation 3.24 we can re-organize them in a matrix equation:

$$\frac{\partial\tilde{\mathbf{A}}(z,t)}{\partial t} + c\frac{\partial\tilde{\mathbf{A}}(z,t)}{\partial z} = N\mathbf{T}\tilde{\sigma}(z,t), \tag{3.31}$$

where $\mathbf{T}$ has the form:

$$\mathbf{T} = \begin{pmatrix} 0 & 0 & 0 & 0 & \cdots & -ig_2^{(1,7)} & 0 & 0 & 0 & \cdots & 0 & 0 & 0 \\ 0 & 0 & 0 & 0 & 0 & \cdots & 0 & ig_2^{(2,10)} & 0 & \cdots & 0 & 0 & 0 \\ 0 & 0 & 0 & -ig_3^{(3,4)} & \cdots & 0 & 0 & 0 & 0 & \cdots & 0 & 0 & 0 \\ 0 & 0 & 0 & \cdots & 0 & 0 & 0 & \cdots & ig_3^{(4,12)} & 0 & 0 & 0 & 0 \end{pmatrix}_{4\times 16}. \tag{3.32}$$

In Equation 3.32, the superscript indicates the position in the matrix. $\mathbf{T}$ is a 4×16; 4 coupling the four field operators and the sixteen atomic transitions.

In the presence of pump and seed beam, we can consider a sufficiently long time for reaching a stationary state $\tilde{\sigma}^{SS}$ such that $\partial\tilde{\mathbf{A}}/\partial t = 0$ [IX]. Consequently, Equation 3.30 follows the relation $\tilde{\sigma}^{SS}(z) = -\tilde{\mathbf{M}}^{-1}\tilde{\mathbf{G}}^{st}\tilde{\mathbf{A}}(z)$ (the fluctuation term is ignored because latter we take the mean value). Together with Equation 3.31 , we find a relation for the field operators as they propagate through the cell

$$\frac{\partial\tilde{\mathbf{A}}(z)}{\partial z} = \mathbf{R}\,\tilde{\mathbf{A}}(z), \tag{3.33}$$

where $\mathbf{R} = -c^{-1}N\mathbf{T}\tilde{\mathbf{M}}^{-1}\tilde{\mathbf{G}}^{st}$. The solution of the last equation is:

[IX] The stationary state referred in this paragraph and denoted with the superscript SS, is different from the stationary state from the latter section st. SS refers tot he stationary state considering the interaction between the pump, the seed, and the atoms. The st stationary state corresponds to the preparation of the atoms after the interaction of the pump and the atoms.

$$\begin{aligned}\tilde{\mathbf{A}}(z) &= \mathrm{e}^{\mathbf{R}\cdot z}\tilde{\mathbf{A}}(0),\\ &= \mathbf{J}(z)\tilde{\mathbf{A}}(0).\end{aligned} \tag{3.34}$$

Therefore, the fields are amplified according to an exponential relation, similar to Equation 3.15. $\mathbf{J}(z)$ is a 4×4 matrix containing information of the relative frequencies of the fields and the atomic levels, the coupling constants and the pump Rabi frequencies. This matrix has the form

$$\mathbf{J}(z) = \begin{pmatrix} A(z) & 0 & 0 & B(z)\\ 0 & A^*(z) & B^*(z) & 0\\ 0 & C^*(z) & D^*(z) & 0\\ C(z) & 0 & 0 & D(z)\end{pmatrix}. \tag{3.35}$$

When considering the components of the fields after propagation ($\tilde{\mathbf{A}}(L)$) it can be seen that they reproduce the phenomenological approach. For instance, the annihilator operator at the output in Equation 3.34 is given by $\tilde{a}(z) = A(z)\tilde{a}(0) + B(z)\tilde{b}^\dagger(0)$, having the same mathematical form as Equation 3.16. However, using the propagator $\mathbf{J}(z)$, effects like Raman scattering are also considered [X]. It is also important to notice that the amplification process is governed by $\mathbf{R}$, hence it depends on the one photon detuning Δ_1 and on the two photon detuning δ_2.

The phase of the fields is also modified at each point during the propagation. According to Equation 3.33, the phase acquired by the probe beam propagating through the medium is:

$$\mathrm{e}^{\phi_a(z)} = \frac{\left(\mathbf{J}(z)\tilde{\mathbf{A}}(0)\right)_{11}}{\sqrt{\left|\mathbf{J}(z)\tilde{\mathbf{A}}(0)_{11}\right|^2}}. \tag{3.36}$$

In the case of the conjugated the relation is similar,

$$\mathrm{e}^{\phi_b(z)} = \frac{\left(\mathbf{J}(z)\tilde{\mathbf{A}}(0)\right)_{31}}{\sqrt{\left|\mathbf{J}(z)\tilde{\mathbf{A}}(0)_{31}\right|^2}}. \tag{3.37}$$

When comparing the outcome field against the input, it is possible to obtain the amplification or *gain factor* for each field. In terms of our theoretical model this can be done through the second moments of Equation 3.34:

[X] Raman scatteering can be understood as an incomplete FWM. The pump beam can stimulate non-resonant transitions evolving two photons with the emission of one at the Stokes or anti-stokes channel, but taking or giving energy from or to the vibrational modes.

$$\begin{aligned}\left\langle \tilde{\mathbf{A}}(z)\,\tilde{\mathbf{A}}^T(z)\right\rangle &= \left\langle \mathbf{J}(z)\tilde{\mathbf{A}}(0)\,\tilde{\mathbf{A}}^T(0)\mathbf{J}^T(z)\right\rangle \\ &= \mathbf{J}(z)\begin{pmatrix} \langle \tilde{a}_{pr}(0)\,\tilde{a}_{pr}(0)\rangle & \langle \tilde{a}_{pr}(0)\,\tilde{a}^\dagger_{pr}(0)\rangle & \langle \tilde{a}_{pr}(0)\,\tilde{a}_{cj}(0)\rangle & \langle \tilde{a}_{pr}(0)\,\tilde{a}^\dagger_{cj}(0)\rangle \\ \langle \tilde{a}^\dagger_{pr}(0)\,\tilde{a}_{pr}(0)\rangle & \langle \tilde{a}^\dagger_{pr}(0)\,\tilde{a}^\dagger_{pr}(0)\rangle & \langle \tilde{a}^\dagger_{pr}(0)\,\tilde{a}_{cj}(0)\rangle & \langle \tilde{a}^\dagger_{pr}(0)\,\tilde{a}^\dagger_{cj}(0)\rangle \\ \langle \tilde{a}_{cj}(0)\,\tilde{a}_{pr}(0)\rangle & \langle \tilde{a}_{cj}(0)\,\tilde{a}^\dagger_{pr}(0)\rangle & \langle \tilde{a}_{cj}(0)\,\tilde{a}_{cj}(0)\rangle & \langle \tilde{a}_{cj}(0)\,\tilde{a}^\dagger_{cj}(0)\rangle \\ \langle \tilde{a}^\dagger_{cj}(0)\,\tilde{a}_{pr}(0)\rangle & \langle \tilde{a}^\dagger_{cj}(0)\,\tilde{a}_{pr}(0)\rangle & \langle \tilde{a}^\dagger_{cj}(0)\,\tilde{a}_{cj}(0)\rangle & \langle \tilde{a}^\dagger_{cj}(0)\,\tilde{a}^\dagger_{cj}(0)\rangle \end{pmatrix}\mathbf{J}^T(z).\end{aligned} \tag{3.38}$$

Considering the input state as a coherent state in the seed channel $|\alpha\rangle_{pr}$ and a vacuum state in the conjugated channel $|0\rangle_{pr}$, the initial state of the atomic operators is:

$$\left\langle \tilde{\mathbf{A}}(0)\,\tilde{\mathbf{A}}^T(0)\right\rangle = \begin{pmatrix} \alpha^2 & |\alpha|^2+1 & 0 & 0 \\ |\alpha|^2 & \alpha^{*2} & 0 & 0 \\ 0 & 0 & 0 & 1 \\ 0 & 0 & 0 & 0 \end{pmatrix} \approx |\alpha|^2 \begin{pmatrix} 1 & 1 & 0 & 0 \\ 1 & 1 & 0 & 0 \\ 0 & 0 & 0 & 0 \\ 0 & 0 & 0 & 0 \end{pmatrix}, \tag{3.39}$$

where we considered that the seed beam is more stronger than the vacuum. After a propagation through the cell by a distance L (Equation 3.38 evaluated in $z = L$), the auto-correlation function for the fields is:

$$\left\langle \tilde{\mathbf{A}}(z)\,\tilde{\mathbf{A}}^T(z)\right\rangle = |\alpha|^2 \begin{pmatrix} A^2(L) & A(L)A^*(L) & A(L)C^*(L) & A(L)C(L) \\ A^*(L)A(L) & A^{*2}(L) & A^*(L)C^*(L) & A^*(L)C(L) \\ C^*(L)A(L) & C^*(L)A^*(L) & C^{*2}(L) & C^*(L)C(L) \\ C(L)A(L) & C(L)A^*(L) & C^*(L)C(L) & C^2(L) \end{pmatrix}. \tag{3.40}$$

The above equation defines the effect of the medium on the incoming beams after a propagation L. Now, one can define the amplification gain as:

$$\begin{aligned} G_a &= \frac{\left\langle \tilde{\mathbf{A}}(L)\tilde{\mathbf{A}}^T(L)\right\rangle_{2,1}}{\left\langle \tilde{\mathbf{A}}(0)\,\tilde{\mathbf{A}}^T(0)\right\rangle_{0,0}} \\ &= |A(L)|^2 \end{aligned} \tag{3.41}$$

$$\begin{aligned} G_b &= \frac{\left\langle \mathbf{A}(L)\tilde{\mathbf{A}}^T(L)\right\rangle_{4,3}}{\left\langle \tilde{\mathbf{A}}(0)\,\tilde{\mathbf{A}}^T(0)\right\rangle_{0,0}} \\ &= |C(L)|^2, \end{aligned} \tag{3.42}$$

where G_a stands for the gain factor of the probe beam and G_b to the gain factor of the conjugated beam. Both terms are normalized by the initial state of the fields.

3.3.2 Noise properties of the FWM

As discussed in section 2.4, we study the noise properties of the quadratures in the frequency domain. In order to find the solution of the fluctuations, we adopt the linearization of the operators such that an arbitrary operator $\hat{O}$ can be written as $\hat{O} = \langle\hat{O}\rangle + \delta\hat{O}$. Furthermore, by applying the Fourier transform to Equation 3.30, the dynamical equation transforms into a linear system for the atomic and light operators in the frequency domain as:

$$i\Omega\delta\tilde{\sigma}(z,\Omega) = \tilde{\mathbf{M}}\,\delta\tilde{\sigma}(z,\Omega) + \tilde{\mathbf{G}}^{st}\delta\tilde{\mathbf{A}}(z,\Omega) + \tilde{\mathbf{F}}(z,\Omega), \tag{3.43}$$

$$i\Omega\delta\tilde{\mathbf{A}}(z,\Omega) + c\frac{\partial\delta\tilde{\mathbf{A}}(z,\Omega)}{\partial z} = N\mathbf{T}\delta\tilde{\sigma}(z,\Omega). \tag{3.44}$$

with $\delta\tilde{\mathbf{A}}(z,\Omega) = \left(\tilde{a}_{pr}(\Omega), \tilde{a}^{\dagger}_{pr}(\Omega), \tilde{a}_{cj}(\Omega), \tilde{a}^{\dagger}_{cj}(\Omega)\right)^{T}$.

Solving for the atomic operators $\tilde{\sigma}$ in Equation 3.43 and replacing it on Equation 3.44 we obtain

$$\begin{aligned}
\delta\tilde{\sigma}(z,\Omega) &= \left(i\Omega - \tilde{\mathbf{M}}^{-1}\right)\tilde{\mathbf{G}}^{st}\,\delta\tilde{\mathbf{A}}(z,\Omega) + \left(i\Omega - \tilde{\mathbf{M}}^{-1}\right)\tilde{\mathbf{F}}(z,\Omega) \\
\frac{\partial\,\delta\hat{\mathbf{A}}(z,\Omega)}{\partial z} &= c^{-1}\left(-i\Omega + N\mathbf{T}\tilde{\mathbf{B}}(\Omega)\tilde{\mathbf{G}}^{st}\right)\,\delta\tilde{\mathbf{A}} + c^{-1}N\mathbf{T}\tilde{\mathbf{B}}(z,\Omega)\tilde{\mathbf{F}}(z,\Omega) \\
&= \mathbf{R}(z,\Omega)\delta\tilde{\mathbf{A}}(z,\Omega) + \mathbf{R}_F(z,\Omega)\tilde{\mathbf{F}}(z,\Omega),
\end{aligned} \tag{3.45}$$

where $\tilde{\mathbf{B}}(\Omega) = (i\Omega - \mathbf{M}^{-1}(\Omega))$, $\mathbf{R}(\Omega) = c^{-1}\left(-i\Omega + N\mathbf{T}\tilde{\mathbf{B}}(\Omega)\right)$ and $\mathbf{R}_F(\Omega) = c^{-1}N\mathbf{T}\tilde{\mathbf{B}}(\Omega)$. Hence, we have a linear differential equation of the first order. Its solution is:

$$\begin{aligned}
\delta\tilde{\mathbf{A}}(z,\Omega) &= \mathrm{e}^{\mathbf{R}(\Omega)\,z}\delta\tilde{\mathbf{A}}(0,\Omega) + \int_0^z \mathrm{e}^{\mathbf{R}(\omega)(z-z')}\mathbf{R}_F(\Omega)\tilde{\mathbf{F}}(z',\Omega)\,dz', \\
&= \mathbf{J}(z,\Omega)\delta\tilde{\mathbf{A}}(0,\Omega) + \mathbf{J}(z,\Omega)\tilde{\mathbf{F}}_{in}(z,\Omega).
\end{aligned} \tag{3.46}$$

being $\mathbf{J}(z,\Omega) = \mathrm{e}^{\mathbf{R}(\Omega)\,z}$ the propagator of the field inside the medium defined identically as in Equation 3.34. Besides, the $\mathbf{R}(\Omega)$ matrix controls the noise properties of the fields through Δ_1 and δ_2. The term $\tilde{\mathbf{F}}_{in}(z,\Omega) = \int_0^z \mathrm{e}^{-\mathbf{R}(\Omega)z'}\mathbf{R}_F(\Omega)\tilde{\mathbf{F}}(z',\Omega)\,dz'$ is the input Langevin term entering at every point "z" through the propagation of the fields on the cell.

3.3.2.1 Noise spectrum

So far, we have described the field fluctuations $\delta\tilde{\mathbf{A}}(z,\Omega)$ as a function of the parameters of the interaction (Equation 3.46). Hereafter, we use the noise spectrum for study the fluctuations of the probe and conjugated beams which results in the description of the quantum correlations generated in the FWM process. In this section, we describe the

theoretical description of the noise spectrum of the system were we include the contribution of the atomic ensemble, the stochastic terms and their influence on the generated fields.

According to Equation 2.58, the noise spectrum is calculated as:

$$\delta(\Omega+\Omega')S(\Omega) = \frac{2\pi c}{L}\left\langle \delta\tilde{\mathbf{A}}(z,\Omega)\delta\tilde{\mathbf{A}}^T(z,\Omega')\right\rangle. \tag{3.47}$$

Substituting Equation 3.46 in the last equation we obtain:

$$\delta(\Omega+\Omega')S(\Omega) = \mathbf{J}(z,\Omega)S(0,\Omega)\mathbf{J}^T(z,\Omega') + \mathbf{J}(z,\Omega)S_{F_{in}}(z,\Omega)\mathbf{J}^T(z,\Omega'), \tag{3.48}$$

where $S(0,\Omega) = (2\pi c/L)\left\langle \delta\tilde{\mathbf{A}}(0,\Omega)\,\delta\tilde{\mathbf{A}}^T(0,\Omega')\right\rangle$ and $S_{F_{in}}(z,\Omega) = (2\pi c/L)\left\langle \tilde{\mathbf{F}}_{in}(z,\Omega)\,\tilde{\mathbf{F}}_{in}^T(z,\Omega')\right\rangle$. Notice that $\mathbf{J}(z,\Omega)$ carries the information of the propagation of the fields through the vapour cell. Additionally, it contains the parameters of the system and controls the compression, amplification or rotation of an input state $S(0,\Omega)$. The second term, originated by the Langevin forces, acts as the noise source for the system.

The noise spectrum of the input state can be calculated by considering the input vacuum state. Similarly as in Equation 3.39, the matrix corresponding to the product $\left\langle \delta\tilde{\mathbf{A}}(0,\Omega)\,\delta\tilde{\mathbf{A}}^T(0,\Omega')\right\rangle$ is

$$\left\langle \delta\tilde{\mathbf{A}}(0,\Omega)\,\delta\tilde{\mathbf{A}}^T(0,\Omega')\right\rangle = \begin{pmatrix} 0 & 1 & 0 & 0\\ 0 & 0 & 0 & 0\\ 0 & 0 & 0 & 1\\ 0 & 0 & 0 & 0 \end{pmatrix}. \tag{3.49}$$

The latest term we need to compute is the contribution from the Langevin forces. This term contemplates the input random noise entering at each point z throughout the propagation of the fields in the cell. Hence, the noise spectrum of the Langevin forces is given by

$$\langle \tilde{\mathbf{F}}_{in}(z,\Omega)\,\tilde{\mathbf{F}}_{in}^T(z,\Omega')\rangle = \int_0^z \mathrm{e}^{-\mathbf{R}(\Omega)z'}\mathbf{R}_F(\Omega)\,\langle \tilde{\mathbf{F}}(z',\Omega)\,\tilde{\mathbf{F}}(z'',\Omega')\rangle\,\mathbf{R}_F^T(\Omega')\mathrm{e}^{-\mathbf{R}^T(\Omega')z''}dz'\,dz'', \tag{3.50}$$

where $\langle \tilde{\mathbf{F}}(z',\Omega)\,\tilde{\mathbf{F}}(z'',\Omega')\rangle$ is the power spectral noise function of the stochastic terms which can be determined by [59]:

$$\langle \tilde{\mathbf{F}}_i(z',\Omega)\,\tilde{\mathbf{F}}_j(z'',\Omega')\rangle = 2\pi\mathcal{D}_{ij}\delta(z'-z'')\delta(\Omega+\Omega'), \tag{3.51}$$

with $\mathcal{D}_{ij}$ the *diffusion coefficients*. Here we have to call attention to the subscripts in $\mathcal{D}$. Each of them refers to an atomic state, being i the atomic state σ_{uv}. The same applies to $j \to \sigma_{nm}$ [XI].

The diffusion coefficients $\mathcal{D}_{uv,nm}$ can be calculated through the *generalized Einstein relation* [59],

$$2\mathcal{D}^{N}_{uv,nm} = \frac{d}{dt}\langle \hat{O}^{\dagger}_{uv}\hat{O}_{nm}\rangle - \left\langle \left(\frac{d}{dt}\hat{O}^{\dagger}_{uv}\right)\hat{O}_{nm}\right\rangle - \left\langle \hat{O}^{\dagger}_{uv}\left(\frac{d}{dt}\hat{O}_{nm}\right)\right\rangle, \tag{3.52}$$

with $\hat{O}$ an arbitrary operator and the superscript N indicates normal ordering of the operators. In the case of the atomic operators, the fact that they obey a closed algebra facilitates the computation of the diffusion terms. Elements to the right of Equation 3.52 are known to as the *drift coefficients*. This is a result of the *fluctuation-dissipation theorem* [60], which relates the fluctuations induced by the reservoir with the dissipation of the system [36].

We can organize the diffusion coefficients into a matrix $\mathbf{D}(z,\Omega,\Omega')$ containing the contribution from each stochastic term denominated the diffusion matrix

$$\mathbf{D}(z,\Omega,\Omega') = \begin{pmatrix} \mathcal{D}_{00,00} & \mathcal{D}_{00,01} & \cdots & \cdots & \mathcal{D}_{00,33} \\ \mathcal{D}_{10,00} & \mathcal{D}_{10,01} & \cdots & \cdots & \vdots \\ \vdots & \cdots & \ddots & \ddots & \vdots \\ \mathcal{D}_{30,00} & \cdots & \cdots & \cdots & \mathcal{D}_{33,33} \end{pmatrix}_{16\times 16}. \tag{3.53}$$

Therefore, the power spectral noise function of the stochastic terms is the following:

$$\langle \tilde{\mathbf{F}}_{in}(z,\Omega)\,\tilde{\mathbf{F}}^{T}_{in}(z,\Omega')\rangle = 2\pi\delta(\Omega+\Omega')\int_0^z \mathrm{e}^{-\mathbf{R}(\Omega)z'}\mathbf{R}_F(\Omega)\mathbf{D}(z,\Omega,\Omega')\mathbf{R}^{T}_F(\Omega')\mathrm{e}^{-\mathbf{R}^{T}(\Omega')z'}dz'.$$

In this subsection we described the theory of the light-atom interaction that depends on different parameters of the system as the Rabi frequency, temperature (atomic density), frequencies or coupling strength. In the following sections we will use the outcome beams after the interaction with the atoms and check the correlations between the generated states in different basis.

3.3.3 Quantum correlations

So far, we expressed the noise spectrum of the FWM process describing the covariance matrix of the fields in the spectral domain. The next step is to define the

[XI] $(u,v),(n,m) \in \{0,1,2,3\}\times\{0,1,2,3\}$.

quadratures of the generated states in terms of the operator $\delta\tilde{\mathbf{A}}(z,\Omega)$, and construct the covariance matrix. The problem can be addressed using two different basis, the symmetric/anti-symmetric (SA) basis and the sideband basis.

During this chapter we organized the field operators for the modes $\tilde{a}_{pr}$ and $\tilde{a}_{cj}$ in the vector $\delta\tilde{\mathbf{A}}$. On the other hand, we are interested in the description of the quadratures' fluctuations. Recalling the definition of the generalized quadratures (Equation 2.4) we can relate the field mode operators $\delta\tilde{\mathbf{A}}$ with the quadrature operator $\delta\tilde{\mathbf{Q}}$ by a unitary transformation $\mathbf{U}(z)$:

$$\begin{aligned}
\delta\tilde{\mathbf{Q}}(z,\Omega) &= \begin{pmatrix} e^{i\phi_{pr}} & e^{-i\phi_{pr}} & 0 & 0 \\ -ie^{-i\phi_{pr}} & ie^{i\phi_{pr}} & 0 & 0 \\ 0 & 0 & e^{i\phi_{cj}} & e^{-i\phi_{cj}} \\ 0 & 0 & -ie^{-i\phi_{cj}} & ie^{i\phi_{cj}} \end{pmatrix} \delta\tilde{\mathbf{A}}(z,\Omega) \\
\delta\tilde{\mathbf{Q}}(z,\Omega) &= \mathbf{U}(z)\,\delta\tilde{\mathbf{A}}(z,\Omega), \qquad (3.54)
\end{aligned}$$

where $\delta\tilde{\mathbf{Q}}(z,\Omega) = (\delta\tilde{p}_{pr},\, \delta\tilde{q}_{pr},\, \delta\tilde{p}_{cj},\, \delta\tilde{q}_{cj})^T$ is a vector containing the quadratures as defined in Equation 2.4.

Our interest is in the construction of the covariance matrix in the *sidebands basis* (section 2.4). To do so, we have to double the size of the vector space given that the two sidebands will be treated independently. Hence, consider the definition of the atomic operator vector $\delta\tilde{\mathbf{A}}$ and double the vector space for considering both frequency components

$$\delta\tilde{\mathbb{A}}(z,\Omega) = \left\{\tilde{a}_{pr}(\Omega), \tilde{a}^{\dagger}_{pr}(-\Omega), \tilde{a}_{cj}(\Omega), \tilde{a}^{\dagger}_{cj}(-\Omega), \tilde{a}_{pr}(-\Omega), \tilde{a}^{\dagger}_{pr}(\Omega), \tilde{a}_{cj}(-\Omega), \tilde{a}^{\dagger}_{cj}(\Omega)\right\},$$

such that the quadratures can be organized in a vector $\delta\tilde{\mathbb{Q}}$

$$\begin{aligned}
\delta\tilde{\mathbb{Q}}(z,\Omega) &= \begin{pmatrix} \mathbf{U} & 0 \\ 0 & \mathbf{U}(z) \end{pmatrix} \delta\tilde{\mathbb{A}}(z,\Omega), \\
&= \mathbb{U}(z)\delta\tilde{\mathbb{A}}(z,\Omega). \qquad (3.55)
\end{aligned}$$

The evolution of the field operators throughout the atomic medium while considering the two frequency modes can be obtained recalling Equation 3.46:

$$\begin{aligned}
\delta\tilde{\mathbb{A}}(z,\Omega) &= \begin{pmatrix} \mathbf{J}(z,\Omega,-\Omega) & 0 \\ 0 & \mathbf{J}(z,-\Omega,\Omega) \end{pmatrix} \left[\delta\tilde{\mathbb{A}}(0,\Omega) + \delta\mathbb{F}_{in}(z,\Omega)\right], \\
&= \mathbb{J}(z,\Omega,-\Omega)\delta\tilde{\mathbb{A}}(0,\Omega) + \mathbb{J}(z,\Omega,-\Omega)\delta\mathbb{F}_{in}(z,\Omega), \qquad (3.56) \\
\delta\mathbb{F}_{in}(z,\Omega) &= \left\{\breve{F}^{a}_{in}(z,\Omega), \breve{F}^{a^{\dagger}}_{in}(z,-\Omega), \breve{F}^{b}_{in}(z,\Omega), \breve{F}^{b^{\dagger}}_{in}(z,-\Omega),\right. \\
&\quad \left.\breve{F}^{a}_{in}(z,-\Omega), \breve{F}^{a^{\dagger}}_{in}(z,\Omega), \breve{F}^{b}_{in}(z,-\Omega), \breve{F}^{b^{\dagger}}_{in}(z,\Omega)\right\} \qquad (3.57)
\end{aligned}$$

where $\delta\mathbb{F}_{in}(z,\Omega)$ is a vector containing the stochastic terms.

Once we have the expression for the quadratures $\delta\tilde{\mathbb{Q}}(\Omega)$, we can determine the quadratures in the *sideband basis* by the transformation Equation 2.51:

$$\begin{aligned}\delta\hat{\mathbf{X}}_\Omega &= \frac{1}{2}\begin{pmatrix}\mathbf{L} & \mathbf{0}_{4\times4}\\ \mathbf{0}_{4\times4} & \mathbf{L}\end{pmatrix}\delta\tilde{\mathbb{Q}}(\Omega),\\ \delta\hat{\mathbf{X}}_\Omega &= \mathbb{L}\,\delta\tilde{\mathbb{Q}}(\Omega),\end{aligned} \tag{3.58}$$

where

$$\delta\tilde{\mathbb{Q}}(\Omega) = \left\{\delta\hat{p}^{(pr)}(-\Omega), \delta\hat{q}^{(pr)}(-\Omega), \delta\hat{p}^{(cj)}(-\Omega), \delta\hat{q}^{(cj)}(-\Omega), \delta\hat{p}^{(pr)}(\Omega), \delta\hat{q}^{(pr)}(\Omega), \delta\hat{p}^{(cj)}(\Omega), \delta\hat{q}^{(cj)}(\Omega)\right\}^T,$$

is the vector of the quadratures defined in Equation 2.51, and

$$\delta\hat{\mathbf{X}}_\Omega = \left\{\delta\hat{p}^{(pr)}_{-\Omega}, \delta\hat{q}^{(pr)}_{-\Omega}, \delta\hat{p}^{(cj)}_{-\Omega}, \delta\hat{q}^{(cj)}_{-\Omega}, \delta\hat{p}^{(pr)}_{\Omega}, \delta\hat{q}^{(pr)}_{\Omega}, \delta\hat{p}^{(cj)}_{\Omega}, \delta\hat{q}^{(cj)}_{\Omega}\right\}^T$$

is the vector of the quadratures in the sideband basis.

After this redefinition of notation, the evolution of the quadratures in the *sideband basis* can be formulated based on the Equation 3.58, Equation 3.55, and Equation 3.56:

$$\begin{aligned}\delta\hat{\mathbf{X}}_\Omega &= \mathbb{L}\,\delta\tilde{\mathbb{Q}}(\Omega),\\ &= \mathbb{L}\,\mathbb{U}(z)\delta\tilde{\mathbb{A}}(z,\Omega),\\ &= \mathbb{L}\,\mathbb{U}(z)\mathbb{J}(z,\Omega,-\Omega)\delta\tilde{\mathbb{A}}(0,\Omega).\end{aligned} \tag{3.59}$$

Finally, the covariance matrix of in the *sideband basis* is defined by

$$\begin{aligned}\mathbb{V}_\Omega &= \left\langle\left\{\delta\hat{\mathbf{X}}_\Omega,\, \delta\hat{\mathbf{X}}_\Omega^T\right\}\right\rangle, \qquad (3.60)\\ \left\langle\delta\hat{\mathbf{X}}_\Omega,\, \delta\hat{\mathbf{X}}_\Omega^T\right\rangle &= \left\langle\mathbb{L}\,\mathbb{U}(z)\mathbb{J}(z,\Omega,-\Omega)\delta\mathbb{A}(0,\Omega),\, \delta\mathbb{A}^T(0,\Omega)\mathbb{J}^T(z,\Omega,-\Omega)\mathbb{U}^T(z)\mathbb{L}^T\right\rangle\end{aligned}$$

Alternatively, the *resonator detection* is capable to a direct measurement of the quadratures in the *symmetric/anti-symmetric* basis (Equation 2.52). Therefore, given a four mode state

$$\hat{\mathbf{X}}_{s/a} = \left\{\hat{p}^{(pr)}_s, \hat{q}^{(pr)}_s, \hat{p}^{(cj)}_s, \hat{q}^{(cj)}_s, \hat{p}^{(pr)}_a, \hat{q}^{(pr)}_a, \hat{p}^{(cj)}_a, \hat{q}^{(cj)}_a\right\}^T,$$

it is possible to determine the quadratures in the SA basis through the transformation Equation 2.54, such that

$$\delta\hat{\mathbf{X}}_{s/a} = \Lambda^{-1}\delta\hat{\mathbf{X}}_\Omega, \tag{3.61}$$

and the covariance matrix in the *symmetric/anti-symmetric basis* becomes

$$\mathbb{V}_{s/a} = \left\langle \left\{ \Lambda \delta \hat{\mathbf{X}}_{s/a},\, \delta \hat{\mathbf{X}}_{s/a}^{T} \Lambda^{T} \right\} \right\rangle . \tag{3.62}$$

As a result, we have the representation of the covariance matrix either in the *sideband basis* and the *symmetric/anti-symmetric basis*, and we are able to describe their dynamics during the interaction with the third-order non-linear medium.

□ □ □

Through this chapter we studied the FWM process in two different approaches. First, in the phenomenological approach, the gain factor for the probe and conjugated beams is determined as a function of the susceptibility which carries all the information about the non-linear process. Afterwards, we introduced the quantum aspect by the quantization of the state operators and described quantum signatures using the noise spectrum. Secondly, we presented the microscopic approach which brings a more complete description of the interaction, since it considers the different parameters available in the system like the pump and probe frequencies, beam power, size of the beams and atomic density. We use a semi-classical description for the interaction of the pump and the atoms, while we use a complete quantum description for the probe and conjugated beam interacting with the atoms. The microscopical approach allowed us to determine the quadratures as a function of the system parameters. In addition, we presented the theoretical description of the covariance matrix as a function of the quadratures. Our methodology enables us to calculate the FWM gain spectrum and study the quantum correlations and its dependence with the system parameters.

Some other works try to describe the FWM process and the intensity correlations [61]. However, their description is based on the phenomenological approach and lacks some of the degrees of freedom that define the non-linear interaction. The presented theory provides a reliable description of the system and allows a direct comparison with the experiment. In the following chapters we show the experimental setup, and the experimental and theoretical results.

II

EXPERIMENTAL SETUP AND RESULTS

4

Experimental Setup

Our experiment is designed in four main steps: source beam, seed generation, four-wave mixing process and detection. In this chapter we describe each of the steps, their control parameters and present the characterization of the electronic response.

Following Figure 12 we illustrate the generalities of the system. The source beam is a home-made Ti:sapphire laser locked at 795 nm (A.). Its frequency is controlled by intracavity components and locked by feedback control. The Ti:sapphire output power is split in two beams, taking most of the power for pumping the FWM process and a small amount for generating the seed beam. The seed beam goes through an AOM that red detunes its frequency by ~ 3 GHz (B.). The seed and the pump beams are directed into a rubidium 85 vapour cell (C.) such that the probe and the conjugated beams are generated. The latter beams are guided to the resonator detection scheme (not shown here).

4.1 Ti:sapphire laser

The source laser is a home made CW Ti:sapphire laser developed in the master thesis [62]. It is pumped by a CW *Coherent Verdi G* laser @532 nm and 8.36 ± 0.01 W. The Ti:sapphire crystal has a broad emission band, from 600 to 1100 nm, hence, several intracavity components and electronic feedback control are required for delicate frequency selection. The Lyot filter is the first and broader frequency filter. It is a birefringent filter that selects the frequency in thousandth of nanometers by introducing losses to the undesired frequencies. Then, there is the optical diode that guarantees a preferential propagation direction of the beam inside the cavity and selects the resonant polarization. It is formed by a half-wave plate and a birefringent cristal; it induce losses in the counter-propagating modes letting the desired mode to oscillate inside the cavity.

The etalon is a Fabry-Perot cavity with a transmission dependent on the incidence angle of the beam. Hence, it selects a single mode while the other modes suffer from losses.

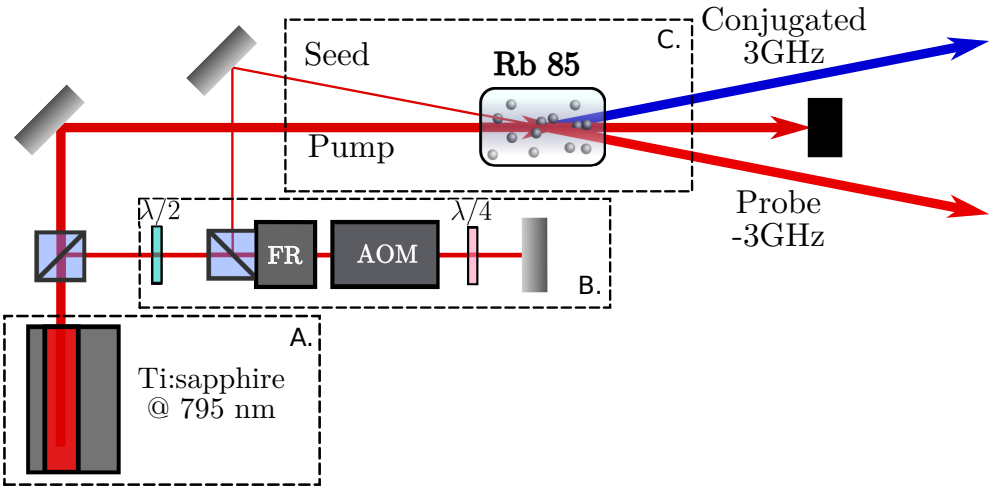

Figure 12. Experimental Setup. **A.** The light source from a Ti:sapphire laser is locked using a saturated absorption profile of rubidium. **B.** A small fraction of power is taken for the generation of the seed beam using a AOM in a double-pass configuration and an optical isolator (beam splitter and Faraday rotator (FR)). **C.** The interaction of the pump and the seed with the rubidium 85 isotopes amplifies the seed, now probe, and generates the conjugated beam.

The etalon is actively stabilized by a *dither and locking* technique where a modulation at 32.6 ± 0.2 kHz is applied to the etalon. This modulation is detected by a photodiode and demodulated for obtaining the error signal in a lock-in amplifier. The error signal can be used to optimize the angle of the etalon in a feedback loop, such that a single mode is resonant inside the cavity.

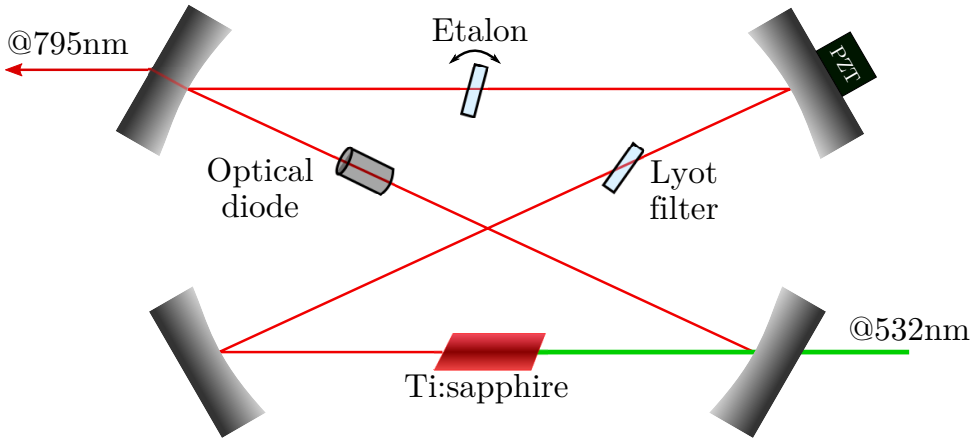

Figure 13. The Ti:sapphire laser is pumped by a CW laser @532 nm. Its output provides a CW laser @795 nm. Several intracavity optical components compose the frequency stabilization system.

The etalon controls the single cavity mode resonance but not the frequency. Therefore, we lock the Ti:sapphire laser frequency with respect to a rubidium saturated absorption spectrum (Figure 14). A small fraction of light passes through an AOM (*Crystal technology Inc. Model: 3200-124*) modulated at 250 MHz. A four-pass scheme was implemented such that the light is red detuned by 1GHz [63]. Afterwards, the detuned beam is used to

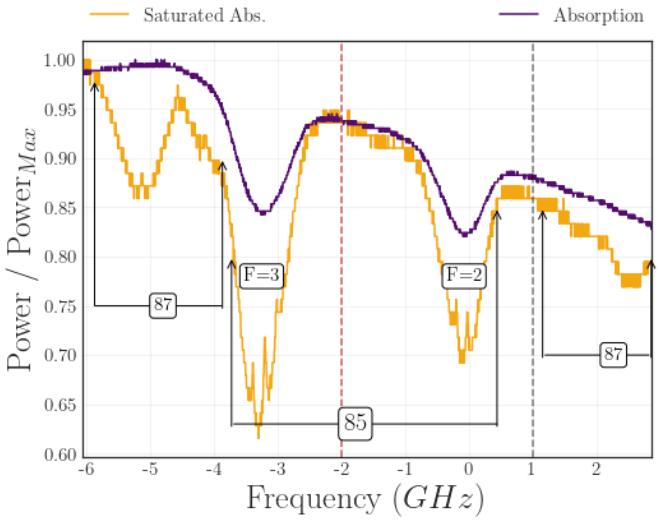

Figure 14. Saturated absorption spectrum of the D1-line rubidium isotope. The purple curve corresponds to the absorption spectrum of the Rubidium 85. The yellow curve is the saturated spectrum from a reference cell containing both Rubidium isotopes, 85 and 87. In this figure, the zero value is located at the crossover signal of rubidium 85. The vertical black dashed line is the frequency of the pump beam. The two frequencies generated from the FWM process, will have frequencies at $3\,GHz$ to the red (red dashed line) and to the blue from the pump frequency.

generate the saturated absorption spectrum at the D1-line of ^{85}Rb, that is used as the frequency reference for locking and the error signal source (yellow curve in figure 14). The frequency locking is completed by a feedback loop acting on the PZT of the Ti:sapphire laser. As a result, the Ti:sapphire laser will be locked at +1GHz from the hyperfine transition or the crossover of the ^{85}Rb isotope which guarantee that the pump, the probe and the conjugated frequencies are far from the absorption regions of the D1-line of ^{85}Rb.

In the saturated absorption spectrum Figure 14, we defined two frequency regions named $F = 3$ and $F = 2$. The first one refers to rubidium 85 transitions coupling the ground state level $5^2S_{1/2}$, $F = 3$ to the excited states $5^2P_{1/2}$. The second, couples the ground state level $5^2S_{1/2}$, $F = 2$ to the same excited states. Hence, the $F = 3$ frequency region corresponds to lower energy transitions and $F = 2$ to higher energy transitions. We defined the zero frequency reference at the *Crossover* signal from the $F = 2$ region given that the pump frequency was locked at this frequency for most of the experimental characterization.

The locking system provides a frequency stabilized laser blue detuned in 1 GHz from the $F = 2$ hyperfine levels of the rubidium 85, shown by the vertical black dashed line in Figure 14. It also limits the excess of noise of the source laser as far as the cavity works as a filter itself, providing a coherent state above the analysis frequency of 3MHz.

4.2 Seed generation

Once the Ti:sapphire laser is locked, it is possible to generate the seed beam. The experimental setup is depicted in Figure 15. We utilize an AOM (Brimrose model GPF-1500-1000-795) that detunes the light frequency in a range of 1.357 ± 0.001 GHz to 1.671 ± 0.001 GHz. The datasheet specifies a broader frequency range however we are limited by our electronic voltage control and this range is sufficient for our system. The light polarization must be horizontal and the maximum intensity is 5 W/mm^2. Given that the waist size of the incoming beam is $63.0 \pm 0.4\mu m$, we dislocate the AOM few millimeters from the waist position and use a maximum power of 20 mW. The AOM source is a voltage controlled oscillator (VCO Mini-circuits $ZX95 - 1750W+$) which allows the frequency tuning by an external voltage control.

Now we describe in detail the optical components of the seed generation according to Figure 15. For this part, lets define the forward propagation as the direction from left to right and the backward propagation in the other direction. Following this convention, there is the half-wave plate that optimizes the transmitted power through the PBS. The PBS and the Faraday rotator (FR) are rotated such that the light polarization became horizontal. The light goes twice through the AOM, once in the forward propagation and a second one in the backward propagation. We correct any polarization deviation with a quarter-wave plate ($\lambda/4$). Following the backward propagation, the FR rotates the polarization such that the PBS reflects the backward beam to one of its outputs. One disadvantage of using the AOM is the astigmatism generated on the beam after the detuning. Therefore, we couple the detuned beam into a monomode optical fiber in order to correct the transverse profile, with an efficiency of 60%. At the end of the process, the seed beam will be red detuned by 3 GHz (Figure 14 vertical dashed light red line), with a well defined transverse mode and a tunable frequency.

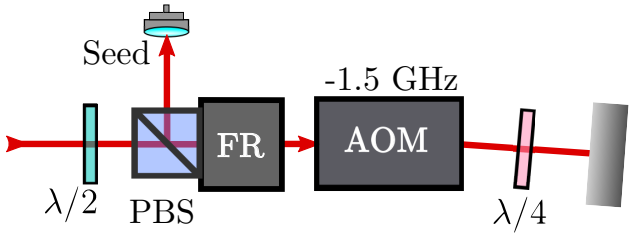

Figure 15. The seed beam is generated by using an AOM in a double pass scheme that red detunes the laser beam by -3.0 GHz.

4.3 FWM generation

The central part of the system is the rubidium vapour cell. The cell contains the isotope of rubidium 85; its length and diameter is 2.54 ± 0.05 cm. We heat the rubidium cell and control the temperature, typically above $100°C$. It has an anti-reflection coating

at 795 nm. For heating the input and output windows of the rubidium cell, we use a resistance and a *Temperature controller Coel K49E*. The controller is a relay switch circuit driven by a a PID controller that defines the ON/OFF time of the current flux with a precision of 0.1 $°C$ (Figure 16a).

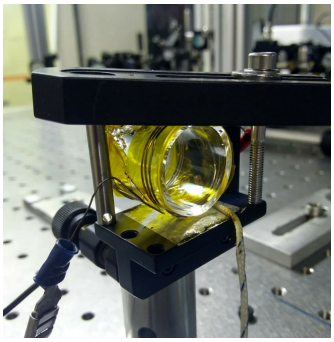

(a) AR coated cell with Rubidium 85 vapour.

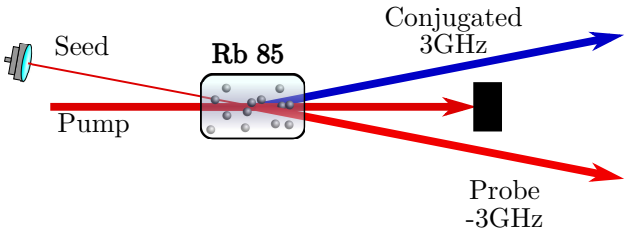

(b) FWM generation setup.

Figure 16. (a) FWM experimental setup. The rubidium cell is heated at $103.0 \pm 0.1°C$. It has a anti-reflecting coating (AR) that reduce the reflection coefficient at 795 nm. **(b)** Coated Rubidium cell with a length of $2.54\,cm$.

The pump and the seed beams cross at an angle of 0.29 ± 0.03 degrees and intersects at the middle of the rubidium cell. At the center of the cell, the pump waist is $525.5 \pm 1.6 \mu m$ while the seed waist is $244.2 \pm 1.9 \mu m$ [I]. At the output of the cell there is the amplified probe beam and the generated conjugated, both polarized orthogonally to the pump beam. The pump power could be varied from 380 to 450 mW and the seed power from 80 to 180 μW (Figure 16b). We decided to work with rubidium 85 guided by previous works where this system shows stronger quantum correlations than rubidium 87 for the set of parameters in our system [19] [II].

4.3.1 FWM spectrum

The typical FWM spectrum ([12]) is show in Figure 17. The vertical axes corresponds to the *gain factor*, defined by

$$Gain^{(j)} = \frac{P_{out}^{(j)}}{P_{in}^{seed}}, \tag{4.1}$$

where j stands for *probe* or *conjugated*, $Gain^{(j)}$ is the gain factor, $P_{out}^{(j)}$ is the output power, and P_{in}^{seed} is the input seed power (horizontal dotted black line). The horizontal axes corresponds to the frequency of the seed beam. For the generation of the spectrum, we used a diode laser in a Littrow configuration as the seed beam [64] which permits a frequency detuning at a range of $12\,GHz$.

I These values corresponds to the final configuration.

II The energy shift generated by the strong pump beam is much bigger than any magnetic field that could disturb the system [50].

In yellow we plotted the saturated absorption spectrum of Rubidium 85 and 87 which defines the frequency scale in accordance with the hyperfine transition levels of the D1 line of ^{85}Rb (Figure 9) [65]. The vertical dashed black line corresponds to the pump frequency (Δ_1 the same frequency shown in Figure 14). The horizontal axes is the seed beam frequency. Δ_2 corresponds to the seed frequency in the FWM process as will be discussed latter. The red curve corresponds to the probe signal and the blue curve to the conjugated signal. As the seed frequency increases, the seed will enters an absorption region between -4 and -2.5 GHz, corresponding to the transitions between levels $5^2S_{1/2}, F = 3 \rightarrow 5^2P_{1/2}, F = 2$ and $5^2S_{1/2}, F = 3 \rightarrow 5^2P_{1/2}, F = 3$. Thereafter, at -2 GHz the seed frequency will close the double-lambda structure in the Stokes channel such that the probe beam is generated at -2 GHz while the conjugated is generated at 4 GHz. Between -1 GHz and 0.5 GHz, the seed beam is in resonance with the hyperfine transitions $5^2S_{1/2}, F = 2 \rightarrow 5^2P_{1/2}, F = 2$ and $5^2S_{1/2}, F = 2 \rightarrow 5^2P_{1/2}, F = 3$. When the seed beam is at 4 GHz, it couples the Anti-Stokes channel and generates the probe beam at 4 GHz and the conjugated beam at -2 GHz. It is worth noting a monotonically decrease of the intensity level in the probe spectrum originated by the change in the Littrow laser power as the cavity size is scanned.

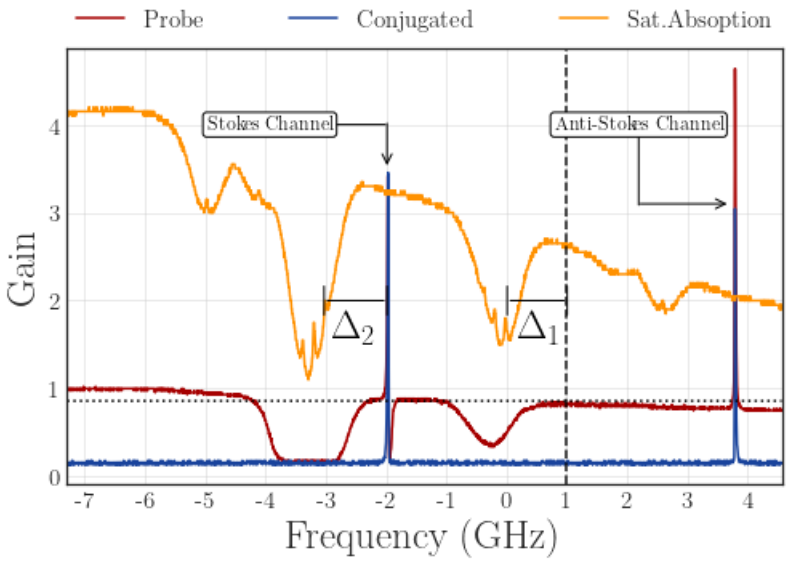

Figure 17. Complete FWM spectrum. In yellow there is the saturated absorption which is used as a ruler for the frequency, its amplitude is not important in this figure. In red there is the probe beam and in blue the conjugated beam. The vertical dashed black line is the frequency of the pump, locked at $+1\,GHz$ from the hyperfine transition or the crossover of Rubidium 85. We can see the amplification process in the Stokes and in the Anti-Stokes channel.

Scanning the atoms with the diode laser is an initial step. It does not allow a detailed spectrum given that the bandwidth of the FWM is around units of MHz. A more suitable characterization must be done such that we could study the influence of

each experimental parameter in the process. This specific characterization can by done by controlling the probe detuning Δ_2 with the AOM shown in Figure 15.

4.4 Photodiode characterization

The characterization of the quantum states is done by implementing a direct measurement in which each of the generated beams goes to a photodiode *First sensor PIN PD PC10-7 TO*. The quantum efficiency is 87.2 % for the probe channel and 89.3 % for the conjugated channel at 795 nm [III]. The photodiode transforms the incoming light into a photocurrent $i(t) = \langle i(t) \rangle + \delta i$ being $\langle i(t) \rangle$ the mean value of the photocurrent, called DC component and δi are the fluctuations called the high frequency HF component (see section 2.4). By using a band-pass filter with a cutoff frequency at 600 kHz, it is possible to separate between the DC component below the cutof frequency, and above it the HF signal. The DC component goes directly to acquisition in the computer and it is used to synchronize the tomography of the states. On the other hand, the high frequency component HF needs a detailed treatment. Considering that the quantum properties of the states are stored in the high frequency region, we have to demodulate the signal before the acquisition. As shown in Figure 18, the high frequency signal from a single photodetector is amplified, splitted in two channels by a power splitter (PS), and mixed with two in-phase orthogonal signals *Cosine* in pink and *Sine* shown in green. Finally, we acquire the data using *National instruments BNC 2110*.

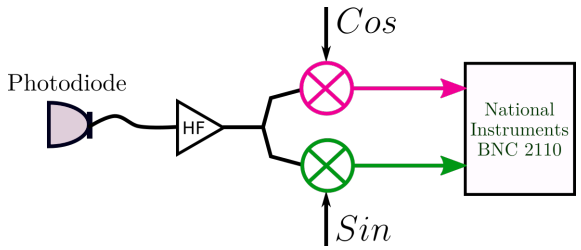

Figure 18. The photodiode convert the light into photocurrent. It is splitted equally and demodulated with two orthogonal signals. The output is acquired on a computer.

Although the orthogonal signals *Cosine* and *Sine* differ only by a phase, they have the same amplitude and frequency, hence, the photocurrent must be identical up to the random electronic noise. Furthermore, if we use a shot noise limited laser (coherent state), every demodulation channel, Cosine and Sine, must measure the same variance on the photocurrent. Consequently, we check this behavior in our system by sending a shot noise

[III] The quantum efficiency can be determined by the relation $i/P_{opt} = \epsilon_q e\lambda/hc$, where i is the generated photocurrent by the photodiode, P_{out} is optical power, ϵ_e is the quantum efficiency, e is the electric charge, λ is the light wavelength, h is the Planck constant and c is the speed of light in vacuum.

limited beam with the same intensity to each of the photodiodes and tuning the laser power.

The first characterization was done at an analysis frequency of 7 MHz. Figure 19 shows the variance of the high frequency signal ($\Delta^2 HF$) as a function of the incoming power on each photodetector for the probe (1.1) and the conjugated (1.2). We observe that the $\Delta^2 HF$ response is linear with respect to the incoming power which is a desired behavior for the detection. We can also check that both demodulation channels have similar slope and y-interception with a difference less than 10%. As far as the detectors must have the same slope and y-intercept, we numerically correct the conjugated channel by the multiplicative factor $(g_1/g_2)^2$, being $g1^2$ the slope of the probe channel and g_2^2 the slope of the conjugated channel. In this way, the incoming signal is detected, and the conjugated channel is corrected before any data analysis. We defined 10% as the maximum difference between the response of the detectors. This value was defined empirically after many tests on the system.

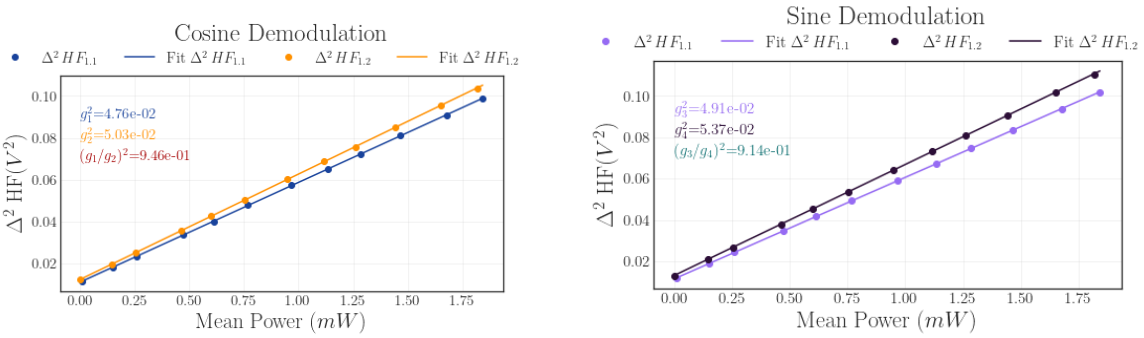

(a) Cosine demodulation 7 MHz. **(b)** Sine demodulation 7 MHz.

Figure 19. HF response for an incoming coherent beam. **(a)** HF Cosine channel for both detectors. **(b)** HF Sine channel.

At Ω =10 MHz (Figure 20) the response of the detection channels have a response difference lower than 10%. Comparing the case of 7 MHz and 10 MHz, we can see a slope difference of 20% which is expected given that the electronic components response depends on the analysis frequency.

4.5 Intensity correlations

Once the beams probe and conjugated are generated, they are directed into the detection scheme. Firstly, we confirm the existence of quantum intensity correlations. The quantum intensity correlations are used as the benchmark for the system meaning that it is the first signal of the generation of quantum properties. It is measured by the variance of the difference of the high-frequency signal of the probe and conjugated beams as follow

$$\delta i_-(\Omega) = |\alpha_{pr}|\delta\hat{p}_{pr}(\Omega) - |\alpha_{cj}|\delta\hat{p}_{cj}(\Omega), \tag{4.2}$$

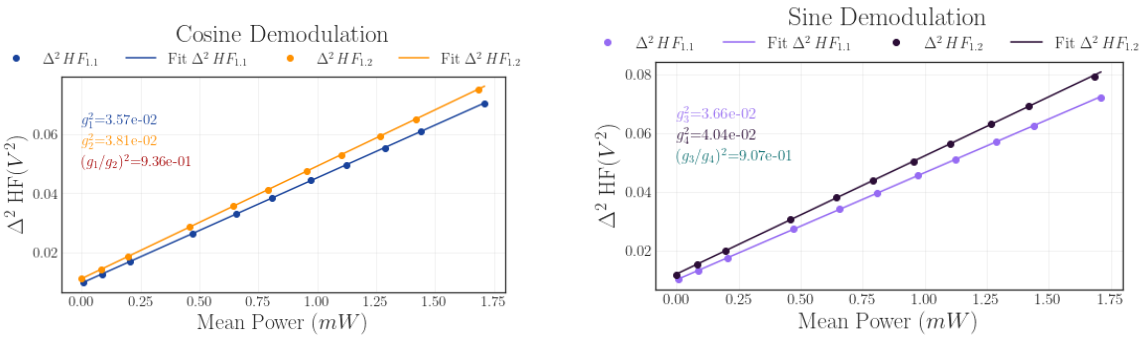

(a) Cosine demodulation 10 MHz. **(b)** Sine demodulation 10 MHz.

Figure 20. HF response for an incoming coherent beam. **(a)** HF Cosine channel for both detectors. **(b)** HF Sine channel.

where α_{pr} and α_{cj} refers to the amplitude of the carrier of two different modes probe and conjugated; $\delta\hat{p}$ refers to the generalized quadrature of the sidebands for each mode (2.4). According to Equation 2.58, the spectral density of the intensity-difference is:

$$\begin{aligned} S_{i\_}(\Omega) &= |\alpha_{pr}|^2 \langle \delta\hat{p}_{pr}(\Omega)\delta\hat{p}_{pr}(\Omega')\rangle \\ &\quad +|\alpha_{cj}|^2 \langle \delta\hat{p}_{cj}(\Omega)\delta\hat{p}_{cj}(\Omega')\rangle \\ &\quad -|\alpha_{pr}||\alpha_{cj}| \langle \delta\hat{p}_{pr}(\Omega)\delta\hat{p}_{cj}(\Omega') + \delta\hat{p}_{cj}(\Omega)\delta\hat{p}_{pr}(\Omega')\rangle \\ &= |\alpha_{pr}|^2\Delta^2\delta\hat{p}_{pr} + |\alpha_{cj}|^2\Delta^2\delta\hat{p}_{cj} - 2|\alpha_{pr}||\alpha_{cj}|C(\delta\hat{p}_{pr}, \delta\hat{p}_{cj}) \end{aligned} \tag{4.3}$$

Figure 21a presents the experimental setup for measuring the intensity quantum correlations of the system. Once the probe and the conjugated beams are generated they are directed into the photodetectors where the high-frequency signal (HF) is collected. The HF signals are subtracted in a power splitter (PS)[IV]. The output is recorded using a spectrum analyzer (SA. Keysight N9010B) working at resolution bandwidth (RBW) of 1 MHz and a video bandwidth (VBW) of 100 kHz.

Three measurements must be done for the characterization of the intensity correlations $\Delta^2 I_-$: the electronic noise, the shot noise, and the intensity difference. The electronic noise is the background noise from the detection apparatus. It defines the lower acceptance noise value of the measurements, in other words, whenever the noise level of an incoming signal is 3 dB above the electronic noise, the measured signal is reliable. The shot noise level is the classical reference and is determined as explained in subsection 2.4.2. Any signal below this level are related to squeezed states. Finally, the intensity difference $\Delta^2 I_-$ will reveal the quantum correlations of the system. In the example shown in Figure 21b, the black dotted line represents the shot noise level and the green continuous line, the

[IV] It is not relevant which signal is phase shifted as far as the the observable is the variance of the subtraction.

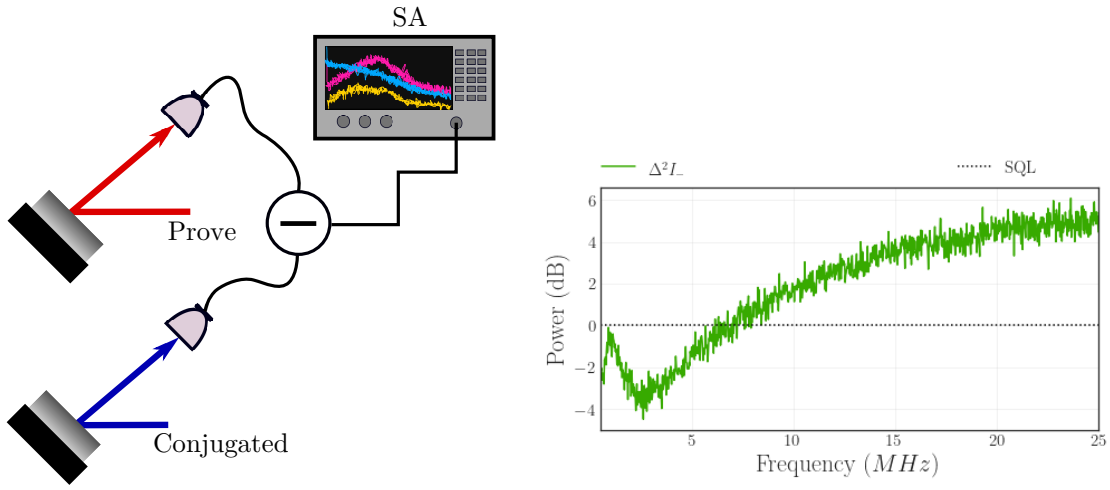

(a) Quantum intensity correlations setup.

(b) Intensity correlations measurement.

Figure 21. (a) Quantum intensity correlations setup. The probe and conjugated beams are directly measured. Their high-frequency signal is sent into a power splitter (PS) that dephase one signal by π such that the output is the subtraction of the signals. The signal is recorded using a Spectrum Analyzer (SA). **(b)** Example of quantum intensity measurement. In green continuous line is the intensity difference correlations $\Delta^2 I_-$. The dotted black line is the shot noise level (SQL). The vertical axis is the noise power in dB units and the horizontal is the analysis frequency. Any signal below the Shot noise level is a signature of quantum correlations. Hence, from 1 MHz to 7 MHz the system presents quantum intensity correlations.

intensity correlations. The electronic noise was already subtracted and the signals were normalized by the shot noise level. For frequencies between 1 an 7 MHz, the system presents quantum intensity correlations or squeezing. Below 1 MHz, the detection system presents a huge excess of noise, hence, measurements below 2 MHz are not reliable.

4.6 Reconstruction of the state

The quantum properties of Gaussian states are determined by the statistics in the sidebands and are resolved by their first and second moments. The first moment corresponds to the mean value (DC) which is recorded separately in the detection scheme. The second moments are obtained from the high frequency HF component. For intense fields, the photodiodes are sufficient for detecting the HF fluctuations since they carry their own local oscillator, the carrier ω_{ca}. However, entanglement requires the observation of a pair of conjugated quadratures $\hat{p}$ and $\hat{q}$. The amplitude quadrature is directly accessed by the direct detection. Conversely, the phase quadrature requires interferometric process that grants access to this fluctuations.

The most common method for detection of the quadratures is the *homodyne detection* [20]. This method uses a local oscillator as an auxiliary beam that would amplify the fluctuations in the sidebands. Under this scheme, it is possible to determine the

fluctuations of the quadratures in the *symmetric/anti-symmetric basis*. The homodyne detection has proven to be a useful tool for the characterization of entanglement in different systems, for instance quantum imaging or multipartite states with rubidium atoms [21, 22, 14], or multipartite entangled states generated by an OPO based on second order non-linear interactions [9, 10]. However, it is blind to the correlations between the upper and the lower sidebands separately. Therefore, it is necessary to measure the statistical properties of the sidebands independently such that the complete state is reconstructed, a goal that can be achieved by using the *resonator detection*.

The *resonator detection* has been implemented widely in our group for the characterization of entanglement in a variety of systems such as second order non-linear OPO [4, 45, 66, 67], and more recently OPO based on rubidium vapour [25]. On every of these experiments, a pair of bright beams were generated presenting entanglement. When measured separately, each of the generated states presented an excess of noise up to 3 SQL units above the shot noise level. Moreover, the coupling between the bright beams and the resonator is considered as perfect. In the experiment this is not the case, and usually coupling factor above 95% are desired for performing the measurements. Despite of this, the reconstruction of the states were effective.

However, systems presenting typical values of excess of noise above 5 SQL presented new challenges for the reconstruction of the state. For instance, the excess of noise could induce some undesired electronic response, any mismatch between the resonator and the light beam would contaminate the measurements or any fluctuation in the phase from the demodulation channels would struggle the detection as well. An example of this can be found in the PhD thesis from Kögler[24], where he studied and OPO on-chip and implemented the resonator detection for the description of the state. During this section we will address this issues and present the implemented solution.

4.6.1 Shot noise in the tomography

When running the experiment for the complete reconstruction of the state, that is reconstructing the covariance matrix, the *shot noise* is determined differently compared to subsection 2.4.2. The implementation of the direct measurement implies that the shot noise calibration must be obtained separately using a coherent source of light, differently from a balance detection scheme where the shot noise can be obtained simultaneously with the tomography of the quantum state [V]. Figure 22 shows the shot noise calibration. A coherent source of light, the Tisapphire laser, pass through a PBS dividing it into two beams with the same intensity that goes to the photodetectors. Each photodetector generates the HF signal which is amplified and demodulated with two orthogonal signals, Cosine and Sine.

[V] The balanced detection is the principal detection method in our laboratory. In it, the shot noise can be obtained directly from the subtraction of the demodulated photocurrents *Sin* and *Cos*.

Finally, the HF data is acquired and a computational treatment determines the shot noise level as a function of the incoming power for the individual channels *Cosine* and *Sine*. In terms of the raw data, the shot noise is calculated by:

$$\Delta^2 I_{SQL} = \Delta^2 \left(HF^{(pr)} - HF^{(cj)} \right), \tag{4.4}$$

where $\Delta^2 I_{SQL}$ is the shot noise level, and $HF^{(pr/cj)}$ is the probe/conjugated high frequency (HF) signal. The shot noise is determined by calculating the variance of the subtraction of the HF signals.

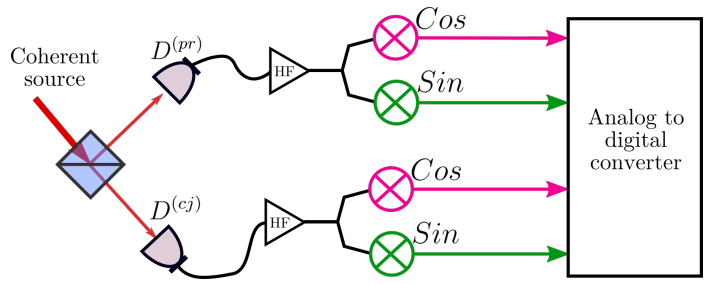

Figure 22. Scheme to measure the Shot noise. A coherent source laser is sent to photodetector $D^{(pr/cj)}$. The $\mathrm{HF}^{(pr/cj)}$ is demodulated with orthogonal signals (Cos and Sine) and thereafter, the shot noise is determined by the variance of the subtraction of the high frequency photocurrents.

Figure 23 presents the shot noise calibration at the analysis frequency $\Omega = 7$ MHz. The vertical axis is the Shot noise $\Delta^2 I_{SQL}$, and the horizontal axis is the total power of the incoming beam. After the numerical correction explained in section 4.4, we can see that both channels Cosine and Sine differ by less than 1%. The shot noise could also be used for defining the minimum total incoming power such that the photocurrent signal is 3 dB above the electronic noise level. This is reported in the figure as the P_{min} value which for 7 MHz corresponds to 0.49 mW. Incoming power below P_{min} may have the risk of been too close to the electronic level and diverge in the data analysis. The same characterization was done for an analysis frequency of 10 MHz. The result is shown in Figure 24. The divergence between slope and the y -intercept is less than 1% and P_{min} =0.56 mW. Compared to the case of 7MHz, notice that P_{min} increases in 0.07 mW, meaning that the electronic noise level is bigger at 10 MHz than at 7 MHz.

The shot noise calibration must be done for every tomography. It is useful for the diagnosis of any electronic trouble, saturation of the high frequency or DC signal, and in general, response of the demodulation channel. As mentioned at the beginning of this subsection, the shot noise in the direct detection must be determined separately from the tomography. Thereafter, we can infer the shot noise level corresponding to the generated beams by associating their total power to the vertical axis in figures 23 and 24.

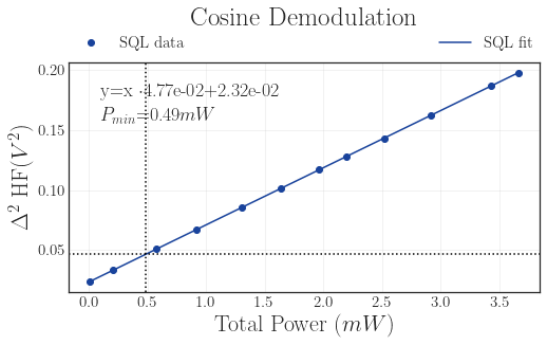

(a) Shot noise calibration at $\Omega = 7MHz$ cosine channel.

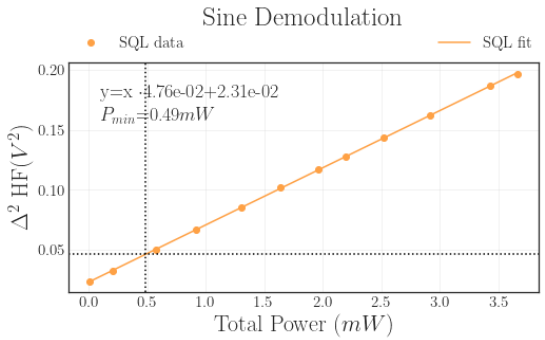

(b) Shot noise calibration at $\Omega = 7MHz$ sine channel.

Figure 23. Shot noise calibration at Ω =7MHz.**(a)**Cosine demodulation channel. **(b)** Sine demodulation channel. P_{min} refers to the minimum input power such that the noise signal is 3 dB above the electronic signal.

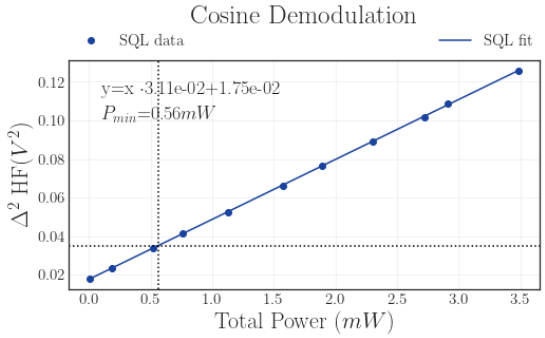

(a) Shot noise calibration at $\Omega = 10MHz$ cosine channel.

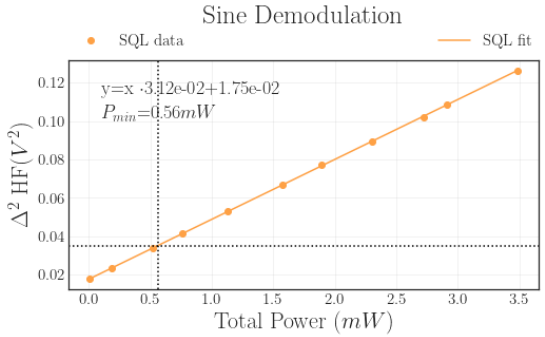

(b) Shot noise calibration at $\Omega = 10MHz$ sine channel.

Figure 24. Shot noise calibration at Ω =10MHz.**(a)**Cosine demodulation channel. **(b)** Sine demodulation channel. P_{min} refers to the minimum input power such that the noise signal is 3 dB above the electronic signal.

4.6.2 Resonator detection

A resonator or an optical cavity, consist of a set of mirrors that are aligned such that an incoming beam oscillates inside of it and interferes with itself after a round trip. Given the case that the length L of the cavity is an integer multiple of the incoming wavelength [VI], the field will interfere constructively and the cavity will be in *resonance*. The resonant frequencies can be determined by the relation

$$\nu_q = qv/L,$$

where q is an integer bigger than 1, $v = c/n$ is the speed of light in the medium of refractive index n, c is the speed of light in vacuum, and L the round-trip distance. The size of the cavity can be scanned such that another resonance condition could be found. This

[VI] The length of the cavity refers to the round-trip distance.

difference is called *free spectral range* (FSR) and is related to the time the light takes to complete a round trip. The FSR is given by

$$FSR = v/L. \tag{4.5}$$

A resonator is not only characterized by its length but also by the reflectivity of the mirrors. In a closed resonator, the mirrors have a high reflectivity and the light oscillates more times before being transmitted. In contrast, an open resonator has low reflective mirrors and the light leave sooner the resonator. This property is related to the lifetime of the light inside the resonator and is known as the *resonator bandwidth* (Γ) corresponding to the *half-width at half maximum*. Finally, we can relate both quantities by defining the *finesse* (F) of the resonator, which describes the build-up of the light given by the interference. The finesse is given by

$$\begin{aligned} F &= \frac{FSR}{2\Gamma} \\ &= \frac{2\pi}{1-\rho_{cav}} \end{aligned} \tag{4.6}$$

where ρ_{cav} stands for the total losses after a round trip. This expression holds for the high finesse regime, around $\rho_{cav} \leq 10\%$. The cavity properties are depicted in figure Figure 25.

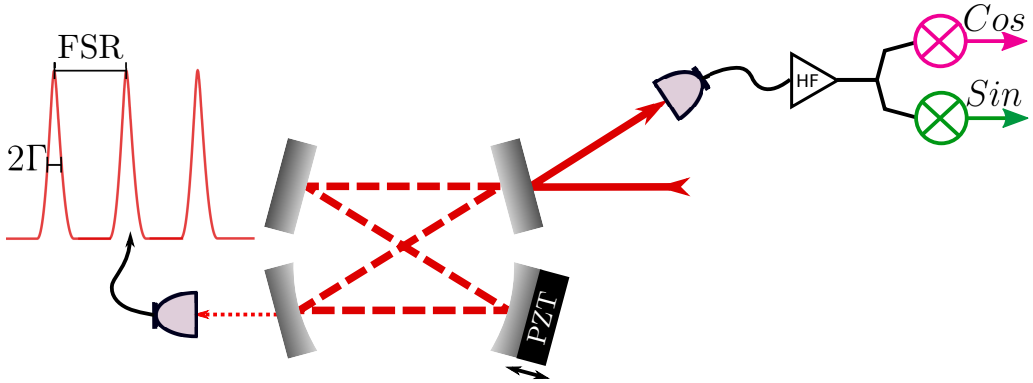

Figure 25. Resonator or optical cavity. The FSR corresponds to the distance between two consecutive resonance frequencies. The bandwidth Γ corresponds to the half-width at half maximum.

The tomography of the state is done by implementing the *resonator detection* [30]. In this method, an analysis cavity (the resonator) induce a dephase sensitive to the frequency such that there is an interference between different frequency components that controls the sideband and their quadratures. The local oscillator would be the carrier centered at frequency ω_{ca}. It will amplify the signal from the sidebands at frequencies $\omega_{ca} \pm \Omega$ where the quantum information can be measured. Simultaneously, the analysis cavity induces a frequency dependent attenuation, detecting individually the sidebands

inasmuch as the detuning of the analysis cavity selects which spectral mode is in resonance. The detunig of the cavity Δ is defined as:

$$\begin{aligned} \Delta_{\pm} &= \Delta_{ca} \pm \frac{\Omega}{2\Gamma}, \\ \Delta_{ca} &= \frac{\omega_{ca} - \omega_{cav}}{2\Gamma} \end{aligned} \tag{4.7}$$

where Ω is the analysis frequency, 2Γ is the analysis cavity bandwidth, ω_{ca} is the carrier frequency, ω_{cav} is the analysis cavity resonance frequency, hence, Δ_{ca} is the relative frequency between carrier and analysis cavity frequency. The detuning of the resonator defines the effect of the resonator on the incoming beam. In the case of the amplitude, the reflection of the cavity presents the following dependence with Δ:

$$r(\Delta_{\pm\Omega}) = r\left(\frac{\omega_{ca} - \omega_{cav}}{2\Gamma} \pm \frac{\Omega}{2\Gamma}\right). \tag{4.8}$$

A detailed explanation of the resonator detection can be done with the help of Figure 26. To the left top, there is the DC signal from the reflection of the cavity **(a)**. To the right, the single mode noise spectrum **(b)**. In the bottom left figure **(c)** we represented the noise ellipse of the quadratures in the symmetric/anti-symmetric basis and the effect of the resonator on the incoming beam. The last figure **(d)** corresponds to the measurement of the quadratures in the sideband basis. Numbers $\boxed{0}$ to $\boxed{7}$ represents an specific region in the tomography of the state. From $\boxed{2}$ to $\boxed{6}$, the resonator detection access the information of the quadratures in the symmetric/anti-symmetric basis. As far as in this region the carrier – represented in light blue in figures **(a)** and **(b)**– is in resonance, its phase will be affected by the dispersive response of the resonator. Starting at region $\boxed{2}$ where there is almost a complete read out of a quadrature, as the resonator detuning Δ is scanned, the carrier "rotates" such that at region $\boxed{4}$ there will be complete measurement of one of the orthogonal quadratures, at $\boxed{6}$ the read out of the conjugated quadrature. Throughout all the light blue region, the carrier is in resonance with the analysis cavity and after region $\boxed{6}$, the process is mirrored such that once the carrier is out of resonance with the resonator, its phase has been rotated by 2π.

Now, we should explain the remaining regions. At region $\boxed{0}$ neither the sidebands nor the carrier are in resonance with the analysis cavity and hence, all the light is reflected and goes into detection. Therefore, we should be reading the total noise from the system in the amplitude quadrature. However, at regions $\boxed{1}$ and $\boxed{7}$, the lower and the upper sidebands are measured. Recall that the sideband modes are thermal states (section 2.2). In $\boxed{1}$, the lower sideband is in resonance with the analysis cavity. Consequently, we would observe a depletion in the noise spectral density due to the attenuation of the fluctuations

from the lower sideband. On the other hand, at region 7 is the upper sideband which is in resonance with the analysis cavity. However, if the fluctuations are not the same, for instance the upper sideband presents smaller fluctuation levels than the lower sideband, the depletion is not going to be the same as region 1 and hence, there will be evident an existent asymmetry in the noise spectral density. This asymmetry will be discussed once we define the covariance matrix parameters.

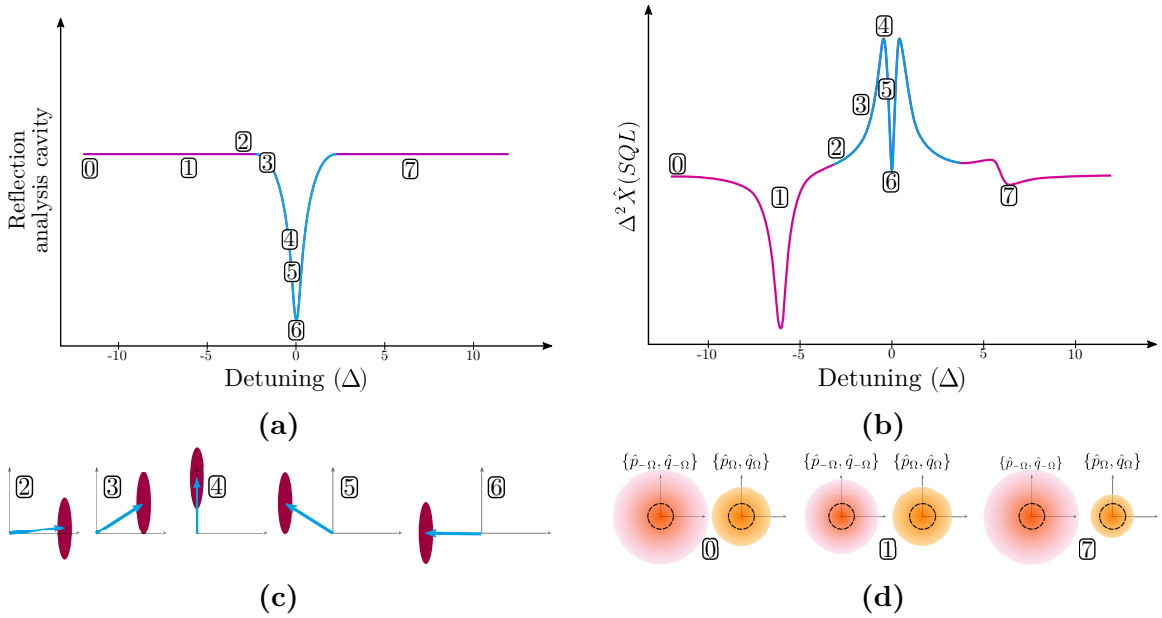

Figure 26. Tomography of the state using the resonator detection. **(a)** DC signal from the reflection of the resonator. **(b)** Single mode noise spectrum. **(c)** Measurement of fluctuations in the symmetric/anti-symmetric basis. **(d)** Measurement of the fluctuations of the sidebands. In light blue we represented the carrier while in purple we represented the sideband region. Numbers zero to seven represent an specific region of measurement. From 2 to 6, the fluctuations in the symmetric/anti-symmetric basis are measured. Regions 0, 1 and 7 represents the sideband regions. A detailed explanation is given in the text.

4.6.3 Mismatch factor f

Our system is able to generate states with a huge excess of noise, ranging from 5 SQL to 20 SQL. This seems to be the source of many problems we had to overcome. First of all, consider the case where the light beam is not coupled perfectly into the analysis cavity. Any mismatch between the beam and the cavity results in a fraction of light that is reflected without dephasing, hence, there light going into the photodetector is a mixture between a fraction of light which do not interfere and hence is an amplitude quadrature, and the fraction of light which is affected by the resonator. Even when the mismatch reach values as small as 5% or lower, the fact that the generated states presents a huge excess of noise, any small mismatch would results into a huge contamination of the HF signal that may affect the reconstruction of the state.

Based on the work done in Appendix B of the article *Assumption free measurement of the quantum state of light: exploring the sidebands of intense fields* [68], we could describe the effect of the mismatch factor on the reconstruction of the state as described as follows.

Consider the spatial mode of the impinging beam as two modes in the spatial basis $\vec{F}_i(r)$ privileged by the resonator:

$$\hat{\mathbf{E}}^+(\mathbf{r},t) = \vec{F}_1(\mathbf{r})\hat{A}(t) + \vec{F}_2(\mathbf{r})\hat{B}(t), \tag{4.9}$$

where $\hat{A}(t)$ is the target resonator spatial mode, and $\hat{B}$ is the mismatch component. $\vec{F}_i(\mathbf{r})$ is the spatial profile of the light beam in the Hermite-Gaussian basis. The photocurrent for a single beam Equation 2.35 now reads

$$\begin{aligned} i(t) &= \int \kappa \hat{\mathbf{E}}^-(\mathbf{r},t)\hat{\mathbf{E}}^+(\mathbf{r},t)dr^2, \\ &= \int \Big(\left|\vec{F}_1(\mathbf{r})\right|^2 \hat{A}^\dagger(t)\hat{A}(t) + \left|\vec{F}_2(\mathbf{r})\right|^2 \hat{B}^\dagger(t)\hat{B}(t) \\ &\quad \vec{F}_1^*(\mathbf{r})\vec{F}_2(\mathbf{r})\hat{A}^\dagger(t)\hat{B}(t) + \vec{F}_2^*(\mathbf{r})\vec{F}_1(\mathbf{r})\hat{B}^\dagger(t)\hat{A}(t)\Big)\, dr^2. \end{aligned} \tag{4.10}$$

where the spatial integral is done over the detector surface. The spatial functions respect orthonormal condition $\int \vec{F}_i(\mathbf{r})\vec{F}_j^*(\mathbf{r})dr^2 = \delta_{ij}$. Hence

$$i(t) = \hat{A}^\dagger(t)\hat{A}(t) + \hat{B}^\dagger(t)\hat{B}(t). \tag{4.11}$$

Consider the mismatch factor f such that

$$1 - f^2 \tag{4.12}$$

is the *resonator coupling factor* defined as the fraction of intensity of light that is not coupled into the analysis cavity. The mismatch factor is such that if $f = 0$ the light beam is perfectly coupled, whereas if $f = 1$ the light beam is completely reflected by the cavity. Therefore, given a mismatch factor $f \neq 0$, the resonator couples the incoming carrier in mode $\hat{a}$, which is considered as a coherent state with amplitude α_{ca}, with the vacuum modes $\hat{c}$ populating different spatial modes. Hence, the target mode of the resonator $\hat{A}$ and the mismatch modes $\hat{B}$ are relted to the incoming modes by a beam splitter transformation (Figure 27):

$$\begin{pmatrix} \hat{B} \\ \hat{A} \end{pmatrix} = \begin{pmatrix} f & \sqrt{1-f^2} \\ \sqrt{1-f^2} & -f \end{pmatrix} \begin{pmatrix} \hat{a} \\ \hat{c} \end{pmatrix}, \tag{4.13}$$

where the $\hat{a}$ corresponds to the carrier mode and $\hat{c}$ are spatial modes in the vacuum state.

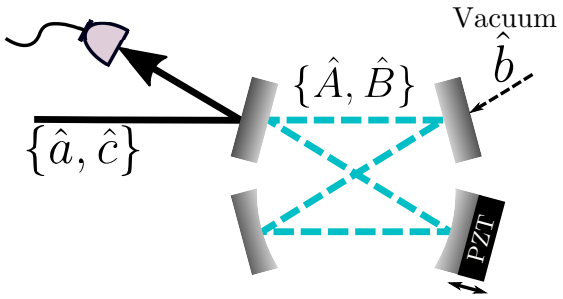

Figure 27. Mismatch between incoming beams and resonator. $\{\hat{a}, \hat{c}\}$ is the basis of the generated beams and detection. $\{\hat{A}, \hat{B}\}$ is the privileged basis of the cavity.

Consequently, the state after the resonator can be written as the tensor product of fraction of the carrier coupled into the target mode $\hat{A}$, the uncoupled fraction of the carrier in mode $\hat{B}$, and the sideband modes,

$$|\Psi\rangle = |\sqrt{1-f^2}\alpha_{ca}\rangle_A \otimes |f\alpha_{ca}\rangle_B \otimes \otimes |\varphi_{\pm\Omega}\rangle_{sd}\,. \tag{4.14}$$

Each of the modes A and B, can be decomposed into its mean value and its fluctuations $\hat{O} = \langle\hat{O}\rangle + \delta\hat{O}$. Therefore, the fluctuations of the photocurrent $i(t)$ is

$$\begin{aligned} \delta i(t) &= \sqrt{1-f^2}\left[\alpha^*\delta\hat{A}(t) + \alpha\delta\hat{A}^\dagger(t)\right] + & (4.15)\\ &\quad f\left[\alpha^*\delta\hat{B}(t) + \alpha\delta\hat{B}^\dagger(t)\right]. & (4.16)\end{aligned}$$

The $\hat{A}$ mode is coupled into the cavity, hence, its amplitude depends on the cavity detuning Δ through the reflection such that $\alpha \to r^*(\Delta)|\alpha|$. Moreover, it is modified by the *resonator coupling factor* by $\sqrt{1-f^2}$. On the other hand, mode $\hat{B}$ is reflected by the cavity modifying its amplitude by the f factor $\alpha^* = \alpha \to f|\alpha|$ but without frequency dependence. Therefore, the fluctuation reads

$$\begin{aligned} \delta i(t) &= \sqrt{1-f^2}|\alpha|\left[|r^*(\Delta_{\pm\Omega})|\delta\hat{A}(t) + |r(\Delta_{\pm\Omega})|\delta\hat{A}^\dagger(t)\right] + & (4.17)\\ &\quad f|\alpha|\left[\delta\hat{B}(t) + \delta\hat{B}^\dagger(t)\right]. & (4.18)\end{aligned}$$

Following the procedure presented in Equation 2.40-Equation 2.41 and the notation in Equation 2.48, the fluctuations can be written in the frequency domain as

$$\begin{aligned} \delta\hat{\mathbf{X}}_\Omega &= \sqrt{1-f^2}|\alpha|\left[|r^*(\Delta_{\pm\Omega})|\delta\hat{A}_\Omega + |r(\Delta_{\pm\Omega})|\delta\hat{A}^\dagger_{-\Omega}\right] + \\ &\quad f|\alpha|\left[\delta\hat{B}_\Omega + \delta\hat{B}^\dagger_{-\Omega}\right]. & (4.19)\end{aligned}$$

Up to this point, we must consider the effect of the analysis cavity into the sideband modes [30]. The target mode $\hat{A}$ is affected by the dispersive reponse of the resonator while a vacuum component $\hat{b}$ is introduced,

$$\hat{A}_\Omega \rightarrow r\left(\Delta_{\pm\Omega}\right)\hat{A}_\Omega + t\left(\Delta_{\pm\Omega}\right)\hat{b}_\Omega. \tag{4.20}$$

The reflectivity of the cavity depends on the detuning $\Delta_{\pm\Omega}$ as follows:

$$\begin{aligned} R(\Delta_{\pm\Omega}) &= \frac{r^*(\Delta_{ca})}{|r(\Delta_{ca})|} r\left(\Delta_{\pm\Omega}\right) \\ r(\Delta_{\pm\Omega}) &= -\frac{\sqrt{d} - 2i\Delta_{\pm\Omega}}{1 - 2i\Delta_{\pm\Omega}}, \\ |r(\Delta_\Omega)| &= |r(\Delta_{-\Omega})|, \\ T(\Delta_{\pm\Omega}) + R(\Delta_{\pm\Omega}) &= 1 \end{aligned}$$

being $d = |r(0)|^2$ the depletion of the reflected beam. The expression for $r(\Delta_{\pm\Omega})$ is valid for high finesse cavities [45].

As a result, the fluctuations of the incoming modes depend on the analysis cavity properties and its response to the incoming frequency:

$$\begin{aligned} \delta\hat{\mathbf{X}}_\Omega = \; & \sqrt{1-f^2}|\alpha||r(\Delta)|\left[R(\Delta_\Omega)\delta\hat{A}_\Omega + T(\Delta_\Omega)\hat{b}_\Omega + \right. \\ & \left. R^*(\Delta_{-\Omega})\delta\hat{A}^\dagger_{-\Omega} + T^*(\Delta_{-\Omega})\hat{b}^\dagger_{-\Omega}\right] + \\ & f|\alpha|\left[\delta\hat{B}_\Omega + \delta\hat{B}^\dagger_{-\Omega}\right]. \end{aligned} \tag{4.21}$$

So far, $\delta\hat{\mathbf{X}}_\Omega$ contemplates the decomposition of the impinging beams in the privileged basis of the cavity. To obtain the states measured by photodetection, it is necessary to change the modal basis $\{\hat{A}, \hat{B}\}$ to the detection basis $\{\hat{a}, \hat{c}\}$

$$\hat{a}_\Omega = \sqrt{1-f^2}\hat{A}_\Omega + f\hat{B}_\Omega \tag{4.22}$$

$$\hat{c}_\Omega = -f\hat{A}_\Omega + \sqrt{1-f^2}\hat{B}_\Omega \tag{4.23}$$

where $\hat{a}$ is the principal generated mode containing the carrier and the sidebands, and $\hat{c}$ are the vacuum modes that go along with the process. Under this transformation, the fluctuations yields,

$$\begin{aligned} \delta\hat{\mathbf{X}}_\Omega &= \left(1-f^2\right)|r\left(\Delta\right)|\left[R(\Delta_\Omega)\hat{a}_\Omega + R^*(\Delta_{-\Omega})\hat{a}^\dagger_{-\Omega}\right] + f^2\left(\hat{a}_\Omega + \hat{a}^\dagger_{-\Omega}\right) + \hat{J}'_v, \\ &= \left(1-f^2\right)|r\left(\Delta\right)|\left[\frac{\hat{I}_{cos} + i\hat{I}_{sin}}{\sqrt{2}}\right] + \frac{f^2}{2}\left[\hat{p}_s + i\hat{q}_a\right] + \hat{J}'_v \end{aligned} \tag{4.24}$$

where $\hat{I}_{cos}$ and $\hat{I}_{sin}$ are two Hermitian operators associated to the demodulated photocurrent and have the form:

$$\begin{aligned}\hat{I}_{cos} &= \frac{1}{\sqrt{2}}\left(\hat{p}_s \cos\varphi_{ca} + \hat{q}_s \sin\varphi_{ca}\right), \\ \hat{I}_{sin} &= \frac{1}{\sqrt{2}}\left(\hat{q}_a \cos\varphi_{ca} - \hat{p}_a \sin\varphi_{ca}\right),\end{aligned}$$

with φ_{ca} standing for the phase of the carrier, $\hat{p}_{s/a}$ and $\hat{q}_{s/a}$ are the symmetric/anti-symmetric amplitude quadrature defined in Equation 2.52. $\hat{J}'_v$ is the vacuum contribution from the process $\hat{c}$ and the analysis cavity $\hat{b}$ and is given by

$$\begin{aligned}\hat{J}'_v &= f\sqrt{1-f^2}\left[\left(1 - R(\Delta_\Omega)\hat{c}_\Omega + (1 - R^*(\Delta_{-\Omega}))\,\hat{c}^\dagger_{-\Omega}\right)\right] + \\ &\quad \sqrt{1-f^2}\left[T(\Delta_\Omega)\hat{b}_\Omega + T^*(\Delta_{-\Omega})\hat{b}^*_{-\Omega}\right].\end{aligned}$$

Notice that if the coupling were perfect ($f = 0$), the fluctuation term would correspond to the addition of the two photocurrent components up to a phase $(r(\Delta)/\sqrt{2})(\hat{I}_{cos} + i\hat{I}_{sin})$, recovering the expression reported in [45]. Therefore, the mismatch adds further terms to the photocurrent $\delta\hat{\mathbf{X}}_\Omega$, where two of them are proportional to the fraction of light reflected by the cavity (f^2), and a vacuum term.

4.6.4 Noise spectral density and covariance matrix

For the reconstruction of the single mode correlations, we must calculate the noise spectrum for a single mode (Equation 2.58):

$$\begin{aligned}S^m(\Omega) &= \left\langle \delta\hat{\mathbf{X}}^{(j)}_\Omega \delta\hat{\mathbf{X}}^{(j)}_{-\Omega} \right\rangle, \\ &= \alpha_j\left[A'C_\alpha + B'Re\{g_+\} + \frac{f^4}{2}\right] + \\ &\quad \beta_j\left[A'C_\beta\right] + \\ &\quad \gamma_j\left[A'C_\gamma + B'Re\{g_-\}\right] + \\ &\quad \delta_j\left[A'C_\delta + B'Im\{g_-\}\right] + \\ &\quad B'Im\{g_-\} + \langle \hat{J}'_v\, \hat{J}'_{-v}\rangle,\end{aligned} \tag{4.25}$$

$$\begin{aligned}A' &= \frac{r^2(\Delta)(1-f^2)^2}{2} \\ B' &= \frac{2r(\Delta)f^2(1-f^2)}{\sqrt{2}}.\end{aligned}$$

Let $j = pr, cj$. α_j, β_j, γ_j and δ_j correspond to the parameters that describe the individual states and their correlations; they are organized in the covariance matrix as shown in Equation 4.28. Each parameter has a weight function that depends on the analysis cavity response such that they are enhanced or diminished according to the reflectivity R and the detuning Δ. In the case of the single mode noise spectrum,

$$\begin{aligned} C_\alpha = |g_+|^2 \quad &; \quad C_\beta = |g_-|^2 \\ C_\gamma = 2Re\{g_+^* g_-\} \quad &; \quad C_\delta = 2Im\{g_+^* g_-\} \\ g_+ = \frac{R(\Delta_\Omega) + R^*(\Delta_{-\Omega})}{2} \quad &; \quad g_- = i\left(\frac{R(\Delta_\Omega) - R^*(\Delta_{-\Omega})}{2}\right) \end{aligned}$$

The vacuum contribution from modes $\hat{c}$ and $\hat{b}$ is

$$\begin{aligned} \left\langle \hat{J}'_v \, \hat{J}'_{-v} \right\rangle &= (1-f^2) r(\Delta)^2 \left\langle \hat{J}_v \, \hat{J}_{-v} \right\rangle + \\ &\quad f^2(1-f^2)\left[r(\Delta)\left(C_\alpha + C_\beta - 2Re\{g_+\} - 2Im\{g_-\}\right) + 1\right] \\ \left\langle \hat{J}_v \, \hat{J}_{-v} \right\rangle &= 1 - C_\alpha - C_\beta. \end{aligned} \tag{4.26}$$

The covariance matrix is completed by computing the correlation between the probe and conjugated beams. According to Equation 4.24 the two-mode noise spectrum –or cross-correlation– is:

$$\begin{aligned} S_{cr}^m(\Omega) &= \left\langle \delta\hat{\mathbf{X}}_\Omega^{(pr)} \, \delta\hat{\mathbf{X}}_{-\Omega}^{(cj)} \right\rangle \\ &= Re\left\{\left\langle \delta\hat{\mathbf{X}}_\Omega^{(pr)} \, \delta\hat{\mathbf{X}}_{-\Omega}^{(cj)} \right\rangle\right\} + iIm\left\{\left\langle \delta\hat{\mathbf{X}}_\Omega^{(pr)} \, \delta\hat{\mathbf{X}}_{-\Omega}^{(cj)} \right\rangle\right\} \\ Re\left\{\left\langle \delta\hat{\mathbf{X}}_\Omega^{(pr)} \, \delta\hat{\mathbf{X}}_{-\Omega}^{(cj)} \right\rangle\right\} &= \mu\left(A\,C_\mu + B\,Re\{g_{+1}\} + C\,Re\{g_{+2}^*\} + D\right) + \\ &\quad \kappa\left(A\,C_\kappa - C\,Im\{g_{-2}^*\}\right) \\ &\quad \xi\left(A\,C_\xi + C\,Re\{g_{-2}^*\}\right) + \\ &\quad \eta\left(A\,C_\eta - B\,Im\{g_{+1} - C\,Im\{g_{+2}^*\}\}\right) + \\ &\quad \lambda\left(A\,C_\lambda - B\,Im\{g_{-1}\}\right) + \\ &\quad \nu A\,C_\nu + \tau A\,C_\tau + \\ &\quad \zeta\left(A\,C_\zeta + B\,Re\{g_{-1}\}\right), \end{aligned} \tag{4.27}$$

$$
\begin{aligned}
Im\left\{\left\langle \delta\hat{\mathbf{X}}_{\Omega}^{(pr)}\,\delta\hat{\mathbf{X}}_{-\Omega}^{(cj)}\right\rangle\right\} &= \mu\left(-A\,C_{\eta}+B\,Im\{g_{+1}\}+C\,Im\{g_{+2}^{*}\}\right)+\\
&\quad \kappa\left(A\,C_{\xi}+C\,Re\{g_{-2}^{*}\}\right)+\\
&\quad \xi\left(-A\,C_{\kappa}+C\,Im\{g_{-2}^{*}\}+D\right)+\\
&\quad \tau A\,C_{\nu}-\nu A\,C_{\tau}+\\
&\quad \zeta\left(-A\,C_{\lambda}+B\,Im\{g_{-1}\}\right)+\\
&\quad \lambda\left(A\,C_{\zeta}+B\,Re\{g_{-1}\}\right),
\end{aligned}
$$

where we defined

$$
\begin{aligned}
A &= |r(\Delta)|_{pr}|r(\Delta)|_{cj}(1-f_{pr}^{2})(1-f_{cj}^{2})\\
B &= \frac{|r(\Delta)|_{pr}(1-f_{pr}^{2})f_{cj}^{2}}{\sqrt{2}}\\
C &= \frac{|r(\Delta)|_{cj}(1-f_{cj}^{2})f_{pr}^{2}}{\sqrt{2}}\\
D &= \frac{f_{pr}^{2}f_{cj}^{2}}{2}.
\end{aligned}
$$

The subscript indicates the analysis cavity for each beam which in general are not equal. The weight C functions for the cross-correlations are

$$
\begin{aligned}
C_{\mu} = Re\{g_{+1}^{*}g_{+2}\} \;&;\; C_{\kappa} = Im\{g_{+1}^{*}g_{-2}\}\\
C_{\xi} = Re\{g_{+1}^{*}g_{-2}\} \;&;\; C_{\eta} = Im\{g_{+1}^{*}g_{+2}\}\\
C_{\lambda} = Im\{g_{-1}^{*}g_{+2}\} \;&;\; C_{\nu} = Re\{g_{-1}^{*}g_{-2}\}\\
C_{\tau} = Im\{g_{-1}^{*}g_{-2}\} \;&;\; C_{\zeta} = Re\{g_{-1}^{*}g_{+2}\}.
\end{aligned}
$$

Now we have the complete toolkit that permits the reconstruction of the generated state and its correlations, meaning the covariance matrix in the *symmetric/anti-symmetric basis* SA and in the sideband basis.

In terms of the quadratures in the *symmetric/anti-symmetric basis* $\hat{\mathbf{X}}_{s/a}$, the covariance matrix is:

$$
\mathbb{V}_{s,a} = \begin{pmatrix} \mathbb{V}_{s} & \mathbb{C}_{s,a} \\ \mathbb{C}_{s,a} & \mathbb{V}_{a} \end{pmatrix}. \tag{4.28}
$$

The covariance matrix in the SA basis is organized in block diagonal form. The diagonals correspond to the symmetric or anti-symmetric part $\mathbb{V}_{s}$ ($\mathbb{V}_{a}$), and the off-diagonal terms, to the cross-correlations between the quadratures of different modes $\mathbb{C}_{s,a}$. Each of the diagonal terms have the explicit form:

$$\begin{aligned}\mathbb{V}_s &= \begin{pmatrix} \Delta^2\hat{p}_s^{(pr)} & \left\langle \hat{p}_s^{(pr)}, \hat{q}_s^{(pr)} \right\rangle & \left\langle \hat{p}_s^{(pr)}, \hat{p}_s^{(cj)} \right\rangle & \left\langle \hat{p}_s^{(pr)}, \hat{q}_s^{(cj)} \right\rangle \\ \left\langle \hat{q}_s^{(pr)}, \hat{p}_s^{(pr)} \right\rangle & \Delta^2\hat{q}_s^{(cj)} & \left\langle \hat{q}_s^{(pr)}, \hat{p}_s^{(cj)} \right\rangle & \left\langle \hat{q}_s^{(pr)}, \hat{q}_s^{(cj)} \right\rangle \\ \left\langle \hat{p}_s^{(cj)}, \hat{p}_s^{(pr)} \right\rangle & \left\langle \hat{p}_s^{(cj)}, \hat{q}_s^{(pr)} \right\rangle & \Delta^2\hat{p}_s^{(cj)} & \left\langle \hat{p}_s^{(cj)}, \hat{q}_s^{(cj)} \right\rangle \\ \left\langle \hat{q}_s^{(cj)}, \hat{p}_s^{(pr)} \right\rangle & \left\langle \hat{q}_s^{(cj)}, \hat{q}_s^{(pr)} \right\rangle & \left\langle \hat{q}_s^{(cj)}, \hat{p}_s^{(cj)} \right\rangle & \Delta^2\hat{q}_s^{(cj)} \end{pmatrix} \\ &= \begin{pmatrix} \alpha^{(pr)} & \gamma^{(pr)} & \mu & \xi \\ \gamma^{(pr)} & \beta^{(pr)} & \zeta & \nu \\ \mu & \zeta & \alpha^{(cj)} & \gamma^{(cj)} \\ \xi & \nu & \gamma^{(cj)} & \beta^{(cj)} \end{pmatrix}. \end{aligned} \tag{4.29}$$

$$\begin{aligned}\mathbb{V}_a &= \begin{pmatrix} \Delta^2\hat{p}_a^{(pr)} & \left\langle \hat{p}_a^{(pr)}, \hat{q}_a^{(pr)} \right\rangle & \left\langle \hat{p}_a^{(pr)}, \hat{p}_a^{(cj)} \right\rangle & \left\langle \hat{p}_a^{(pr)}, \hat{q}_a^{(cj)} \right\rangle \\ \left\langle \hat{q}_a^{(pr)}, \hat{p}_a^{(pr)} \right\rangle & \Delta^2\hat{q}_a^{(pr)} & \left\langle \hat{q}_a^{(pr)}, \hat{p}_a^{(cj)} \right\rangle & \left\langle \hat{q}_a^{(pr)}, \hat{q}_a^{(cj)} \right\rangle \\ \left\langle \hat{p}_a^{(cj)}, \hat{p}_a^{(pr)} \right\rangle & \left\langle \hat{p}_a^{(cj)}, \hat{q}_a^{(pr)} \right\rangle & \Delta^2\hat{p}_a^{(cj)} & \left\langle \hat{p}_a^{(cj)}, \hat{q}_a^{(cj)} \right\rangle \\ \left\langle \hat{q}_a^{(cj)}, \hat{p}_a^{(pr)} \right\rangle & \left\langle \hat{q}_a^{(cj)}, \hat{q}_a^{(pr)} \right\rangle & \left\langle \hat{q}_a^{(cj)}, \hat{p}_a^{(cj)} \right\rangle & \Delta^2\hat{q}_a^{(cj)} \end{pmatrix} \\ &= \begin{pmatrix} \beta^{(pr)} & -\gamma^{(pr)} & \nu & -\zeta \\ -\gamma^{(pr)} & \alpha^{(pr)} & -\xi & \mu \\ \nu & -\xi & \beta^{(cj)} & -\gamma^{(cj)} \\ -\zeta & \mu & -\gamma^{(cj)} & \alpha^{(cj)} \end{pmatrix}. \end{aligned} \tag{4.30}$$

$$\begin{aligned}\mathbb{C}_{s,a} &= \begin{pmatrix} \left\langle \hat{p}_s^{(pr)}, \hat{p}_a^{(pr)} \right\rangle & 0 & \left\langle \hat{p}_s^{(pr)}, \hat{p}_a^{(cj)} \right\rangle & \left\langle \hat{p}_s^{(pr)}, \hat{q}_a^{(cj)} \right\rangle \\ 0 & \left\langle \hat{q}_s^{(pr)}, \hat{q}_a^{(pr)} \right\rangle & \left\langle \hat{q}_s^{(pr)}, \hat{p}_a^{(cj)} \right\rangle & \left\langle \hat{q}_s^{(pr)}, \hat{q}_a^{(cj)} \right\rangle \\ \left\langle \hat{p}_s^{(cj)}, \hat{p}_a^{(pr)} \right\rangle & \left\langle \hat{p}_s^{(cj)}, \hat{q}_a^{(pr)} \right\rangle & \left\langle \hat{p}_s^{(cj)}, \hat{p}_a^{(cj)} \right\rangle & 0 \\ \left\langle \hat{q}_s^{(cj)}, \hat{p}_a^{(pr)} \right\rangle & \left\langle \hat{q}_s^{(cj)}, \hat{q}_a^{(pr)} \right\rangle & 0 & \left\langle \hat{q}_s^{(pr)}, \hat{q}_a^{(cj)} \right\rangle \end{pmatrix} \\ &= \begin{pmatrix} \delta^{(pr)} & 0 & \kappa & -\eta \\ 0 & \delta^{(pr)} & \tau & -\lambda \\ -\lambda & \eta & \delta^{(cj)} & 0 \\ -\tau & \kappa & 0 & \delta^{(cj)} \end{pmatrix}. \end{aligned} \tag{4.31}$$

The covariance matrix $\mathbb{V}_{s,a}$ represents a two-mode state, for instance, a two-mode squeezed state. The covariance matrix in the SA basis (Equation 4.28) can be transformed into the *sideband basis* by the Equation 2.54 yielding:

$$\begin{aligned}\mathbb{V}_{\pm\Omega} &= \Lambda\mathbb{V}_{s,a}\Lambda^T \\ &= \begin{pmatrix} \mathbb{V}_{-\Omega} & \mathbb{C}_{\pm\Omega} \\ \mathbb{C}_{\pm\Omega} & \mathbb{V}_{\Omega} \end{pmatrix}. \end{aligned} \tag{4.32}$$

For instance, the first diagonal block has the form:

$$\mathbb{V}_{-\Omega} = \begin{pmatrix} \Delta^2\hat{p}_{-\Omega}^{(pr)} & 0 & \left\langle \hat{p}_{-\Omega}^{(pr)}, \hat{p}_{-\Omega}^{(cj)} \right\rangle & \left\langle \hat{p}_{-\Omega}^{(pr)}, \hat{q}_{-\Omega}^{(cj)} \right\rangle \\ 0 & \Delta^2\hat{q}_{-\Omega}^{(pr)} & \left\langle \hat{q}_{-\Omega}^{(pr)}, \hat{p}_{-\Omega}^{(cj)} \right\rangle & \left\langle \hat{q}_{-\Omega}^{(pr)}, \hat{q}_{-\Omega}^{(cj)} \right\rangle \\ \left\langle \hat{p}_{-\Omega}^{(cj)}, \hat{p}_{-\Omega}^{(pr)} \right\rangle & \left\langle \hat{p}_{-\Omega}^{(cj)}, \hat{q}_{-\Omega}^{(pr)} \right\rangle & \Delta^2\hat{p}_{-\Omega}^{(cj)} & 0 \\ \left\langle \hat{q}_{-\Omega}^{(cj)}, \hat{p}_{-\Omega}^{(pr)} \right\rangle & 0 & \left\langle \hat{q}_{-\Omega}^{(cj)}, \hat{p}_{-\Omega}^{(cj)} \right\rangle & \Delta^2\hat{q}_{-\Omega}^{(cj)} \end{pmatrix}. \tag{4.33}$$

Notice that in the *sideband basis*, $\Delta^2\hat{p}_{\pm\Omega}^{(j)} = \Delta^2\hat{q}_{\pm\Omega}^{(j)} = 0.5(\alpha^{(j)} + \beta^{(j)} \pm \delta^{(j)})$, and $\left\langle \hat{p}_{\pm\Omega}^{(j)}, \hat{q}_{\pm\Omega}^{(j)} \right\rangle = 0$. As a consequence, in the *sideband basis* the generated states are coherent thermal states as the ones presented in Figure 4a, contrary to the representation in the SA basis.

We must highlight some parameters from the covariance matrix which have direct interpretation. α_j corresponds to the amplitude fluctuations, it can be accessed by direct detection. β_j is the phase fluctuations which are detected implementing interferometric detection. γ_j is a parameter that appears when cross-phase modulation appears in the interaction.

A final and special mention must be done on the δ_j parameter. Consider the energy of a single mode in the *sideband basis* $\mathcal{E}_{\pm\Omega} = (1/2)\left(\Delta^2\hat{p}_{\pm\Omega} + \Delta^2\hat{q}_{\pm\Omega}\right)$, where the subscript $\pm$ refers to the upper $(+)$ or lower $(-)$ frequency mode. The difference between the upper and lower sideband from the same spatial mode (probe or conjugated) [66]

$$\mathcal{E}_{+\Omega}^{(j)} - \mathcal{E}_{-\Omega}^{(j)} = 2\delta_j. \tag{4.34}$$

Therefore, δ_j is the energy imbalance between the upper and the lower sideband. This was represented in Figure 26 **(d)** as the imbalance between the fluctuations of the lower and the upper sidebands, which was seen in the single mode noise spectrum as an asymmetry between the lower and the upper sideband read out.

Shot Noise and normalization of the spectrum

In subsection 2.4.2 we introduced the concept of the *shot noise level* as normalization factor for any measurement. It benchmarks the limit between quantum and classic correlations. The *shot noise* was shown to depend on the amplitude of the local oscillator which corresponds to the carrier in the *resonator detection* (Equation 2.63). Furthermore, when considering the mismatch factor f the shot noise is modified such that it depends explicitly on the reflectivity and the mismatch fraction. Hence, the *shot noise* takes the form:

$$\Delta^2\hat{I}_- = |\alpha_{ca}|^2| \left[|r(\Delta)|^2 \left(1 - f^2\right) + f^2 \right] \Delta^2\hat{X}_v, \tag{4.35}$$

leading to the noise spectrum

$$\left\langle \hat{J}_{\Omega}^{(j)} \hat{J}_{-\Omega}^{(j)} \right\rangle = \frac{\left\langle \delta\hat{\mathbf{X}}_{\Omega}^{(j)} \delta\hat{\mathbf{X}}_{-\Omega}^{(j)} \right\rangle}{\Delta^2 I_{-}^{(j)}} \tag{4.36}$$

$$\left\langle \hat{J}_{\Omega}^{(pr)} \hat{J}_{-\Omega}^{(cj)} \right\rangle = \frac{\left\langle \delta\hat{\mathbf{X}}_{\Omega}^{(pr)} \delta\hat{\mathbf{X}}_{-\Omega}^{(cj)} \right\rangle}{\sqrt{\Delta^2 I_{-}^{(pr)} \Delta^2 I_{-}^{(cj)}}},$$

where

$$\hat{J}_{\pm\Omega}^{(j)} = \frac{\delta\hat{\mathbf{X}}_{\pm\Omega}^{(j)}}{\sqrt{\Delta^2 I_{-}^{(j)}}} \tag{4.37}$$

$$= \hat{J}_{cos}^{(j)} \pm i\hat{J}_{sin}^{(j)}, \tag{4.38}$$

where the subscript cos/sin refers to the demodulation signal used to access the information in the fluctuations, and j stands for probe or conjugated.

Experimental details of the tomography

The complete reconstruction of the covariance matrix demands three sequential measurements of the state such that the weight functions C access the parameters as a function of the cavity detuning Δ. The analysis frequency Ω is limited by experimental conditions (Figure 28). On the one hand, its lower value must respect $\Omega > (2\Gamma)\sqrt{2}$, where 2Γ is the bandwidth of the analysis cavity [30]. This condition must be satisfied in order to guarantee a complete transformation between quadratures. On the other hand, the upper value depends on the linewidth of the spectrum of the FWM process Γ_{FWM}.

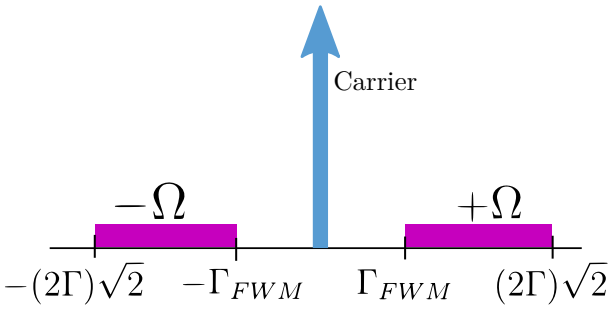

Figure 28. Analysis frequency bounds. The lower bound is defined as a function of the bandwidth of the analysis cavity by $2\Gamma\sqrt{2}$. The upper bound is defined by the emission linewidth and the phase-matching condition FWM (Γ_{FWM}).

The reconstruction of the covariance matrix rely on the assumption that the generated states are stationary. The *stationary conditions* guarantee the covariance matrix to be symmetric and have real eigen-values. Accordingly to Equation 2.58, if

$\Omega' = +\Omega \rightarrow S(\Omega + \Omega') = 0$. Hence, for the single mode case the generated states must respect

$$\Delta^2 \hat{J}^{(j)}_{cos} - \Delta^2 \hat{J}^{(j)}_{sin} = 0 \tag{4.39}$$

$$\left\langle \hat{J}^{(j)}_{cos}\, \hat{J}^{(j)}_{sin} \right\rangle = 0 \tag{4.40}$$

where $j = pr, cj$; on the other hand, for the two mode correlations

$$\left\langle \hat{J}^{(pr)}_{cos}\, \hat{J}^{(cj)}_{cos} \right\rangle = \left\langle \hat{J}^{(pr)}_{sin}\, \hat{J}^{(cj)}_{sin} \right\rangle \tag{4.41}$$

$$\left\langle \hat{J}^{(pr)}_{sin}\, \hat{J}^{(cj)}_{cos} \right\rangle = -\left\langle \hat{J}^{(pr)}_{cos}\, \hat{J}^{(cj)}_{sin} \right\rangle \tag{4.42}$$

Respecting the *stationary conditions* is important for the validity of the construction of the covariance matrix and moreover. They become relevant in the reconstruction of states with huge excess of noise as will be shown in the next section.

Analysis cavity configuration

For our experiment, the analysis cavities are in a bow-tie configuration as shown in Figure 25. Each cavity is 101.70 ± 0.05 cm length, have two plane-plane high reflectance (HR) mirrors and two mirrors with a curvature radius of 2 m. The waist between the plane mirrors is 378.53 ± 0.05 μm while the waist between the curve mirrors is 454.41 ± 0.05 μm. For the probe cavity, the bandwidth is Γ =3.37±0.01 MHz and its finesse 87.4±0.2. In the case of the conjugated cavity, its bandwidth is Γ =3.36±0.01 MHz and its finesse is 87.7±0.2. Hence, to guarantee a complete rotation of the noise ellipse we should measure above an analysis frequency of 5 MHz [30]. After the analysis cavities, the light goes to the photodiodes and follows the electronic scheme explained at the beginning of the chapter (see Figure 18).

4.6.5 Demodulation phase

As mentioned earlier in this chapter, the photocurrent is demodulated using a pair of orthogonal signals *Cosine* and *Sine*. Any deviation from the relative phase of $\pi/2$ will ruin the stationary conditions. This sensitivity was not observed in other works from our group, and can be associated to the fact that the generated states have typical values of excess of noise above 10 SQL.

Consider a single mode and the photocurrent $\hat{J}^{(j)}$ and the two demodulated signals $\hat{J}^{(j)}_{cos}$ and $\hat{J}^{(j)}_{\theta}$ as shown in Figure 29, such that

$$\hat{J}^{(j)} = \hat{J}^{(j)}_{cos} + i\hat{J}^{(j)}_{\theta} \tag{4.43}$$

$$\hat{J}^{(j)}_{\theta} = \sin(\theta)\hat{J}^{(j)}_{cos} + \cos(\theta)\hat{J}^{(j)}_{sin}. \tag{4.44}$$

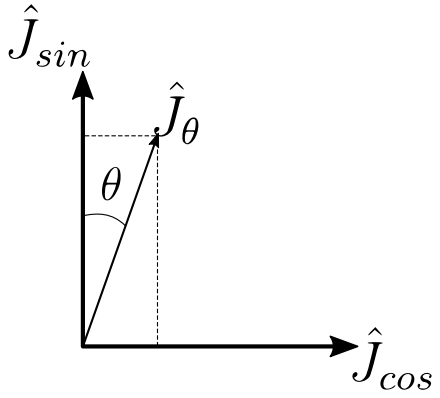

Figure 29. Electronic local oscillator can access any combination $\hat{J}_{\theta}$. Nevertheless, in quadrature observation depends on careful phase adjustment in order to avoid contamination of cross-correlation terms.

The stationary condition for single mode (equations 4.39 and 4.40) yields:

$$\Delta^2 \hat{J}^{(j)}_{cos} - \Delta^2 \hat{J}^{(j)}_{\theta} = 0, \tag{4.45}$$

$$\left\langle \hat{J}^{(j)}_{cos}\, \hat{J}^{(j)}_{\theta} \right\rangle = \Delta^2 \hat{J}^{(j)}_{cos}, \tag{4.46}$$

showing that a misalignment in the demodulation phase could contaminate the measurement. A careful adjustment of the demodulation phases that compensated the inherent electronic shifts of the circuits, could provide a fully compatible response measurements (Figure 30). With all these corrections a good agreement of the curves to the experiment could be obtained, that in principle would reveal a complete four mode covariance matrix.

For a given analysis frequency Ω and electronic configuration, we determined the proper phase by running the experiment with different phases and evaluating the condition for a stationary conditions. Figure 31 shows the characterization of the stationary conditions for single and two-mode correlations as a function of the relative phase between the demodulation channels measured at an analysis frequency of $\Omega = 10$MHz. We vary the phase from 30° to 150°. Notice that the single mode conditions, namely $\langle J^{i}_{Cos} J^{i}_{Sin} \rangle$ (i=pr, cj) are the most affected by the relative phase, and as a consequence the cross-correlation between these photocurrents $\langle J^{pr}_{Cos} J^{cj}_{Sin} \rangle + \langle J^{pr}_{Sin} J^{cj}_{Cos} \rangle$. For every single tomography, the covariance matrix was non-physical except for the case of a relative phase of 90° as expected.

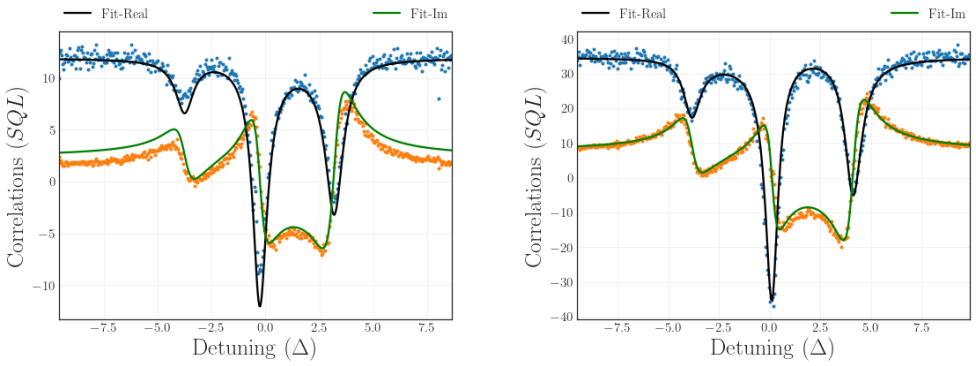

Figure 30. Cross-correlations demodulation phase correction. **(a)** Two-mode correlations without phase correction. Even when to excess of noise is about 10 SQL, the stability condition was not satisfied. **(b)** Two mode correlations with correct adjustment of demodulator phase.

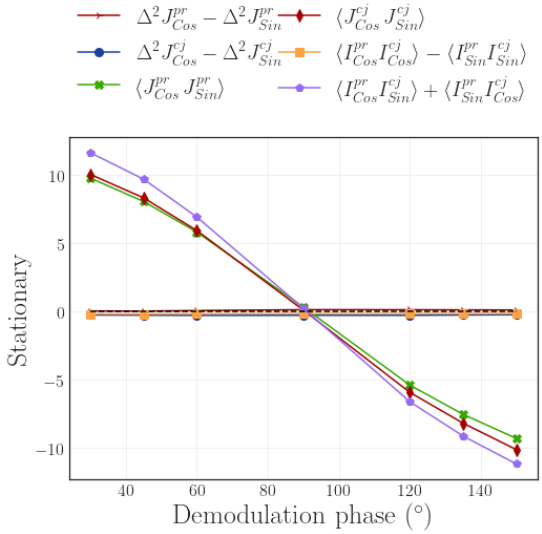

Figure 31. Stationary conditions as a function of the demodulation phase at Ω =10 MHz. The single mode stationary conditions are completely affected by the relative phase between the two demodulation channels.

The stationary conditions are necessary for the adopted approach in the reconstruction of the state. For non-stationary states, the covariance matrix would have a different configuration. However, in Figure 32 we observe the reconstruction of the covariance matrix parameters as we tune the relative phase between demodulation signals. Notice that the single-mode correlations, that is $\alpha_{pr/cj}$, $\beta_{pr/cj}, \gamma_{pr/cj}$ and $\delta_{pr/cj}$, vary at most 10% compared to the parameter at 90°. Conversely, when studying the cross-mode correlations, we find a deviation around 60% in the λ and the τ parameter, which could cause the non-physical covariance matrices.

The calibration presented in Figure 31 is rough and a more detailed characterization must be done around 90° in order to fulfill the stationary conditions. This is why in most

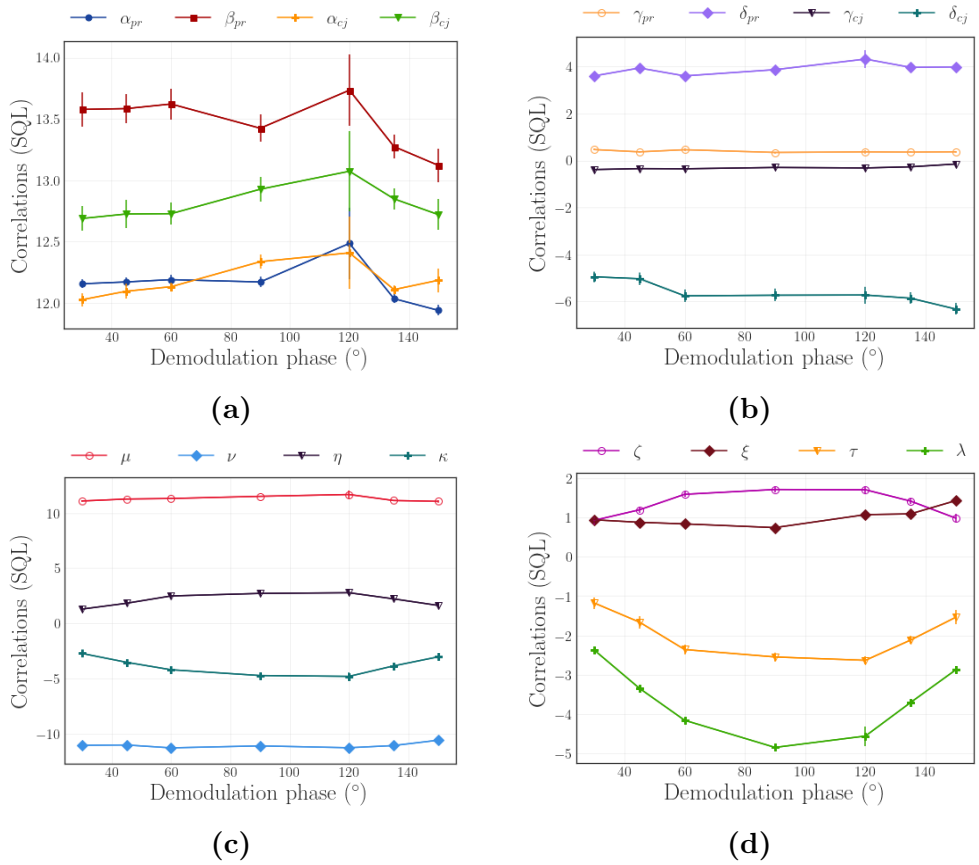

Figure 32. Stationary conditions as a function of the demodulation phase at Ω =10MHz.

of the tomographies that will be shown latter, the relative phase would oscillates around 90 and 92°, according to the analysis frequency Ω.

4.6.5.1 Stationary condition as a function of the analysis frequency

One interesting parameter for the characterization of the system is the analysis frequency Ω. It determines the distance between the carrier and the sidebands. Furthermore, as it will be discussed in the results, it indicates the dependence of the asymmetry of the system with it. However, we found a dependence between the stationary conditions and the analysis frequency Ω.

Figure 33 presents the stationary conditions as a function of the analysis frequency Ω. We measured at Ω = 7, 10, 12, 15 MHz. As explained in the latter subsection, for each analysis frequency we tune the demodulation phase such that we find the lowest value for every stationary condition. Notice that there are three conditions which oscillates around zero for every Ω. In comparison, the there are conditions that increases with Ω. Comparing with Figure 31 we can observe that the stationary conditions presenting the most of the problems are the same in both figures. Up to the day we finished the measurements we were not able to find the source of the problem but its influence in the tomography is critical since the reconstructed states were more difficult to characterize as

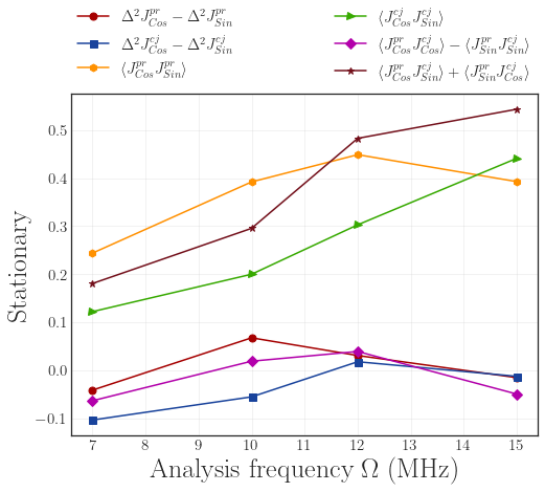

Figure 33. Dependence of the stationary conditions with Ω.

the analysis frequency increases. At the analysis frequency of 15 MHz and above, there were non-physical covariance matrices. This restricted our characterization to 7 and 10 MHz.

4.6.6 Mismatch factor f

In the resonator detection the incoming beam must be coupled into the analysis cavity. Any mismatch turns into some fraction of light that does not experience the effect of the phase transformation from the cavity. In other words, there will be a continuous measuring of the amplitude quadrature of this fraction of the light. The *resonator coupling factor* $1 - f^2$ is a measurement of the quality of the phase and spatial matching of the light beam (probe/conjugated) and the intracavity mode (respect to the analysis cavities). In a perfect scenario, the resonator coupling factor is one ($f = 0$), meaning that the incoming beam enters completely into the cavity. The opposite case is a resonator coupling factor equal to zero ($f = 1$), where the beam is reflected by input mirror of the analysis cavity.

Figure C.3.1 shows the single mode noise spectrum for the probe (in red) and the conjugated (in blue) beams. Notice that the experimental data exhibit a central peak at $\Delta = 0$. If we do not consider the uncoupled light ($f = 0$), neither the theoretical model nor the numerical fit describe this behavior Figure 34a. The best theoretical and numerical description corresponds to a small peak that does not surpass the border values at $\Delta = \pm 6$. Conversely, considering the uncoupled fraction ($f \neq 0$), the numerical fit describes the central peak. The coupling factor happens to be determinant in the tomography of the state regarding the fact that its consideration results into physical covariance matrix whereas neglecting it leads to unphysical states. The depth of the central peak is related to the coupling factor, the better the coupling ($f \to 0$) the smaller the depth. In the specific case of Figure C.3.1, 91.1±0.3% of the probe beam is coupled into the cavity whereas 96.5±0.2% of the conjugated beam is coupled.

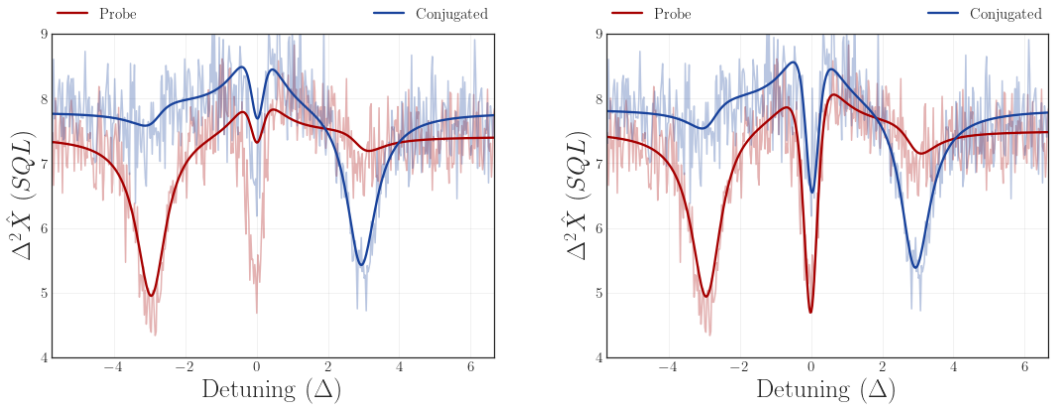

(a) $f = 0$. A small central peak appears. In this description, this effect could not surpass the extreme values of the figure at $\Delta = \pm 6$.

(b) $f \neq 0$. Considering the coupling factor describes the central peak. The probe beam has a coupling of 91.1±0.3% and the conjugated 96.5±0.2%.

Figure 34. The coupling factor takes into account the small fraction of light that does not enter into the cavity. This fraction will go directly to photodetection and will add an extra noise signal to the tomography.

The coupling factor is an important parameter for the reconstruction of the single mode noise spectrum. Typically, in our laboratory we have been working with optical parametric oscillators (OPO) using $\chi^{(2)}$ that generates similar states with an excess of noise up to 3 units of shot noise [69, 70]. More recently, we were able to construct and characterize an OPO using rubidium cell [25], a system that generates beams with 2.5 units of excess of noise. In each of the latter systems, a small fraction of uncoupled light would not generate a deep central peak since the excess of noise carried by the uncoupled light is will not surpass 2 units of noise and and the central peak can not decrease below the shot noise level. On the other hand, our system generates states approximately 10 units above the shot noise level. Therefore, any fraction of light that is not coupled into the analysis cavity already carriers a huge amount of noise that contaminates the tomography.

□ □ □

In this chapter we describe the different controlling mechanisms of the system and the connection between the measurement and the reproduction of the state. We started by a broader view of the setup and then went into the details. In general the system is composed by four branches: the Ti:sapphire laser working as the pump beam and precisely tuned into frequencies of the desired rubidium 85 hyperfine levels. The generation of the seed beam by an AOM that permits the frequency control and the scanning of the FWM Gain profile. The generation of the FWM by the interaction of the pump and the seed with the hot rubidium 85 atoms, and finally, the selective detection of the sidebands of the probe and conjugated beams by the implementation of the resonator detection scheme. At the end of the chapter, we studied the *resonance detection* and the reconstruction of the covariance matrix by the detection of in-phase photocurrents. We show how the measured photocurrent carries the desired information and how the covariance matrix was determined by the noise spectrum. We pointed out the importance of a detailed calibration of the demodulation phase to compensate the phase shift from the electronics and show how important it could be for systems presenting huge excess of noise. Finally, we compared the reconstruction of a state when the mismatch factor is considered.

5

Results and discussion

This chapter present the most important results from this thesis. We focus on the characterization of the quantum correlations as a function of the probe detuning Δ_2. We begin by the characterization of the intensity correlations as a first signal of quantumness. In the second part, we present the characterization of entanglement. A complete characterization is shown in the appendix of this document.

5.1 FWM profile

The FWM profile is obtained by locking the pump frequency Δ_1 using the saturated absorption spectrum as explained in section 4.1. In Figure C.2.1 we show the saturation absorption spectrum with the pump locking frequencies. The solid vertical lines represents the FWM process where the pump detuning is at $\Delta_1 = \text{Crossover} + 1GHz$, named *Lock I*. The black vertical line corresponds to the pump frequency, the red solid vertical line corresponds to the probe frequency and the solid blue vertical line to the conjugated frequency. The second pump frequency is locked at $\Delta_1 = 5^2S_{1/2}, F = 2 \rightarrow 5^2P_{1/2}, F = 3 + 1GHz$, denominated *Lock II*, which is represented by the vertical dashed lines. Given that the *Lock II* is around 180 MHz above the *Lock I* frequency, the generated beams, the probe and the conjugated, will also be shifted the same amount to higher frequencies. During this chapter we will show the results when locking at *Lock I*. Further characterizations are found in the appendix C.2.1.

The gain profile is shown in Figure 36. The experimental profile was obtained by tuning Δ_2 and calculating the gain according to Equation 4.1. The pump frequency is locked at *Lock I* (Crossover $+ 1GHz$ in figure C.2.1), the cell temperature is $103 \pm 0.1°C$. Seed waist $(244.2 \pm 1.9)\mu m$, the pump waist $(525.5 \pm 1.6)\mu m$, and the angle between them is $0.30 \pm 0.03°C$. The FWM profile presents a maximum gain factor of 22 and a linewidth of 50 MHz (Figure 36a). The reproduction of the profile with the theoretical description

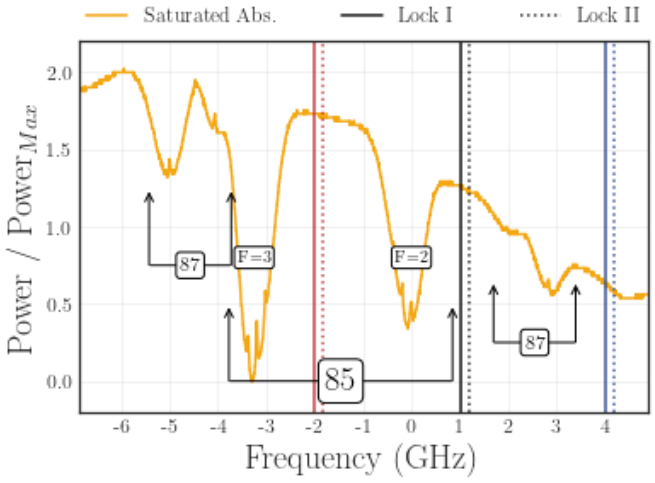

Figure 35. Pump detuning frequency locking. The vertical solid lines corresponds to the FWM process when locket at the *Lock I* frequency (Crossover $+ 1GHz$). The vertical dashed lines corresponds to the FWM process when the pump detuning islocked at $5^2S_{1/2}$, $F = 2 \rightarrow 5^2P_{1/2}$, $F = 3 + 1GHz$ (*Lock II*).

was done qualitatively, meaning the gain factor should be around 20 while the linewidth must be the same (35 MHz), as can be observed in Figure 36b.

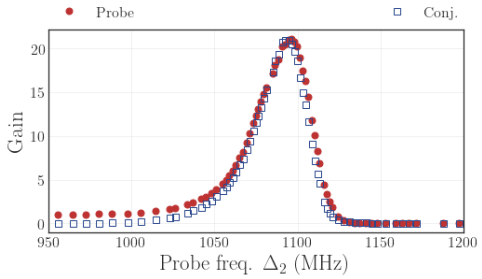

(a) Chosen configuration for tomography.

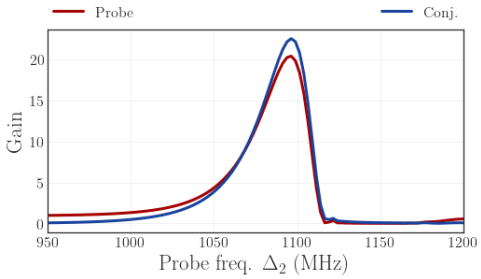

(b) Theoretical model gain profile.

Figure 36. Experimental parameters: Seed waist $= (244.2 \pm 1.9)\mu m$; Pump waist $= (525.5 \pm 1.6)\mu m$; Temp $= (103.0 \pm 0.1)°C$; Angle $= (0.30 \pm 0.03)°C$. The theoretical model have similar gain factor and linewidth.

It is worth to emphasize that the profile is shown as a function of the probe detuning, hence, the emission profile of the conjugated would be inverted since the conservation of energy locks the conjugated frequency to the probe frequency. In this way, as the probe frequency increases, the conjugated frequency must decrease and vice-versa. Consequently, the emission profile of the conjugated should be mirrored if plotted as a function of the conjugated frequency.

5.2 Intensity correlations as a function of the probe detuning Δ_2

In FWM using rubidium atoms, the gain factor is not the ultimate parameter in the generation of quantum correlated states. There are many parameters that affect the generated state. As discussed in section 4.5, the intensity correlations are the first signal of a quantum behavior. If there is no squeezing it should not be expected any entanglement. In this section, we show the experimental characterization of the intensity correlations present in the FWM as a function of the probe detuning Δ_2 which is controlled by controlling the AOM that generates the seed beam, as explained in section 4.2.

The plots have the vertical axes that corresponds to the noise level in dB, and the horizontal axis is the analysis frequency Ω. At $dB = 0$ we have the standard quantum limit (SQL a state with minimum uncertainty), such that above this level the state has excess of noise, and below it the state is squeezed, thus it presents a behavior that is not possible with classical resources. This characterization also have the aim of reproducing results presented in [12, 7, 71].

Figure 37 shows the characterization of the correlations as a function of Δ_2. The seed waist was $(244.2 \pm 1.9)\mu m$, the pump waist $(525.5 \pm 1.6)\mu m$, and the angle between them was $0.30 \pm 0.03°C$. The pump power was 420 mW, the seed power 140 μW, and the temperature was $103°C$. Notice that when the probe detuning is at 1063 MHz, the squeezing bandwidth reaches values around 15 MHz. As Δ_2 grows, the squeezing bandwidth is reduced to values around 8 MHz with a small decrease in the squeezing level. In the appendix we show the behavior of the system in a different configuration (subsection C.2.5 figure C.2.8) were the effect of Δ_2 is more dramatic. Therefore, the probe detuning allows a direct control on the squeezing level and the squeezing bandwidth.

We mentioned before that the FWM profile was reproduced and compared qualitatively. However, it is clear that this is not a reliable criteria for the reproduction of the experimental system. Hence, in subsection C.2.6 you will find the calibration of the theoretical parameters using experimental data. We checked for the reproduction of the intensity correlations as a function of the probe detuning Δ_2, and for the noise level of the probe and the conjugated beams. With this, we guarantee a reliable set of theoretical parameters and could continue to the study of the entanglement.

The characterization of the intensity correlations is useful for defining regions where there is squeezing or not. We notice that at lower probe detuning Δ_2 the gain factor increases slowly compared to the behavior after the maximum of gain, where the change is dramatic and more steep. In the case of the conjugated, the behavior is mirrored.

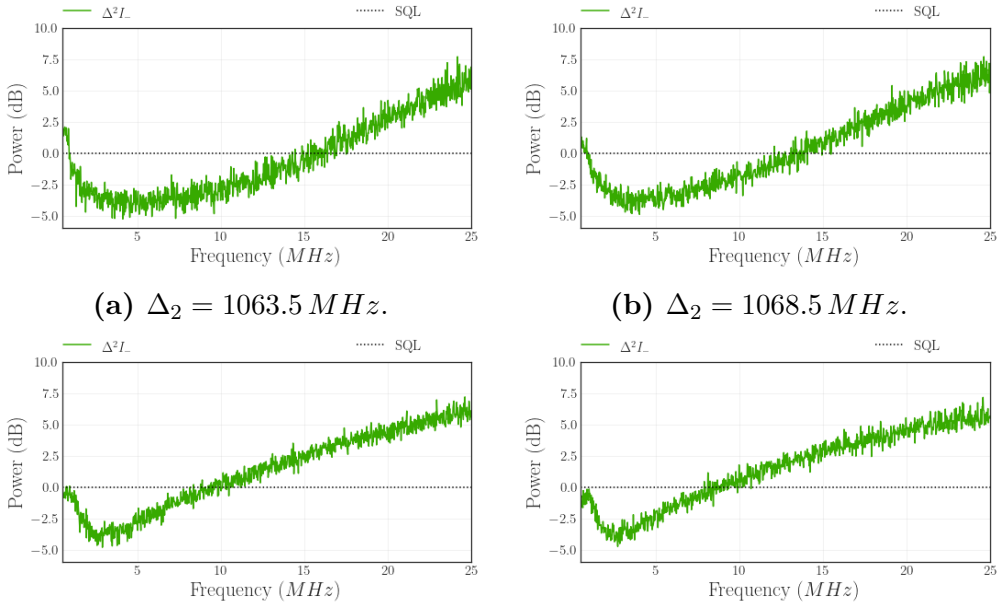

(a) $\Delta_2 = 1063.5\,MHz$. **(b)** $\Delta_2 = 1068.5\,MHz$.

(c) $\Delta_2 = 1072.6\,MHz$. **(d)** $\Delta_2 = 1075.4\,MHz$.

Figure 37. Intensity correlations as a function of the probe detuning Δ_2. Parameters: pump power $= 420.0 \pm 0.3\,mW$; seed power $= 140.1 \pm 0.3\,\mu W$; pump waist $525.5\,\mu m$; seed waist $244.2\,\mu m$; cell temperature: $103 \pm 0.1°C$; angle $= 0.3\,°$. Pump frequency locked at Crossover $+ 1GHz$.

5.3 Covariance matrix reconstruction

The tomography of the state is the determination of every parameter on the covariance matrix (4.28, 4.32), in other words, the complete knowledge of the generated state. In the current thesis we achieve this goal by the implementation of the *resonator detection* (subsection 4.6.2). This section contains the characterization of the covariance matrix as a function of the probe detuning Δ_2. Since the intensity correlations are not a sufficient condition for entanglement, we use the reconstructed state for studying the entanglement of the system by using the entanglement witness described in section 2.5.

5.3.1 Probe detuning Δ_2 at $\Omega = 7$ MHz

The probe detuning Δ_2 controls the squeezing level and the bandwidth (section 5.2) as well as the gain factor (see Figure 36a). In this subsection, we study the covariance matrix parameters as a function of the probe detuning Δ_2. The figures presented in this section were obtained after ten consecutive tomographies and a statistical analysis. This had to be done given the difficulty in the reproduction of physical covariance matrices.

The probe and conjugated beams are amplified differently at a given probe detuning Δ_2 which can be seen by the difference in the output power of the probe and the conjugated Figure 38. The characterization is done in a frequency range from 1052 to 1076 MHz which corresponds to a small frequency region in Figure 36. In principle, we could explore

Table 1. Experimental parameters probe detuning Δ_2 characterization (see Figure 36) at Ω =7MHz.

Pump power (mW)	Seed power (μW)	Temp. ($^{\circ}C$)	Analysis freq. (MHz)
420.0 ± 0.3	140.0±0.3	103.0 ± 0.1	7.0±0.1

the states at greater frequencies Δ_2. However, values above $\Delta_2 = 1080$ MHz increased the difficulty of reproducing physical states. During the whole process, the probe power is 120 μW bigger than the conjugated power due to the incoming seed power.

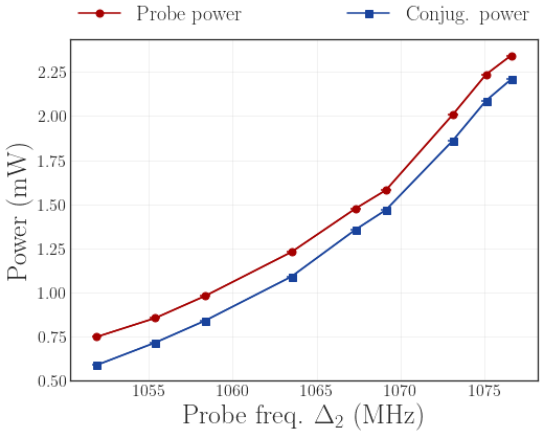

Figure 38. Probe and conjugated power as a function of Δ_2 at Ω =7MHz.

Figure 39 presents the experimental and the theoretical results for the tomography as a function of Δ_2 at an analysis frequency of 7 MHz. Evidently, the values achieved in the experimental analysis are much lower than the theoretical description. Nonetheless, the aim of the theoretical description is a comparison based on a qualitative approach. Notice that the phase noise $\beta_{pr/cj}$ presents more excess of noise than the amplitude noise $\alpha_{pr/cj}$. Even more, β_{cj} is greater than β_{pr} and increases monotonically with the probe detuning Δ_2. In the case of the amplitude noise level, we can observe a *plateau* after 1068 MHz whereas the theoretical description continues its smooth increment in the noise level. This will affect the description of the entanglement as will be shown latter.

The characterization for $\gamma_{pr/cj}$ and $\delta_{pr/cj}$, is shown in Figure 40. The $\gamma_{pr/cj}$ is around zero and increases its value at higher frequencies. The experimental results shows a flip in the sign between γ_{pr} and γ_{cj}, contrary to the theoretical results. Even so, its value remains around zero indicating that there is no rotation of the noise ellipse. In terms of the asymmetry between the sidebands $\delta_{pr/cj}$, a given Δ_2 defines an amplification factor for each sideband which are close at low frequencies and more distinct at higher Δ_2. Hence, it is expected that the asymmetry increases with the probe detuning.

We also compared the cross-correlations terms. In Figure 41 we present some of the parameters. Regarding the behavior of μ, which is related to the amplitude cross-

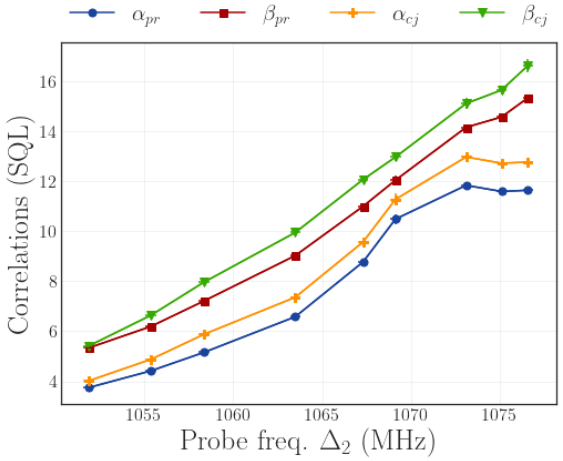

(a) Single mode parameters of the covariance matrix.

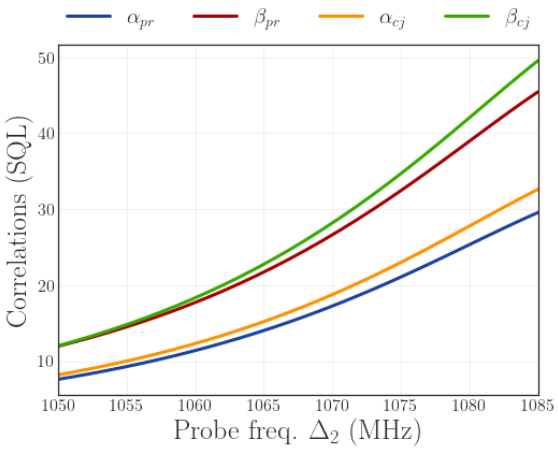

(b) Theoretical description of the single mode parameters of the covariance matrix.

Figure 39. $\alpha_{pr/cj}$, $\beta_{pr/cj}$ as a function of Δ_2 at Ω =7MHz.

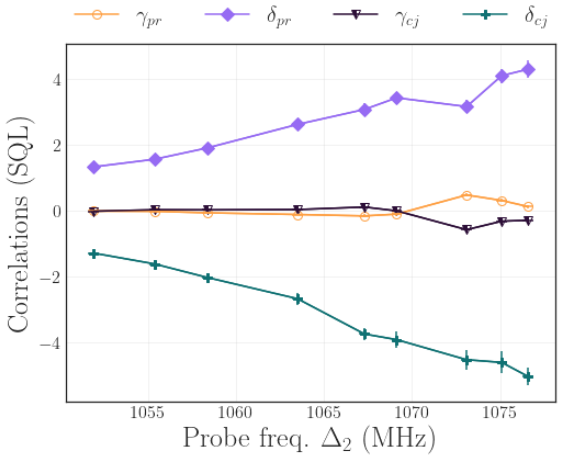

(a) Single mode parameters of the covariance matrix.

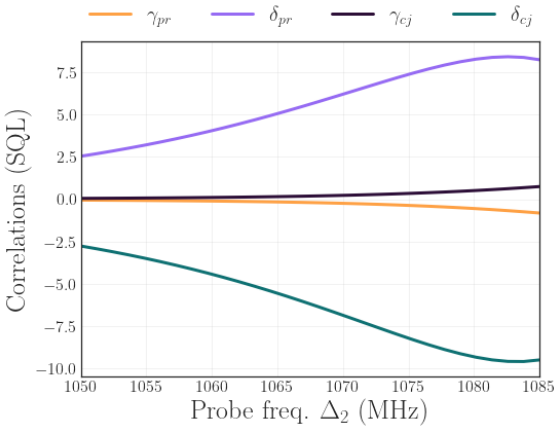

(b) Theoretical single mode parameters covariance matrix.

Figure 40. $\gamma_{pr/cj}$, $\delta_{pr/cj}$ as a function of Δ_2 at Ω =7MHz.

correlations, we observe the *plateau* after 1068 MHz, the same appearing at the single mode correlations $\alpha_{pr/cj}$. The theoretical description does not reproduce the flat region. Similarly, the phase cross-correlation ν follows the behavior of $\beta_{pr/cj}$. Finally, the second set of cross-correlations parameters are shown in Figure 42. In general, the theoretical model describes the behavior of the experimental results. The main differences are found in the amplitude correlations $\alpha_{pr/cj}$ and μ, and in the flipped signal of the values of ζ, ξ, and $\gamma_{pr/cj}$. Later in this chapter we will discuss about the possible reasons for the discrepancy.

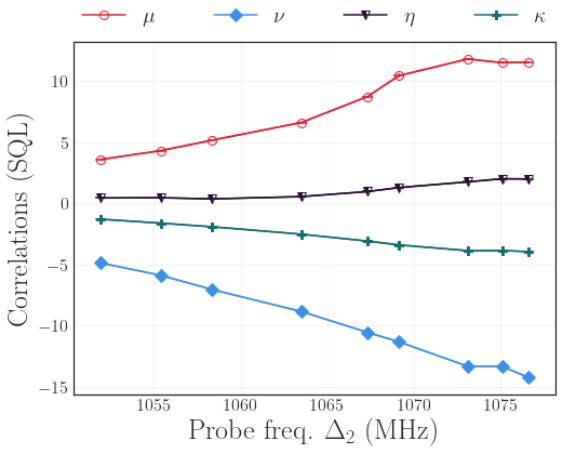

(a) Two mode cross-correlations parameters covariance matrix.

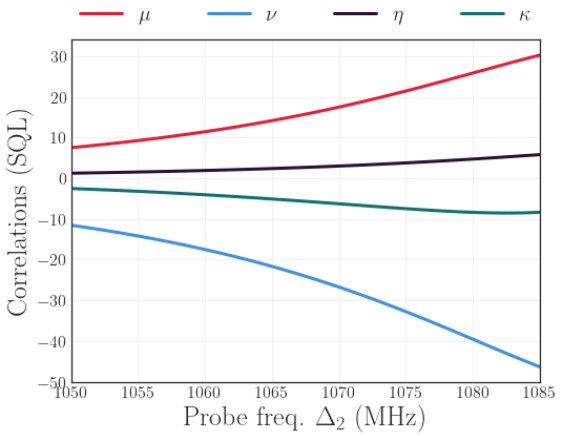

(b) Two mode cross-correlations parameters covariance matrix.

Figure 41. μ, ν, η, κ as a function of Δ_2 at Ω =7MHz.

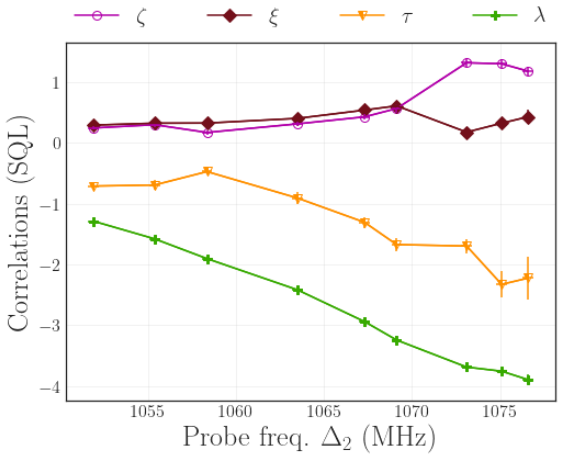

(a) Two mode cross-correlations parameters covariance matrix.

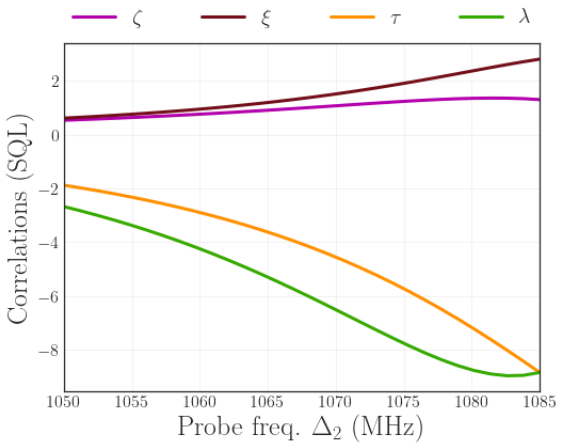

(b) Two mode cross-correlations parameters covariance matrix.

Figure 42. ζ, ξ, τ, λ as a function of Δ_2 at Ω =7MHz.

5.3.2 Probe detuning Δ_2 at $\Omega = 10$ MHz

The analysis of sidebands at higher frequencies is interesting given that the sidebands would have a much different gain factor between them. For instance, at an analysis frequency of Ω =10MHz, seeding at a probe detuning Δ_2 =1075 MHz, the upper sideband would be amplified by a factor of 17 units contrary to the lower sideband amplified by a factor of 7.5 units (Figure 36). The distinct amplification for the upper and lower sidebands would generate asymmetries between the sidebands and the entanglement.

Figure 43 compares the experimental data and the theoretical model of the system. At regions of low gain, the generated beams present low noise level which increases as Δ_2 reaches the high gain factor regions. Similarly to the case of 7MHz shown in Figure 39, the amplitude single mode correlations exhibit a plateau.

Table 2. Experimental parameters probe detuning Δ_2 characterization (see Figure 36) at Ω =10 MHz.

Pump power (mW)	Seed power (μW)	Temp. ($^{\circ}C$)	Analysis freq. (MHz)
420.0 ± 0.3	140.0±0.3	103.0 ± 0.1	10.0±0.1

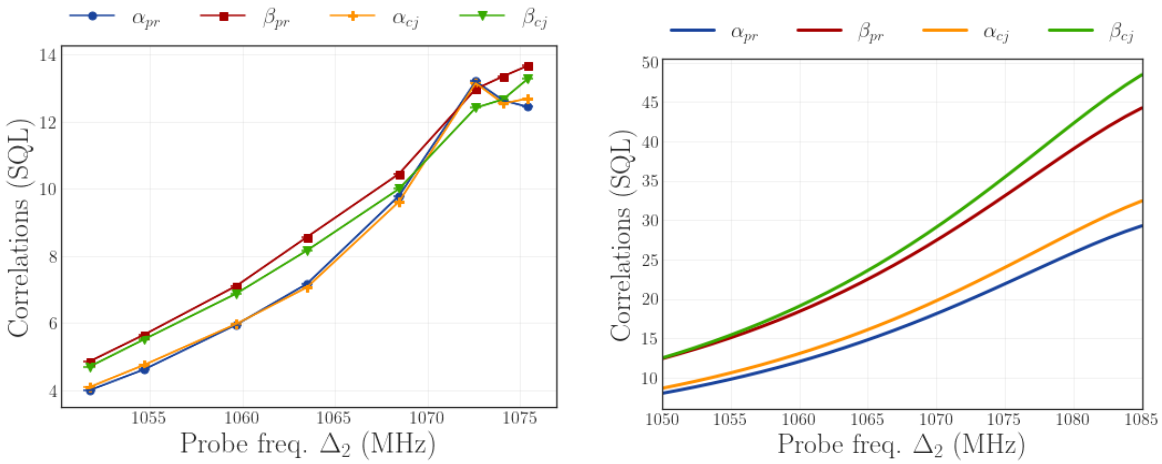

(a) Experimental single mode parameters of the covariance matrix.

(b) Theoretical single mode parameters covariance matrix.

Figure 43. $\alpha_{pr/cj}$ and $\beta_{pr/cj}$ parameters as a function of the probe detuning Δ_2 at Ω =10MHz.

The characterization of the $\gamma_{pr/cj}$ and $\delta_{pr/cj}$ parameters are shown in Figure 44 where we notice that $\gamma_{pr/cj}$ is close to zero at low detuning but it increases its value at high frequencies which could be generated by the factor of 15 in the gain which could induce more non-linear effects. We can also see that the asymmetry between the sidebands increases with Δ_2. Notice that compared to the case of 7MHz (Figure 40), the absolute values of $\delta_{pr/cj}$ at 10MHz are greater either in the experimental and the theoretical results. This is explained by the difference between the gain factor of the sidebands. At 10MHz, the difference between the gain factor of the upper and the lower sideband is greater than at 7MHz, generating the asymmetry to be magnified.

For completeness of the covariance matrix characterization, we present in figure Figure 45 the cross-correlation terms between the two-mode state. We can see that the amplitude cross-correlation μ have the inflection from the monotonic raise and its discrepancy with the theoretical approach even when exploring at higher detuning Δ_2. At this analysis frequency we also find the crossing point at 1068 MHz between the parameters ζ and ξ, which is not described by the theoretical model.

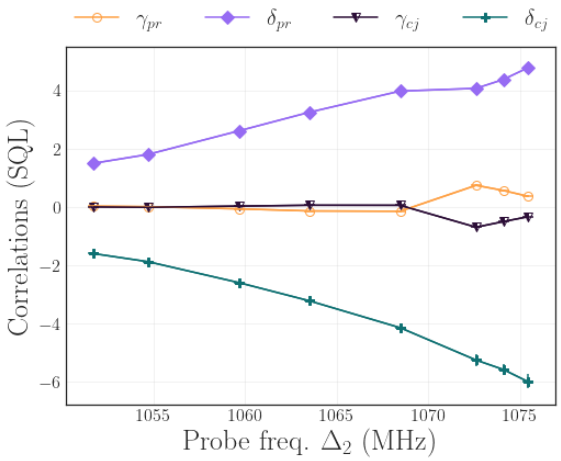

(a) Experimental single mode parameters of the covariance matrix.

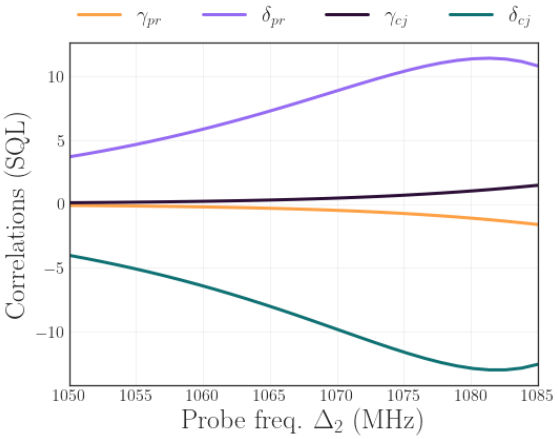

(b) Theoretical single mode parameters covariance matrix.

Figure 44. $\gamma_{pr/cj}$ and $\delta_{pr/cj}$ parameters as a function of the probe detuning Δ_2 at Ω =10MHz.

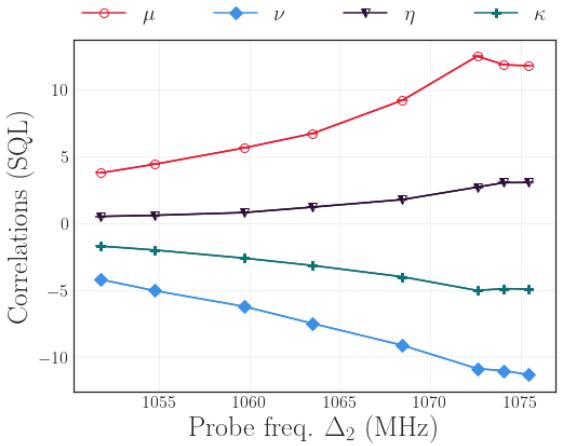

(a) Experimental two mode cross-correlations.

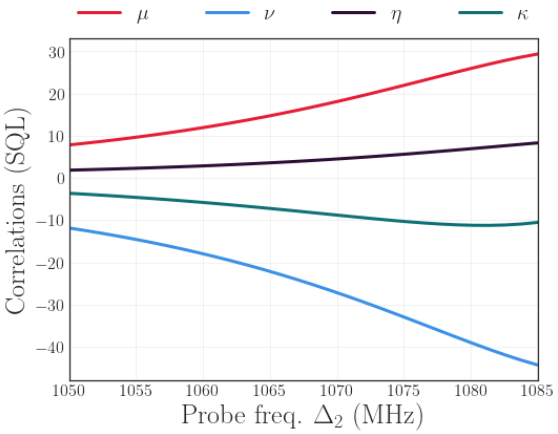

(b) Theoretical two mode cross-correlations.

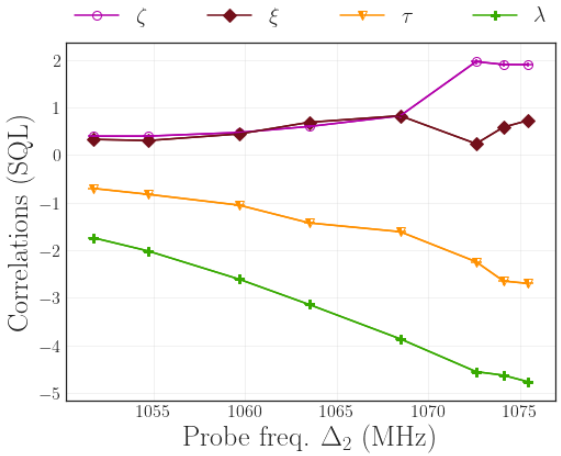

(c) Experimental two mode cross-correlations.

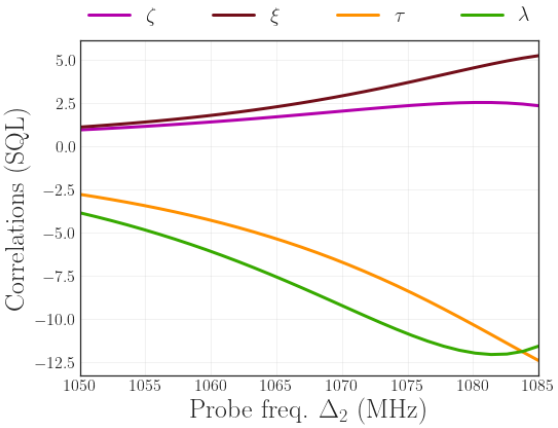

(d) Theoretical two mode cross-correlations.

Figure 45. Cross-correlations as a function of the probe detuning Δ_2 at Ω =10MHz.

5.4 Entanglement witness

In this section we present the results on entanglement. We use the Duan criterion and the PPT criterion as the entanglement witness, evaluate the criterion at two different analysis frequencies either in the symmetric/anti-symmetric basis and in the sideband basis. At the end of the section we compare the Duan criterion with the PPT criterion.

5.4.1 Duan criterion in the Symmetric/anti-symmetric basis

Figures 46 and 47 shows the experimental and theoretical results of the Duan criterion in the symmetric/anti-symmetric basis at an analysis frequency $\Omega = 7$ and 10 MHz, as a function of the probe detuning Δ_2 for the bipartition $[S_{pr}, S_{cj}]$. The violation of the criterion is reduced as Δ_2 grows. Notice that the violation of the criterion reaches larger probe detuning (Δ_2) at $\Omega = 7$ MHz than at $\Omega = 10$ MHz. For instance, in the theoretical description the Duan criterion at $\Omega = 7$ MHz is violated up to the probe detuning $\Delta_2 = 1085$ MHz (Figure 47a). Conversely, at an analysis frequency of $\Omega = 10$ MHz, the violation of the criterion reaches $\Delta_2 = 1070$ MHz (Figure 47b). In the experimental results this could be observed as well, at $\Omega = 7$ MHz the critarion is not violated for probe detuning above $\Delta_2 = 1073$ MHz whereas at an analysis frequency of $\Omega = 10$ MHz it is not violated from frequencies larger than $\Delta_2 = 1070$ MHz.

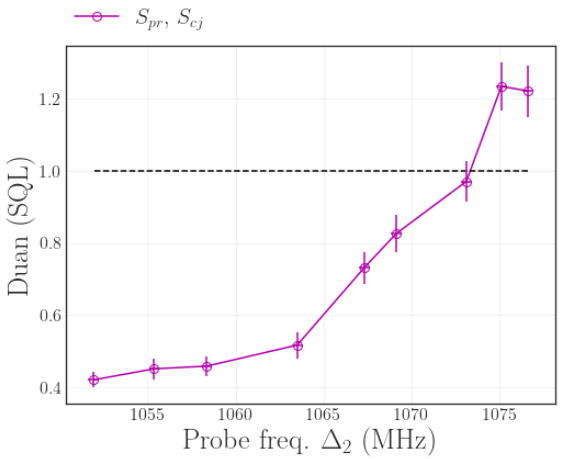

(a) Experimental Duan criterion in the symmetric/anti-symmetric basis at $\Omega = 7$ MHz.

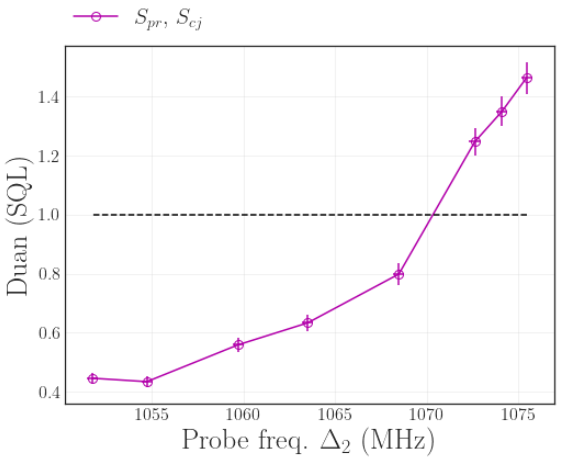

(b) Experimental Duan criterion in the symmetric/anti-symmetric basis at $\Omega = 10$ MHz.

Figure 46. Experimental description of the Duan criterion in the symmetric/anti-symmetric basis.

A closer look to the sidebands allows to understand the described behavior. We have seen that by increasing the value of Δ_2 we attain regions were there are no quantum correlations (see section 5.2). Consider the probe detuning $\Delta_2 = 1075$ MHz and the sidebands around it. When the analysis frequency $\Omega = 7$ MHz, we would be studying sidebands around the carrier, one above $\Delta_2 = 1075$ MHz and the other below. If we

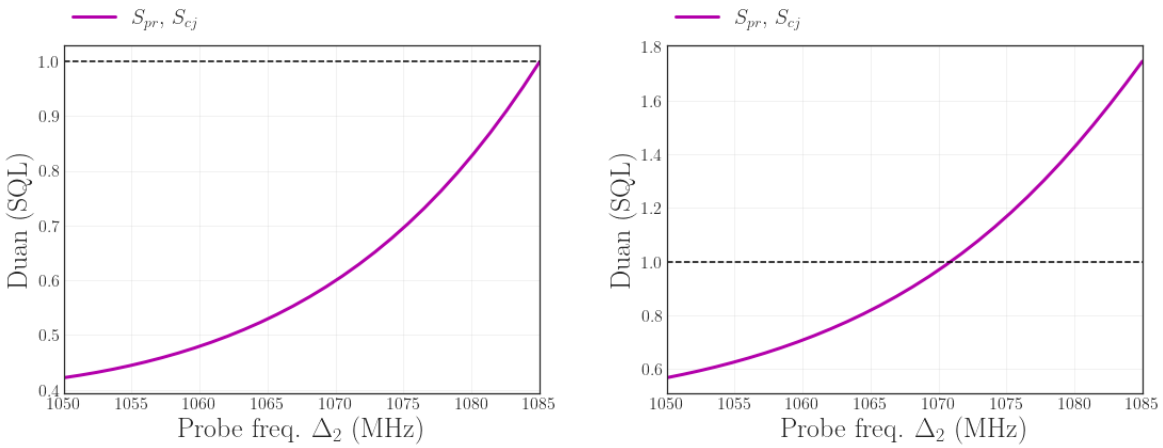

(a) Theoretical Duan criterion in the symmetric/anti-symmetric basis at $\Omega =$ 7 MHz.

(b) Theoretical Duan criterion in the symmetric/anti-symmetric basis at $\Omega =$ 10 MHz.

Figure 47. Theoretical description of the Duan criterion in the symmetric/anti-symmetric basis.

increase the analysis frequency to $\Omega = 10$ MHz, it means that the sideband which is above the carrier frequency would attain the regions where there are no squeezing, destroying the quantum correlations between sidebands.

5.4.2 Duan criterion in the Sideband basis

The Duan criterion can also be studied in the sideband basis. Figure 48 represents the pair of bipartitions studied in this section. In blue we plot the inner bipartition $[\Omega_{pr}, -\Omega_{cj}]$; in green the outer bipartition $[-\Omega_{pr}, \Omega_{cj}]$. The other bipartitions did not violate the criterion.

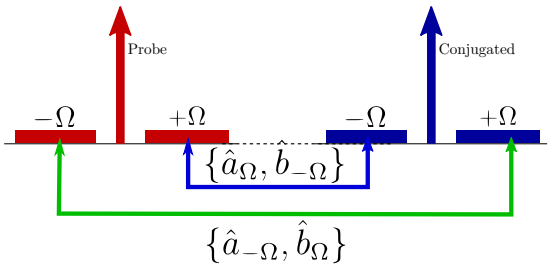

Figure 48. Bipartitions for the Duan criterion in the sideband basis. The blue line represent the inner bipartition $[\Omega_{pr}, -\Omega_{cj}]$. The green line represents the outer bipartition $[-\Omega_{pr}, \Omega_{cj}]$.

Figures 49 and 50 shows the experimental and theoretical characterization of Duan criterion in the sideband basis. Observe that different bipartitions present different levels of violation of the criterion. The inner bipartition in blue, violates the criterion for a lower range of probe detuning Δ_2 compared to the outer bipartition. The theoretical results show the decrease in the violation range of Δ_2 when the analysis frequency changes from

$\Omega = 7$ MHz to $\Omega = 10$ MHz. In the case of the experimental results, some unexpected behavior appears above $\Delta_2 = 1070$ MHz which could be generated by the contamination of the HF signal due to electronic down-conversion or by cross-talk between the orthogonal signals *Cosine* and *Sine* in the demodulation (see subsection 4.6.5).

We can also observe that the bipartition $[\Omega_{pr}, -\Omega_{cj}]$ in blue, lost the violation of the criterion before the green bipartition $[-\Omega_{pr}, \Omega_{cj}]$. For the interpretation of this behavior, consider the FWM profile shown in Figure 36. As the probe detuning grows, the upper sideband of the probe Ω_{pr} will attain the regions where the profile is more steep and there is no squeezing. Simultaneously, the conjugated lower sideband will decrease its frequency going to the region where the profile is steep. On the contrary, the green bipartition $[-\Omega_{pr}, \Omega_{cj}]$ preserve the entanglement given that the sidebands goes in the direction where the FWM profile vary slowly and there is squeezing (see section 5.2).

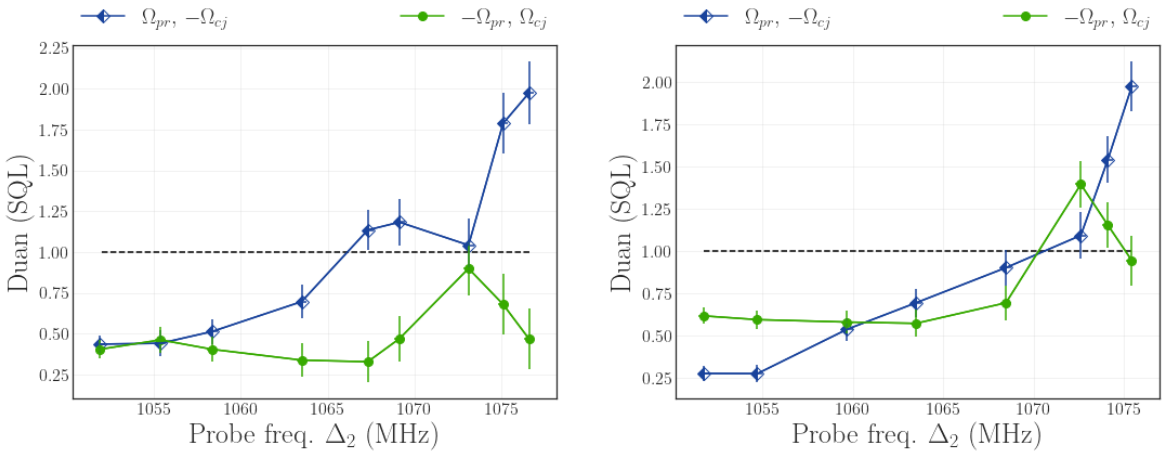

(a) Experimental Duan criterion in the sideband basis at $\Omega = 7$ MHz.

(b) Experimental characterization of the Duan criterion in the sideband basis at $\Omega = 10$ MHz.

Figure 49. Experimental characterization of the Duan criterion in the sideband basis.

Notice that the experimental and the theoretical curves present some important differences. At $\Omega = 7$ MHz, when the probe detuning is above $\Delta_2 = 1070$ MHz, there is a recover of the violation of the criterion. At $\Omega = 10$ MHz, the theoretical results for the blue bipartition follows the experimental behavior with a strong decrease in the violation of the criterion. However, it presents an offset of the overall curve. In the case of the green bipartition, we can describe a slowly decrease of the violation and then a dramatic increase in the criteria value. Further measurements may clarify the origin of this unexpected response of the system.

5.4.3 PPT criterion

The PPT criterion characterization in the SA basis is shown in Figure 51. We observe that the bipartition $[S_{pr}, S_{cj} \times A_{pr}, A_{cj}]$ is not entangled, neither for the analysis

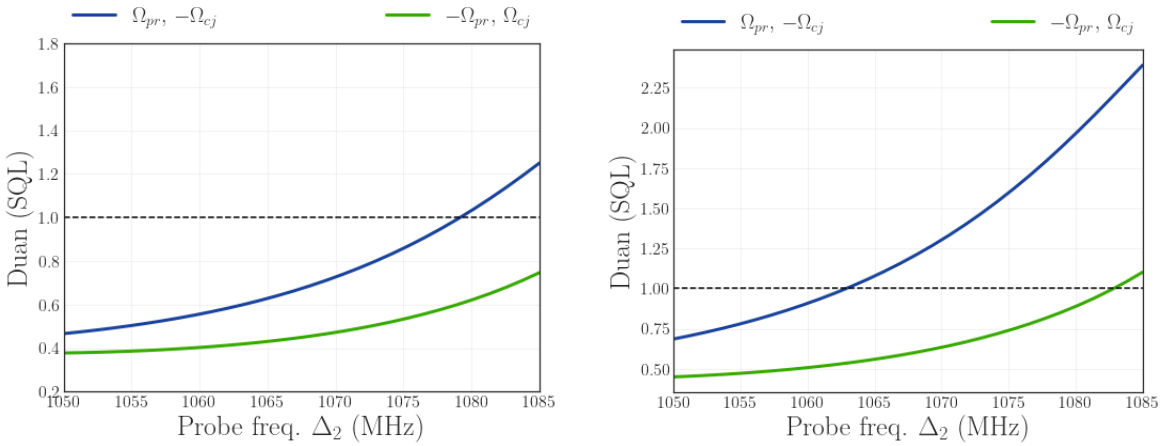

(a) Experimental Duan criterion in the sideband basis at $\Omega = 7$ MHz.

(b) Theoretical Duan criterion in the sideband basis at $\Omega = 10$ MHz.

Figure 50. Theoretical characterization of the Duan criterion in the sideband basis as a function of probe detuning Δ_2.

frequency of $\Omega = 7$ MHz nor $\Omega = 10$ MHz. Every other bipartition are entangled. Comparing the experimental and theoretical results, we can check that the theory follows the experiment.

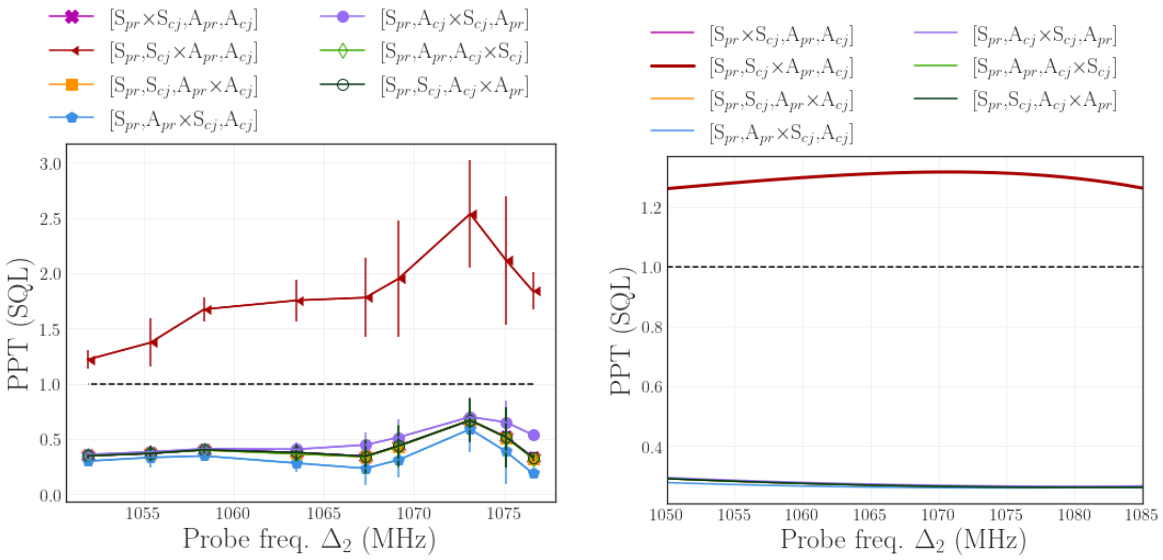

(a) Experimental PPT criterion in the symmetric/anti-symmetric basis at Ω =7MHz.

(b) Theoretical PPT criterion in the sideband basis at Ω =7MHz

Figure 51. Characterization of the PPT criterion n the SA basis, as a function of the probe detuning Δ_2 at $\Omega = 7$ MHz.

The study in the sideband basis, shown in Figure 52, reveals that the bipartition that does not violate the criterion is $[\Omega_{pr}, -\Omega_{cj} \times -\Omega_{pr}, \Omega_{cj}]$. The sidebands that are generated simultaneously and conserve energy and momentum are $\Omega_{pr}, -\Omega_{cj}$ and $-\Omega_{pr}, \Omega_{cj}$. Therefore, it is expected that there were no correlations between these bipartitions.

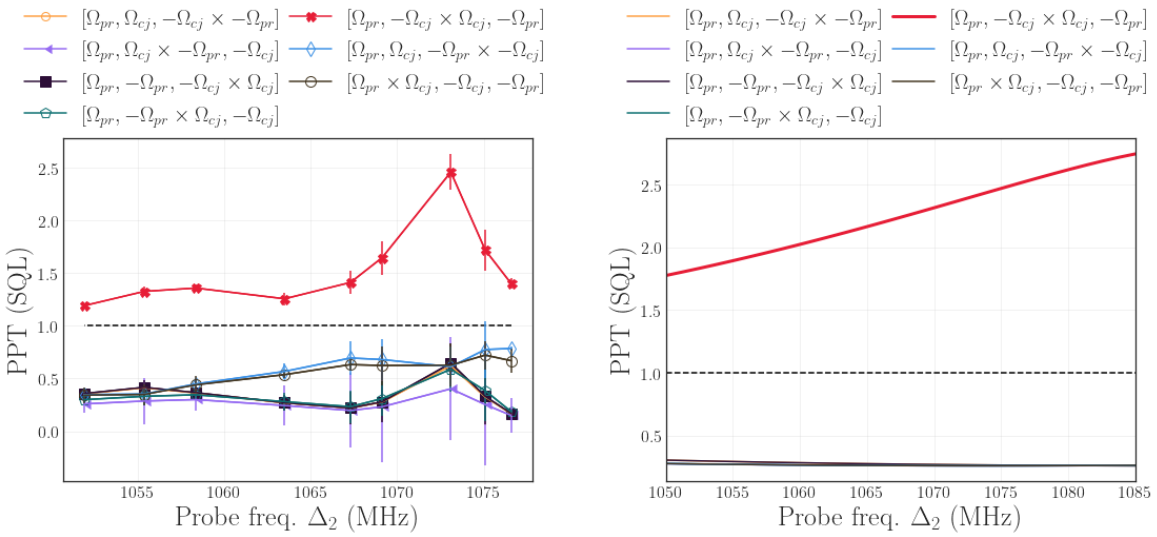

(a) Experimental PPT criterion in the sideband basis at Ω =7MHz.

(b) PPT criterion in the sideband basis at Ω =7MHz.

Figure 52. Characterization of the PPT criterion in the sideband basis, as a function of the probe detuning Δ_2 at $\Omega = 7$ MHz.

The PPT criteria allows to consider a subspace in the covariance matrix such that we can compare directly this criterion with the Duan criterion. Figure 53 presents the results of the characterization of the correlations between the bipartitions $[\Omega_{pr}, -\Omega_{cj}]$ in light blue, and $[-\Omega_{pr}, \Omega_{cj}]$ in light green, using the PPT criterion. Comparing with Figure 49a we notice that the PPT criterion describes a more robust violation of the entanglement which corresponds to the fact that in the PPT criterion, more parameters of the covariance matrix are involved. Moreover, the characterization of the entanglement using the resonator detection reveals a richer structure of the quantum correlations available since it is capable to evidence the asymmetry in the violation of the criterion between the blue bipartition $[\Omega_{pr}, -\Omega_{cj}]$ and the green bipartition $[-\Omega_{pr}, \Omega_{cj}]$.

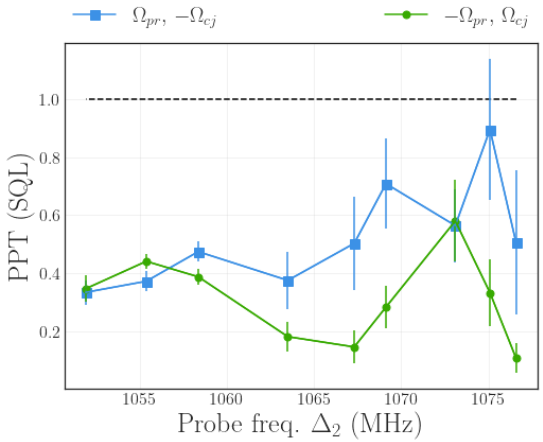

Figure 53. PPT criterion for the sideband subspace as a function of the probe detuning at Ω =7MHz.

5.5 Discussion

During this thesis we were looking for a complete characterization of the entanglement available in a FWM process. This was done by implementing the *resonator detection* were the light is coupled into a resonator and according to a dispersive response and a selective frequency attenuation, we had access to the individual sideband modes of each of the generated beams. All of this experimental work was done in parallel with a theoretical model based on the Heisenberg-Langevin equations which considers the light-matter interaction, and the coupling of the system with the noise reservoir.

We started by the generation and characterization of the FWM spectrum. We determined that the ideal temperature was 103 $°C$, the pump waist 525.5±1.6 μm, the seed waist 244.2±1.9 μm, and the angle between pump and seed 0.29±0.03 °. This generates a FWM spectrum with a maximum gain factor of 22 units and a linewidth of 50 MHz, sufficient for generating intense fields with noise signals above 3 dB from the electronic background noise (Figure 36a).

Thereafter, we study the intensity correlations, or squeezing, trying to find the configuration with the most squeezing level and squeezing bandwidth (section 5.2). We locked the pump frequency at the Crossover $+1GHz$ (*Lock I*), and describe the dependence of squeezing as a function of the probe detuning Δ_2. We observed that the probe detuning allows a precise control on the squeezing properties on the generated beams. At lower probe detuning Δ_2, the squeezing bandwidth is larger but the squeezing level may decrease. As the probe detuning increases, the squeezing level and bandwidth are reduced. At probe detuning Δ_2 around the maximum of the gain factor, the squeezing is completely lost and further frequencies only shows excess of noise in the intensity correlations. Theis characterization also permitted to determine the huge amount of noise on each of the generated beams, reaching values above 10 dB above the standard quantum limit (SQL).

We identify two different regions of the FWM profile. On the one hand, the gain profile at probe detuning below the maximum gain frequency (around $\Delta_2 = 1088$ MHz) that presents a slow monotonical increase and generates quantum correlations. On the other hand, at probe detuning above the maximum gain, the FWM profile is steep and there are no quantum correlations. In terms of the sidebands we can consider that at the region of probe detuning below the maximum gain factor, the sidebands present similar values of amplification. Conversely, at regions of high detuning, each of the sidebands experience a completely different amplification. This behavior is not completely understood and we are still working on the description of it.

The intensity correlations were also useful as a calibration for the theoretical model since we look for the set of theoretical parameters that describes the experimental results (Appendix C.2.6). The developed theoretical approach reproduces correctly the gain

spectrum and the intensity correlations. However, it presents some drawback, namely, it does not take into account the atomic velocity distribution, the mismatch factor, and the angle between seed and pump beams. To begin with, the velocity distribution generated by the temperature of the atoms, would only affect the linewidth of the emission and the computation power for running the model, but not the gain factor neither the noise properties. One visible effect of the velocity distribution is the flat region shown in Figure C.1.1a at frequencies above Δ_2 =1020 MHz, compared to the oscillations appearing in Figure C.1.1b above the same frequency. Nonetheless, our analysis is focused in frequencies below the maximum gain factor such that this effect would not contribute to the measured state nor the noise properties. The second drawback is the mismatch factor. It depends on the impedance matching between the beams and the analysis cavity, and, even when it is not 100% coupled, for every measurement it was constant around 92% for the probe and 98% for the conjugated which is a coupling factor acceptable from our experience in the laboratory. Finally, the consideration of the seed and the pump as colinear beams do not interfere in the theoretical description given that once the phase-matching is satisfied, the equations have the same structure.

Afterwards, we presented the reconstruction of the covariance matrix as a function of the probe detuning Δ_2. This was done for two different analysis frequencies, $\Omega = 7$ MHz and $\Omega = 10$ MHz. Overall, the reconstruction of the covariance matrix shown that as the amplitude and phase noise (α_i and β_i respectively) increases with the growth of the probe detuning. The asymmetry between the energy of the sidebands δ_i increases and the cross-correlation effects, described by the γ_i parameter, appears as the gain factor becomes larger. The theoretical model presents some discrepancies with the experimental results at probe detuning above $\Delta_2 \geq 1070$ MHz which could be generated by a cross-talk between electronic channels or by electronic down-conversion generated by the huge excess of noise of the individual detected beams.

Thereafter, we show the Duan criterion characterization in the symmetric/anti-symmetric basis (SA) and the sideband basis. In the SA basis the experiment and the theory showed that the bipartition $[S_{pr}, S_{cj}]$ presented entanglement (subsection 5.4.1). When the study was made in the sideband basis, we found a richer structure of quantum correlations where two different bipartitions, $[\Omega_{pr}, -\Omega_{cj}]$ in blue, and $[-\Omega_{pr}, \Omega_{cj}]$ in green, presented entanglement (subsection 5.4.2). The behavior of the Duan criteria in the sideband basis can be understood by looking at the conservation of energy in the FWM process. The lower sideband of the probe beam must be generated simultaneously with the upper sideband of the conjugated beam. Likewise the upper sideband of the probe and the lower sideband of the conjugated. Hence, it is expected that these two bipartitions present quantum correlations. In terms of the SA basis, each quadrature is a linear combination of the upper and lower sidebands, and therefore, the ones generated in phase (symmetric) must have quantum correlations.

Even more, we found that the entanglement structure on each bipartition was different and could present higher violation level according to the probe detuning Δ_2. The blue bipartition $[\Omega_{pr}, -\Omega_{cj}]$ had lower violation level and the violation band was smaller than the green bipartition $[-\Omega_{pr}, \Omega_{cj}]$. This could be inferred by the sideband modes in the FWM profile. Consider a given probe detuning Δ_2 and the blue bipartition $[\Omega_{pr}, -\Omega_{cj}]$. The upper sideband from the probe Ω_{pr} will be blue detuned from the carrier frequency, that is, near from the region of no quantum correlations. Hence, if the probe detuning is increased, the upper sideband of the probe will be nearer the region of no quantum correlations. In the case of the lower sideband of the conjugated, as far as its spectrum is mirrored, it will be directed into the region of no quantum correlations. In the case of the green bipartition $[-\Omega_{pr}, \Omega_{cj}]$, the lower sideband of the probe and the upper sideband of the conjugated, are directed into region of squeezing which only disappear when the amplification process is not enough for the generation of correlations. Notice that the experimental and the theoretical curves present some important differences. At $\Omega = 7$ MHz, when the probe detuning is above $\Delta_2 = 1070$ MHz, there is a recover of the violation of the criterion. At $\Omega = 10$ MHz, the theoretical results for the blue bipartition follows the experimental behavior with a strong decrease in the violation of the criterion. However, it presents an offset of the overall curve. In the case of the green bipartition, we can describe a slowly decrease of the violation and then a dramatic increase in the criteria value. Further measurements may clarify the origin of this unexpected response of the system.

We also use the PPT criteria as an entanglement witness of the system (subsection 5.4.3). The characterization was done in the SA basis and the sideband basis. In the SA basis this bipartition was $[\mathrm{S}_{pr},\mathrm{S}_{cj}\times\mathrm{A}_{pr},\mathrm{A}_{cj}]$. Looking at the Duan characterization, we can find an explanation. Given that the the entangled bipartitions was $[S_{pr}, S_{cj}]$ (it can also be shown that a similar behavior is expected for $[A_{pr}, A_{cj}]$ up to a $\pi/2$ phase), the bipartition $[\mathrm{S}_{pr},\mathrm{S}_{cj}\times\mathrm{A}_{pr},\mathrm{A}_{cj}]$ could not be entangled. Similarly, when looking at the PPT criteria in the sideband basis, Ω_{pr} and $-\Omega_{cj}$ are generated simultaneously, and in the same way $-\Omega_{pr}$ and Ω_{cj}. Therefore, there could not be quantum correlations between the bipartition $[\Omega_{pr}, -\Omega_{cj} \times \Omega_{cj}, -\Omega_{pr}]$.

By the study of the PPT criteria in the subspace of the bipartitions $[\Omega_{pr}, -\Omega_{cj}]$ and $[-\Omega_{pr}, \Omega_{cj}]$, we could find a more robust violation rate of the criteria compared to the Duan criterion. At an analysis frequency of $\Omega = 7$MHz, the criteria was violated for any probe detuning Δ_2 whereas at $\Omega = 10$MHz, only at $\Delta_2 > 1072$ MHz the criteria was not violated. Using the PPT criteria in this subspace takes into account more terms from the covariance matrix, therefore, we are considering more correlations between the states.

This is the first measurement of the asymmetry in the quantum correlations between four-modes of sideband, in a FWM process. The measurement using *resonator detection*

over a Four-wave mixing process, reveals a richer structure of entanglement by considering the details of the four modes involved. This work will continue with the generation and characterization of 1D cluster states using rubidium atoms.

III

NEXT STEPS AND CONCLUSION

6

Conclusion

During this thesis we studied and characterized the quantum correlations of the FWM process between four frequency modes, measuring the asymmetry between bipartitions in the *sideband basis*, a property not shown before.

Our approach aimed to describe both theoretically and experimentally, such that we would have a broad picture of the system. The theoretical description embraces the fluctuations in the dynamical equations by using the Heisenberg-Langevin equations, where the pump beam was considered as a classical state, whereas the seed as a quantum state. We described their interaction with the rubidium atoms and included the coupling with vacuum modes and stochastic terms. This approach is an improvement over the naïve description by parametric amplification since most of the experimental parameters are considered and it permits a description of their affection on the system. Every theoretical curve we reproduced was previously calibrated with a set of experimental data. The main result of the theoretical model is that it predicted the spectral profile of the quantum correlation of the bipartite and quadripartite system of independent sidebands.

Simultaneously, we worked in the experimental setup. The current setup is the first implementation of this atomic system in our laboratory, we started from scratch and configured every part of the experiment. The experiment was planned in three main branches. The source laser, the FWM process and the resonator detection. The source laser provided a high power CW beam with a stabilized frequency. It was used as the pump laser and the seed beam. The second stage of the system was the FWM process, where pump and seed interacted with the hot rubidium atoms, and generated the probe and conjugated beams. Finally, the resonator detection allowed an isolated characterization of the upper and the lower sidebands of the individual beams. The beam fluctuation was measured in photodiodes, demodulated in a given analysis frequency, and recorded.

Many different geometrical configurations of the FWM were tested, we reported a

few of them. Most of the problems were related to the colimation of the beams, electronic limitations, excessive noise of light, among others. The final configuration was chosen such that most of the problems were solved. Despite of this, we were able to measure the intensity squeezing, implement the resonator detection, describe the mismatch effect within the analysis cavities, characterize the electronic response of the system, and reconstruct the complete covariance matrix. We found that states presenting excess of noise above 5 SQL require the a delicate adjustment of the experimental parameters. Firstly, we must consider the small fraction of light that is not coupled into the analysis cavity, otherwise the resultant estimated covariance matrix could not describe a *physical* state or could not even be reconstructed. Secondly, a careful adjustment of the demodulation phase is mandatory for obtaining a good agreement of the experimental curves. This is different from the systems that we usually work with in our laboratory that present noise of the order of 2 SQL.

Once the geometrical configuration was settled, we measured the gain profile and determined the gain factor at distinct probe detuning Δ_2. We found a profile with a maximum gain factor of 22 and a linewidth of 35 MHz. At the same time, we theoretically reproduce the profile such that the linewidth and the maximum gain matched the experiment. Afterwards, we explored the first signature of quantum behavior, the intensity squeezing. We realize that at high temperatures, above $110°C$, the squeezing was degradated due to the huge excess of noise of the individual states. The characterization with the power and the frequencies demonstrated the crucial role that the probe has in the control of the squeezing level and the squeezing bandwidth. The experimental characterization ended with the reconstruction of the full covariance matrix for a set of different experimental parameters.

Having both theoretical description and experimental measurements is a great advantage due to the direct comparison between them. We calibrated the parameters in the theoretical description with the FWM gain profile and the intensity squeezing. Afterwards, we reconstructed the full covariance matrix and studied the Duan and the PPT criterion for entanglement witness in the *symmetric/anti-symmetric basis* (SA) and the *sideband basis*. The reconstruction of the full covariance matrix from the experimental data allows the full characterization of the quantum correlations and the entanglement of the system in the *sideband basis*. Therefore, with the first measurement using *resonator detection* over a Four-wave mixing process, we can demonstrate the advantage of the detection to reveal entanglement that would be hidden if the usual two-mode description is used. Moreover, the result points to a richer structure of entanglement if we consider the details for the four modes involved.

This thesis will continue with the generation and characterization of 1D cluster states using rubidium atoms. This is the Phd proposal of my colleague Théo Louzada

Meirelles. The network of entangled states will be generated by using a dual frequency pump that will induce a cascaded process between multiple frequency modes. We are already working in the generation of the dual frequency pump. The results presented during this thesis reveals a non-trivial entanglement structure and will be convenient for understanding the entanglement structure of the cluster state, structures that will allow us to generate and test architectures of entanglement in the spectral domain.

Bibliography

1 FURUSAWA, A. et al. Unconditional quantum teleportation. **science**, American Association for the Advancement of Science, v. 282, n. 5389, p. 706–709, 1998.

2 LUKIN, M. Colloquium: Trapping and manipulating photon states in atomic ensembles. **Reviews of Modern Physics**, APS, v. 75, n. 2, p. 457, 2003.

3 CERF, N. J. et al. **Quantum information with continuous variables of atoms and light**. 57 Shelton Street, Covent Garden-London WC2H 9HE: Imperial College Press, 2007. ISBN 978-1-86094-760-5.

4 COELHO, A. et al. Three-color entanglement. **Science**, American Association for the Advancement of Science, v. 326, n. 5954, p. 823–826, 2009.

5 DUTT, A. et al. On-chip optical squeezing. **Physical Review Applied**, APS, v. 3, n. 4, p. 044005, 2015.

6 ARCINIEGAS, C. A. G. **Propiedades da luz emitida por um oscilador parametrico otico em Chips**. 2017. Tese (Doutorado) — Universidade de São Paulo, 2017.

7 GLORIEUX, Q. et al. **Strong quantum correlations in four wave mixing in 85Rb vapor**. 2010. 772703 p.

8 TAKASE, K. et al. Generation of Schrödinger cat states with Wigner negativity using a continuous-wave low-loss waveguide optical parametric amplifier. **Optics Express**, Optica Publishing Group, v. 30, n. 9, p. 14161–14171, 2022.

9 CHEN, M. et al. Experimental realization of multipartite entanglement of 60 modes of a quantum optical frequency comb. **Physical review letters**, APS, v. 112, n. 12, p. 120505, 2014.

10 LARSEN, M. V. et al. Deterministic generation of a two-dimensional cluster state. **Science**, American Association for the Advancement of Science, v. 366, n. 6463, p. 369–372, 2019.

11 KOUADOU, T. et al. Spectrally shaped and pulse-by-pulse multiplexed multimode squeezed states of light. **arXiv preprint arXiv:2209.10678**, 2022.

12 MCCORMICK, C. et al. Strong relative intensity squeezing by four-wave mixing in rubidium vapor. **Optics letters**, Optical Society of America, v. 32, n. 2, p. 178–180, 2007.

13 GLORIEUX, Q. et al. Double-Λ microscopic model for entangled light generation by four-wave mixing. **Physical Review A**, v. 82, n. 3, p. 033819, 2010.

14 ZHANG, K. et al. Reconfigurable hexapartite entanglement by spatially multiplexed four-wave mixing processes. **Physical Review Letters**, APS, v. 124, n. 9, p. 090501, 2020.

15 SLUSHER, R. et al. Observation of squeezed states generated by four-wave mixing in an optical cavity. **Physical Review Letters**, APS, v. 55, n. 22, p. 2409, 1985.

16 MA, R. et al. Generating quantum correlated twin beams by four-wave mixing in hot cesium vapor. **Physical Review A**, APS, v. 96, n. 4, p. 043843, 2017.

17 SWAIM, J. D.; GLASSER, R. T. Squeezed-twin-beam generation in strongly absorbing media. **Physical Review A**, APS, v. 96, n. 3, p. 033818, 2017.

18 GLORIEUX, Q. et al. Quantum correlations by four-wave mixing in an atomic vapor in a nonamplifying regime: Quantum beam splitter for photons. **Physical Review A**, APS, v. 84, n. 5, p. 053826, 2011.

19 POOSER, R. C. et al. Quantum correlated light beams from non-degenerate four-wave mixing in an atomic vapor: the $D1$ and $D2$ lines of $85Rb$ and $87Rb$. **Opt. Express**, Optica Publishing Group, v. 17, n. 19, p. 16722–16730, Sep 2009.

20 BACHOR, H.-A.; RALPH, T. C. **A guide to experiments in quantum optics**. 3rd. ed. 12, 69469 Weinheim, Germany: Wiley Online Library, 2013. 556 p. ISBN 978-3-527-41193-1.

21 BOYER, V. et al. Entangled images from four-wave mixing. **Science**, American Association for the Advancement of Science, v. 321, n. 5888, p. 544–547, 2008.

22 PAN, X. et al. Orbital-angular-momentum multiplexed continuous-variable entanglement from four-wave mixing in hot atomic vapor. **Physical Review Letters**, APS, v. 123, n. 7, p. 070506, 2019.

23 BARBOSA, F. et al. Hexapartite entanglement in an above-threshold optical parametric oscillator. **Physical review letters**, APS, v. 121, n. 7, p. 073601, 2018.

24 KÖGLER, R. A. **Covariance matrix reconstruction of nonclassical light generated in an on-chip optical parametric oscillator**. 2022. Tese (Doutorado) — Universidade de São Paulo, 2022.

25 GUERRERO, A. M. et al. Continuous Variable Entanglement in an Optical Parametric Oscillator Based on a Nondegenerate Four Wave Mixing Process in Hot Alkali Atoms. **Physical Review Letters**, APS, v. 129, n. 16, p. 163601, 2022.

26 TURNBULL, M. et al. Role of the phase-matching condition in nondegenerate four-wave mixing in hot vapors for the generation of squeezed states of light. **Physical Review A**, APS, v. 88, n. 3, p. 033845, 2013.

27 CORZO, N. V. et al. Rotation of the noise ellipse for squeezed vacuum light generated via four-wave mixing. **Physical Review A**, APS, v. 88, n. 4, p. 043836, 2013.

28 LI, C. et al. Simple security proofs for continuous variable quantum key distribution with intensity fluctuating sources. **npj Quantum Information**, Nature Publishing Group, v. 7, n. 1, p. 1–8, 2021.

29 ANDERSEN, U. L. et al. Continuous-variable quantum information processing. **Laser & Photonics Reviews**, Wiley Online Library, v. 4, n. 3, p. 337–354, 2010.

30 VILLAR, A. S. The conversion of phase to amplitude fluctuations of a light beam by an optical cavity. **American Journal of Physics**, American Association of Physics Teachers, v. 76, n. 10, p. 922–929, 2008.

31 DUBOST, B. et al. Efficient quantification of non-Gaussian spin distributions. **Physical Review Letters**, APS, v. 108, n. 18, p. 183602, 2012.

32 OLSEN, M.; CORNEY, J. Non-Gaussian continuous-variable entanglement and steering. **Physical Review A**, APS, v. 87, n. 3, p. 033839, 2013.

33 POOSER, R.C. **Nonlinear cascades and concurrences for multipartite-entanglement and Non-Gaussian States of Light**. jan 2007. Tese (Doutorado) — University of Virginia, jan 2007.

34 ADESSO, G. et al. Continuous variable quantum information: Gaussian states and beyond. **Open Systems & Information Dynamics**, World Scientific, v. 21, n. 01n02, p. 1440001, 2014.

35 GRYNBERG, G. et al. **Introduction to quantum optics: from the semi-classical approach to quantized light**. The Edinburgh Building, Cambridge CB2 8RU, UK: Cambridge university press, 2010. ISBN 9780511778261.

36 SCULLY, M. O.; ZUBAIRY, M. S. **Quantum optics**. 1. ed. The Edinburgh Building, Cambridge CB2 2RU, UK: Cambridge University Press, 1999. ISBN 9780511813993.

37 WU, L.-A. et al. Generation of squeezed states by parametric down conversion. **Physical review letters**, APS, v. 57, n. 20, p. 2520, 1986.

38 WU, L.-A. et al. Squeezed states of light from an optical parametric oscillator. **JOSA B**, Optical Society of America, v. 4, n. 10, p. 1465–1475, 1987.

39 ANDERSEN, U. L. et al. 30 years of squeezed light generation. **Physica Scripta**, IOP Publishing, v. 91, n. 5, p. 053001, 2016.

40 MANDEL, L.; WOLF, E. **Optical Coherence and Quantum Optics**. University of Rochester, Rochester, N. Y., USA: Cambridge University Press, 1995. ISBN 9780521417112.

41 BARNETT, S.; RADMORE, P. M. **Methods in theoretical quantum optics**. Great Clarendon Street, Oxford OX2 6DP: Oxford University Press, 2002. v. 15. ISBN 9780191714245.

42 EINSTEIN, A. et al. Can quantum-mechanical description of physical reality be considered complete? **Physical review**, APS, v. 47, n. 10, p. 777, 1935.

43 MENICUCCI, N. C. Fault-tolerant measurement-based quantum computing with continuous-variable cluster states. **Physical review letters**, APS, v. 112, n. 12, p. 120504, 2014.

44 GLAUBER, R. J. The quantum theory of optical coherence. **Physical Review**, APS, v. 130, n. 6, p. 2529, 1963.

45 BARBOSA, F. A. et al. Quantum state reconstruction of spectral field modes: Homodyne and resonator detection schemes. **Physical Review A**, APS, v. 88, n. 5, p. 052113, 2013.

46 WERNER, R. F.; WOLF, M. M. Bound entangled Gaussian states. **Physical review letters**, APS, v. 86, n. 16, p. 3658, 2001.

47 DUAN, L.-M. et al. Inseparability criterion for continuous variable systems. **Physical Review Letters**, APS, v. 84, n. 12, p. 2722, 2000.

48 PERES, A. Separability criterion for density matrices. **Physical Review Letters**, APS, v. 77, n. 8, p. 1413, 1996.

49 SIMON, R. Peres-Horodecki separability criterion for continuous variable systems. **Physical Review Letters**, APS, v. 84, n. 12, p. 2726, 2000.

50 GLORIEUX, Q. et al. Hot atomic vapors for nonlinear and quantum optics. **arXiv preprint arXiv:2209.04622**, 2022.

51 SILVA, N. A. et al. Effective nonlinear parameter measurement using FWM in optical fibers in a low power regime. **IEEE Journal of Quantum Electronics**, IEEE, v. 46, n. 3, p. 285–291, 2009.

52 STECK, D. Rubidium 85 D Line Data. 2013.

53 GLORIEUX, Q. **Etude theorique et experimentale des correlations quantiques obtenues par melange a quatre ondes dans une vapeur atomique**. 2010. Tese (Doutorado) — Université Paris Diderot, 2010.

54 BOYD, R. W. **Nonlinear optics**. 525 B Street, Suite 1900, San Diego, CA 92101-4495, USA: Academic press, 2008. ISBN 9780123694706.

55 YAMAN, F. et al. CHAPTER 7 - Fiber Optic Parametric Amplifiers for Lightwave Systems. In: PAL, B. P. (Ed.). **Guided Wave Optical Components and Devices**. Burlington: Academic Press, 2006. p. 101–117.

56 TRÄGER, F. **Springer handbook of lasers and optics**. 2. ed. New York: Springer Nature, 2012. ISBN 978-3-642-19409-2.

57 COHEN-TANNOUDJI, C. et al. **Atom-photon interactions: basic processes and applications**. 12, 69469 Weinheim, Germany: Wiley Online Library, 1998. ISBN 978-0-471-29336-1.

58 FLEISCHHAUER, M.; RICHTER, T. Pulse matching and correlation of phase fluctuations in Λ systems. **Physical Review A**, APS, v. 51, n. 3, p. 2430, 1995.

59 DAVIDOVICH, L. Sub-Poissonian processes in quantum optics. **Reviews of Modern Physics**, APS, v. 68, n. 1, p. 127, 1996.

60 DAVIDOVICH, L. **Teoría Quântica do Laser**. UFRJ: Universidade Federal do Rio de Janeiro, 2015. v. 1.

61 JASPERSE, M. et al. Relative intensity squeezing by four-wave mixing with loss: an analytic model and experimental diagnostic. **Optics express**, Optica Publishing Group, v. 19, n. 4, p. 3765–3774, 2011.

62 MORAES, F. C. D. d. **Construção e caracterização de um laser contínuo de titânio-safira**. 2013. Master thesis – Universidade de São Paulo.

63 MONTANA, A. **Oscilador Paramétrico Ótico baseado em mistura de quatro ondas em vapor de rubídio**. 2017. Master thesis – Universidade de São Paulo.

64 LITTMAN, M. G. Single-mode operation of grazing-incidence pulsed dye laser. **Optics Letters**, Optical Society of America, v. 3, n. 4, p. 138–140, 1978.

65 FOOT, C. J. et al. **Atomic physics**. Great Clarendon Street, Oxford OX2 6DP: Oxford University Press, 2005. v. 7. ISBN 978-0-471-29336-1.

66 BARBOSA, F. A. et al. Beyond spectral homodyne detection: complete quantum measurement of spectral modes of light. **Physical review letters**, APS, v. 111, n. 20, p. 200402, 2013.

67 ANDRADE, R. B. d. **An optical parametric oscillator for a light-atomic media interface**. 2018. Tese (Doutorado) — Universidade de São Paulo, 2018.

68 BARBOSA, F. et al. Assumption-free measurement of the quantum state of light: Exploring the sidebands of intense fields. **Physical Review A**, APS, v. 102, n. 6, p. 063705, 2020.

69 CASSEMIRO, K. N. **Correlações quânticas multicolores no oscilador paramétrico ótico**. 2008. Tese (Doutorado) — Universidade de São Paulo, 2008.

70 COELHO, A. S. O. **Emaranhamento multicor para redes de informação quântica**. 2013. Tese (Doutorado) — Universidade de São Paulo, 2013.

71 QIN, Z. et al. Compact diode-laser-pumped quantum light source based on four-wave mixing in hot rubidium vapor. **Optics letters**, Optical Society of America, v. 37, n. 15, p. 3141–3143, 2012.

72 SAUTENKOV, V. et al. Self-focusing of cw laser beam with variable radius in rubidium atomic vapor. **Optics Communications**, Elsevier, v. 431, p. 131–135, 2019.

73 CERULLO, G. et al. Optical Parametric Amplifiers. In: GUENTHER, B. D.; STEEL, D. G. (Ed.). **Encyclopedia of Modern Optics (Second Edition)**. Second edition. Oxford: Elsevier, 2018. p. 290–301. ISBN 978-0-12-814982-9.

IV

APPENDIX

A

Separatility criteria

A.1 Duan criterion

While the Duan criterion is enough for characterizing the entanglement for quantum teleportation [1], it ignores a certain amount of correlations since it only depends on few elements of the covariance matrix. Consider the pair of quadratures defining a state in the *symmetric/anti-symmetric basis* (SA) as $S_j = \{\hat{p}_s^{(j)}, \hat{q}_s^{(j)}\}$ ($A_j = \{\hat{p}_a^{(j)}, \hat{q}_a^{(j)}\}$). The bipartitions can be organized in different sets as shown in Figure A.1.1.

Figure A.1.1. Bipartitions Duan criterion in the *symmetric/anti-symmetric basis*. Duan (i): $[S_{pr} \times S_{cj}]$. Duan (ii): $[A_{pr} \times A_{cj}]$. Duan (iii): $[S_{pr} \times A_{cj}]$. Duan (iv): $[A_{pr} \times S_{cj}]$.

Therefore, we can calculate the Duan criterion in terms of the covariance matrix $\mathbb{V}_{s,a}$, yielding [I],

$$\text{Duan SA (i)} : [S_{pr} \times S_{cj}] \tag{A.1}$$
$$\Delta^2\hat{p}_s^{(pr)} + \Delta^2\hat{p}_s^{(cj)} - 2C(\hat{p}_s^{(pr)}, \hat{p}_s^{(cj)}) + \Delta^2\hat{q}_s^{(pr)} + \Delta^2\hat{q}_s^{(cj)} + 2C(\hat{q}_s^{(pr)}, \hat{q}_s^{(cj)}) \geq 4$$
$$\alpha_{pr} + \alpha_{cj} - 2\mu + \beta_{pr} + \beta_{cj} + 2\nu \geq 4$$

[I] There is a factor of 4 in the Duan criterion which comes from the definition of quadratures. Nevertheless, is a normalization factor that does not change the interpretation of the results.

Duan SA (ii) : $[A_{pr} \times A_{cj}]$ (A.2)

$$\begin{aligned}\Delta^2\hat{p}_a^{(pr)} + \Delta^2\hat{p}_a^{(cj)} - 2C(\hat{p}_a^{(pr)}, \hat{p}_a^{(cj)}) + \Delta^2\hat{q}_a^{(pr)} + \Delta^2\hat{q}_a^{(cj)} + 2C(\hat{q}_a^{(pr)}, \hat{q}_a^{(cj)}) &\geq 4 \\ \beta_{pr} + \beta_{cj} - 2\nu + \alpha_{pr} + \alpha_{cj} + 2\mu &\geq 4\end{aligned}$$

Duan SA (iii) : $[S_{pr} \times A_{cj}]$ (A.3)

$$\begin{aligned}\Delta^2\hat{p}_s^{(pr)} + \Delta^2\hat{p}_a^{(cj)} - 2C(\hat{p}_s^{(pr)}, \hat{p}_a^{(cj)}) + \Delta^2\hat{q}_s^{(pr)} + \Delta^2\hat{q}_a^{(cj)} + 2C(\hat{q}_s^{(pr)}, \hat{q}_a^{(cj)}) &\geq 4 \\ \alpha_{pr} + \beta_{cj} - 2\kappa + \beta_{pr} + \alpha_{cj} - 2\lambda &\geq 4\end{aligned}$$

Duan SA (iv) : $[A_{pr} \times S_{cj}]$ (A.4)

$$\begin{aligned}\Delta^2\hat{p}_a^{(pr)} + \Delta^2\hat{p}_s^{(cj)} - 2C(\hat{p}_a^{(pr)}, \hat{p}_s^{(cj)}) + \Delta^2\hat{q}_a^{(pr)} + \Delta^2\hat{q}_s^{(cj)} + 2C(\hat{q}_a^{(pr)}, \hat{q}_s^{(cj)}) &\geq 4 \\ \beta_{pr} + \alpha_{cj} + 2\lambda + \alpha_{pr} + \beta_{cj} + 2\kappa &\geq 4\end{aligned}$$

Even when distinct bipartitions could be considered, this corresponds to the ones that are typically presented in the literature [27]. In contrast, in the *sideband basis* the pair of quadratures describing the states are $\Omega_j = \{\hat{p}_\Omega^{(j)}, \hat{q}_\Omega^{(j)}\}$, and $-\Omega_j = \{\hat{p}_{-\Omega}^{(j)}, \hat{q}_{-\Omega}^{(j)}\}$. The Duan criterion for the chosen bipartitions shown in Figure A.1.2, can be written in terms $\mathbb{V}_{\pm\Omega}$ matrix and is given by:

Figure A.1.2. Bipartitions Duan criterion in the *sideband basis*. Duan (i): $[\Omega_{pr} \times \Omega_{cj}]$. Duan (ii): $[-\Omega_{pr} \times -\Omega_{cj}]$. Duan (iii): $[\Omega_{pr} \times -\Omega_{cj}]$. Duan (iv): $[-\Omega_{pr} \times \Omega_{cj}]$.

Duan sideband (i) : $[\Omega_{pr} \times \Omega_{cj}]$ (A.5)

$$\begin{aligned}\Delta^2\hat{p}_\Omega^{(pr)} + \Delta^2\hat{p}_\Omega^{(cj)} - 2C(\hat{p}_\Omega^{(pr)}, \hat{p}_\Omega^{(cj)}) + \Delta^2\hat{q}_\Omega^{(pr)} + \Delta^2\hat{q}_\Omega^{(cj)} + 2C(\hat{q}_\Omega^{(pr)}, \hat{q}_\Omega^{(cj)}) &\geq 4 \\ \alpha_{pr} + \beta_{pr} + 2\delta_{pr} + \alpha_{cj} + \beta_{cj} + 2\delta_{cj} &\geq 4.\end{aligned}$$

Duan sideband (ii) : $[-\Omega_{pr} \times -\Omega_{cj}]$ (A.6)

$$\begin{aligned} \Delta^2\hat{p}_{-\Omega}^{(pr)} + \Delta^2\hat{p}_{-\Omega}^{(cj)} - 2C(\hat{p}_{-\Omega}^{(pr)}, \hat{p}_{-\Omega}^{(cj)}) + \Delta^2\hat{q}_{-\Omega}^{(pr)} + \Delta^2\hat{q}_{-\Omega}^{(cj)} + 2C(\hat{q}_{-\Omega}^{(pr)}, \hat{q}_{-\Omega}^{(cj)}) &\geq 4 \\ \alpha_{pr} + \beta_{pr} - 2\delta_{pr} + \alpha_{cj} + \beta_{cj} - 2\delta_{cj} &\geq 4. \end{aligned}$$

Duan sideband (iii) : $[\Omega_{pr} \times -\Omega_{cj}]$ (A.7)

$$\begin{aligned} \Delta^2\hat{p}_{\Omega}^{(pr)} + \Delta^2\hat{p}_{-\Omega}^{(cj)} - 2C(\hat{p}_{\Omega}^{(pr)}, \hat{p}_{-\Omega}^{(cj)}) + \Delta^2\hat{q}_{\Omega}^{(pr)} + \Delta^2\hat{q}_{-\Omega}^{(cj)} + 2C(\hat{q}_{\Omega}^{(pr)}, \hat{q}_{-\Omega}^{(cj)}) &\geq 4 \\ \alpha_{pr} + \beta_{pr} + 2\delta_{pr} + \alpha_{cj} + \beta_{cj} - 2\delta_{cj} + 2(-\mu + \kappa + \lambda + \nu) &\geq 4 \end{aligned}$$

Duan sideband (iv) : $[-\Omega_{pr} \times \Omega_{cj}]$ (A.8)

$$\begin{aligned} \Delta^2\hat{p}_{-\Omega}^{(pr)} + \Delta^2\hat{p}_{\Omega}^{(cj)} - 2C(\hat{p}_{-\Omega}^{(pr)}, \hat{p}_{\Omega}^{(cj)}) + \Delta^2\hat{q}_{-\Omega}^{(pr)} + \Delta^2\hat{q}_{\Omega}^{(cj)} + 2C(\hat{q}_{-\Omega}^{(pr)}, \hat{q}_{\Omega}^{(cj)}) &\geq 4 \\ \alpha_{pr} + \beta_{pr} - 2\delta_{pr} + \alpha_{cj} + \beta_{cj} + 2\delta_{cj} + 2(-\mu - \kappa - \lambda + \nu) &\geq 4 \end{aligned}$$

B

Microscopic description of the FWM - Complement

B.1 Perturbative approach

During the microscopical description in section 3.3, we write a dynamical equation for the atomic operator $\tilde{\sigma}$ of the form

$$\frac{d\tilde{\sigma}(z,t)}{dt} = \tilde{\mathbf{M}}\,\tilde{\sigma}(z,t) + \tilde{\mathbf{G}}\tilde{\mathbf{A}}(z,t) + \tilde{\mathbf{F}}(z,t), \tag{B.1}$$

where $\tilde{\mathbf{M}}$ only depends on the relative frequencies between fields and atomic levels Δ_i, Rabi frequencies Ω_i and decaying term. However, $\tilde{\mathbf{G}}$ seems problematic since it depends on the coupling coefficients and on atomic operators σ_{ij} resulting in a coupling differential equation.

To simplify the pointed problem, we can adopt a perturbative approach in which the pump beam, being much more intense than the seed, prepares the atoms in a stationary state. Consider the states $|0\rangle$ and $|1\rangle$ equally populated, 50% each and ignore the seed beam (which implies the coupling matrix $\tilde{\mathbf{G}} = 0$). Therefore, after taking the mean value, equation Equation 3.29 becomes:

$$\frac{d\,\langle\tilde{\sigma}(z,t)\rangle}{dt} = \tilde{\mathbf{M}}_{Pump}\,\langle\tilde{\sigma}(z,t)\rangle \tag{B.2}$$

where $\tilde{\mathbf{M}}_{Pump}$ refers to the system where only the pump beam is considered and $\langle\tilde{\mathbf{F}}(z,t)\rangle = 0$. In a stationary condition $\frac{d\langle\tilde{\sigma}(z,t)\rangle}{dt} = 0$. Hence, we have a homogeneous linear equation for the mean value for the atomic states. The latter equation can be solved by calculating the eigenvalues and finding the eigenstates that satisfy the equality. A second option includes the conservation of populations $\sum_{ii}\sigma_{ii} = 1$. We decided to solve the equation by

a less formal way that includes physical effects and decrease the required computational power.

In our procedure, the atoms that interact with the pump for a sufficient period of time will reach a stationary state where most of its populations are in the $|1\rangle$ state [53] [I]. The prepared atoms could leave the region of interaction and collide against other atoms or the cell walls. Later, they can re enter into the interaction region with a complete different phase. This will ruin the coherence of the process. Hence, we include in Equation B.2 the *decoherence rate* $-\Gamma_{de}\left(\langle\tilde{\sigma}(z,t)\rangle - \tilde{\sigma}_0\right)$, where $\tilde{\sigma}_0$ corresponds to the state of thermal atoms; Γ_{de} is much smaller than the decaying rates between allowed transitions γ_{ij}, and also $\Gamma_{de} \ll \tilde{\mathbf{M}}$ guaranteeing the reproduction of the results obtained by either the diagonalization or the normalization procedure. Notice that the decoherence term is such that if there were no pump beam, $\tilde{\mathbf{M}} = 0$ and the initial thermal state of the atoms is retrieved $\tilde{\sigma}(z,t) = \tilde{\sigma}_0$.

Taking in account the decoherence Γ_{de}, Equation B.2 is:

$$\frac{d\left\langle\tilde{\sigma}(z,t)\right\rangle}{dt} = \tilde{\mathbf{M}}_{Pump}\left\langle\tilde{\sigma}(z,t)\right\rangle - \Gamma_{de}\left(\left\langle\tilde{\sigma}(z,t)\right\rangle - \tilde{\sigma}_0\right). \tag{B.3}$$

Considering the stationary state, the time derivative cancels and the solution is given by

$$\left\langle\tilde{\sigma}(z,t)\right\rangle^{st} = -\left(\tilde{\mathbf{M}}_{Pump} - \Gamma_{de}\right)^{-1}\Gamma_{de}\,\tilde{\sigma}_0. \tag{B.4}$$

As a consequence, $\tilde{\mathbf{G}}$ can be written in terms $\left\langle\tilde{\sigma}(z,t)\right\rangle^{st}$ corresponding to the stationary state of the atoms prepared by the pump beam. Therefore, Equation B.1 now reads:

$$\frac{d\tilde{\sigma}(z,t)}{dt} = \tilde{\mathbf{M}}\,\tilde{\sigma}(z,t) + \tilde{\mathbf{G}}^{st}\tilde{\mathbf{A}}(z,t) + \tilde{\mathbf{F}}(z,t). \tag{B.5}$$

Equation B.5 is a differential equation of the first order on $\tilde{\sigma}$ with an inhomogeneous term corresponding to the field operators and the stochastic terms.

[I] The pump waist and the speed of the atoms passing a cross-section of the beam define a lower bound for the interaction time between light and atoms. The interaction time must be equal to or greater than the time taken for the atoms to reach the stationary state.

C

Complementary Results

C.1 Gain characterization

As discussed in section 3.3, the gain of the FWM process depends strongly on the experimental parameters (see Equation 3.41 and Equation 3.42). For instance, temperature controls the gain factor and the absorption linewidth. The ratio between the seed waist and the pump waist would also modify the spectrum. Whenever the ratio is too small, it means that the seed waist is much smaller than the pump waist and the interaction region between atoms would be small. This could generate some undesired effects as self-action effects [54, 72]. During this section we report some of these behaviors and characterize the gain profile of the FWM process. We start by a theoretical reproduction of the experimental gain profile. Afterwards, we characterize experimentally, the dependence of the gain profile with the geometry of the beams and the temperature.

Figure C.1.1 shows the experimental and theoretical gain factor (Equation 4.1) as a function of the probe detuning Δ_2. On the caption of the figure we find the experimental parameters. The theoretical gain profile is obtained by qualitative comparison between the theoretical spectrum linewidth and the maximum gain factor, against the experimental data. For this, we have control over the theoretical parameters like beam waist, atomic density, cell length, Rabi frequency, coupling factor among others. Therefore, some differences between the gain spectrum can be observed. Firstly, the pump power can induce a AC Stark effect that shifts the energy levels. Hence, in the theoretical description we have to tune the pump frequency Δ_1 in order to match the experiment. For instance, in the case we are discussing, the experimental Δ_1 is 1 GHz whereas the theoretical is 980 MHz. As will be shown later in subsection C.2.1, such a small change in the pump frequency is not relevant for the quantum correlations. The second difference is the gain profile at high frequencies. The experimental result shows a flat region with a small increase in the gain factor for the probe beam. Conversely, in the theoretical description

we see that at 1040 MHz the gain factor increases. This difference is explained by the Doppler effect as explained in [26]. Inside the vapor cell, the high temperature broaden the FWM spectrum due to the velocity distribution resulting in a flat region at high frequencies Δ_2. Contrary to that, the theoretical description does not consider the velocity distribution, we only consider the temperature as a factor that controls the atomic density (N in Equation 3.28). Anyway, this frequency region is not interesting for us given that, as will be discussed in section 5.2 and subsection C.2.5, there are no quantum correlations for these values of Δ_2.

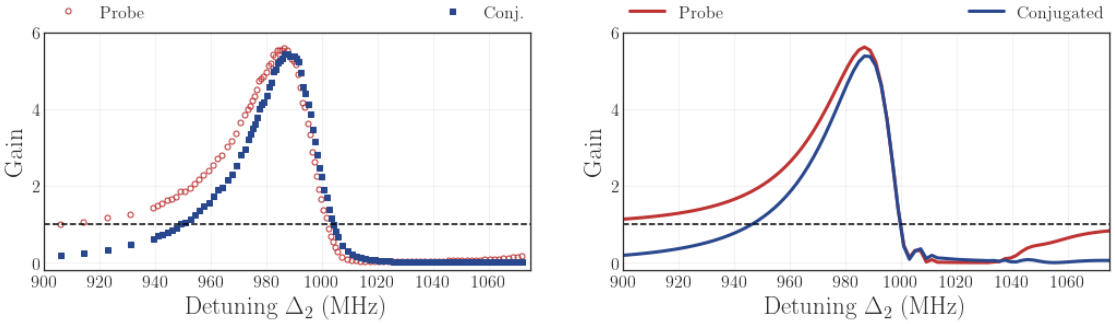

(a) Experimental characterization of the gain profile.

(b) Theoretical description of the gain profile.

Figure C.1.1. Reproduction of the gain profile. Experimental parameters: Seed power =60.3±0.5 μW; Seed waist =224.0±3.3μm; Pump power =420.0±0.3 W;Pump waist =523.6±0.6 μm;Temperature =120±1°C; Angle =0.31±0.03°. Theoretical parameters: Atomic density (N)= $0.88\times10^9 m^{-3}$; Cell length = 2.5 cm; Coupling factor $g = 0.28$

As part of the characterization of the system, we modify the geometrical parameters of the beams and the temperature looking for the best set of parameters that produce the more quantum correlated states. Table 3 shows a set of experimental parameters used for studying different gain profile and Figure C.1.2 shows the gain characterization of the FWM spectrum. Figure C.1.2a and Figure C.1.2b corresponds to the geometric configuration, where the seed waist is $(123.1 \pm 3.3)\mu m$, the pump waist $(528.0 \pm 0.6)\mu m$, the angle between seed and pump beams is $(0.31 \pm 0.03)°$. Notice that the amplification of the FWM increases from a maximum of 3 units at 112°C, to a maximum of 25 at 121°C. In terms of the spectrum bandwidth, at 112°C the width at half maximum is 30 MHz whereas at 121°C it raises to 50 MHz. For the second geometrical configuration (rows c. and d. in Table 3), the seed waist is $(244.2 \pm 1.9)\mu m$, the pump waist is $(525.5 \pm 1.6)\mu m$ and the angle is $(0.29 \pm 0.03)°$. The effect of increasing the temperature is similar as before, raising from 22 units at 103°C, to 40 at 107 °C. In this case the broadening effect is not substantial.

Each characterization was made using different seed power. We observed that the seed power increases the total amount of power after the FWM process but does not affect neither the amplification nor the quantum correlations as far as it is much smaller than the

Fig.	Pump power (mW)	Seed power (μW)	Seed waist (μm)	Pump waist (μm)	Temp ($^{\circ}C$)	Angle ($^{\circ}$)
a.	415.0±0.3	80.2±0.5	123.1±3.3	528.0±0.6	112 ±1	0.31 ±0.03
b.	415.0±0.3	80.1±0.5	123.1±3.3	528.0±0.6	121 ±1	0.31 ±0.03
c.	420.0±0.3	130.0±0.5	244.2±1.9	525.5±1.6	103.0±0.1	0.30 ±0.03
d.	420.0±0.3	130.0±0.5	244.2±1.9	525.5±1.6	107.0±0.1	0.29 ±0.03

Table 3. Experimental parameters gain characterization.

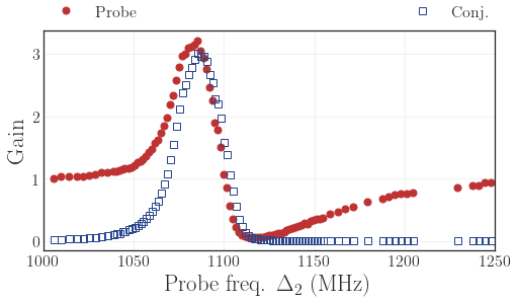

(a) Seed waist = $(123.1 \pm 3.3)\mu m$; Temp=112°C.

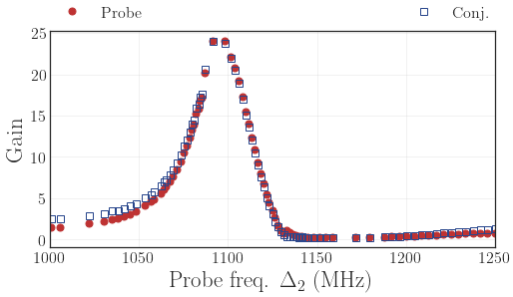

(b) Seed waist = $(123.1 \pm 3.3)\mu m$; Temp=121°C.

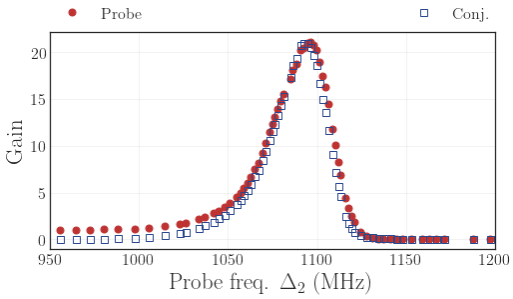

(c) Seed waist = $(244.2 \pm 1.9)\mu m$; Temp=103°C.

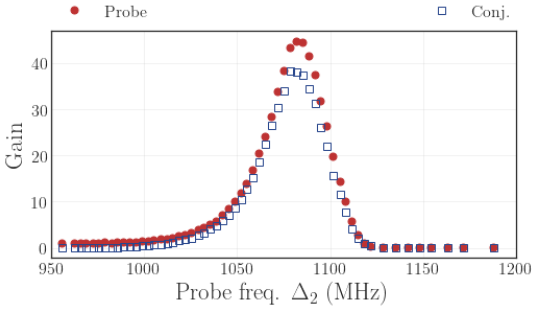

(d) Seed waist = $(244.2 \pm 1.9)\mu m$; Temp=107°C.

Figure C.1.2. Gain profile against the probe detuning. Two main configurations are shown: **(a.)** and **(b.)** having a seed waist of $(123.1 \pm 3.3)\mu m$, and a pump waist $(528.0 \pm 0.6)\mu m$. **(c.)** and **(d.)** with a seed waist of $(244.2 \pm 1.9)\mu m$, and the pump waist $(525.5 \pm 1.6)\mu m$. Observe that the increase in the temperature modifies the FWM spectrum, increasing the amplification rate and broadening the spectrum.

pump power. This will be discussed latter. The main difference between the geometrical configurations is the ratio between the waist of the pump and the seed. In the case of Figure C.1.2a and Figure C.1.2b, the rate between the seed and the pump waist is 0.23 and therefore, the interaction region between seed and pump is too small which could lead to two different scenario. At a temperature of $112^{\circ}C$, the amplification is weak, up to 3 units, such that the measured signal started to mix with the electronic background noise level. When increasing the temperature to $121^{\circ}C$, the amplification increases to 25 units. In the second case, corresponding to Figure C.1.2c and Figure C.1.2d, we increase the seed waist obtaining a ratio of 0.46 between the seed and the pump waist's. Thus, the interaction region between the light and the atoms becomes bigger, such that the intensity decreases making more difficult to induce undesired Kerr effects. In this configuration we

could achieve 22 units of gain at $103°C$ and 43 at $107°C$.

In Figure C.1.2 we presented the gain characterization implemented in two different geometric configurations. We show that the relative size between the seed and the pump waist is a key factor in the amplification process. The first configuration (**(a), (b)**) needed higher temperatures for reaching the same gain regions as the second one (**(c), (d)**). This increases the probability of generation of thermal lensing even when the size of the beams is smaller [72]. Nonetheless, this configuration had two drawbacks. At lower temperature the gain was not enough to overcome the safety lower limit (electronic level figures 23, 24) and at high temperature the quantum correlations were weak. The second configuration presented a ratio of 0.46 between the seed and the pump waist, increasing the light atom interaction. We could achieve amplification levels above 20 units at $103°C$ and twice the amplification with a temperature of $107°C$. This configuration will be the chosen for quantum measurements.

C.1.1 Gain Spectrum frequency shift by Rabi frequency

The FWM profile in Figure C.1.2 is modified by the pump Rabi frequency Ω_R (proportional to the pump power section 3.3). As it increases, the gain profile suffers from power broadening, that is, broadening of the emission profile while the gain is reduced. Another effect is the frequency shift of the spectrum profile [53].

In Figure C.1.3 we show the frequency shift of the spectrum as a function of the Rabi frequency Ω_R. The vertical axes corresponds to the output power of the probe or the conjugated beams. The lower $x-$axes corresponds to the variation of the pump power, and the upper $x-$axes corresponds to the frequency Δ_2 where the maximum gain is found. The pump laser was locked at $5^2S_{1/2},\ F = 2 \rightarrow 5^2P_{1/2},\ F = 3 + 1GHz$; the seed power was $(70.4 \pm 0.3)\,\mu W$, its temperature was $(110 \pm 1)\,°C$; the pump waist was $W_o = 523.6\,\mu m$ and the seed waist was $W_s = 133.3\,\mu m$; $\Delta_2 = 996.9\,MHz$. The measurement was done by increasing the pump power and looking for the frequency Δ_2 that corresponds to the highest amplification. Every other experimental parameter was unmodified.

From Figure C.1.3 we can observe that increasing in the pump power the spectrum is detuned in frequency. Notice that the frequency at maximum gain ranges from 955 MHz at the minimum pump power to 985 MHz at a pump power of 450 mW. Increasing the pump power shift the FWM spectrum to the blue. Notice that the dependence of the output intensity of the FWM as a function of the pump power should follow an exponential relation as shown in Equation 3.13. However, the characterization shows a threshold of the amplification process at 100 mW. This was non expected since the amplification process have been broadly studied [73].

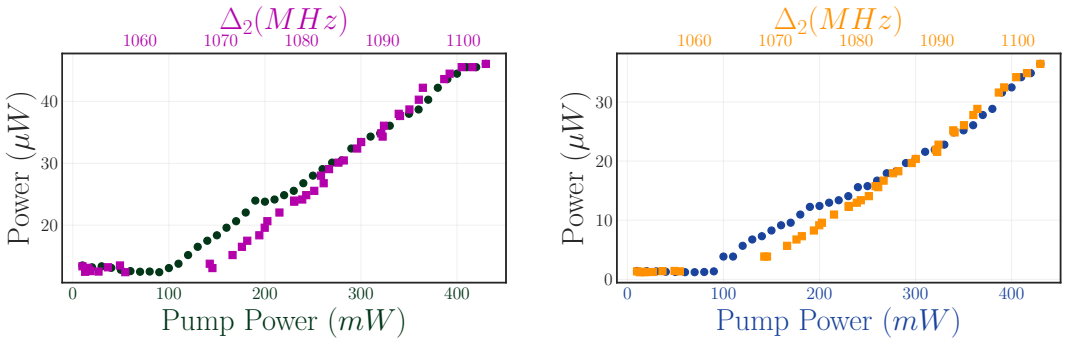

(a) Black circle: Probe beam power as a function of pump power. Red squares: Frequency shift at the gain peak from the probe beam.

(b) Blue circle: Conjug. beam power as a function of pump power. Yellow squares: Frequency shift at the gain peak from the conjug. beam.

Figure C.1.3. The pump power shifts the position of the maximum of the FWM peak. Parameters: $\Delta_1 = 5^2S_{1/2}, F = 2 \rightarrow 5^2P_{1/2}, F = 3 + 1GHz$; Temp= $110°C$; Seed power= $70.4\mu W$.

C.2 Intensity Correlations - Complement

C.2.1 Intensity correlations as a function of the pump detuning Δ_1

The pump detuning (Δ_1 in Figure 9) defines the frequency of the pump laser. It is relevant since it defines the frequencies at which the probe and conjugated beams are generated, that is, near or far from the absorption regions of the rubidium atoms [Figure 14].

Here we characterize the squeezing as a function of Δ_1. As explained in section 4.1, the Ti:sapphire laser is locked using the saturated absorption which allow us to lock the laser at six different frequencies, three for the $F = 2$ transitions and other three for the $F = 3$ transitions of rubidium 85. In Figure C.2.1 we show the saturation absorption spectrum with the pump locking frequencies. The solid vertical lines represents the FWM process where the pump detuning is at Crossover $+1GHz$ (*Lock I*), corresponding to the solid black vertical line at the frequency of 1GHz. The red solid vertical line corresponds to the probe frequency and the solid vertical blue line to the conjugated frequency when the pump is at Lock I. The second pump frequency is locked at $5^2S_{1/2}, F = 2 \rightarrow 5^2P_{1/2}, F = 3 + 1GHz$, denominated *Lock II*, which is represented by the vertical dashed lines. Given that the *Lock II* is around 180 MHz above the *Lock I* frequency, the generated beams, the probe and the conjugated, will also be shifted the same amount to higher frequencies.

We show in Figure C.2.2 the intensity correlations at the two pump detuning, *Lock I* (Figure C.2.2a) and *Lock II* (Figure C.2.2b). The geometric configuration corresponds to the first row in Table 3 **(a.)**. The probe detuning is $\Delta_2 = 1073.1 \pm 0.3$ MHz (Figure C.1.2a). The two pump detunig presented similar behavior. Their squeezing bandwidth reaches 12 MHz and at an analysis frequency of 2.5 MHz, the squeezing level is slightly better in

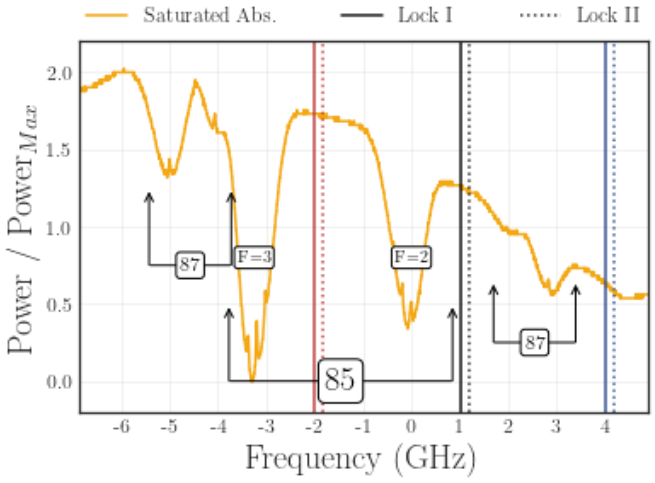

Figure C.2.1. Pump detuning frequency locking. The vertical solid lines corresponds to the FWM process when locket at the *Lock I* frequency (Crossover + $1GHz$). The vertical dashed lines corresponds to the FWM process when the pump detuning islocked at $5^2S_{1/2}$, $F = 2 \rightarrow 5^2P_{1/2}$, $F = 3 + 1GHz$ (*Lock II*).

figure C.2.2a.

In figure Figure C.2.3 we show the measurement done at a higher probe detuning $\Delta_2 = 1088.1 \pm 0.3$ MHz. As seen in Figure C.1.2a, the amplification factor increases in 0.4. When the pump frequency is at *Lock I*, and the squeezing bandwidth surpass 5 MHz. Conversely, when the pump detuning is at *Lock II* the squeezing bandwidth barely reaches 5 MHz.

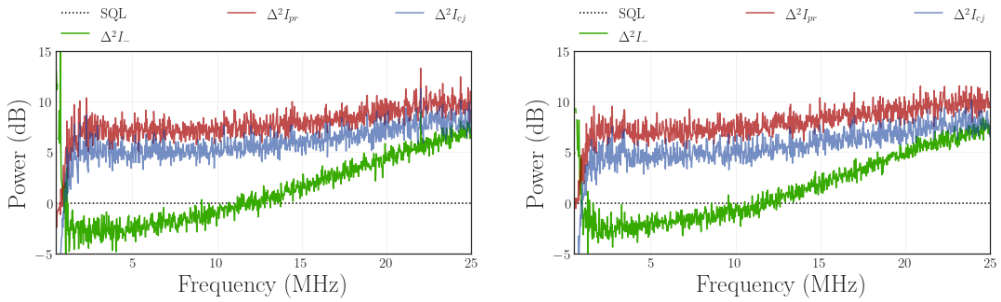

(a) Δ_1 = Crossover $+1GHz$ (Lock I).

(b) $\Delta_1 = 5^2S_{1/2}$, $F = 2 \rightarrow 5^2P_{1/2}$, $F = 3 + 1GHz$ (Lock II).

Figure C.2.2. Pump detuning Δ_1 characterization . Parameters: pump power $= 450.2 \pm 0.3\,mW$; seed power $= 80.3 \pm 0.5\,\mu W$; pump waist $528.0 \pm 0.6\mu m$; seed waist $W_s = 123.1 \pm 3.3\,\mu m$; cell temperature: $112 \pm 1°C$; angle $= 0.31\,°$.$\Delta_2 = 1073.1 \pm 0.3$ MHz.

A further characterization on the pump detuning can be done by locking the pump frequency at -2GHz, in Figure C.2.1. This is shown in Figure C.2.4. Notice that there is no signal below the shot noise level, a complete absence of quantum correlations is observed which could be caused by the frequencies where the probe and conjugated beams are generated. The probe beam is generated at -5 GHz (Figure 14) far from an absorption

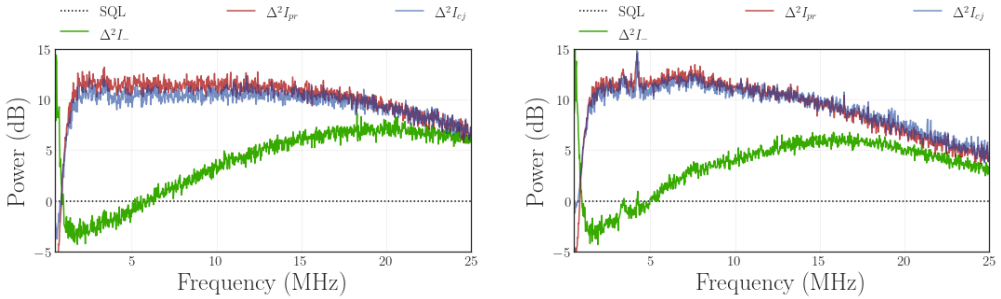

(a) $\Delta_1 = \text{Crossover} + 1GHz$.

(b) $\Delta_1 = 5^2S_{1/2}, F = 2 \rightarrow 5^2P_{1/2}, F = 3 + 1GHz$.

Figure C.2.3. Pump detuning characterization at Δ_1. Parameters: pump power $= 450.2 \pm 0.3\,mW$; seed power $= 80.8 \pm 0.5\,\mu W$; pump waist $528.0 \pm 0.6\mu m$; seed waist $123.1 \pm 3.3\mu m$; cell temperature: $112 \pm 1°C$; angle $= 0.31\,°$. $\Delta_2 = 1088.2 \pm 0.3$ MHz.

region, wheres the conjugated beam is generated at +1 GHz near the absorption region $F = 2$.

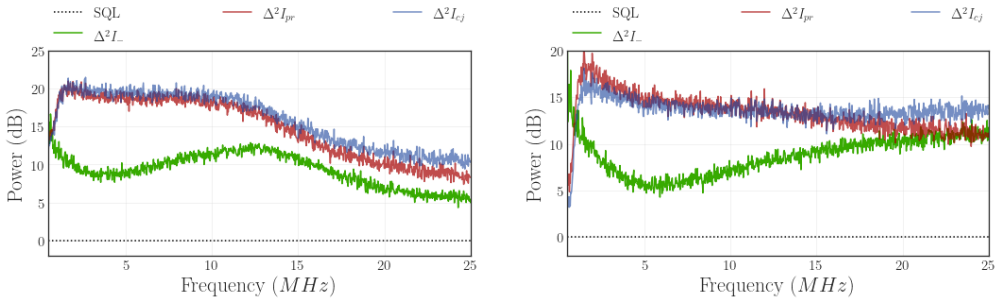

(a) $\Delta_1 = 5^2S_{1/2}, F = 3 \rightarrow 5^2P_{1/2}, F = 2 + 1\,GHz$. $\Delta_2 = 943.4 \pm 0.3\,MHz$.

(b) $\Delta_1 = 5^2S_{1/2}, F = 3 \rightarrow 5^2P_{1/2}, F = 3 + 1\,GHz$. $\Delta_2 = 883.5 \pm 0.3\,MHz$.

Figure C.2.4. One photon detuning characterization as a function of Δ_1. Parameters: pump power $= 450.2 \pm 0.3\,mW$; seed power $= 80.8 \pm 0.5\,\mu W$; pump waist $528.0 \pm 0.6\mu m$; seed waist $123.1 \pm 3.3\mu m$; cell temperature: $117 \pm 1°C$; angle $= 0.31\,°$.

The pump frequency Δ_1 is not the essential parameter in the generation of quantum correlations if we were to lock the pump frequency in the frequency region named $F = 2$. We decided to lock the pump frequency at Crossover $+ 1GHz$ given that the squeezing level and bandwidth is slightly better.

C.2.2 Intensity correlations as a function of Pump Power

The pump power (Rabi frequency) can increase the gain factor and the bandwidth by enhancing the coupling between atoms and light. It can also generate undesired Kerr effects like self-phase modulation or cross-phase modulation, that can destroy the correlations [56]. Therefore, we study the behavior of the correlations as a function of the pump power.

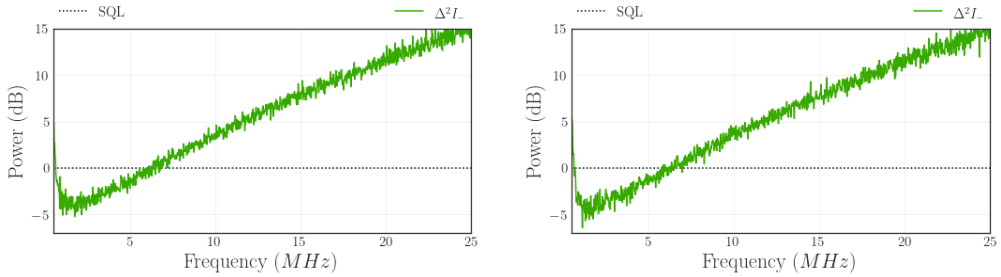

(a) Pump power = $360.7 \pm 0.3\,mW$ **(b)** Pump power = $380.8 \pm 0.3\,mW$

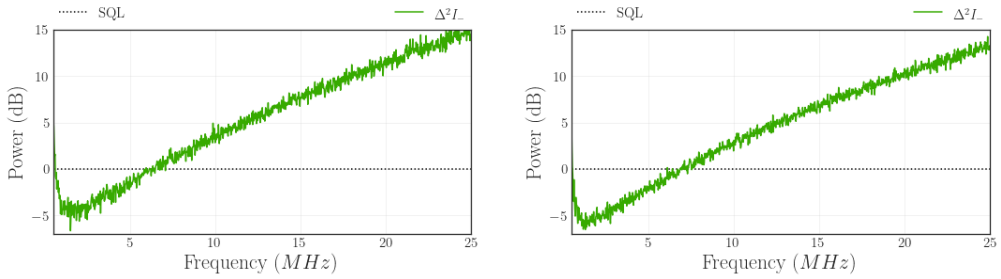

(c) Pump power = $400.2 \pm 0.3\,mW$ **(d)** Pump power = $450.1 \pm 0.3\,mW$

Figure C.2.5. Intensity correlations as a function of pump power. Parameters: Pump frequency+Crossover $+ 1GHz$; $\Delta_2 = 990.6 \pm 0.3\,MHz$; Seed power= $80.0 \pm 0.3\,\mu W$; Temp.= $110 \pm 0.1°C$; Angle between seed and pump= 0.3°. Pump waist $525.5 \pm 1.6\,\mu m$; Seed waist $244.2 \pm 1.9\,\mu m$. Table 4 c. and d. $\Delta_2 = 1054.8 \pm 0.3$.

In this characterization, we used the geometrical configuration reported in Table 4 c. and d., with a seed power of $110.2 \pm 0.3\,\mu W$, $\Delta_2 = 1054.8 \pm 0.3\,MHz$, and a temperature of $110°C$. The green curve corresponds to the intensity correlations $\Delta^2 I_-$. The black dotted line at 0 dB represents the shot noise level. At a pump power of 360 mW (Figure C.2.5a) the system presents -4 dB of squeezing at an analysis frequency of 2.0 MHz and a squeezing bandwidth of 6 MHz. While the pump power increases, the squeezing level grows and the bandwidth becomes broader reaching -5.2 dB of squeezing at 2.0 MHz and a bandwidth of 6.3 MHz. The dependence of the noise compression with the pump power is not strong within this short range. Nevertheless, it can be seen that the best squeezing level and bandwidth is achieved at the higher pump power. In subsection C.2.4 we extend this discussion by taking a different geometric configuration and covering a broader power range.

The effect of the pump power on the squeezing level and bandwidth involves many other parameters of the system. As shown in subsection C.1.1, the pump power also shifts the FWM spectrum. As it was mentioned, in this characterization Δ_2 is fixed while the pump power increases. The FWM spectrum is being shifted to the blue while the amplification factor decreases, hence we are modifying simultaneously the gain factor, the probe detuning Δ_2 and the pump power. In the following section we show the characterization as a function of the pump frequency and the two photon detuning.

C.2.3 Intensity correlations as a function of the seed power

The seed power is another experimental parameter that can be controlled individually allowing a characterization of the squeezing as a function of this parameter. Figure C.2.6 presents this characterization for 80 and 120 μW. The noise spectrum shows that there is no difference between the generated states, both have a bandwidth of 6.3 MHz and a squeezing level of -4.7 dB at an analysis frequency of 2.0 MHz. There are few differences between them that could be generated by statistical fluctuations in the detection or the stabilization of the frequencies. For a seed power below 80 μW, the detected photocurrent reaches the background electronic noise level which prevents the correct data analysis. Seed power above 120 μW was not possible given that we could surpass the damage threshold of the AOM used for the generation of the seed beam (section 4.2).

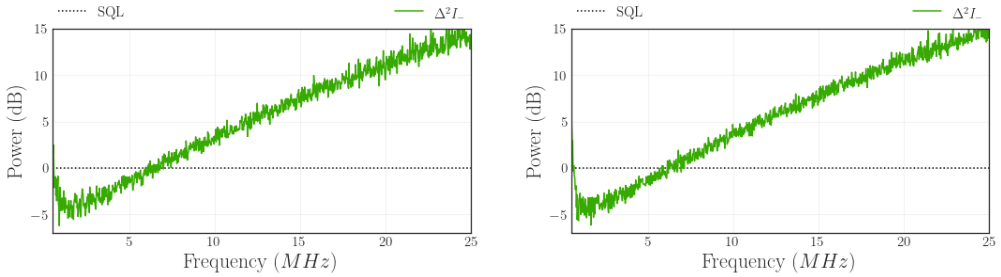

(a) Seed power = 80.0 $\pm$0.5 μW. **(b)** Seed power = 120.0 $\pm$0.5 μW.

Figure C.2.6. Intensity correlations as a function of seed power. The seed power is not a relevant parameter for the squeezing generation.

C.2.4 Intensity correlations as a function of Pump Power - Complement

In this appendix we present the squeezing as a function of the pump power for the geometric configuration a. and b. in Table 4 with a seed power of $80.2 \pm 0.3\,\mu W$ and $\Delta_2 = 1073.7 \pm 0.3\,MHz$. The red/blue curve corresponds to the probe/conjugated fluctuations $\Delta^2 I_{pr/cj}$, and the green curve to the intensity correlations $\Delta^2 I_-$. The black dotted line at 0 dB represents the shot noise level. At a pump power of 260 mW (Figure C.2.7a) the system presents -2 dB of squeezing at an analysis frequency of 2.0 MHz and a squeezing bandwidth of 2.5 MHz. While the pump power increases, the squeezing level grows and become broader reaching -5.0 dB of squeezing at 2.0 MHz and a bandwidth of 9 MHz. Compared to the results in C.2.2, in this characterization it is clear that the more the pump power, the best the squeezing. However, the system could saturates and even more, increasing the pump power could stimulate other Kerr effects that would destroy the squeezing.

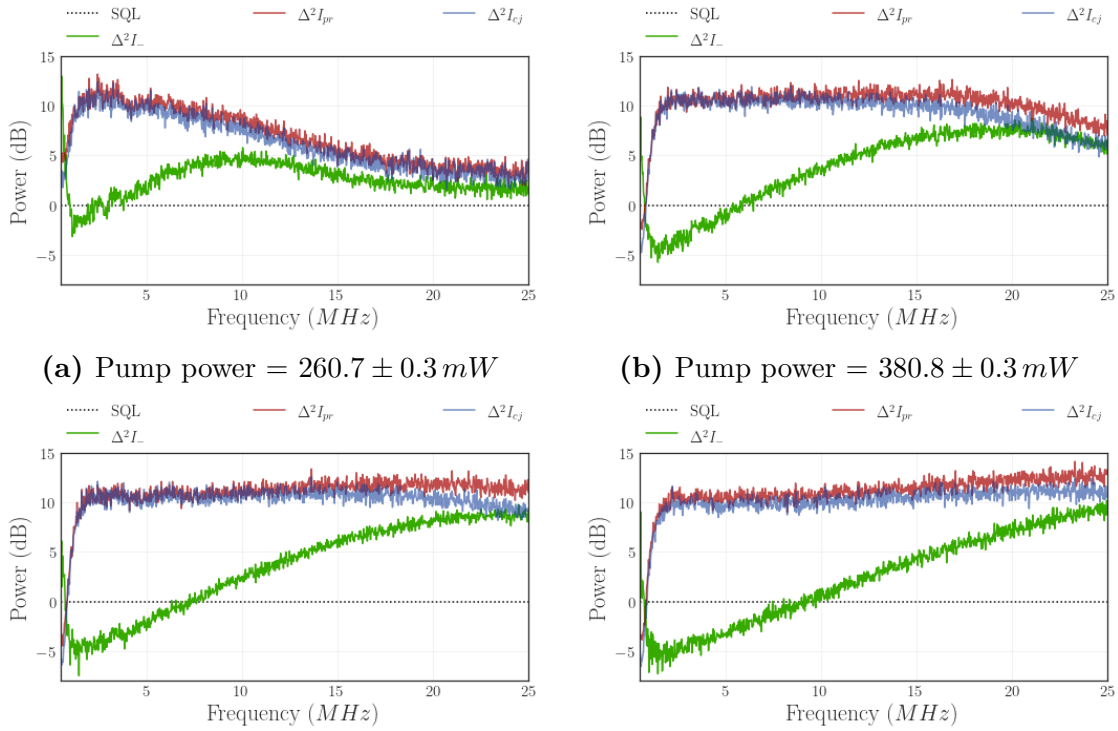

(a) Pump power $= 260.7 \pm 0.3\,mW$

(b) Pump power $= 380.8 \pm 0.3\,mW$

(c) Pump power $= 400.2 \pm 0.3\,mW$

(d) Pump power $= 450.1 \pm 0.3\,mW$

Figure C.2.7. Intensity correlations as a function of pump power. Parameters: Pump frequency+Crossover $+ 1GHz$; $\Delta_2 = 990.6 \pm 0.3\,MHz$; Seed power$= 80.0 \pm 0.3\,\mu W$; Temp.$= 110 \pm 0.1°C$; Angle between seed and pump$= 0.3°$. Pump waist $525.5 \pm 1.6\,\mu m$; Seed waist $244.2 \pm 1.9\,\mu m$. Table 4 c. and d. $\Delta_2 = 1054.8 \pm 0.3$.

The effect of the pump power on the squeezing level and bandwidth involves many other parameters of the system. As shown in subsection C.1.1, the pump power also shifts the FWM spectrum. As it was mentioned, in this characterization Δ_2 is fixed while the pump power increases. The FWM spectrum is being shifted to the blue while the amplification factor decreases, hence, we are modifying simultaneously the gain factor, the probe detuning Δ_2 and the pump power. In the following section we show the characterization as a function of the pump frequency and the two photon detuning.

C.2.5 Intensity correlations as a function of the probe detuning Δ_2 - Complement

The theoretical model allow us to study in detail the behavior of the system as we change its parameters. In this appendix we show the characterization of the gain spectrum, the correlations in intensity and in quadratures as we change the Rabi frequency and the probe detuning.

C.2.6 Adjustment of the theoretical model

The theoretical model must be tested to check for its validity, moreover when the FWM profile was obtained by a qualitative comparison. For that reason, we calibrate

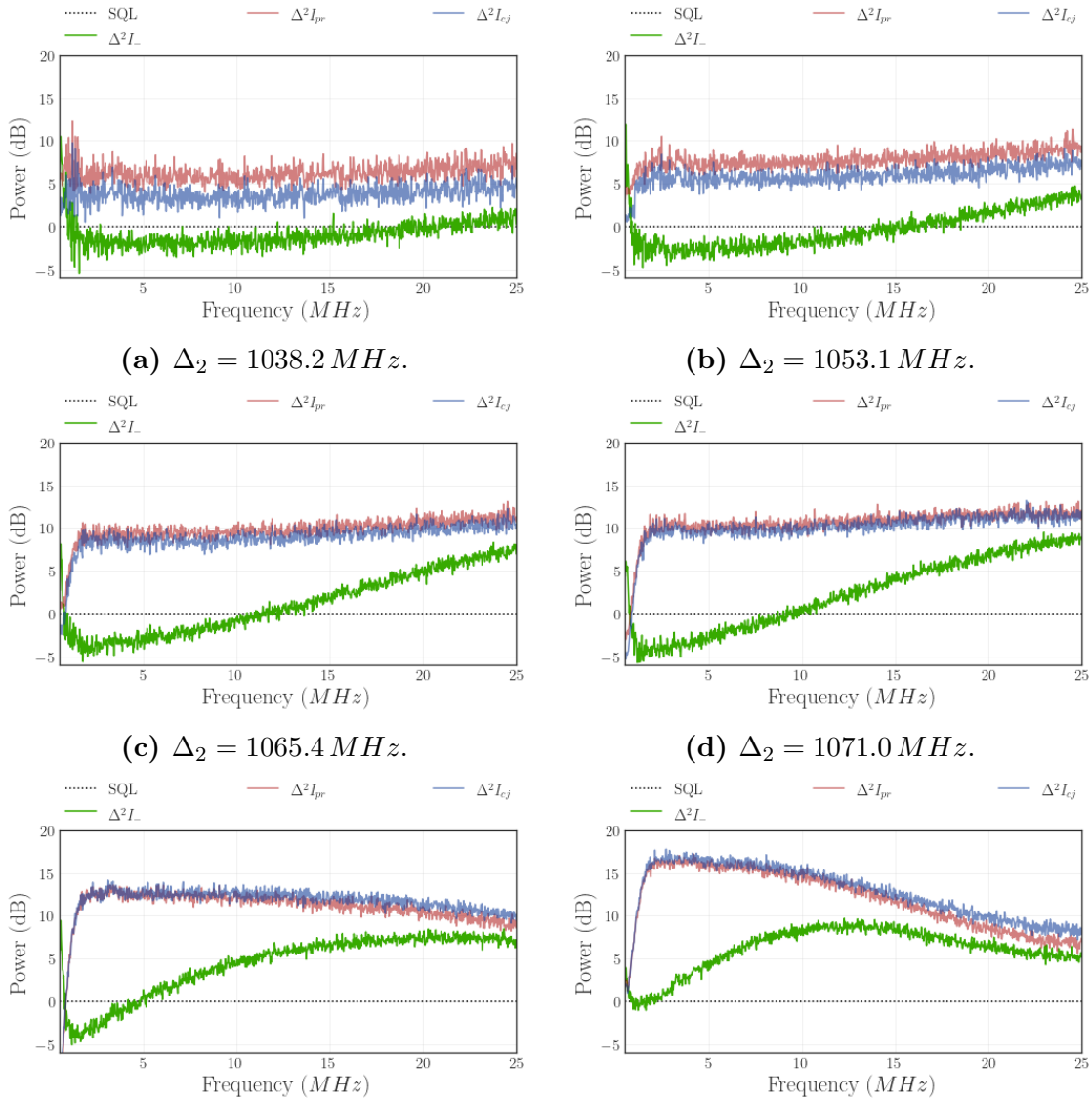

(a) $\Delta_2 = 1038.2\,MHz$. **(b)** $\Delta_2 = 1053.1\,MHz$.

(c) $\Delta_2 = 1065.4\,MHz$. **(d)** $\Delta_2 = 1071.0\,MHz$.

(e) $\Delta_2 = 1082.8\,MHz$. **(f)** $\Delta_2 = 1098.1\,MHz$.

Figure C.2.8. Intensity correlations as a function of the probe detuning Δ_2. Parameters: pump power $= 453.0 \pm 0.3\,mW$; seed power $= 80.1 \pm 0.3\,\mu W$; pump waist $528\,\mu m$; seed waist $123\,\mu m$; cell temperature: $121 \pm 1°C$; angle $= 0.3°$. Pump frequency locked at Crossover $+ 1GHz$.

the theoretical parameters such that the squeezing and the noise from the probe and conjugated beams are described as a function of Δ_2. This guarantee a reliable theoretical reproduction of the experiment.

In Figure C.2.9 we report the intensity noise spectrum for the experiment and the theoretical description. The superscript Exp indicates the experimental data; the superscript Th stands for the theoretical model. Both the experimental and the theoretical description show the intensity correlations $\Delta^2 I_-$, the excess of noise $\Delta^2 I_+$, and the individual noise level $\Delta^2 I_{pr/cj}$. As far as the characterization was done for different probe detuning Δ_2, we found the same behavior reported in the latter section. Even more,

our theoretical model is capable of describing the change in the profile of the squeezing bandwidth. At $\Delta_2 = 984$ MHz the gain factor is around 5 units and the squeezing level and bandwidth are degraded. As we decrease Δ_2, the gain factor also decreases and the squeezing level and bandwidth are enhanced achieving -5 dB of squeezing and 22 MHz of bandwidth. The deviation of the experiment to the theory is more dramatic at $\Delta_2 = 984$ MHz where the squeezing level at 2.5 MHz is -2 dB in the experimental data ($\Delta^2 I_-^{Exp}$) and -3.8 dB in the theory ($\Delta^2 I_-^{Th}$). In the case of the squeezing bandwidth, the experimental data shows 5 MHz of bandwidth whereas the theory shows 8 MHz. The discrepancy is reduced as the Δ_2 decreases.

In terms of the individual noise level $\Delta^2 I_{pr}$ and $\Delta^2 I_{cj}$, at higher probe detuning Δ_2 the noise from the probe and conjugated beams are balanced, which agree with the fact that the gain factor is very similar for both of the beams. In this case the experiment and the theoretical approach reproduce this behavior correctly. In the case of a probe detuning equal to $\Delta_2 = 964$ MHz, the gain factor for the probe beam is 3.5 while for the conjugated is 3 units. Hence, it is expected that the probe beam has more noise than the conjugated, as it is shown in the experimental plot. Nevertheless, the experimental data is well described by the model. We observe the change in the squeezing level and bandwidth, and even with different noise values, the theoretical description follows the experimental behavior across the analysis frequency range and the probe detuning.

So far we have been exploring different geometric configurations in order to find the one that provides the best squeezing. We check that the probe detuning Δ_2 is one of the main factors for the control of the squeezing level and the squeezing bandwidth. The best case in the configuration **(a.)** and **(b.)** (Table 3) is presented in subsection C.2.4 where we could find a squeezing level of -5 dB and a squeezing bandwidth of 9 MHz at a cell temperature of $121 \pm 1°C$. Even when the squeezing level and bandwidth would be enough for the development of the project, the temperature could be problematic as far as such a high value could deteriorate the anti-reflection coating of the rubidium cell. Besides, it is well above the reported temperatures (around 100 $°C$ e.g. [26, 14, 27]). On the other hand, working with configuration **(c.)** and **(d.)** we were able to find similar squeezing level and by adjusting the probe detuning, increase the squeezing bandwidth. At a temperature of 107 $°C$, the gain factor is as big as 40 units and the generated beams were far from the electronic noise level. However, the fluctuations of the generated beams were huge, above 10 dB of excess of noise, which could stimulate some non-linear response in the electronic setup. Therefore, we decided to continue the experimental characterization with the configuration **(c.)** (Figure C.1.2c) with a temperature of 103 $°C$.

We also tested our model and found that, even with some small differences between the experiment and the theoretical results, we can rely on its outcome. The divergences could be caused by the disregard of the angle between seed and pump. This calibration

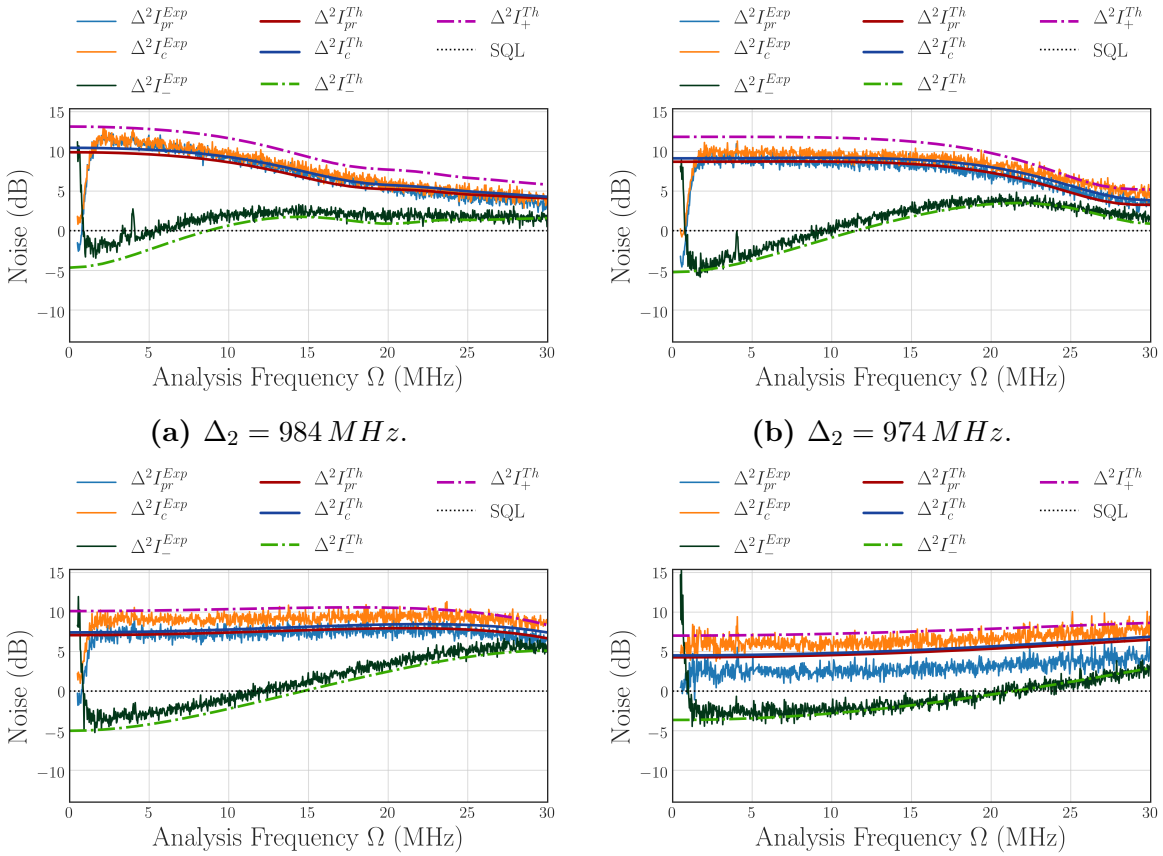

(a) $\Delta_2 = 984\,MHz$. **(b)** $\Delta_2 = 974\,MHz$.

(c) $\Delta_2 = 964\,MHz$. **(d)** $\Delta_2 = 944\,MHz$.

Figure C.2.9. Experimental and theoretical description of the intensity correlations. Starting from a detuning Δ_2 near the maximum, we scan over $30\,MHz$ and measure the noise spectrum of the system. The superscript identifies the experimental (*Exp*) and the theoretical (*Th*) plots. A subscript identifies the signal: *pr* for probe; *c* conjugated; I_- intensity-difference; I_+ intensity addition; *SQL* standard quantum limit. The theoretical description already takes into account the quantum efficiency of detection $\eta = 85\,\%$.

is necessary in order to guarantee a reliable theoretical characterization of the quantum entanglement.

C.2.7 Testing squeezing

There is an important test to do to be sure that we are actually measuring squeezing. In Figure C.2.10 we show in the vertical axes the squeezing level, and in the horizontal the total power in the detectors (probe plus conjugated). The way to corroborate the squeezing is to introduce losses on the generated beams and measure the squeezing level as we increase the losses. This is done using an neutral attenuator that affect equally probe and conjugated beams. When the beams are completely attenuated, we should recover the shot noise level. The squeezing have to decrease linearly with the attenuation. If we think the losses as a beam splitter operator where one input is one beam and the other is vacuum, as we increase the reflection (losses of our beam), the contribution of the vacuum increases by a factor of R whereas the contribution of the beam decreases as T.

There is only linear relations in this process so a linear behavior is expected, if not, some problem in the detection scheme such as saturation of the detectors must be the cause of this misbehavior.

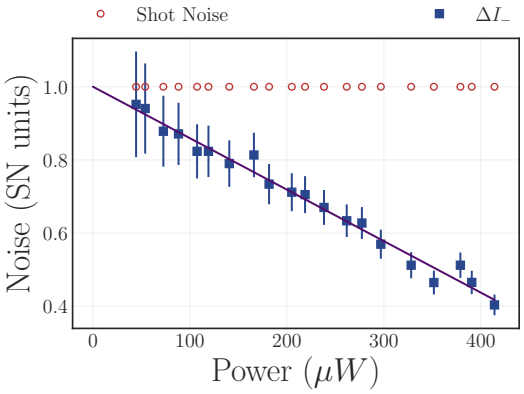

Figure C.2.10. Squeezing level as a function of the total power of the generated beams. The generated beams are attenuated and the squeezing level recorded. When the beams are completely attenuated we should reach the shot noise level. Parameters: Pump power $= 414\,mW$; probe power $= 86\,\mu W$; Temperature $= 120°C$; $\Delta_2 = 996\,MHz$; Pump frequency $=5^2S_{1/2}, F = 2 \rightarrow 5^2P_{1/2}, F = 3 + 1\,GHz$. Analysis frequency $= 3\,MHz$.$R^2 = 98.1\%$.

C.3 Covariance matrix reconstruction and entanglement - Complement

C.3.1 Matching the detection system

As discussed in subsection 4.6.3, the mismatch factor f plays an important role in the tomography of the state. Hence, we decided to characterize its effect by misaligning the beam with respect to their analysis cavities. Table 4 shows the experimental parameters for this characterization.

Table 4. Experimental parameters for the coupling factor characterization.

Pump power (mW)	Seed power (μW)	Temp ($°C$)	Analysis freq. (MHz)	Δ_2 (MHz)
420.0 ± 0.3	140.1 ± 0.3	103.0±0.1	7.0±0.1	1074.6 ±0.3

In Figure C.3.1 we present two conditions for the matching of the beams with the analysis cavities. In figs. C.3.1a and C.3.1c corresponds to the transmission from the analysis cavities; it can be used for determining the resonator coupling factor $1 - f^2$ of the beam into the resonator. In figs. C.3.1b and C.3.1d there are the single mode noise spectrum for the probe and conjugated. In the best coupling configuration, the probe is coupled at 96 % and the conjugated at 98%. Far from resonance, the amplitude noise reaches 12 units above the shot noise level. When scanning around the resonance ($\Delta = 0$) the noise spectrum reaches its maximum 13 units of excess of noise, corresponding to the

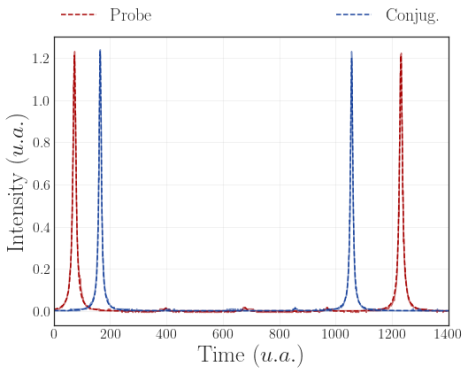

(a) 96.6 ± 0.2% of the probe is coupled into its cavity. 98.1±0.3% of the conjugated.

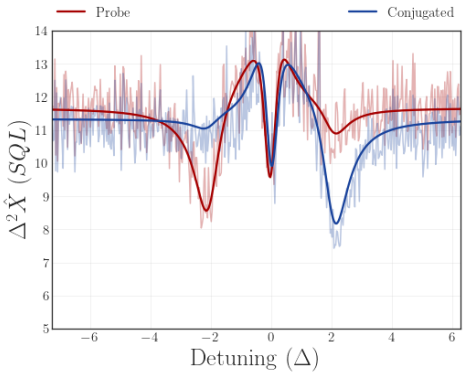

(b) Single mode noise spectrum. This is the best coupling case.

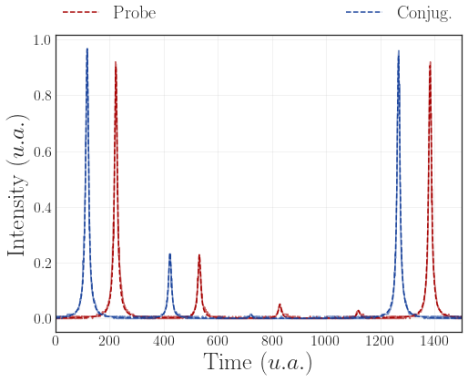

(c) 87.5±0.3% of the probe is coupled into its cavity. 91.7±2.0% of the conjugated.

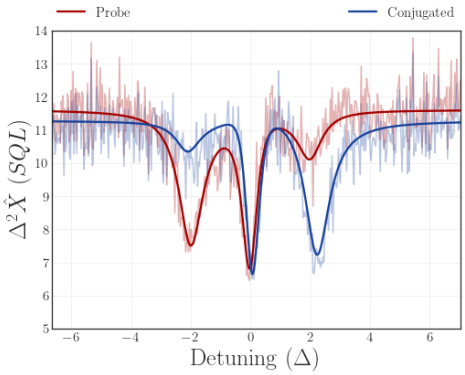

(d) We could decrease the coupling factor up to 87% before obtaining non-physical states.

Figure C.3.1. The coupling factor takes into account the small fraction of light that does not enter into the cavity. This fraction will go directly to photodetection and will add an extra noise signal to the tomography.

phase noise, and due to the mismatch, the amplitude noise at exact resonance is reduced in 2 SQL units compared to the noise far from resonance. The worst configuration presented a probe coupled at 75% and a conjugated at 78 %. Under this configuration, we find that out of resonance the noise level remains at 12 units which is consistent given that most of the incoming beam is being reflected. When the beam enters into resonance the noise spectrum is greatly distorted. The phase noise measured at $\Delta = \pm 0.5$ decrease from 13 to 12 units, and the central depth diminish from 10 to 7 units.

The resonator coupling factor describes the effect of the extra signal going into the detection without rotating its quadratures (subsection 4.6.3). A more exhaustive study at different resonator coupling factors is shown in Figure C.3.2, where we plotted the fitted values of the covariance matrix parameters as a function of the probe resonator coupling factor (Equation 4.12). When the beam is out of resonance, the system is detecting the amplitude correlations. At this point, most of the beam is being reflected by the analysis cavity, and hence, the covariance matrix parameters μ, α_{pr}, α_{cj} are expected to

have few variation. In that sense, we can observe that α (Figure C.3.2a) and $\mu = \langle \hat{p}_S^{pr}, p_S^{cj} \rangle$ (Figure C.3.2c) change less than 4% from the worst coupling to the best. When the carrier is near the resonance ($|\Delta| < 1$) the phase quadratures are accessed. We observe that for the case of the individual modes (β_{pr} and β_{cj} in Figure C.3.2a) the variation is below 7%. However, $\nu = \langle \hat{q}_S^{pr}, \hat{q}_S^{cj} \rangle$ in figure C.3.2d doubles its magnitude as the coupling goes to one. It is worth noticing that the asymmetry δ_{pr} in the probe beam differs up to 5%. In the case of δ_{cj} the total variation is 45%.

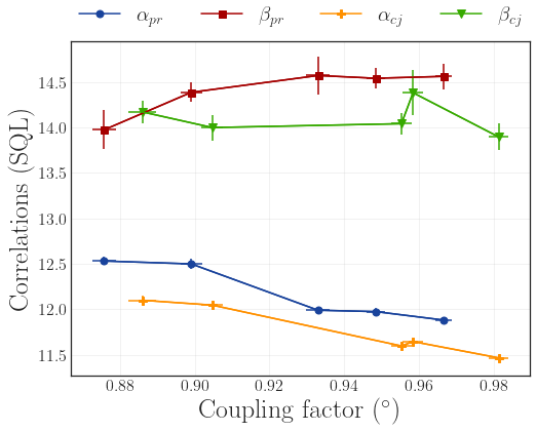

(a) Single mode parameters of the covariance matrix.

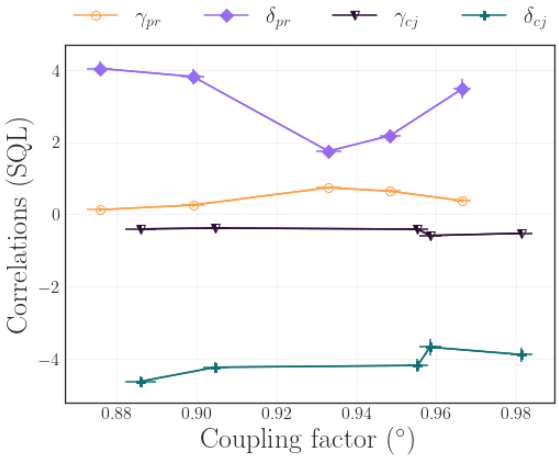

(b) Single mode parameters covariance matrix.

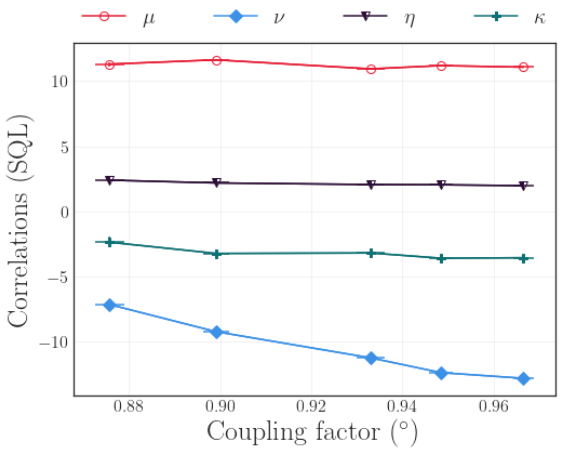

(c) Cross-mode correlations covariance matrix.

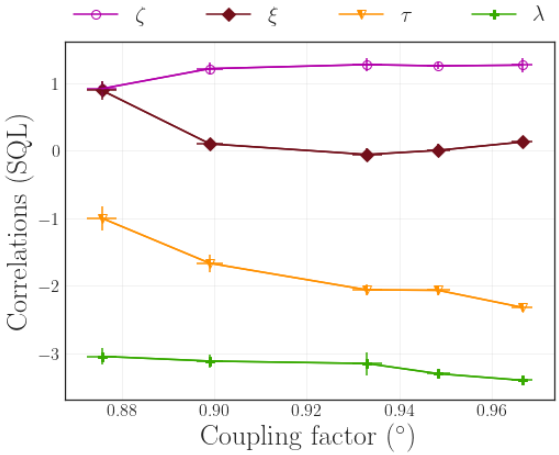

(d) Cross-mode correlations covariance matrix.

Figure C.3.2. The coupling factor takes into account the small fraction of light that does not enter into the cavity. This fraction will go directly to photodetection and will add an extra noise signal to the tomography.

Resonator coupling factors above the reported ones are difficult to achieve due to the lack of spatial mode selection in our system, differently from the OPO system where a cavity selects the resonant spatial mode [25]. As an empirical rule we established 95% as a recommendable coupling percentage for the tomography. However, we are able to

perform a feasible reconstruction of the state at resonator coupling factors as low as 90%. Below 87 %, we were not able to reconstruct a physical covariance matrix.

Once the covariance matrix is reconstructed, we can study the quantum entanglement available in the system. We use the Duan (subsection 2.5.1) and the PPT (subsection 2.5.2) criterion for the different bipartitions. The Duan criterion in the *symmetric/anti-symmetric basis* (SA) is shown in Figure C.3.3a. We show the bipartition [S_{pr},S_{cj}]. Notice that at low resonator coupling factor, the measured state is far from violating the Duan criterion. Low resonator coupling factor means that a bigger fraction of light is unaffected by the analysis cavity, hence, there is no rotation of the amplitude quadrature. Given the huge excess of noise in the amplitude quadrature, its measurement screens the information from the resonating fraction of light. When the resonator coupling factor reaches its maximum at 97% we retrieve the information of the state equating the Duan criteria in the SA basis.

The Duan criterion could also be considered in the sideband basis. This is shown in Figure C.3.3b. Among the set of bipartitions, we are showing $[\Omega_{pr}, -\Omega_{cj}$ and $-\Omega_{pr}, \Omega_{cj}]$. The two bipartitions behave differently. On the one hand, $[\Omega_{pr}, -\Omega_{cj}]$ decreases monotonically, and barely violates the criteria. The witness of entanglement for the bipartition $[-\Omega_{pr}, \Omega_{cj}]$ is steady around 2, and reaches values near the violation at the maximum coupling rate.

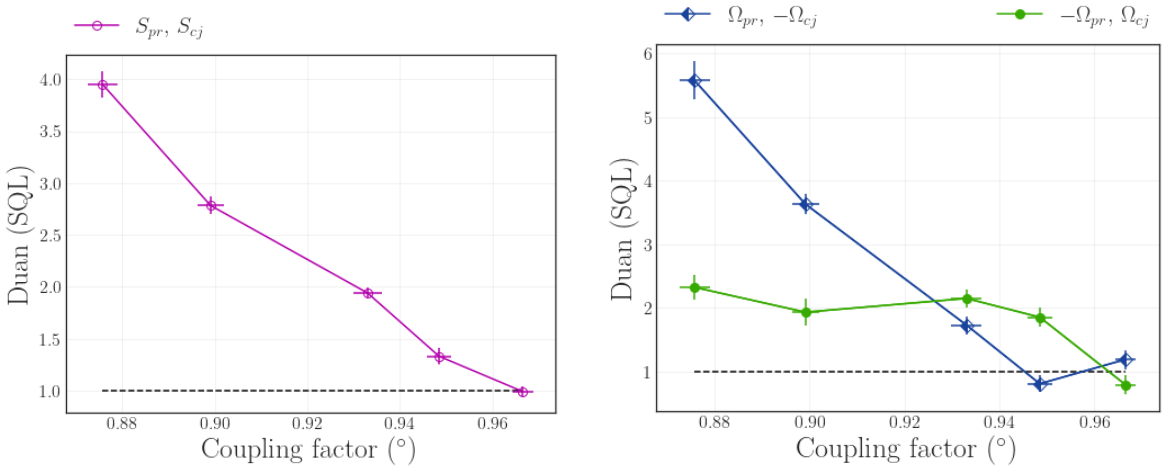

(a) Duan criterion in the symmetric/anti-symmetric basis.

(b) Duan criterion in the sideband basis.

Figure C.3.3. Duan criterion as a function of the coupling factor. The dashed line indicates the condition of entanglement.

As explained in section 2.5, the PPT criteria is also an entanglement witness with the advantage of being a necessary and sufficient condition for bipartitions $1 \times N$ for Gaussian states. The Figure C.3.4 shows the minimum of the symplectic values calculated for different bipartitions. In the *symmetric/anti-symmetric basis* (Figure C.3.4a) the

$[S_{pr},S_{cj}\times A_{pr},A_{cj}]$ is the only bipartition which does not violate the PPT criteria. The bipartitions $[S_{pr}\times S_{cj},A_{pr},A_{cj}]$ and $[S_{pr},S_{cj},A_{pr}\times A_{cj}]$ are superimposed and show entanglement at coupling factor above 95%. The other bipartitions retrieve the entanglement as the coupling of the light into the cavities is improved, achieving a violation of 0.65 SQL. Considering the *sideband basis*, the $[\Omega_{pr}, -\Omega_{cj} \times \Omega_{cj}, -\Omega_{pr}]$ bipartition does not violate the entanglement witness. The other considered bipartitions sustain the entanglement even at a coupling of 87%.

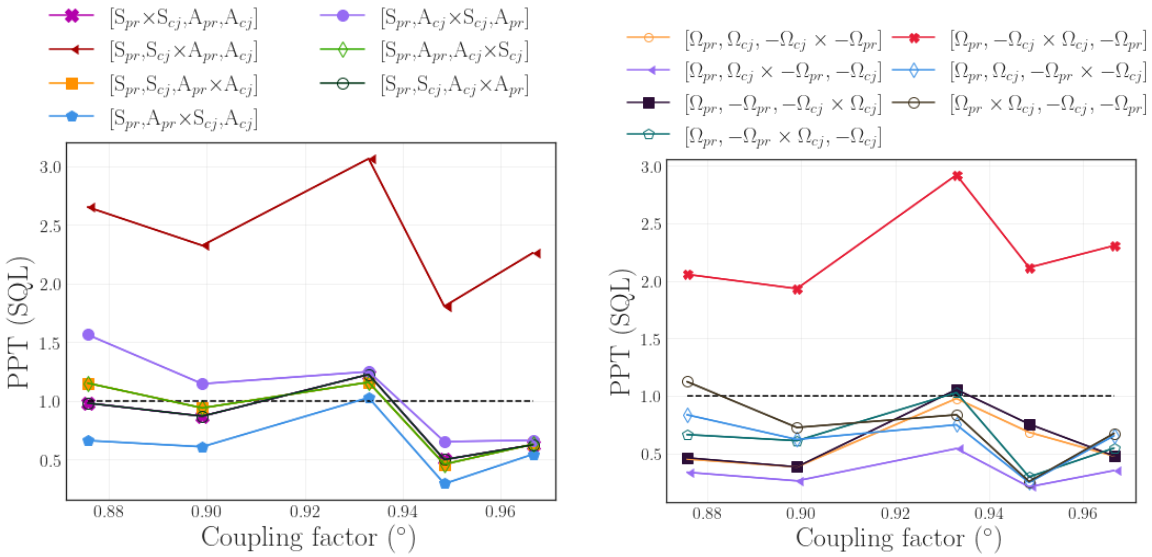

(a) PPT criterion in the symmetric/anti-symmetric basis.

(b) PPT criterion in the sideband basis.

Figure C.3.4. PPT criterion as a function of the coupling factor. The horizontal dashed line is the benchmark of the entanglement.

The characterization of the states considering the mismatch factor shows that it is an important parameter for obtaining a physical covariance matrix. Nonetheless, it is not sufficient for retrieve the information lost in the tomography process. Therefore, the resonator coupling factor has to be maximized ($f \sim 0$) for any reconstruction of a state, as well as the mismatch factor must be taken into account for correcting the physicality.

C.3.2 Seed power

The seed power was shown to be a minor parameter when studying the squeezing (see subsection C.2.3). However, we will show that depending on the chosen basis, the entangled bipartitions have different response as a function of the seed power.

Table 5. Experimental parameters for the seed power characterization.

Pump power (mW)	Temp. ($°C$)	Analysis freq. (MHz)	Δ_2 (MHz)
420.0 ± 0.3	103.0 ± 0.1	10.0±0.1	1071.8 ±0.3

The individual noise of the probe and conjugated beams increases as a function of the seed power (Figure C.3.5a). Nonetheless, the asymmetry δ_j and the two-mode correlations remain almost constant. This behavior coincide with the results in subsection C.2.3.

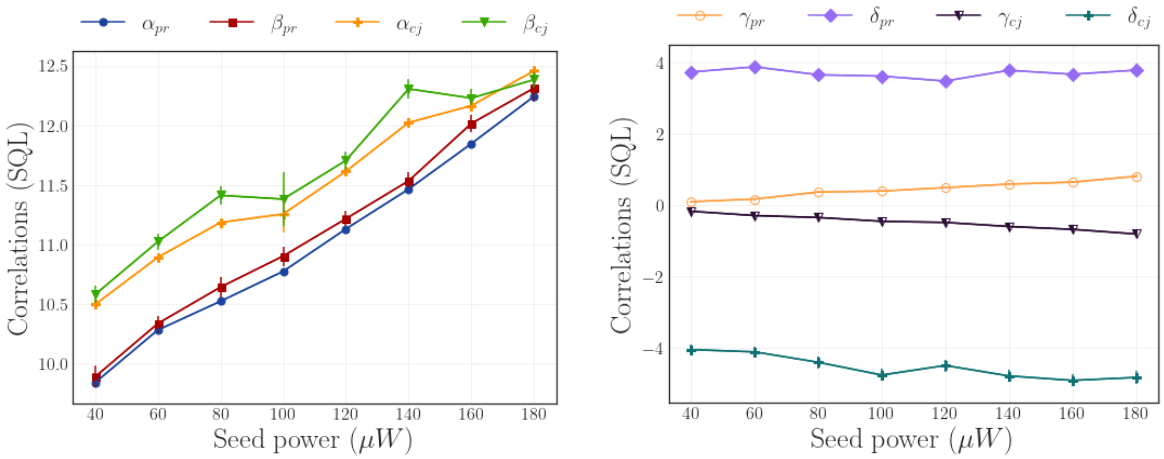

(a) Single mode parameters of the covariance matrix.

(b) Single mode parameters covariance matrix.

Figure C.3.5. Covariance matrix single-mode correlations as a function of the seed power.

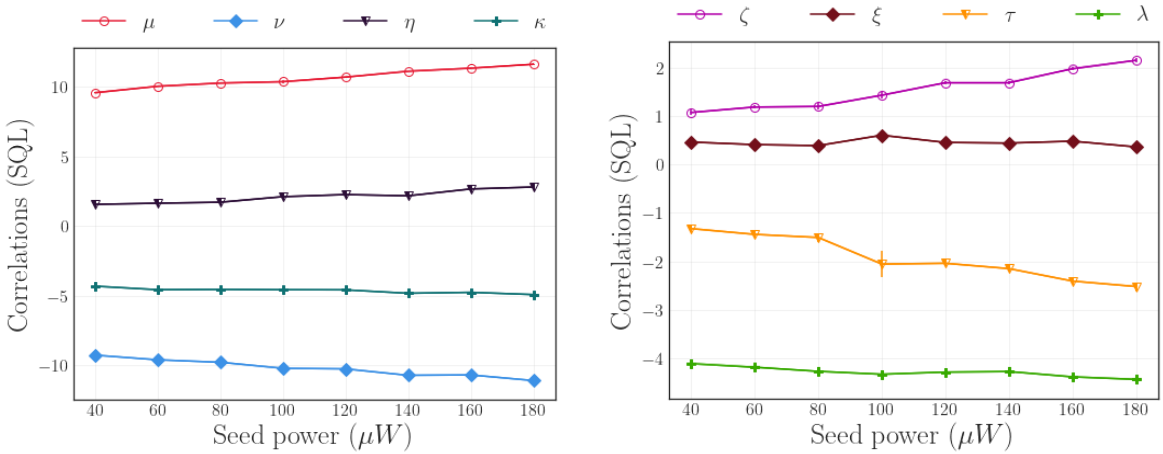

(a) Cross-mode correlations covariance matrix.

(b) Cross-mode correlations covariance matrix.

Figure C.3.6. Covariance matrix cross-correlations as a function of the seed power.

As for the entanglement, the Duan criterion in the SA basis presents a dependence with the seed power. In Figure C.3.7a we observe violation of the Duan criteria for power below $120\mu W$. This dependence was not seen before when studying the intensity correlations (subsection C.2.3). On the sideband basis, we extract extra information about the entanglement. Figure C.3.7b shows that the $[\Omega_{pr}, -\Omega_{cj}]$ bipartition is entangled whereas the bipartion $[-\Omega_{pr}, \Omega_{cj}]$ does not violate the criteria. In the PPT criteria (figure C.3.8) we observe that the $[\mathrm{S}_{pr}, \mathrm{S}_{cj} \times \mathrm{A}_{pr}, \mathrm{A}_{cj}]$ and $[\Omega_{pr}, -\Omega_{cj} \times \Omega_{cj}, -\Omega_{pr}]$ does not violate the criteria.

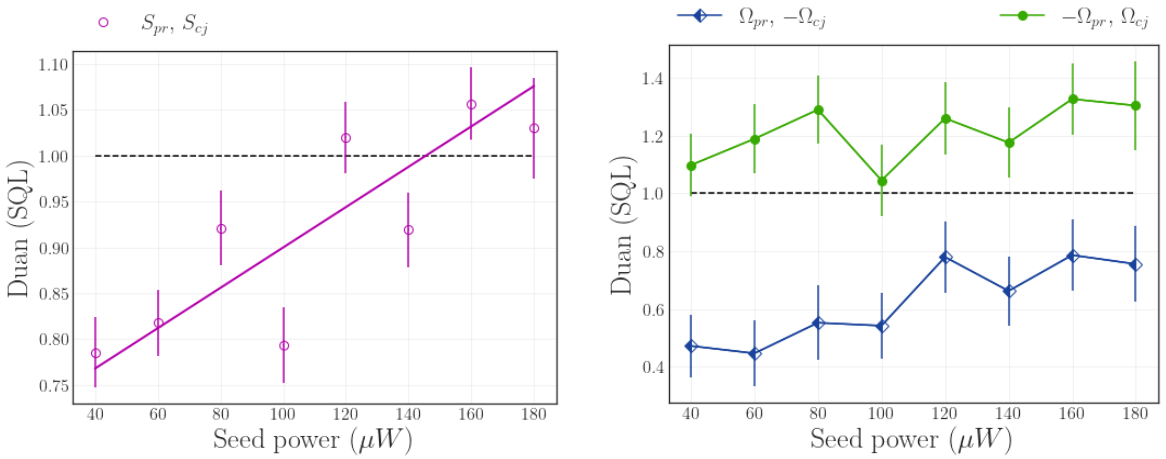

(a) Duan criterion in the symmetric/anti-symmetric basis. The straight line is guide to the eye.

(b) Duan criterion in the sideband basis.

Figure C.3.7. Duan criterion as a function of the seed power.

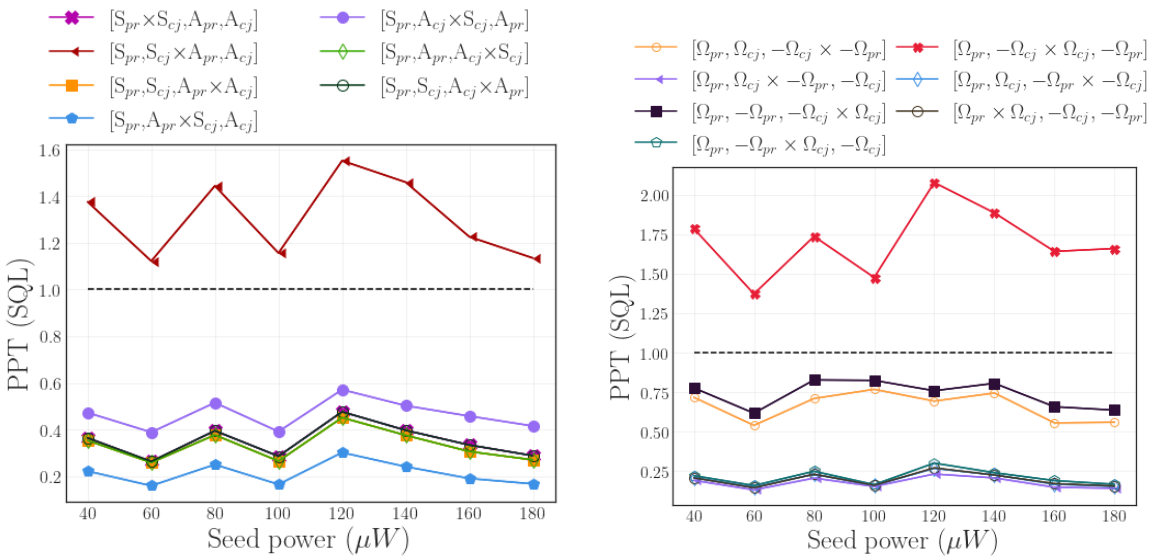

(a) PPT criterion in the symmetric/anti-symmetric basis.

(b) PPT criterion in the sideband basis.

Figure C.3.8. PPT criterion as a function of the seed power.

The seed power is not a decisive parameter for the generation or the control of the entanglement. However, the study of the Duan criteria showed interesting results. Under the SA basis, at low seed power the criteria was violated, behavior that disappears as the seed power increases. On the contrary, the *sideband basis* reveals that one bipartition is always entangled whereas the other one does not reveal entanglement. Furthermore, the PPT criteria is unaffected by the change of basis preserving the information of the correlations.

C.3.3 Temperature

The cell temperature have a strong impact on the FWM spectrum. Higher temperatures increases the gain and broadens the spectrum (see section C.1). Temperature will also alter the covariance matrix terms. The following study will be performed with the experimental conditions described in Table 6.

Table 6. Experimental parameters temperature characterization.

Pump power (mW)	Seed power (μW)	Analysis freq. (MHz)	Δ_2 (MHz)
420.0 ± 0.3	110.0 ± 0.3	10.0±0.1	1071.8 ±0.3

As discussed in section C.1, the temperature is an important factor in the amplification of the seed and the generation of the conjugated. This can be seen in Figure C.3.9a where the generated power of the beams raises with the temperature. Below 97°C, the probe and conjugated power are inferior to 0.49 mW, the lower limit established in subsection 2.4.2 for a reliable measurement. In Figure C.3.9b we observe that the coupling factor varies with temperature which is probably associated to Kerr effects as self-phase modulation leading to a lensing effect.

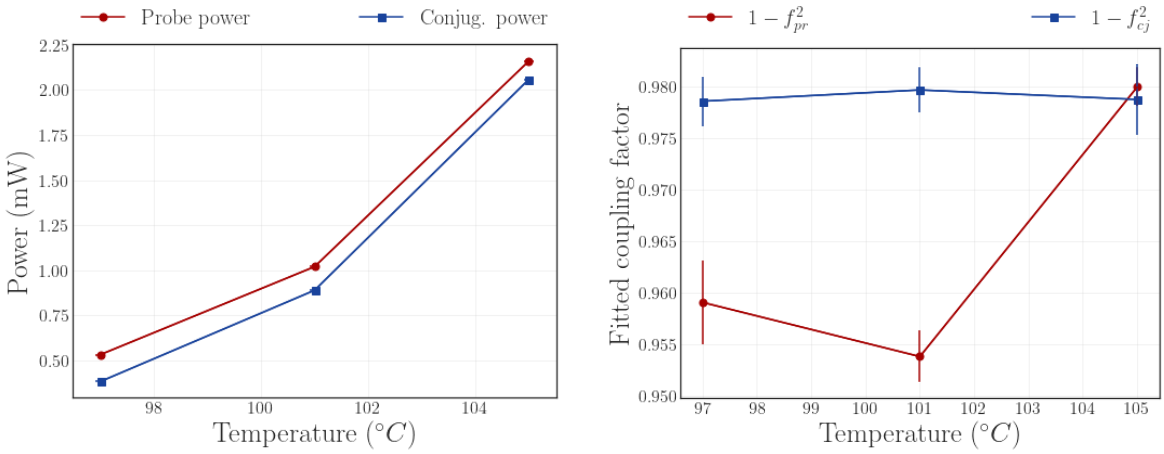

(a) Probe and conjugated power as a function of temperature.

(b) Coupling factor as a function of temperature.

Figure C.3.9. The power of the generated beams increases with temperature. The Gaussian profile of the beams is modified by the temperature.

The generated states increase their noise as we raise the temperature starting from values of $\alpha_{pr,cj}$ and $\beta_{pr,cj}$ around 5 SQL up to 17 SQL. The asymmetry is also enhanced reaching values of $|\delta_{pr,cj}| = 6$ (Figure C.3.10a,Figure C.3.10b). Notice that in general, the absolute value of the two-mode parameters raise their value with temperature denoting a more noisy state. For instance, $\mu = \langle \hat{p}_s^{pr}, \hat{p}_s^{cj} \rangle$ starts at 5 and reach 16 SQL, $\nu = \langle \hat{q}_s^{pr}, \hat{q}_s^{cj} \rangle$ starts at -5 and reach -15 SQL. As long as these parameters define the Duan inequality in the symmetric/anti-symmetric basis (figure C.3.11a), we can observe that at 97°C and 101

$°C$ the criteria is violated. However, at 105 $°C$ the noise of the quadratures of individual beams increase much more than the correlations and the entanglement is destroyed. In the sideband basis, the asymmetry $\delta_{pr,cj}$ affects the criteria (equations A.8 and A.9). Even when $\delta_{pr,cj}$ increases with the temperature, the entanglement is lost at 105 $°C$ (figure C.3.11b).

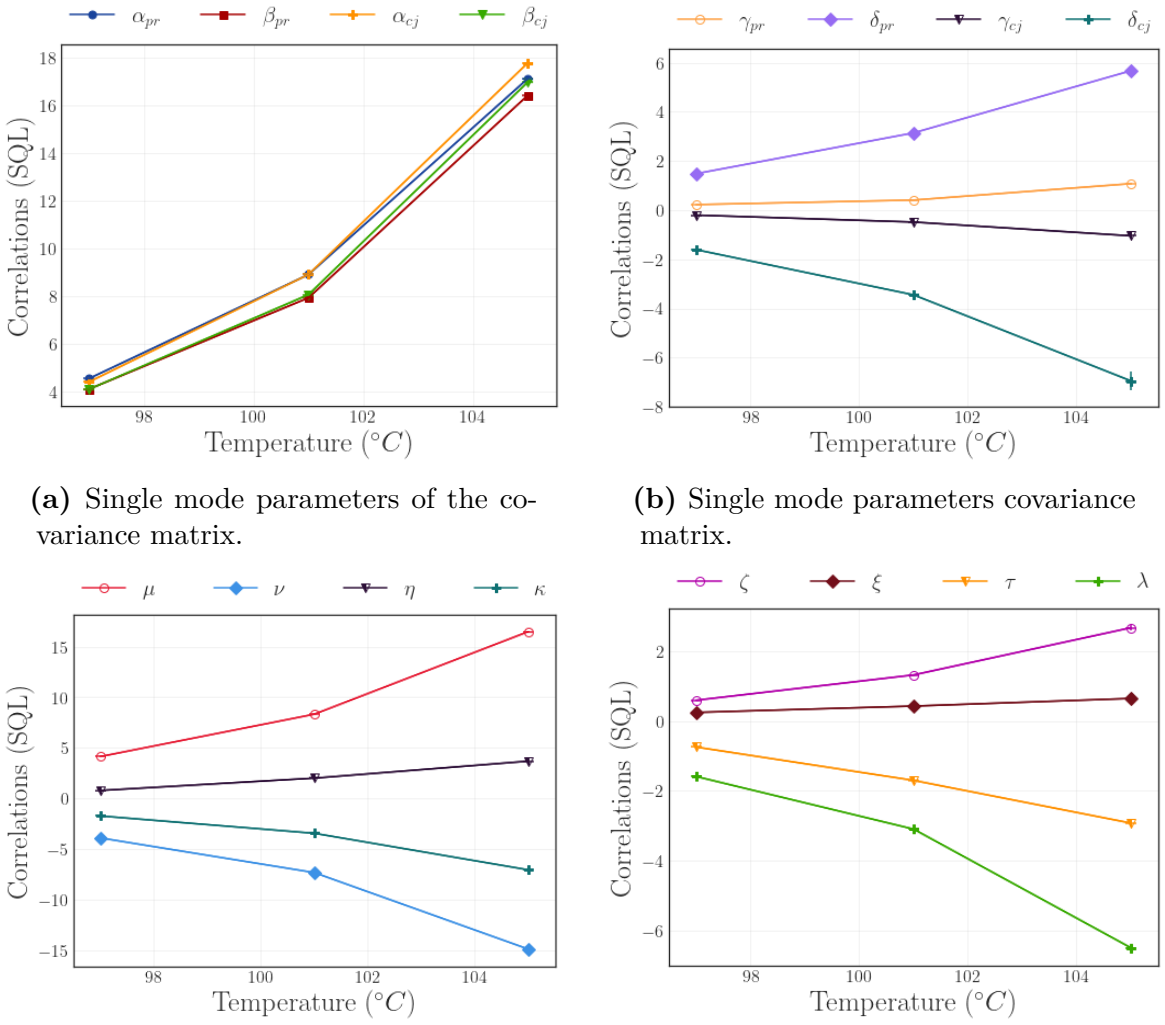

(a) Single mode parameters of the covariance matrix.

(b) Single mode parameters covariance matrix.

(c) Cross-mode correlations covariance matrix.

(d) Cross-mode correlations covariance matrix.

Figure C.3.10. Covariance matrix parameters as a function of the temperature. The generated states increase the noise level when the temperature raises. The asymmetry also increases.

The study of the entanglement using the PPT criterion in the SA basis shown in Figure C.3.12a, shows that there is entanglement at 97$°C$ and above. On the contrary, at higher temperatures the bipartition $[S_{pr},S_{cj}\times A_{pr},A_{cj}]$ does not violated the critarion. In the sidebands basis the bipartition $[\Omega_{pr},-\Omega_{cj}\times\Omega_{cj},-\Omega_{pr}]$ does not violate the entanglement witness. Notice that the bipartitions $[\Omega_{pr},-\Omega_{cj},-\Omega_{pr}\times-\Omega_{cj}]$ and $[\Omega_{pr}\times\Omega_{cj},-\Omega_{cj},\Omega_{pr}]$ have the same violation rate at any temperature. A similar behavior is presented between bipartitions $[\Omega_{pr},\Omega_{cj}\times-\Omega_{pr},-\Omega_{cj}]$ and $[\Omega_{pr},-\Omega_{pr}\times\Omega_{cj},-\Omega_{cj}]$.

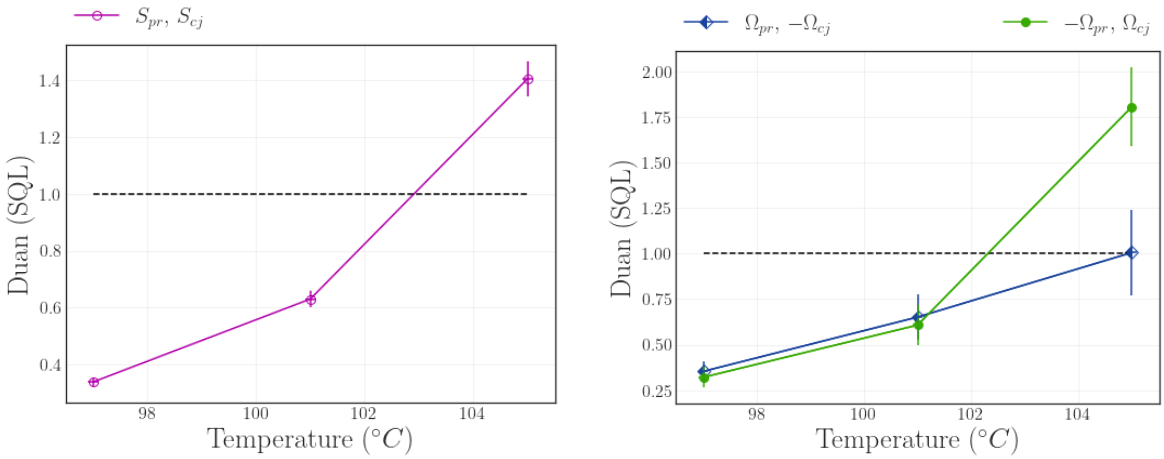

(a) Duan criterion in the symmetric/anti-symmetric basis.

(b) Duan criterion in the sideband basis.

Figure C.3.11. Duan criterion as a function of the temperature.

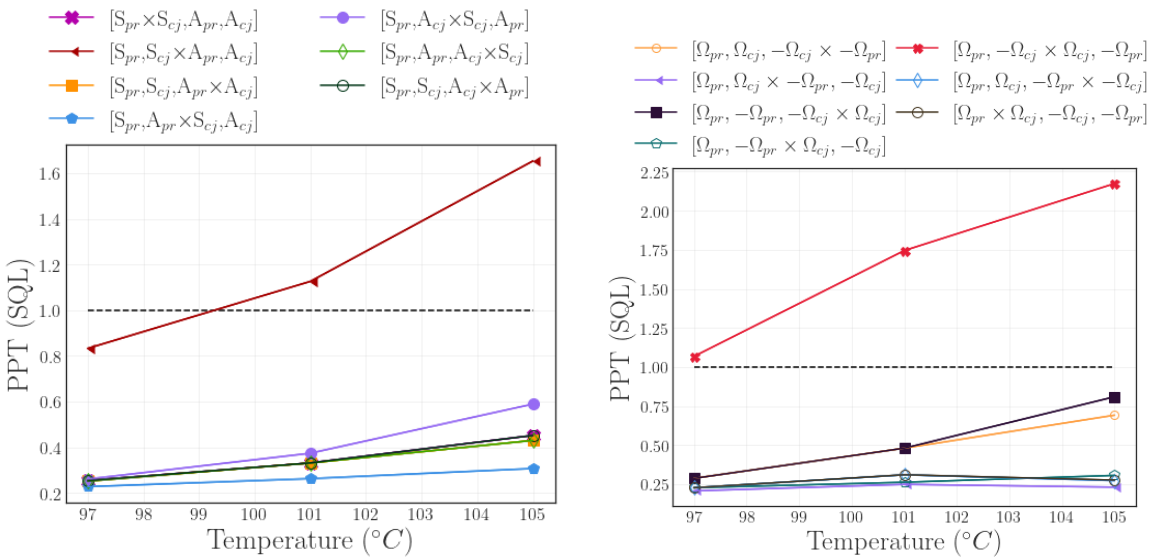

(a) PPT criterion in the symmetric/anti-symmetric basis.

(b) PPT criterion in the sideband basis.

Figure C.3.12. PPT criterion as a function of the temperature.

Increasing the range of temperatures for the tomography was a difficult task. On one side, lower temperatures were not enough to amplify the seed beam such that the detected noise is greater than the background electronic noise . Above 105°C the generated beams had a huge excess of noise with values of $\alpha_{pr,cj}$ around 30 SQL units. In this regime, unexpected electronic limitations are affecting the measurements of the FWM signal making every reconstructed state non-physical.

C.3.4 Duan criterion as a function of the analysis frequency: theoretical model

The electronic configuration presented some problems at analysis frequencies above Ω =10 MHz. Specifically, the stationary conditions were not satisfied such that the tomographies were not reliable most likely due to a nonlinear response of the electronics at a higher amplitude in the input. However, we could explore the response of the system considering the exposed theoretical model. Figure C.3.13 shows the results for the Duan criterion in the SA basis as a function of the analysis frequency Ω. We study the system response at two different probe detuning Δ_2. In figure Figure C.3.13a we show the results at $\Delta_2 = 1010$ MHz corresponding to a region of low gain. Notice that at this detuning, the violation of the criterion reaches values of 0.5 SQL at and a bandwidth of 25 MHz. The study at $\Delta_2 = 1055$ MHz reveals an increase in the violation criterion at low frequencies but a decrease in the violation bandwidth reaching values of 10MHz. This behavior recalls the characterization done for the intensity correlations (section 5.2).

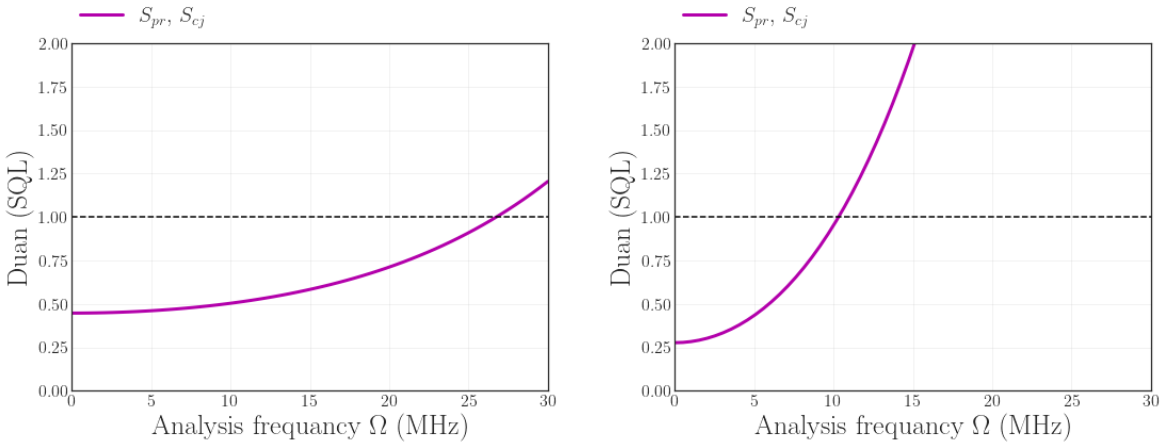

(a) Duan criterion SA basis at Δ_2 =1010 MHz.

(b) Duan criterion SA basis at Δ_2 =1055 MHz.

Figure C.3.13. Duan criterion SA basis as a function of the analysis frequency Ω.

Figure C.3.14 presents the theoretical model in the sideband basis. When the probe detuning is 1010 MHz, we observe the asymmetrical response of the two bipartitions. The bipartition $[\Omega_{pr}, -\Omega_{cj}]$ has a bandiwdth of 23 MHz, differently from the bipartition $[-\Omega_{pr}, \Omega_{cj}]$ that violates the Duan criterion at frequencies above Ω =30MHz. The maximum violation rate is the same for both bipartitions, and morover, is the same as the obtained in Figure C.3.13a. When the system is studied at $\Delta_2 = 1055$ MHz, the violation rate increases whereas the bandwidth is diminished reaching only values of 8 MHz for the bipartition $[\Omega_{pr}, -\Omega_{cj}]$, and 16 MHz for $[-\Omega_{pr}, \Omega_{cj}]$.

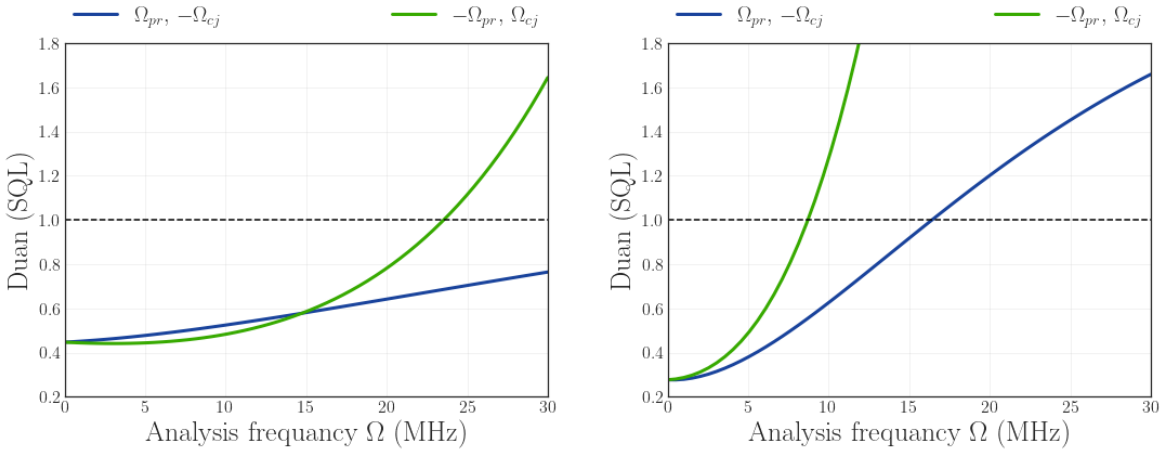

(a) Duan criterion sideband basis at Δ_2 =1010 MHz.

(b) Duan criterion sideband basis at Δ_2 =1055 MHz.

Figure C.3.14. Duan criterion sideband basis as a function of the analysis frequency Ω.